Development and Application of an Integrated Hydro-environmental Model for Predicting the Distribution of Nutrients in Estuarine and Coastal Waters

by

Xiaolin Wang

Thesis submitted for the degree of Doctor of Philosophy

Cardiff School of Engineering, Cardiff University

March 2011

ProQuest LLC
789 East Eisenhower Parkway
P.O. Box 1346
Ann Arbor, MI 48106-1346

Singed..Xiaolin Wang..... (Xiao Wang)

Date....26/05/2011.....

STATEMENT 1

This thesis is being submitted in partial fulfillment of the requirements of t degree of PhD.

Singed....Xiaolin Wang..... (Xiao Wang)

Date.....26/05/2011.....

STATEMENT 2

This thesis is the result of my own independent work/investigation, exc where otherwise stated. Other sources are acknowledged by expli references.

Singed....Xiaolin Wang..... (Xiao Wang)

Date.....26/05/2011.....

STATEMENT 3

I hereby give consent for my thesis, if accepted, to be available f photocopying and for inter-library loan, and for the title and summary to made available to outside organizations.

Singed....Xiaolin Wang..... (Xiao Wang)

Date....26/05/2011.....

ACKNOWLEDGEMENTS

I would like to express my gratitude and appreciation to my supervisors Professor Roger Falconer and Dr. Bettina Bockelmann-Evans, for their constant support and guidance throughout the duration of my PhD study.

I would like to thank all my colleagues in Hydro-environmental Research Centre at Cardiff University for their kindness and continuous assistance during my study.

Special thanks to Professor Binliang Lin for his generous support and helpful advices. My thanks are also extended to my friends and my office mates, for their encouragement and friendship.

I would like to say that I am eternally grateful to my husband, Dongfang, for his continuous love, support and understanding. I would like to express my appreciation to my son, Luke, who brought a lot of happiness to my life. I am also indebted to my family for their consistent help and support.

Abstract

This study presents the development and application of an integrated hydrodynamic and water quality model for predicting the distribution of nutrients in estuaries and coastal waters.

The integrated model consists of four major components. The first is a two-dimensional hydrodynamic model, which solves the shallow water equations using either the Alternate Direction Implicit (ADI) scheme or the Total Variation Diminishing (TVD) MacCormack scheme. This hydrodynamic model has been applied to predict the tidal oscillations of: (i) the Persian/Arabian Gulf, where good agreement has been obtained between computational and Admiralty Tide Table (ATT) predicted tidal elevations, and (ii) the Loughor Estuary, sited in Bristol Channel U.K., where the computational results matched field measurements with an encouraging level of agreement. The second component is a solute transport model, which solves the depth-integrated advection/diffusion/reaction equation with the TVD-MacCormack scheme. This solute transport model has been validated against benchmark examples and compared with other shock-capturing methods. The results show that the newly-developed solute transport model is highly efficient with a high level of numerical accuracy. The third component is a nutrients and dissolved oxygen (DO) interaction model, which is based on the QUAL2E and WASP6 algorithms. The fourth component is a sediment-nutrients interaction model, which accounts for the nutrient adsorption/desorption processes during the sediment deposition and re-suspension phases in estuarine morphodynamic processes. The latter two components enable the representation of the complex biological conversions of nutrients and the nutrient exchange between the water column and the bed sediments.

In order to calibrate the water quality parameters for the Loughor Estuary,

field data have been collected and analysed. Empirical formulae have been proposed for ammonium adsorption isotherms and salinity effects on nitrogen and phosphorous adsorption rates. The integrated model is finally applied to simulate the hydro-environmental processes in the Loughor Estuary to find out the contributions of different pollution sources on the receiving water nutrient concentration levels, and the influences of pollutant discharging schemes and temperature. The results show that the refined model is accurate and provides a valuable state-of-the-art novel tool for predicting nutrient concentration distributions in estuarine and coastal waters.

CONTENTS

LIST OF FIGURES

CHAPTER 3

CHAPTER 4

CHAPTER 5

CHAPTER 6

CHAPTER 7

CHAPTER 8

LIST OF TABLES

CHAPTER 2

CHAPTER 3

CHAPTER 5

CHAPTER 7

CHAPTER 8

NOTATIONS

a	reference elevation above the bed
a_i	Amplitude of an astronomic tide
A	concentrations of the algal biomass
$AFACT$	light averaging factor
c_o	maximum volumetric concentration
c_b	volumetric concentration
c_e	eddy viscosity coefficient
C	Chézy roughness coefficient
C_0	initial concentration
C_d	dissolved concentration
C_D	drag coefficient
C_e	dissolved concentration at equilibrium
C_f	dimensionless friction coefficient
C_p	particulate concentration
C_r	Courant number
C_{SAL}	salinity level (ppt)
C_T	total concentration
C_T^0	initial concentration of total nutrient in the water column
C_w	air/fluid resistance coefficient
$Chla$	concentrations of the chlorophyll a
d	sediment diameter
d	the average water depth
D	cohesive sediment deposition rate
D_g	algal grazing rate
D_{loss}	algal death rate
D_m	algal mortality rate

D_s	characteristic particle size
D_*	dimensionless particle parameter
D_{xx}	longitudinal dispersion coefficient in x-direction
D_{xy}	depth averaged turbulent diffusion coefficient in x-direction
D_{yx}	depth averaged turbulent diffusion coefficient in y-direction
D_{yy}	longitudinal dispersion coefficient in y-direction
D_{50}	median particle diameter
E	cohesive sediment erosion rate
f	Coriolis coefficient;
f	fraction of daylight hours
f_d	fraction of nutrient dissolved in the water column
f_{D2}	Fraction of dissolved organic nitrogen
f_{D3}	Fraction of dissolved organic phosphorus in the water column
f_{D4}	Fraction of dissolved inorganic phosphorus in the water column
f_i	height of each tidal constituent
f_{ON}	Fraction of dead and respired algae recycled to the organic nitrogen pool
$(1-f_{ON})$	Fraction of dead and respired algae recycled to the ammonia nitrogen pool
f_{op}	Fraction of dead and respired algae recycled to the organic phosphorus pool
$(1-f_{op})$	Fraction of dead and respired algae recycled to the phosphate phosphorus pool
f_p	fraction of nutrient attached to the suspended sediment
F	fraction of algal nitrogen taken from ammonia pool
F_{dep}	settlement flux from the water column to the bed sediment
F_{net}	net nutrient flux
FL	light limitation factor
FN	nitrogen limitation factor

FP	phosphorus limitation factor
g	gravitational acceleration
h	total water depth
h_b	thickness of the bed sediment
H	total water depth
I	daylight average light intensity
k_0	partition coefficient in fresh water
k_s	roughness height
K_1	carbonaceous BOD deoxygenation rate
K_2	oxygen reaeration rate
K_3	CBOD settling rate at 20 °C
K_4	sediment oxygen demand rate
K_a	Langmuir adsorption constant
K_{BOD}	Half saturation constant for oxygen limitation
K_d	partition coefficient
K_L	half saturation coefficient for light
K_{mpc}	Half saturation constant for algae limitation of nitrogen recycle
K_N	Michaelis-Menton half-saturation constants for nitrogen
K_P	Michaelis-Menton half-saturation constants for phosphorus
K_{NIT}	Half saturation constant for oxygen limitation of nitrification
K_{NO3}	Michaelis constant for denitrification
L	concentration of ultimate carbonaceous BOD
M_b	mass of the bed sediment per unit area
n	Manning coefficient
N_1	concentration of organic nitrogen
N_2	concentration of ammonia nitrogen
N_3	concentrations of nitrate nitrogen
O	concentration of dissolved oxygen
O^*	dissolved oxygen saturation concentration

p	instantaneous pressure
p	discharges per unit width in x direction
P	mass of nutrient attached to the suspended sediment
P_1	concentration of organic phosphorus
P_2	concentrations of inorganic phosphorus
P_b	amount of nutrient attached to the bed sediment
P_N	Preference for ammonia uptake term
q	discharges per unit width in y direction
q	the amount of fixed ammonium on the sediment
q_0	adsorption in fresh water
q_b	volumetric bed-load transport rate
q_{dep}	is the sediment deposition rate
q_e	adsorption capacity
q_m	source discharge per unit horizontal area
q_m	maximum adsorption capacity
q_s	source/sink of solute per unit area
s	specific density of sediment
s_ρ	specific particle gravity
S	suspended sediment concentration
S_0	initial concentration of suspended sediment in the water column
S_a	sediment concentration at a reference level a
$S_{a,e}$	equilibrium sediment concentration at reference level a
S_b	bed sediment concentration
$S_b{}^p$	source term defining particulate flux from or to the bed
S_e	depth averaged equilibrium sediment concentration
$S_o{}^d$	source or sink of dissolved nutrients; and is the
S_t^d	transformation term defining adsorbed or desorbed particulate fluxes to or from the suspended sediments
$S_o{}^p$	source or sink of particulate nutrients

S_t^p	transformation term defining adsorbed or desorbed particulate fluxes to or from the suspended sediments
T_a	absolute temperature
T	temperature (°C)
T	sediment transport stage parameter
T_i	period for each tidal constituent
U	depth averaged velocity component in x direction
u	instantaneous velocity component in x direction
u_b	particle velocity
u_{*cr}	critical shear velocity
V	depth averaged velocity component in y direction
v	instantaneous velocity component in y directions
w	instantaneous velocity component in z direction
w_s	sediment settling velocity
X_T	value of the coefficient at the local temperature (T)
X_{20}	value of the coefficient at standard temperature (20°C)
z_b	bed elevation below datum
α	sediment concentration profile parameter
α_0	conversion factor between chlorophyll a and algal biomass
α_1	Fraction of algal biomass that is nitrogen
α_2	Fraction of algal biomass (A) that is phosphorus (P)
α_3	rate of oxygen production from algal photosynthesis
α_4	Oxygen uptake per unit of algae respired
α_5	Oxygen uptake per unit of ammonia nitrogen oxidation
β	momentum correction factor for a non-uniform vertical velocity profile;
β_1	Organic nitrogen mineralization rate at 20 °C
β_2	Nitrification rate at 20 °C
β_3	Denitrification rate at 20 °C

β_4	Dissolved organic phosphorus mineralization at 20 °C
γ	sediment concentration profile factor
δ_b	thickness of bed load layer
δ_i	phase of an astronomic tide
ε	depth averaged turbulent eddy viscosity
ε_l	dimensionless constants for longitudinal dispersion
ε_t	dimensionless constants for turbulent diffusion
η	water surface elevation above datum
θ	temperature correction coefficient
θ	dimensionless mobility parameter
θ_{cr}	critical Shields' parameter
θ_1	Temperature coefficient for β_1
θ_2	Temperature coefficient for β_2
θ_3	Temperature coefficient β_3
θ_4	Temperature coefficient for β_4
θ_{K3}	Temperature coefficient for K_3
θ_{K1}	Temperature coefficient for K_1
θ_{K4}	Temperature coefficient for K_4
κ	von Karman's constant
λ	light extinction coefficient
λ_0	non-algal portion of the light extinction coefficient
λ_1	linear algal self shading coefficient
λ_2	nonlinear algal self shading coefficient
μ	viscosity coefficient
μ	algal growth rate
μ_{max}	maximum algal growth rate
ν	kinematic viscosity
ρ	algal respiration rate

ρ	fluid density
ρ_a	air density
ρ_s	specific particle density
σ_1	algal settling rate
σ_2	Organic nitrogen settling rate
σ_3	Organic phosphorus settling rate
σ_4	Inorganic phosphorus settling rate
$\tau,\ \tau_b$	bed shear stress
$\tau_d,\ \tau_{c,d}$	critical shear stress for deposition
$\tau_e,\ \tau_{c,e}$	critical shear stress for erosion (re-suspension)
ϕ	source or sink term of sediment
ω_i	angular speed(or frequency) of an astronomic tide

ABBREVIATIONS

WFD	Water Framework Directive
DIVAST	Depth Integrated Velocities and Solute Transport)
HEMAT	Hydro-Environmental Modelling and Analysing Tool
FDM	Finite Difference Method
FEM	Finite Element Method
FVM	Finite Volume Method
MUSCL	Monotone Upstream-centred Scheme for Conservation Law
TVD	Total Variation Diminishing
ADI	Alternating Direction Implicit
BOD	Biological Oxygen Demand
DO	Dissolved Oxygen
CBOD	Carbonaceous Biochemical Oxygen Demand
ATT	Admiralty Tide Table
SHM	Simplified Harmonic Method
UKHO	United Kingdom Hydrographic Office
EAW	Environment Agency Wales
STWs	Sewage Treatment Works
LiDAR	Light Detection And Ranging
DTM	Digital Terrain Models
DSM	Digital Surface Models
CD	Chart Datum
OD	Ordnance Datum
DIN	Dissolved Inorganic Nitrogen
DIP	Dissolved Inorganic Phosphorus
TON	Total Oxidized Nitrogen
AMN	Ammonium Nitrogen

Chapter 1

Introduction

1.1 Overview

Water pollution may be caused by agricultural, industrial or municipal wastes. With the increasing awareness of environmental issues, understanding and predicting the fate of pollutants in water bodies become more and more necessary. The European Union (EU) launched the Water Framework Directive (WFD, 2000/60/EC), to establish a framework for protection of all aquatic ecosystems and, with regard to water needs, ensuring the ecosystems meet "good status" by 2015. Some key policy instruments also have been taken to address the most significant pressure to water problems, such as Nitrate Directive (ND, 91/676/EEC), which considers the agricultural contribution and the Urban Waste Water Treatment Directive (UWWTD, 91/271/EEC), which focuses on urban sewage discharges. Among those concerns of water pollution, eutrophication has been described as one of the greatest contemporary threats to the integrity of coastal ecosystems (Vitousek et al., 1997; Vidal et al., 1999) and it is widely accepted that the increased availability of nutrients (generally nitrogen and phosphorus) is a major factor that drives eutrophication in estuaries (Nixon, 1995; Nedwell et al., 1999; Scott et al., 1999; de Jonge and Elliott, 2001). Excessive nutrients stimulate algae growth. When algae die and accumulate on the bottom, where bacteria consume them, oxygen is depleted with an associated loss of plant and animal species, which may cause an ecosystem imbalance and can be detrimental to human health. Therefore, the ability to predict the nutrient distribution and processes in such water areas is important for the hydro-environmental management.

Nutrients come from various sources, such as surface runoff, waste water

treatment works discharge, organism decomposition in the water body, as well as bottom sediment re-suspension. Nutrients enter into the water column in mainly two ways, either as point source or as non point source (diffuse source). Point source pollution comes from a specific location which is relatively easy to be investigated and controlled, while diffuse source pollution derives from different sources with no specific solution to rectify the problem, making it difficult to regulate.

Nitrogen (N) and phosphorus (P) fractions in the water column can be inorganic or organic and conceptually divided as dissolved phase or particulate phase. Organic and inorganic N and P are produced and consumed through biological, chemical and physical processes, and they occur in a dynamic balance in a static water body. The inorganic species are readily utilized by primary producers and appear to have more potential to limit plant growth. The dissolved phase is defined as solute which can go through a 0.45μm sieve, and the particulate phase is defined as the nutrient ions that can be adsorbed on the sediment surface due to cation exchange (Berner, 1980; Mackin and Robert, 1984; Morin and Morse, 1999). Dissolved N and P may adsorb onto the sediments, transforming to particulate phase, and the attached N and P can be desorbed from sediment becoming dissolved phase. Deposition of the sediments can take particulate nutrients out of the water column and to the bed. The sediments can subsequently be re-suspended to the water column, which can then lead to re-suspension of the nutrients of the attached forms back into the water column. Therefore the adsorption of the nutrients by sediment has an important role on nutrients cycling, which affects not only the diffusion flux to the overlying water, but also the coupled process in the water column. Moreover, the behaviour of suspended sediment can also affect the water quality by changing the turbidity, whose effect on the underwater light climate is an important environmental condition for algae growth. The presence of suspended sediment increases the attenuation of light in the water column, which leads to an inhibition of photosynthetic activity, and hence a reduction in primary production.

The distribution and transport processes for nutrients are very complex, and include the processes of advection, dispersion/diffusion, deposition/re-suspension, adsorption/desorption and biological decay. Each process is affected by different environmental and natural conditions. Advection and dispersion are dominated mainly by flow conditions. Deposition and re-suspension are controlled by sediment transport. The biological decay rates are influenced by many environmental factors, such as light intensity, temperature, salinity, turbidity levels and pH value etc. The sediment-nutrients adsorption processes are affected by the sediment particle size and mineralogy, salinity, charge density and the temperature (Abdulgawad, 2010). The key variables affecting the N and P adsorption processes are investigated in this study.

Numerical simulations have been proven to be an effective way to address the complex hydro-environmental challenges. The integrated hydrodynamic and water quality model can predict the flow field and water quality indicator as well as sediment transport levels in estuarine and coastal waters. In general, numerical modelling of nutrient distributions is a very complex process, which can be sub-divided into three parts: hydrodynamic modelling, solute transport modelling and biological process modelling. Hydrodynamic modelling is used to study the flow field and provide an accurate level of prediction for velocity and the turbulent diffusion and dispersion mixing processes. Solute transport modelling is used to predict the advection, dispersion /diffusion and the bio-chemical processes for a tracer or solute by using the flow field data from the hydrodynamic modelling. The biological process is used to provide the source/sink terms for nutrient cycling in the solute transport model, with the terms including the kinetic processes of nutrients, which include both the biological decay process and physical losses.

In previous studies numerical models for predicting nutrient transport processes generally treated N and P as dissolved in the water column, the deposition/re-suspension and adsorption/desorption processes were not included and little attempt has been made to model such processes in terms of predicting the impact of the sediment fluxes on nutrients levels. There is a current lack of

sophisticated numerical models which are capable to simulate the sediment effects on nutrients processes.

1.2 Objectives of the thesis

This study aims to establish an effective numerical model to simulate the distribution and transport of nutrients, focusing on sediment-nutrient interaction, using a sediment-nutrient adsorption model based on experimental data from both laboratory and field work. Numerical models have been refined for predicting hydrodynamic, sediment transport and nutrient biological cycling processes, as well as sediment-nutrient interaction in the bed and water column. The main objectives and achievements can be summarized as follows:

(1) Refinement of the water quality model

The profound understanding of the reaction processes among water quality constituents is the base of further study on the hydro-environment modelling in this study. A detailed yet pragmatic water quality model is necessary to simulate the complex chemical, biological and physical processes. An existing numerical model has been refined under the framework of QUAL2E (Brown and Barnwell, 1987). New formulae and coefficients have been introduced, based on WASP6 (Wool et al., 2001), to consider more factors in various conditions. The improved model inherits the simplicity and clarity of QUAL2E, and combines it with more practical and experienced parameters of WASP6.

(2) Development of a solute transport model

A new simple five-point TVD-MacCormack scheme has been employed to solve the depth-averaged solute transport equation, which considers advection, diffusion and reaction. The model runs independently and can be linked with a related hydrodynamic model. This development enables the modelling of solute or pollutant transport, after the flow field is solved. As the same numerical scheme is used for both the hydrodynamic and water quality processes, the integration of the

simulations is efficient and flexible.

(3) Numerical modelling of sediment-nutrient interactions

Sediment re-suspension and deposition may have important effects on the flux of nutrients taken into or from the overlying water. In previous studies, models for nutrients prediction generally considered the dissolved nutrients in the water column, the sediment attached nutrients and their adsorption/desorption with the sediment deposition and re-suspension processes were not included. This study established a new sub-model to describe the nutrients exchange between the sediment and the water column.

(4) Hydrodynamic models comparison and application

Two types of numerical models, namely, ADI model and TVD-MacCormak model, are compared in terms of their performances in solving the two dimensional shallow water equations. Apart from hypothetical examples, the two types of hydrodynamic models are applied to simulate the tidal processes of the Persian/Arabian Gulf, where the water motion is mainly caused by the astronomic tide. The Simplified Harmonic Method (SHM) for tidal predictions based on the Admiralty Tide Tables (ATT) is used to verify the predicted results by the hydrodynamic models.

(5) Analysis of adsorption experiments

Two types of adsorption models are applied to describe the ammonium nitrogen adsorption process on four types of commercial sediments, and the results are compared with the theoretical solutions derived for dissolved and particulate concentrations. Field sediment samples are also analyzed and the salinity effects on the adsorption of ammonium nitrogen and orthophosphate have been quantified by two types of equations. The applicability of the sediment adsorption isotherms for different equilibrium concentrations are also discussed, as well as the amount of the fixed ammonium on the sediment during the adsorption/desorption processes.

(6) Numerical testing of the water quality and sediment-nutrient interaction processes

The numerical solutions are compared with the analytical solutions of a time variable process for two reactors by solving the first order ordinary differential equations. This study also compares the numerical solutions against the analytical solutions for the sediment deposition and re-suspension processes accompanied by the nutrient reduction and increase through their interaction, and the sensitivities of some key coefficients during these processes are also tested.

(7) Numerical model application to the Loughor Estuary

The integrated hydro-environmental model was applied to simulate the hydrodynamic and water quality processes in the river Loughor and its estuary. It is a shallow, muddy estuary with the largest tidal range of approximately 8m, which sometimes suffers from the threat of eutrophication. The model was firstly calibrated against field data and then run for simulations of different scenarios to study the effects of different hydro-environmental conditions on the nutrient distributions in the Loughor Estuary.

1.3 Outline of the thesis

Details of the remaining chapters can be outlined as follows.

Chapter 2 reviews the recent development of hydrodynamic and water quality models, introduces the widely used sediment transport model with researches related to the sediment effects on nutrients.

Chapter 3 discusses the derivation of hydrodynamic governing equations, as well as the parameters quantifying the hydrodynamic processes occurring specifically in coastal and estuarine water systems. The comparisons between the ADI model and TVD-MacCormack model have been investigated, for both hypothetical examples and real terrain application to the Persian/Arabian Gulf.

Chapter 4 establishes a new method to solve the advection-diffusion problem

numerically. The model has been tested against the analytical solutions, and also compared with the results from other models like DIVAST, HEMAT and MacCormack standard model.

Chapter 5 describes the biological processes for nitrogen and phosphorus cycles, as well as algae growth and dissolved oxygen consumption processes. The conceptual framework of the related reactions among each water quality constituent is based on QUAL2E, the formulae and parameters used in chemical and biological transformation are based on WASP 6.

Chapter 6 develops a conceptual model to study the nutrient exchange between the interface of bed sediment and the overlying water. Idealised cases are designed to validate the correctness of the numerical model, and the sensitivities to some coefficients in the model are also discussed.

Chapter 7 studies the adsorption isotherms for both ammonium and orthophosphate, and concludes that both Langmuir and linear equations can be fitted for low nutrient concentrations, while the Langmuir equation is more favourable for high concentrations. The salinity effects on the adsorption capacity and the partition coefficient are also addressed.

Chapter 8 provides the simulation results for the river Loughor and its estuary. The model was calibrated for the water level, tidal current, salinity and suspended sediment concentration before its application to the nutrients in the Loughor area.

Chapter 9 summarizes the conclusions drawn from this research work and gives recommendations for future studies.

Chapter2

Literature review

2.1 Hydrodynamic and solute transport models

2.1.1 Introduction

A hydrodynamic model is the basic tool to understand the mechanisms governing the mixing processes and predicting the flow field and the distribution of the contaminant quantities. With the rapid progress in computer science and numerical methods, computational simulations play an increasingly important role to address the hydro-environmental challenges (Holly and Usseglio-Polatera, 1984; Falconer, 1991; Lin and Falconer, 1997). Numerous practical models have been developed and applied in the past decades. Hydrodynamic and solute transport models are the common parts of these models. There are various criteria to categorize them. For example, they can be classified as one-dimensional (1D), two-dimensional (2D) and three-dimensional (3D) models, according to the method of solving the governing equations. They can also be classified by other aspects, such as the numerical methods of discretization in time and space, the techniques of processing boundaries, as well as by how they are handling wetting and drying cells in inter-tidal areas. In this chapter the development of different numerical models and the related numerical techniques involved in this study are reviewed.

2.1.2 The Navier-Stokes equations

The common basis for these modelling activities is the numerical solution of the Navier-Stokes equations, which describe the conservation of mass and

momentum in a fluid. There are a few implicit assumptions on how the equations are written in the partially derivative form (Martin et al, 1999). These include: the fluid being hydrostatic, incompressible and Boussinesq (density differences are negligible unless multiplied by gravity). One-dimensional models based on the St Venant equation, such as HEC-RAS (USACE, 2004) and DYNHYD5 (USEPA, 1993), have proved their capability for practical purpose. They are suitable for the simulation of river channel flow, with simple geometry and deep water, but they can not simulate rapid flow variation in shallow waters. Two dimensional depth integrated model based on Shallow Water Equations (SWEs), have advantages in simulating flows in large water areas, where the horizontal scale is much larger than the vertical scale, such as river, estuarine and coastal waters, where the acceleration along the vertical direction is negligible, and hydrostatic pressure can be assumed along the depth. These models, such as DIVAST (Falconer et al, 2001) and HEMAT (Namin et al, 2004), have been applied broadly, and produced accurate results (Kashefipour et al, 2002; Lin et al., 2006; Liang et al., 2006; Schnauder et al., 2007). Three-dimensional models are used to simulate flow in deep and large water bodies where the vertical scale can not be neglected. Widely used models include POM (Blumberg and Mellor, 1983, 1987), ECOMSED (HydroQual, 2002), EFDC (USEPA, 2002) and FVCOM (Chen et al., 2003).

2.1.3 Grid systems

The geometry and topography of a given water body must be approximated by a computational finite grid system to solve the aforementioned governing equations. Grid systems can be categorized as structured and unstructured. Structured grid systems are simple and efficient in solving the governing equations, and the stability of the fluid flow solution algorithm on the structured grid system is essentially higher than on the unstructured grid system. The widely used structured grids are rectangular grids with fixed grid spacing (Wang et al., 1990; Kankara et al., 2007), stretched rectangular grids (Butler, 1980), and curvilinear,

boundary-fitted coordinate systems which allow better adaptation of complicated shorelines and irregular boundaries (Bao et al., 2000; Blumberg and Herring, 1987). Unstructured grid systems can easily refine and coarsen the grid according to the complexity of the geometries, the flexibility make it more suitable for simulating domain with irregular boundaries and numerous barrier islands and tidal creeks. Triangles and tetrahedras are the commonly used unstructured girds (Levasseur et al., 2007; Liu et al., 2008) in finite volume scheme, quadrilateral (4-noded) and hexahedral (8-noded) elements are often used in finite element simulation.

2.1.4 Numerical approach and algorithms

The finite difference method (FDM) is the simplest discrete scheme with an advantage of computational efficiency, but it can only be applied with rectangular grid or orthogonal curvilinear grid, which is less flexible in fitting complex boundaries. Moreover, since the FDM method is based on Taylor series analysis, there must be truncation errors in the calculation, so the result is not guaranteed in mass and momentum conservation (Chen, 1994; Armenio, 1997). The finite element method (FEM) has an advantage of geometric flexibility which can provide an accurate fitting of the irregular boundary, but it needs to solve a large matrix of equations in every calculating time step, which makes it run slowly with a low efficiency (Horsburgh, 1999). The finite volume method (FVM) has the same advantage of flexibility with FEM and similar efficiency with FDM, its discretization complies with conservation laws which make it more accurate than FDM (Levasseur et al., 2007; Xia et al., 2010). But FVM has a disadvantage of low precision which makes it difficult to run in high order discrete scheme.

2.1.5 Solution of advection and diffusion equation

Advection and diffusion are the two fundamental transport mechanisms for solutes within the water body, and the advection is the predominant factor in most

of the practical solute transport problems. Numerical difficulties often arise from the advection process, which is governed by a hyperbolic type of partial differential equation. This equation admits discontinuities in the solution, which are often called shocks. Traditional numerical schemes exhibit large numerical errors close to the discontinuities and regions with steep changes, as they either smear out the sharp variations due to excessive artificial damping or incur spurious oscillations – Gibbs phenomenon – in the vicinity of shocks. The method of characteristics is a powerful tool to probe the mathematical properties of hyperbolic equations. If implemented numerically, however, it unavoidably requires frequent numerical interpolation to relate the values on the characteristic lines to those at the computational grid, hence numerical damping and oscillations may still arise. Godunov (1959) pioneered the development of modern shock-capturing schemes for fluid mechanics. In Godunov's original scheme, the conservative variable is regarded as a piecewise constant over each computational cell and the flux at the cell interface is determined by solving a Riemann problem. The Monotone Upstream-centred Scheme for Conservation Law (MUSCL) by van Leer (1979) replaces the piecewise constant approximation of Godunov's scheme with the slope-limited left and right extrapolated state variables, which are used to calculate the flux at the cell interface. The MUSCL scheme results in high resolution with the help of an appropriate slope limiter. To facilitate the development of Godnov-type schemes, different approximate Riemann solvers have been proposed in fluid dynamics (e.g. Roe 1981). For the case of scalar advection, degenerate Riemann problem has trivial exact solution (e.g. Mingham and Causon, 2008). Godunov-type schemes have been popular for being "physical". From mathematical perspective, Harten (1983) introduced the Total Variation Diminishing (TVD) concept. According to the Godunov Theorem (Godunov 1959), any TVD linear scheme can be at most first-order accurate, Harten (1983) thus established high-resolution TVD schemes by devising nonlinear coefficients for unknown variables. Various Essentially Non-Oscillatory (ENO) schemes developed by Harten et al. (1987) achieve uniformly high order

accuracy by shifting the interpolation stencil, yet still retain numerically non-oscillatory behaviour. There are also some very accurate algorithms to solve the pure advection equation for interface tracking (e.g. Hirt and Nichols, 1981), but it should be noted that these algorithms only deal with insoluble tracers and cannot be applied to solute transport problems.

2.2 Water quality models and eutrophication criteria

2.2.1 Overview of water quality models

Water quality changes in rivers and coastal areas are due to physical transport and exchange processes (such as advection and diffusion/dispersion), and biological, chemical, biogeochemical and physical conversion processes. Water quality models can be classified according to particular problems they are focused on, such as heavy metal contaminant model, eutrophication model, bacteria pollution model, toxin pollution model, etc. Components of state variables have been gradually incorporated into models over the past decades following the evolution of water quality problems. The water quality model has originated from as early as 1925, raised by Streeter and Phelps, for stream simulation of biological oxygen demand and dissolved oxygen (BOD and DO) level with a linear relationship (Streeter and Phelps, 1925). The improved linear system modeling (based on BOD and DO model) extended to include nitrogen cycle, introducing variables of organic nitrogen, ammonia nitrogen, nitrate and nitrite nitrogen (Thomann, 1970) for simulation of water quality in streams, estuaries and coastal waters. Since 1970s, eutrophication problems caused by nutrient excess have become more significant and have taken more public concern. Non-linear ecosystem models were established for describing the biological processes of nitrogen cycle, phosphorus cycle, as well as phytoplankton and zooplankton cycles. These models included non-linear effects of the nutrient levels, light intensity and temperature on the phytoplankton growth and decay rate, such as QUAL2E and

similar tools describing comprehensively oxygen, nitrogen, phosphorus and algae biomass cycling with about ten variables (Brown and Barnwell, 1987). These models were suitable for simulation of water quality of streams, estuaries and coastal waters in one and two dimensions. More sophisticated ecosystem models that consider suspended solids, several classes of algae, zooplankton, invertebrates, plants and fish (Wlosinski and Minshall, 1983) have been applied in recent years. Nowadays, many well-developed ecosystem models have shown their capabilities in water quality evaluation and prediction. However, both types of water quality models have advantages and disadvantages, and a few of them are discussed in the following.

QUAL2E and its enhanced version QUAL2K can simulate the major reactions such as nutrient cycles, algal production, atmospheric reaeration and their effects on the dissolved oxygen balance. This conceptual model is easy to implement and improve, but the model can not quantify the exchange between water and bed biota, the benthic effect on the overlying water is only represented by some simple coefficients.

The Computational Aquatic Ecosystem Dynamics Model (CAEDYM) is a detailed aquatic ecological model that simulates the nutrients, phytoplankton, zooplankton, fish, and benthic habitat (Hipsey et al., 2006). The model requires external hydrodynamic models to provide temperature, salinity, and transport driving forces. It is a complex model with a very large number of coupled modules interrelated within a system, which make it hard to implement it by users. Moreover, the numerous parameters and coefficients add more uncertainty to the results.

The USEPA's WASP6 (Water Quality Simulation Program) is an enhancement of the original WASP (Di Toro et al., 1983; Connolly and Winfield, 1984; Ambrose, et al., 1988). This model helps users interpret and predict water quality responses to natural phenomenon and man-made pollution for various types of pollution management decisions. WASP6 is a dynamic compartment-modeling program for aquatic systems, including both the water

column and the underlying benthos (Wool et al., 2001).

Water quality processes are represented in special kinetic subroutines that are either chosen from a library or written by the user. WASP is structured to permit easy substitution of kinetic subroutines into the overall package to form problem-specific models. WASP6 comes with two such models -- TOXI for toxicants and EUTRO for conventional water quality. Earlier versions of WASP have been used to examine eutrophication of Tampa Bay; phosphorus loading to Lake Okeechobee; eutrophication of the Neuse River and estuary; eutrophication and PCB pollution of the Great Lakes (Thomann, 1975; Thomann et al., 1976; Thomann et al, 1979; Di Toro and Connolly, 1980), eutrophication of the Potomac Estuary (Thomann and Fitzpatrick, 1982), kepone pollution of the James River Estuary (O'Connor et al., 1983), volatile organic pollution of the Delaware Estuary (Ambrose, 1987), and heavy metal pollution of the Deep River, North Carolina (JRB, 1984). WASP6 permits the modeler to structure one, two, and three dimensional models; allows the specification of time-variable exchange coefficients, advective flows, waste loads and water quality boundary conditions; and permits tailored structuring of the kinetic processes, all within the larger modeling framework without having to write or rewrite large sections of computer code.

2.2.2 Eutrophication and the role of nutrients

Eutrophication is a process whereby water bodies, such as lakes, estuaries, or slow-moving streams receive excess nutrients that stimulate excessive plant growth (algae, phytoplankton, and nuisance plants such as weeds). This enhanced plant growth, often called an algal bloom, reduces dissolved oxygen in the water when dead plant material decomposes and can cause other organisms to die (USGS, http://toxics.usgs.gov/definitions/eutrophication.html). Nutrients can come from many sources, such as fertilizers applied to agricultural fields, erosion of soil containing nutrients, and sewage treatment plant discharges. In recent years,

atmospheric deposition of nitrogen has been an important contributing factor in some coastal ecosystems (Vitousek et al., 1997, Paerl and Whitall, 1999). Various types of eutrophication model have been employed (e.g. Straˇskraba, 1994; Jørgensen, 1999; Kalff, 2002), with differences relating to target variables (biotic and abiotic), modeling time scales (day to annual predictions), and mathematical formulation (from empirical/regression models to multivariate differential equations, etc.). From among many processes associated with eutrophication, the impact of hydro-environmental conditions on nutrient availability is the main aspect considered in this study.

In estuaries, nitrogen, silica and phosphorus limit phytoplankton growth, with the latter becoming particularly important during periods of high freshwater runoff (Fisher et al., 1992). Variations in freshwater flow can therefore lead to seasonal and regional shifts in these limiting factors (e.g., D'Elia et al., 1986; Fisher et al., 1988).

2.2.3 Trophic criteria and nutrient standards

Water bodies are often classified as to their trophic states. The general terms are:

- Oligotrophic (poorly nourished)
- Mesotrophic (moderately nourished)
- Eutrophic (well-nourished)
- Hypereutrophic (overnourished)

Oligotrophic lakes generally host very little or no aquatic vegetation and are relatively clear, while eutrophic lakes tend to host large quantities of organisms, including algal blooms. Each trophic class typically supports different types of fish and other organisms. If the algal biomass in a lake or other water body reaches too high a concentration, massive fish die-offs may occur as decomposing biomass deoxygenates the water. Although such terms were originally developed for and are most commonly applied to lakes, they are also appropriate descriptors of

streams and estuaries (Chapra, 1997). The tables below demonstrate how the trophic status can be classified. In Table 2-1, $[P]_\lambda$ and Chl_a represent the average concentration of phosphorus and chlorophyll a respectively.

Table 2-1 Definition of trophic categories of lakes according to Vollenweider and Kerekes (1982)

Trophic Category	$[P]_\lambda$ [mg/m^3]	Chl_a [mg/m^3]
Ultra-oligotrophic	≤ 2.5	≤ 0.7
Oligotrophic	2.5 - 8	0.7 – 2.1
Mesotrophic	8 – 25	2.1 – 6.25
Eutrophic	25 - 80	6.25 – 19.2
Hypertrophic	≥ 80	≥ 19.2

Table 2-2 Relationships between Trophic Index (TI), chlorphyll (Chl), phosphorus (P), Secchi depth (SD, metres), and Trophic Class (after Carlson, 1996)

TI(μg/l)	Chl(μg l)	P(μg/l)	SD(m)	Trophic Class
<30-40	0-2.6	0-12	>8-4	Oligotrophic
40-50	2.6-7.3	12-24	4-2	Mesotrophic
50- 0	7.3-56	24-96	2-0.5	Eutrophic
70-100+	56-155+	96-384+	0.5-<0.25	Hypereutrophic

Inorganic nutrients provide chemical building blocks for life in aquatic systems. Water quality modeling has focused on four macronutrients: phosphorous, nitrogen, carbon and silica. Nitrogen and phosphorous are the primary controllable nutrients, and they have been the focus of most efforts to control eutrophication.

The Environment Agency has assessed the quality of rivers and canals in the UK by looking at nutrients sampled from 7000 sites 12 times a year. They analyzed the nitrate and orthophosphate, and assigned a grade for each nutrient, as shown in Table 2-3 (http://www.environment-agency.gov.uk/homeandleisure

/37813.aspx). They classify the nutrient levels as ranging from grade 1 with a very low presence of nutrients up to grade 6 with a very high presence of nutrients, instead of indicating "good" or "bad" in the water quality assessment, because rivers across the country naturally have different levels of nutrients that are not necessarily bad for the environment.

Table 2-3 Nutrients level classification for rivers and canals in the UK

Classification for phosphate	Grade limit (mgP/L) average	Description
1	0.02	Very low
2	0.06	Low
3	0.1	Moderate
4	0.2	High
5	1.0	Very high
6	>1.0	Excessively high
Classification for nitrate	Grade limit (mg NO_3/L) average	Description
1	5	Very low
2	10	Low
3	20	Moderately low
4	30	Moderate
5	40	High
6	>40	Very high

2.3 Sediment transport models

Sediment transport in rivers, estuaries and coastal waters has been studied extensively in the past several decades, and a wide variety of formulas have been derived describing the sediment transport as a function of flow parameters and sediment characteristics. The sediment entrained in a flow can be transported

along the bed as bed load in the form of sliding and rolling grains, or in suspension as suspended load advected by the main flow. The suspended sediment can also settle on the bed due to gravity, while the bed sediment can be re-suspended due to increased levels of turbulence and increased bed shear stresses. In sediment transport modeling, the sediment particles are usually classified as either cohesive or non-cohesive. In general, sediment is described as being cohesive if the particle diameter is less than about 0.063mm, with the particles having cohesive properties due to electronic forces compared with gravity forces acting between the particles (Van Rijn, 1993).

2.3.1 Settling velocity

Assume a single sphere particle falling in a still water body where it gets to its terminal velocity quickly. This velocity is called settling velocity, which can be demonstrated as a balance of its immersed self-weight and the fluid drag force:

$$\frac{\pi d^3}{6}(\rho_s - \rho)g = C_D \frac{\pi d^2}{4}\frac{1}{2}\rho w_s^{\ 2} \tag{2-1}$$

$$w_s = \sqrt{\frac{4gd(s_\rho - 1)}{3C_D}} \tag{2-2}$$

where C_D is the drag coefficient, d is the sphere diameter, ρ is the water density, ρ_s is the specific particle density, and s_ρ is the specific particle gravity.

In general situations, the settling velocity can be determined through various empirical formulae. This study employs the formulae from Van Rijn (1993):

$$w_s = \begin{cases} \dfrac{(s_\rho - 1)gD_s^{\ 2}}{18\nu} & (1 < D_s \le 100\mu m) \\ \dfrac{10\nu}{D_s}[(1 + \dfrac{0.01(s_\rho - 1)gD_s^{\ 3}}{\nu^2})^{0.5} - 1] & ((100 < D_s \le 1000\mu m) \\ 1.1[(s_\rho - 1)gD_s]^{0.5} & (D_s > 1000\mu m) \end{cases} \tag{2-3}$$

where D_s is the characteristic particle size, and ν is the kinematic viscosity.

2.3.2 Deposition and re-suspension of cohesive sediment

Cohesive sediments are composed primarily of clay-sized material, which have strong inter-particle forces due to their surface ionic charges. Cohesive sediments are a concern in many waterways and are closely linked to water quality. Many pollutants, such as heavy metals, pesticides, and nutrients preferentially adsorb to cohesive sediments, which serve as a carrier, strongly relating water quality to cohesive sediment transport.

In practical engineering, the cohesive sediment processes are generally described by a comparison of the bed shear stress with a critical value for deposition or erosion. When the bed shear stress (τ) falls below a critical value for deposition (τ_d), the deposition process is predominant. When the bed shear stress (τ) exceeds a critical value for erosion (τ_e), sediment particles will be eroded (re-suspension). The critical bed shear stress for erosion is dependent on the bed material characteristics (mineral composition, organic materials, salinity, density etc.) and bed structures, and was found to be larger than the critical bed shear stress for full deposition (van Rijn, 1993). At present, there is no generally accepted formula to calculate the value of critical bed shear stress for erosion, thus this value is usually estimated based on laboratory tests using natural mud or on in-situ field test.

The widely used formulation for deposition rate is as following (Raudkivi, 1998), which was originally proposed by Krone (1962):

$$D = \begin{cases} w_s S_b (1 - \dfrac{\tau_b}{\tau_{c,d}}) & for\ \tau_b < \tau_{c,d} \\ 0 & for\ \tau_b \geq \tau_{c,d} \end{cases} \tag{2-4}$$

The formulation for erosion rate was originally proposed by Partheniades (1963) and generalized in Winterwerp and Van Kesteren (2004):

$$E = \begin{cases} M\left[\left(\frac{\tau_b}{\tau_{c,e}(z,t)} - 1\right)\right]^{n_0} & for\ \tau_b > \tau_{c,e}(z,t) \\ 0 & for\ \tau_b \le \tau_{c,e}(z,t) \end{cases} \quad (2\text{-}5)$$

where D and E are cohesive sediment deposition and erosion rates, respectively. τ_b is the bed shear stress, S_b is the near bed sediment concentration, $\tau_{c,d}$ and $\tau_{c,e}$ are the critical shear stress for deposition and erosion, respectively. The critical deposition bed shear stress is generally determined from laboratory or field experiments and the values are ranging from 0.06 to 0.11 N/m^2 (HydroQual, 2002) and 0.05 to 0.1 N/m^2 (Winterwerp and Van Kesteren, 2004). In the absence of site specific data, it can generally be treated as a calibration parameter (HydroQual, 2002, Tetra Tech, 2002). The typical value for critical erosion bed shear stress is 0.1 to 5 N/m^2, and M is the erosion parameter which should vary with time and depth, but, in general is taken as a constant valued with a range of 10^{-5} to 5×10^{-4} kg/m^2/s.

2.3.3 Deposition and re-suspension of non-cohesive sediment

The motion of non-cohesive sediment depends on the particle size, shape and density. Total load of non-cohesive sediment can be divided into two modes of transport, bed load and suspended load (Falconer and Chen, 1996). The bed load is defined as that part of the total load where the sediment is almost continuously in contact with the bed, being carried by rolling, sliding or hopping, whereas the suspended load is that part of the total load which is maintained in suspension for considerable periods of time by the turbulence of the flow (Van Rijn, 1993).

To assess the non-cohesive sediment re-suspension from the bed, a Shields curve is introduced. Shields curve was originally proposed by Shields (1936) and later refined by Bonnefille (1963), see van Rijn, (1993) and Yalin (1972), expressed in terms of a dimensionless mobility parameter (θ) and a dimensionless particle parameter (D_*).

$$\theta_{cr} = \begin{cases} 0.24(D_*)^{-1} & D_* < 4 \\ 0.14(D_*)^{-0.64} & 4 \le D_* < 10 \\ 0.04(D_*)^{-0.1} & 10 \le D_* < 20 \\ 0.013(D_*)^{0.29} & 20 \le D_* < 150 \\ 0.055 & D_* \ge 150 \end{cases} \quad (2\text{-}6)$$

where D_* and θ are calculated as:

$$D_* = \left[\frac{(s-1)g}{\nu^2}\right]^{\frac{1}{3}} D_s \quad (2\text{-}7)$$

$$\theta = \frac{u_*^2}{(s-1)gD_s} = \frac{\tau}{(\rho_s - \rho)gD_s} \quad (2\text{-}8)$$

Where s is the specific densityUsually, the median particle diameter (D_{50}) is used as the characteristic particle diameter.

When the bed shear velocity u_* ($u_* = \sqrt{\frac{\tau}{\rho}}$) is less than the critical shear velocity u_{*cr} ($u_{*_{cr}} = \sqrt{(s-1)gD_s\theta_{cr}}$), no erosion or re-suspension takes place and there is no bed load. Sediment in suspension in this condition will deposit to the bed. Once the bed shear velocity u_* exceeds the critical shear velocity u_{*cr} but remains less than the settling velocity w_s, sediment will be eroded from the bed and transported as bed load. Sediment in suspension under this condition will also deposit to the bed. When the bed shear velocity exceeds both the critical shear velocity and settling velocity, sediment will be transported as suspended load (Van Rijn 1993;1984a; 1984b).

Many researchers have proposed mechanisms and formulae to calculate bed load and suspended load, such as Yalin (1972), Engelund and Hansen (1967), Einstein (1942) and van Rijn (1984a, b, 1993). In this study, the van Rijn formulae have been adopted.

2.4 Sediment-nutrient interaction model

Sediment transport plays an important role in water quality modeling.

Researches on sediment influence on the water quality have been studied extensively in the past decades (James et al., 1997), partly because it is a source of heavy metal pollution, and it increases the possibility of eutrophication in river, estuarine and coastal areas, where large amount of nutrients adsorbed by the sediment particles can enter into the overlying water and be moved with the flow currents (Anggara-Kasih and Kitada, 2004; Fevre and Lewis, 2003; Reddy et al., 1996).

2.4.1 Sediment adsorption

2.4.1.1 Adsorption mechanisms

Adsorption is a process that occurs when a dissolved substance accumulates on the surface of a solid, forming a molecular or atomic film. The substance that is adsorbed is called the adsorbate and the solid is called the adsorbent (Chapra, 1997). Desorption is the reverse of adsorption. Sediment adsorption and desorption with solutes (chemicals or heavy metals) is a wide spread phenomenon in natural waters. Nutrient substances prone to adsorb on the sediment surfaces are usually ammonium and phosphate. The ammonium ion has positive charge and can be easily adsorbed to negatively charged surfaces of clay and organic matter, while the phosphate ion has negative charge and often attaches to the mineral clay in fresh water and marine sediments.

2.4.1.2 Types of adsorption

Depending on the nature of attractive forces between the adsorbate and adsorbent, adsorption can be classified as physical or chemical adsorption.

Physical adsorption: If the forces of attraction existing between adsorbate and adsorbent are Van der Waals forces, the adsorption is called physical adsorption. This type of adsorption is also known as physisorption or Van der Waals adsorption. Since the adsorbed molecule is not affixed to a particular site on

the solid surface, but is free to move about over the surface, the adsorption can be easily reversed by heating or decreasing the pressure.

Chemical adsorption: If the forces of attraction existing between adsorbate particles and adsorbent are almost of the same strength as chemical bonds, the adsorption is called chemical adsorption. This type of adsorption is also called chemisorption or Langmuir adsorption, which is seldom reversible – the adsorbent must generally be heated to higher temperatures to remove the adsorbed material. Physical adsorption can involve the formation of a multi-molecular layer, while pure chemisorption is completed in a mono-layer (Ludersen, 1983).

In addition, the exchangeable adsorption is used to describe adsorption characterized by electrical attraction between the adsorbent and the adsorbate, known as ion exchange. Ions with greater charge are attached more strongly towards a site of opposite charge than molecules with a lesser charge. Smaller size ions have a relatively greater attraction with the adsorbent surface (Rao, 1994; Ludersen, 1983).

2.4.1.3 Partitioning

Adsorption is a dynamic process, and the rate of adsorption can be expressed in the same manner as any kinetic process. At equilibrium, the solutes in the water can be classified as dissolved phase and adsorbed material as particulate phase, which can be connected by a partition coefficient, which is defined as the ratio of concentrations in the two phases of a mixture of two immiscible solvents (Leo et al., 1971). The dimensionless ratio of the dissolved to the particulate concentration is the product of the partition coefficient and the concentration of suspended sediment, assuming local equilibrium:

$$C_p / C_d = K_d S \qquad (2\text{-}9)$$

where C_p is the particulate concentration (mg/l), C_d is the dissolved concentration (mg/l), K_d is the distribution coefficient between the solid and the

dissolved phase, also called partition coefficient (l/g), and S is the suspended sediment concentration (g/l).

The particulate and dissolved concentrations can be calculated from knowledge of the total concentration, C_T, as stated in Equations (2-10) and (2-11):

$$C_p = \frac{K_d S}{1 + K_d S} C_T \tag{2-10}$$

$$C_d = \frac{1}{1 + K_d S} C_T \tag{2-11}$$

These concentrations can be calculated for the water column or the bed sediment, by using the concentration of suspended sediment in the water (S) or in the bed (S_b), where $S_b=S/n$, the bed sediment concentration in kg/m^3 of pore water, and n is the porosity of the bed sediment (Karickhoff et al., 1979).

2.4.1.4 Adsorption isotherms

Adsorption is usually described through isotherms, that is, the amount of adsorbate on the adsorbent as a function of its pressure (if gas) or concentration (if liquid) at constant temperature. The quantity adsorbed is nearly always normalized by the mass of the adsorbent to allow comparison of different materials. The different parameters and the underlying thermodynamic assumption of these equilibrium models often provide some insight into the adsorption mechanism, the surface properties and affinity of adsorbent. Some of the isotherm equations that can explain solid–liquid adsorption systems are: linear adsorption isotherms based on Henry's law (Hills and Pirzada, 1984), Langmuir equation (Langmuir, 1916) and Freundlich equation (Chapra, 1997).

Linear adsorption model

An empirical expression of equilibrium adsorption is frequently used:

$$q_e = K_d C_e \tag{2-12}$$

where C_e (mg/L) is the dissolved solute concentration at equilibrium, q_e (mg/g) is the amount of solute adsorbed at equilibrium, K_d is the partition coefficient.

Langmuir adsorption isotherm

The Langmuir adsorption equation is defined by a limiting (maximum) adsorption capacity that is related to a monolayer coverage of surface sites. We may think of the chemical reaction equation below with K_a as the equilibrium constant.

$$q_e = \frac{q_m K_a C_e}{1 + K_a C_e} \tag{2-13}$$

where, q_m is the Langmuir monolayer sorption capacity (mg/g), K_a is related to the energy of adsorption (L/mg).

The Langmuir adsorption equation is one of the most useful options in chemical equilibrium models, and the assumption of limited (monolayer) coverage is representative of a wide range of equilibrium adsorption isotherm data in the literature for metal and organic adsorbates on particles in nature waters (Chapra, 1997).

Freundlich adsorption isotherm

$$q_e = K_F C_e^{1/n} \tag{2-14}$$

K_F $(L/g)^n$ is the Freundlich constant related to adsorption capacity, n is the Freundlich exponent related to adsorption intensity.

The Freundlich isotherm is often used to describe organic chemical adsorption onto activated carbon at relatively high concentrations in water and wastewater. It is less frequently used for modeling adsorption in natural waters. If n=1, the Freundlich model reduces to the linear adsorption model.

2.4.2 Factors affecting the sediment adsorption of nutrients

Researches have shown some factors determining the nutrient adsorption capacity of natural water bodies. Many earlier studies indicate that grain size, mineralogy, and organic matter content can affect ammonium adsorption (Rosenfeld, 1979; Boatman and Murray, 1982). For sediments rich in organic matter, organic matter dominates the ammonium adsorption process. While for

sediments poor in organic matter, clay minerals play a more important role in the ammonium adsorption (Boatman and Murray 1982). Changing and fluctuating salinity in estuarine sediments plays a major part in the control of the ammonium adsorption capacity of the sediment (Hou et al., 2003; Rodrigues et al. 2007). Weston et al. (2010) reported that the amount of adsorbed ammonium was lower in estuarine sediments compared to sediment in fresh water. Gardner et al. (1991) suggested that the increased ion exchange and ion pairing of ammonium caused by increasing numbers of seawater cations and anions reduces the ammonium residence time within the sediment, resulting in an increase of ammonium that becomes desorbed from the sediment. Gao et al (2008) studied the effects of the highly dynamic suspended particulate matter (SPM) on nutrients (SiO_3^{2-}, NO_3^-, and PO_4^{3-}) in Yangtze estuary and found that three parameter (salinity, SPM, nutrients) regressions generally produced better results of simulating nutrient concentrations than two parameter (salinity and nutrients) regressions.

Researches on phosphorus (Andrieux-Loyer and Aminot, 2001; Wang et al, 2005) shows that the phosphate adsorption capacity has a significant correlation with the contents of iron, aluminum, total organic carbon (TOC), cationic exchange capacity, etc. The phosphate adsorption rate was also closely related to the concentration of fine particles. And the phosphate sorption efficiency had a strong positive correlation with iron content. Hou et al (2009) studied the different forms of sedimentary phosphorous in the intertidal area of Yangtze Estuary and the results reveal that the tidal sediment is a significant internal source of phosphorous for the estuarine and coastal ecosystem. Del Bubba et al (2003) reported that among the physico-chemical properties of the sediments, calcium and magnesium content, grain size, porosity, bulk density and hydraulic conductivity were significantly related to the maximum adsorption capacity. Phosphorous-binding energy constants were not significantly related to the physico-chemical properties of the sands.

Other factors such as temperature, velocity fields and the surrounding nutrient concentrations also have been investigated in connection with the nutrient

adsorption process.

2.4.3 Modelling sediment effects on nutrients transport and distribution

Sediment effect was firstly considered as an empirical parameter in water quality modeling. Based on Streeter-Phelps model, Thomas (1948) introduced a coefficient k_3 to take into account the loss of BOD decay rate due to sediment settling, scour and flocculation, which do not exert an oxygen demand. Followed researches added more coefficients to water quality models to represent the impacts of sediment adsorption, re-suspension and sediment oxygen demand (Camp, 1963; Dobbins, 1964). Since sediment transport is a complex process, the empirical parameters or relationships can not be accurate, either theoretically or practically.

Current numerical models considering the sediment influence on a specific water quality constituency simulation usually focus on sediment deposition and re-suspension. The mass transfer between sediment surface and water column can be quantified by adsorption and desorption processes. Fitzsimons et al. (2006) found that the desorption of the NH_4^+ from the re-suspended sediments accounted for approximately 50% of increase in the concentrations of dissolved NH_4^+ in Thames Estuary over a tidal cycle. Sediment-phosphorus interactions may control phosphorus levels in water bodies with high sediment concentrations (Chao et al. 2006). Numerical models have been developed to simulate the phosphorus concentrations in lakes, rivers and coastal waters (Ishikawa and Nishmura 1989; Chapra and Canale 1991; Cerco and Cole 1993; Ruley and Rusch 2004), some of these models simulate the processes of adsorption-desorption and bed release.

2.5 Summary

In this chapter, previous studies on hydro-environmental modelling have been

reviewed from their basic principles, equation discretization schemes and numerical algorithms, followed by an overview of different water quality models in addressing the eutrophication processes. Standards and criteria relating to nutrients and trophic status were also discussed. Sediment transport and its subsequent effect on the fate and distribution of nutrients were investigated, with particular attentions being paid on the sediment-nutrient interaction through adsorption and desorption processes.

Chapter3

Hydrodynamic models and verifications

3.1. Introduction

Numerical modelling has become an important approach to predict the hydrodynamic processes in rivers, coastal and estuarine waters. This chapter covers an overview of the governing equations of hydrodynamic models. The parameters quantifying the hydrodynamic processes occurring specifically in coastal and estuarine water systems are discussed. Two types of numerical models, namely, ADI model and TVD-MacCormack model, are compared in terms of their performances in solving the two dimensional shallow water equations. Apart from hypothetical examples, the Simplified Harmonic Method (SHM) for tidal predictions based on the Admiralty Tide Tables (ATT) is used to verify the predicted results by the hydrodynamic models.

3.2 Theoretical background

3.2.1 Three dimensional Navier-Stokes equation

Numerical modelling of fluid flow is based on the principles of the conservation of mass and momentum within the body of fluid to be modelled. The Navier-Stokes equations for an incompressible fluid in Cartesian coordinates can be written as:

$$\rho(\frac{\partial u}{\partial t}+u\frac{\partial u}{\partial x}+v\frac{\partial u}{\partial y}+w\frac{\partial u}{\partial z})=-\frac{\partial p}{\partial x}+\mu(\frac{\partial^2 u}{\partial x^2}+\frac{\partial^2 u}{\partial y^2}+\frac{\partial^2 u}{\partial z^2}) \quad (3\text{-}1)$$

$$\rho(\frac{\partial v}{\partial t}+u\frac{\partial v}{\partial x}+v\frac{\partial v}{\partial y}+w\frac{\partial v}{\partial z})=-\frac{\partial p}{\partial y}+\mu(\frac{\partial^2 v}{\partial x^2}+\frac{\partial^2 v}{\partial y^2}+\frac{\partial^2 v}{\partial z^2}) \quad (3\text{-}2)$$

$$\rho(\frac{\partial w}{\partial t}+u\frac{\partial w}{\partial x}+v\frac{\partial w}{\partial y}+w\frac{\partial w}{\partial z})=-\frac{\partial p}{\partial z}+\mu(\frac{\partial^2 w}{\partial x^2}+\frac{\partial^2 w}{\partial y^2}+\frac{\partial^2 w}{\partial z^2})-\rho g \tag{3-3}$$

$$\frac{\partial u}{\partial x}+\frac{\partial v}{\partial y}+\frac{\partial w}{\partial z}=0 \tag{3-4}$$

where u, v, w are the instantaneous velocity components in the x, y, z directions, ρ is the fluid density, p is the instantaneous pressure, μ is the kinematic viscosity coefficient, and g is the gravitational acceleration in the negative z direction. Equations (3-1) to (3-3) are the momentum conservation equations in x, y, z directions respectively, and Equation (3-4) is the mass continuity equation.

3.2.2 Hydrostatic pressure assumption

In large water bodies where the horizontal scale is much larger than the vertical scale, such as wide rivers, estuaries and coastal waters, the vertical velocity is relatively small and the acceleration along vertical direction is negligible compared with gravitational acceleration. Therefore, hydrostatic pressure distribution can be assumed along the vertical axis, and then the momentum equation in the vertical direction (eq. 3-3) is reduced to the following equation:

$$\frac{\partial p}{\partial z}=-\rho g \tag{3-5}$$

3.2.3 Depth integrated shallow water equations

The governing equations for two dimensional shallow water flows can be derived by integrating the Navier-Stokes equations (3-1, 3-2 and 3-4) over the water depth. Defining U, V as the depth averaged velocities in the x and y directions, then they can be written as:

$$U=\frac{1}{h}\int_{z_b}^{\eta} u\,dz \tag{3-6}$$

$$V = \frac{1}{h}\int_{z_b}^{\eta} v dz \tag{3-7}$$

where h is the water depth given by $h=\eta+z_b$, , z_b is the bed elevation below datum and η is the water surface elevation above datum (Figure 3-1).

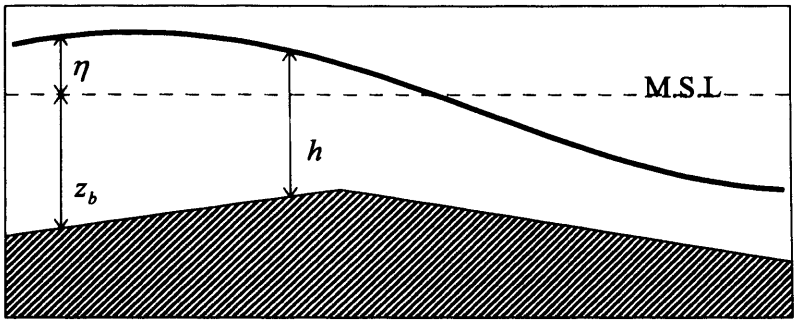

Figure 3-1 Definition of depth, bed level and water surface elevation

3.2.3.1 Boundary conditions

Using a hydrostatic pressure assumption, we have the following boundary conditions.

Firstly, the pressure on the free surface is taken to be zero. Then we use the kinetic free surface condition that fluid particles on the surface remain on the surface. An equation defining the free surface is given as:

$$w_\eta = \frac{d\eta}{dt} = \frac{\partial \eta}{\partial t} + u_\eta \frac{\partial \eta}{\partial x} + v_\eta \frac{\partial \eta}{\partial y} \tag{3-8}$$

which leads to:

$$\frac{\partial \eta}{\partial t} = u_\eta \frac{\partial \eta}{\partial x} + v_\eta \frac{\partial \eta}{\partial y} - w_\eta \tag{3-9}$$

Secondly, on the fixed solid bed boundary where $z = z_b$, fluid particles always remain on the boundary. Similar to the situation of the free surface, the boundary equation at the bed can be written as:

$$u_{z_b} \frac{\partial z_b}{\partial x} + v_{z_b} \frac{\partial z_b}{\partial y} - w_{z_b} = 0 \tag{3-10}$$

The subscripts η and z_b denote the velocities at the surface and the bed

respectively. (Liggett 1994; Vreugdenhil 1994)

3.2.3.2 Depth integration of the continuity equation

The continuity equation (3-4) can be integrated over depth by integration as follows:

$$\frac{1}{h}\int_{z_b}^{\eta}\frac{\partial u}{\partial x}dz+\frac{1}{h}\int_{z_b}^{\eta}\frac{\partial v}{\partial y}dz+\frac{1}{h}\int_{z_b}^{\eta}\frac{\partial w}{\partial z}dz=0 \tag{3-11}$$

The Leibnitz rule defines the derivative of an integral with variable limits, giving rise to a derivative inside the integral and the flux term in those limits as follows:

$$\frac{\partial}{\partial x}\int_{z_b}^{\eta}Fdz=\int_{z_b}^{\eta}\frac{\partial F}{\partial x}dz-F(x,y,\eta)\frac{\partial \eta}{\partial x}+F(x,y,z_b)\frac{\partial z_b}{\partial x} \tag{3-12}$$

Applying Leibnitz rule to Equation (3-11) leads to:

$$\int_{z_b}^{\eta}\frac{\partial u}{\partial x}dz=\frac{\partial(hU)}{\partial x}-u_\eta\frac{\partial \eta}{\partial x}+u_{z_b}\frac{\partial z_b}{\partial x} \tag{3-13}$$

$$\int_{z_b}^{\eta}\frac{\partial v}{\partial y}dz=\frac{\partial(hV)}{\partial y}-v_\eta\frac{\partial \eta}{\partial y}+v_{z_b}\frac{\partial z_b}{\partial y} \tag{3-14}$$

$$\int_{z_b}^{\eta}\frac{\partial w}{\partial z}dz=w_\eta-w_{z_b} \tag{3-15}$$

If no-slip condition is to be applied at the bed, then this gives:

$$u_{z_b}=v_{z_b}=w_{z_b}=0 \tag{3-16}$$

Adding Equations (3-13) - (3-15) together under the condition of (3-16) gives:

$$\frac{\partial(hU)}{\partial x}+\frac{\partial(hV)}{\partial y}-u_\eta\frac{\partial \eta}{\partial x}-v_\eta\frac{\partial \eta}{\partial y}+w_\eta=0 \tag{3-17}$$

Applying Equation (3-9) to (3-17) will result in the depth integrated continuity equation as:

$$\frac{\partial \eta}{\partial t}+\frac{\partial(hU)}{\partial x}+\frac{\partial(hV)}{\partial y}=0 \tag{3-18}$$

3.2.3.3 Depth integration of the momentum equations

Equation (3-1) will be integrated in the vertical direction, with the shear stress terms neglected at first. They will be represented later by "friction" terms (F_x and F_y explained in the next section) that are evaluated empirically.

$$\int_{z_b}^{\eta}\left[\frac{\partial u}{\partial t}+\frac{\partial}{\partial x}\left(u^2\right)+\frac{\partial}{\partial y}(uv)+\frac{\partial}{\partial z}(uw)\right]dz=\int_{z_b}^{\eta}(-\frac{1}{\rho}\frac{\partial p}{\partial x})dz+\int_{z_b}^{\eta}(\nu\nabla u^2)dz+\int_{z_b}^{\eta}F_x dz \qquad (3\text{-}19)$$

Different parts of Equation (3-19) will be simplified separately and then put together in the final stage to obtain the depth integrated form of the whole momentum equation.

(1) Time derivative term:

Applying Equation (3-12) for derivation of u with respect to time gives:

$$\int_{z_b}^{\eta}\frac{\partial u}{\partial t}dz=\frac{\partial(hU)}{\partial t}-u_\eta\frac{\partial\eta}{\partial t}+u_{z_b}\frac{\partial z_b}{\partial t} \qquad (3\text{-}20)$$

(2) Advection derivative terms:

The x-derivative is:

$$\int_{z_b}^{\eta}\frac{\partial(u^2)}{\partial x}dz=\frac{\partial}{\partial x}\int_{z_b}^{\eta}u^2dz-u_\eta^2\frac{\partial\eta}{\partial x}+u_{z_b}^2\frac{\partial z_b}{\partial x} \qquad (3\text{-}21)$$

To avoid the appearance of the integral on the right hand side, the momentum correction factor is defined as

$$\beta_{xx}=\frac{\int_{z_b}^{\eta}u^2dz}{U^2h} \qquad (3\text{-}22)$$

So that

$$\int_{z_b}^{\eta}\frac{\partial(u^2)}{\partial x}dz=\frac{\partial(\beta_{xx}U^2h)}{\partial x}-u_\eta^2\frac{\partial\eta}{\partial x}+u_{z_b}^2\frac{\partial z_b}{\partial x} \qquad (3\text{-}23)$$

The y-derivative is

$$\int_{z_b}^{\eta}\frac{\partial(uv)}{\partial y}dz=\frac{\partial(\beta_{xy}UVh)}{\partial y}-u_\eta v_\eta\frac{\partial\eta}{\partial y}+u_{z_b}v_{z_b}\frac{\partial z_b}{\partial y} \qquad (3\text{-}24)$$

With the definition

$$\beta_{xy} = \frac{\int_{z_b}^{\eta} uv dz}{UVh} \tag{3-25}$$

The z-derivative is:

$$\int_{z_b}^{\eta} \frac{\partial(uw)}{\partial z} dz = u_\eta w_\eta - u_{z_b} w_{z_b} \tag{3-26}$$

Adding Equations (3-20), (3-23), (3-24) and (3-26), which constitute the left hand side of Equation (3-19), and applying boundary conditions give:

$$\begin{aligned} &\frac{\partial(hU)}{\partial t} - u_\eta \frac{\partial \eta}{\partial t} + u_{z_b} \frac{\partial z_b}{\partial t} + \frac{\partial(\beta_{xx} U^2 h)}{\partial x} + \frac{\partial(\beta_{xy} UVh)}{\partial y} \\ &- u_\eta (u_\eta \frac{\partial \eta}{\partial x} + v_\eta \frac{\partial \eta}{\partial y} - w_\eta) + u_{z_b}^2 \frac{\partial z_b}{\partial x} + u_{z_b} v_{z_b} \frac{\partial z_b}{\partial y} - u_{z_b} w_{z_b} \\ &= \frac{\partial(hU)}{\partial t} + \frac{\partial(\beta_{xx} U^2 h)}{\partial x} + \frac{\partial(\beta_{xy} UVh)}{\partial y} \end{aligned} \tag{3-27}$$

(3) Pressure gradient term:

Applying Leibnitz rule to the hydrostatic equation (3-5) and employing Bousinesq's hypothesis, which allows for the replacement of ρ with a reference density ρ_0 everywhere, except for the pressure p itself, gives:

$$\int_{z_b}^{\eta} \frac{1}{\rho_0} \frac{\partial p}{\partial x} dz = gh \frac{\partial \eta}{\partial x} + \frac{1}{\rho_0} \frac{\partial p_a}{\partial x} + \frac{gh^2}{2\rho_0} \frac{\partial \rho}{\partial x} \tag{3-28}$$

where p_a represent the air pressure on the water surface.

(4) Diffusion terms:

By defining the stress term as:

$$T_{ij} = \nu(\frac{\partial u_i}{\partial x_j} + \frac{\partial u_j}{\partial x_i}) \tag{3-29}$$

The diffusion part of Equation (3-19) can be integrated as follows:

$$\begin{aligned} &\int_{z_b}^{\eta} \left(\frac{\partial T_{xx}}{\partial x} + \frac{\partial T_{xy}}{\partial y} + \frac{\partial T_{xz}}{\partial z} \right) dz = \frac{\partial}{\partial x} \int_{z_b}^{\eta} T_{xx} dz + \frac{\partial}{\partial y} \int_{z_b}^{\eta} T_{xy} dz \\ &- \left[T_{xx} \frac{\partial \eta}{\partial x} + T_{xy} \frac{\partial \eta}{\partial y} - T_{xz} \right]_\eta + \left[T_{xx} \frac{\partial z_b}{\partial x} + T_{xy} \frac{\partial z_b}{\partial y} - T_{xz} \right]_{z_b} \end{aligned} \tag{3-30}$$

The integral part of the above equation may be written as:

$$\frac{\partial}{\partial x}\int_{z_b}^{\eta} T_{xx}dz + \frac{\partial}{\partial y}\int_{z_b}^{\eta} T_{xy}dz = \frac{\partial}{\partial x}\left(\nu\int_{z_b}^{\eta}(2\frac{\partial u}{\partial x})dz\right) + \frac{\partial}{\partial y}\left(\nu\int_{z_b}^{\eta}(\frac{\partial u}{\partial y}+\frac{\partial v}{\partial x})dz\right)$$
$$= 2h\nu\frac{\partial}{\partial x}(\frac{\partial U}{\partial x}) + h\nu\frac{\partial}{\partial y}(\frac{\partial V}{\partial y}) + h\nu\frac{\partial}{\partial y}(\frac{\partial U}{\partial x}) \quad (3\text{-}31)$$

The last two brackets of Equation (3-30) represent the external momentum exchanges acting as wind or bed shear stresses on the surface or bed respectively. They will be discussed more fully in the following sections. It should be noted that the above derivations use instantaneous quantities of the flow and thus consider only the viscous shear stress. In practice, the flow is turbulent and the Reynolds-averaged quantities are used. The overall effects of turbulence can be modelled by increasing the magnitude of the viscosity coefficient, but keeping the formulation of the derivations unchanged. Then, the molecular viscosity coefficient ν in the above equations should be substituted by depth-averaged eddy viscosity coefficient ε.

Adding the different integrated parts of the momentum equation and considering the turbulence effects gives the depth integrated momentum equation in the x-direction as:

$$\frac{\partial(hU)}{\partial t} + \frac{\partial(\beta_{xx}U^2h)}{\partial x} + \frac{\partial(\beta_{xy}UVh)}{\partial y} + gh\frac{\partial\eta}{\partial x} + \frac{1}{\rho_0}\frac{\partial p_a}{\partial x} + \frac{gh^2}{2\rho_0}\frac{\partial\rho}{\partial x} + F_x$$
$$= 2h\varepsilon\frac{\partial}{\partial x}(\frac{\partial U}{\partial x}) + h\varepsilon\frac{\partial}{\partial y}(\frac{\partial V}{\partial y}) + h\varepsilon\frac{\partial}{\partial y}(\frac{\partial U}{\partial x}) \quad (3\text{-}32)$$

The y-momentum equation can also be derived in a similar manner giving:

$$\frac{\partial(hV)}{\partial t} + \frac{\partial(\beta_{yy}V^2h)}{\partial y} + \frac{\partial(\beta_{yx}UVh)}{\partial x} + gh\frac{\partial\eta}{\partial y} + \frac{1}{\rho_0}\frac{\partial p_a}{\partial y} + \frac{gh^2}{2\rho_0}\frac{\partial\rho}{\partial y} + F_y$$
$$= 2h\varepsilon\frac{\partial}{\partial y}(\frac{\partial V}{\partial y}) + h\varepsilon\frac{\partial}{\partial x}(\frac{\partial U}{\partial x}) + h\varepsilon\frac{\partial}{\partial x}(\frac{\partial V}{\partial y}) \quad (3\text{-}33)$$

3.2.3.4 Source terms and external forces

Equations (3-32) and (3-33) are the basic equations for shallow water flows which include local accelerations, advective accelerations, viscous shear stresses,

as well as pressure gradients, while all other constituents, such as Coriolis acceleration, bed shear stress and wind shear stress, are included in the term F_i and are discussed below.

Coriolis force: The rotation of the earth around its axis forces an object to deflect to right or left if the object moves horizontally in the northern or southern hemisphere respectively. This force is called the Coriolis force, which can have a considerable effect for the movement of a large water body. It is dependent on the latitude and the flow velocity, and always acts at right angle to the flow direction. It can be included in the momentum equations by the product of the water depth, the flow velocity and the Coriolis coefficient f, which is defined as $f=2\omega sin\varphi$, where ω is the angular speed of the earth's rotation at 7.27×10^{-5} *Rad/s* and φ is the geographical angle of latitude of the site.

Bed shear stress τ_b: Bed shear stress is induced by bottom friction which has a non-linear, retarding effect on the flow. The evaluation of the bed shear stress is generally based on empirical or semi-empirical calculations that are usually defined as

$$\frac{\tau_{bx}}{\rho_0}=\frac{1}{\cos(\alpha)}C_f U\sqrt{U^2+V^2} \quad \text{and} \quad \frac{\tau_{by}}{\rho_0}=\frac{1}{\cos(\alpha)}C_f V\sqrt{U^2+V^2} \tag{3-34}$$

where α is the angle of the steepest bed slope at a specific point, C_f is the dimensionless friction coefficient that can be expressed in terms of the Chézy coefficient C, Manning coefficient n or the bed roughness height k_s as follows:

$$C_f=\frac{g}{C^2}=\frac{gn^2}{h^{1/3}}=\frac{g}{\left(18\log\left(\frac{12h}{k_s}\right)\right)^2} \tag{3-35}$$

Wind shear stress τ_w: Analogous to the derivation of the bed shear stress, and ignoring free surface gradients, the resistance of the wind generally takes the following form:

$$\frac{\tau_{wx}}{\rho_0}=\frac{\rho_{air}}{\rho_0}C_D U_w\sqrt{U_w^2+V_w^2} \quad \text{and} \quad \frac{\tau_{wy}}{\rho_0}=\frac{\rho_{air}}{\rho_0}C_D V_w\sqrt{U_w^2+V_w^2} \tag{3-36}$$

where U_w, V_w are wind velocity components in the x and y directions, respectively,

ρ_{air} = air density(=1.023kg/m^3) and C_D is the air-water drag coefficient, which may be specified according to the Institute of Oceanographic Science (UK) suggestion as:

$$\begin{cases} C_D = 0.565\times10^{-3} & \text{IF} \quad \left|\vec{U}_w\right| \le 5.0m/s \\ C_D = \left(0.137\left|\vec{U}_w\right| - 0.12\right)\times10^{-3} & \quad 5.0 < \left|\vec{U}_w\right| \le 19.22m/s \\ C_D = 2.513\times10^{-3} & \quad \left|\vec{U}_w\right| > 19.22m/s \end{cases} \tag{3-37}$$

Considering all the external and internal force terms and adding into the shallow water equations, the final equations in the x-and y-directions can be written as:

$$\frac{\partial(hU)}{\partial t}+\frac{\partial(\beta_{xx}U^2h)}{\partial x}+\frac{\partial(\beta_{xy}UVh)}{\partial y}+gh\frac{\partial\eta}{\partial x}+\frac{1}{\rho_0}\frac{\partial p_a}{\partial x}+\frac{gh^2}{2\rho_0}\frac{\partial\rho}{\partial x}-fhV$$
$$-\frac{1}{\rho_0}(\tau_{bx}+\tau_{wx})=2h\varepsilon\frac{\partial}{\partial x}(\frac{\partial U}{\partial x})+h\varepsilon\frac{\partial}{\partial y}(\frac{\partial V}{\partial y})+h\varepsilon\frac{\partial}{\partial y}(\frac{\partial U}{\partial x}) \tag{3-38}$$

$$\frac{\partial(hV)}{\partial t}+\frac{\partial(\beta_{yy}V^2h)}{\partial y}+\frac{\partial(\beta_{yx}UVh)}{\partial x}+gh\frac{\partial\eta}{\partial y}+\frac{1}{\rho_0}\frac{\partial p_a}{\partial y}+\frac{gh^2}{2\rho_0}\frac{\partial\rho}{\partial y}-fhU$$
$$-\frac{1}{\rho_0}(\tau_{by}+\tau_{wy})=2h\varepsilon\frac{\partial}{\partial y}(\frac{\partial V}{\partial y})+h\varepsilon\frac{\partial}{\partial x}(\frac{\partial U}{\partial x})+h\varepsilon\frac{\partial}{\partial x}(\frac{\partial V}{\partial y}) \tag{3-39}$$

3.3 DIVAST model

DIVAST (Depth Integrated Velocities and Solute Transport) is a two-dimensional, depth-integrated, time-variant model, which has been developed for estuarine and coastal water modelling. It is suitable for water bodies that are dominated by horizontal, unsteady flow and do not display significant vertical stratification. The model simulates two-dimensional distributions of currents, water surface elevations and various water quality parameters within the modelling domain as functions of time, taking into account the hydraulic characteristics governed by the bed topography and boundary conditions.

3.3.1 Hydrodynamic governing equations

The depth-integrated continuity and momentum equations have been derived. Using the symbols that are consistent with the DIVAST model, they are rewritten as below:

$$\frac{\partial \eta}{\partial t}+\frac{\partial p}{\partial x}+\frac{\partial q}{\partial y}=q_m \tag{3-40}$$

$$\frac{\partial p}{\partial t}+\frac{\partial \beta pU}{\partial x}+\frac{\partial \beta pV}{\partial y}=fq-gH\frac{\partial \eta}{\partial x}+\frac{\rho_a}{\rho}C_w W_x\sqrt{W_x^2+W_y^2} -\frac{gp\sqrt{p^2+q^2}}{H^2C^2}+\varepsilon\left[2\frac{\partial^2 p}{\partial x^2}+\frac{\partial^2 p}{\partial y^2}+\frac{\partial^2 q}{\partial x\partial y}\right] \tag{3-41}$$

$$\frac{\partial q}{\partial t}+\frac{\partial \beta qU}{\partial x}+\frac{\partial \beta qV}{\partial y}=fp-gH\frac{\partial \eta}{\partial y}+\frac{\rho_a}{\rho}C_w W_y\sqrt{W_x^2+W_y^2} -\frac{gq\sqrt{p^2+q^2}}{H^2C^2}+\varepsilon\left[\frac{\partial^2 q}{\partial x^2}+2\frac{\partial^2 q}{\partial y^2}+\frac{\partial^2 p}{\partial x\partial y}\right] \tag{3-42}$$

where:

p $(=UH)$, q $(=VH)$ = discharges per unit width in the x and y directions respectively ($m^3/s/m$);

q_m = source discharge per unit horizontal area ($m^3/s/m^2$);

U, V = depth average velocity components in the x and y directions respectively (m/s);

β = momentum correction factor for a non-uniform vertical velocity profile;

f = Coriolis coefficient;

g = gravitational acceleration (m/s^2);

H = total water depth (m);

η = water surface elevation above datum (m);

ρ_a = density of air ($\cong 1.292$ kg/m^3);

ρ = density of fluid (kg/m^3);

C = Chézy roughness coefficient ($m^{1/2}/s$);

C_w = air/fluid resistance coefficient (assumed to be 2.6×10^{-3})

ε = depth averaged turbulent eddy viscosity (m^2/s)

x, y = co-ordinates (m)

The above equations are an extension to Equations (3-38) and (3-39). There are some parameters and coefficients that are worthwhile elaborating further in the next session.

3.3.1.1 The momentum correction factor

For an assumed logarithmic vertical velocity profile, the momentum correction factor may be calculated from:

$$\beta = 1 + \frac{g}{C^2 \kappa^2} \tag{3-43}$$

where κ = von Karman's constant = 0.4. For an assumed seventh power law velocity profile, the value of β is 1.016. For an assumed quadratic velocity profile, the value of β is 1.20.

3.3.1.2 Turbulence

The turbulent shear stress refers to the flow resistance associated with the random fluctuation of water motions in space and time. The momentum exchange brought about by turbulence causes the velocity-depth distribution to be more non-uniform than under laminar conditions. DIVAST only considers the turbulence generated by the bottom wall. The turbulence model in DIVAST relates to Boussinesq's approximation for the mean shear stress τ_e in turbulent flow:

$$\tau_e = \varepsilon \frac{dv}{dy} \tag{3-44}$$

where ε is the eddy viscosity, which is dependent on the turbulence characteristics of the flow and generally many thousand times larger than the molecular viscosity. For the turbulence within a fully-developed plane boundary layer, a relationship between the Chézy coefficient and the eddy viscosity exists. In DIVAST the depth-integrated eddy viscosity is calculated from:

$$\varepsilon = c_e \frac{H}{C} \sqrt{g\left(U^2 + V^2\right)} \tag{3-45}$$

where c_e = eddy viscosity coefficient Fischer's (1979) suggestion of c_e = eddy viscosity coefficient ≈ 0.15 is based upon laboratory and field data. For actual tidal flows in estuaries and coastal areas, the value of c_e is frequently much larger and $c_e \approx 1.0$ is typically in the current version of the model.

3.3.2 Numerical schemes

DIVAST uses a particular type of finite difference scheme, which is based upon the Alternating Direction Implicit (ADI) technique. It involves the sub-division of each time step into two half time steps, and only considers one spatial dimension implicitly in each half time step. This method can avoid the restrictive time step constraints of the explicit schemes and exploit the efficient solution algorithm for tri-diagonal matrices.

In the first half time step, the water elevation and U velocity component (or the unit width discharge p) are solved implicitly in the x-direction, whilst the other variables are represented explicitly. Similarly, for the second half time step, the water elevation η and the V velocity component (or the unit width discharge q) are solved implicitly in the y-direction, with other variables being represented explicitly. With the boundary conditions included, the resulting finite difference equations for each half time step are solved using the method of Gauss elimination and back substitution.

A space staggered grid system is used, with the variables η (elevation) and S (solute concentration) being located at the grid centre and with U and V at the centre of the grid sides as shown in Figure 3-2. The adoption of a staggered grid configuration prevents the appearance of oscillatory solutions, which tend to occur in a non-staggered grid for space centered differences (Fletcher 1991).

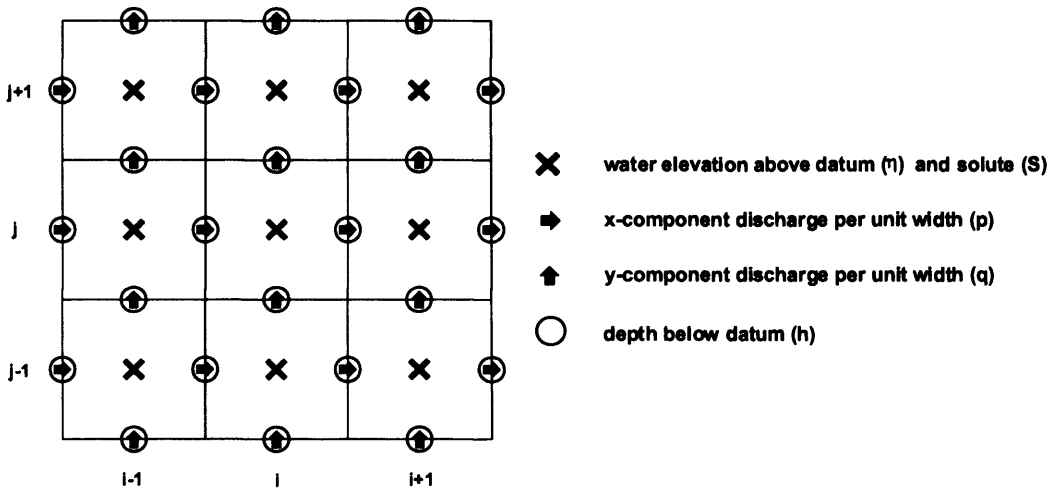

Figure 3-2 Computational space staggered grid system

Depths are specified directly in the middle of the grid sides so that twice as much bathymetric detail can be included as in the traditional way, which stores depths at the corners. This present method allows the bed topography to be represented more accurately, particularly for non-linear bed variations and complicated bed elevations. Moreover, the velocity and water depth occupy the same location, which also attribute to a higher accuracy.

The continuity Equation (3-40) can be expressed for the first and second half time steps, respectively, in the forms:

$$\frac{2}{\Delta t}\left(\eta_{i,j}^{n+\frac{1}{2}}-\eta_{i,j}^{n}\right)+\frac{1}{\Delta x}\left(p_{i+\frac{1}{2},j}^{n+\frac{1}{2}}-p_{i-\frac{1}{2},j}^{n+\frac{1}{2}}\right)+\frac{1}{\Delta y}\left(q_{i,j+\frac{1}{2}}^{n}-q_{i,j-\frac{1}{2}}^{n}\right)=0 \tag{3-46}$$

$$\frac{2}{\Delta t}\left(\eta_{i,j}^{n+1}-\eta_{i,j}^{n+\frac{1}{2}}\right)+\frac{1}{\Delta x}\left(p_{i+\frac{1}{2},j}^{n+\frac{1}{2}}-p_{i-\frac{1}{2},j}^{n+\frac{1}{2}}\right)+\frac{1}{\Delta y}\left(q_{i,j+\frac{1}{2}}^{n}-q_{i,j-\frac{1}{2}}^{n+1}\right)=0 \tag{3-47}$$

where i, j represent the grid point location in the x and y directions respectively and superscripts n, $n+\frac{1}{2}$ and $n+1$ represent variables evaluated at time $t=n\Delta t$, $t=\left(n+\frac{1}{2}\right)\Delta t$ and $t=(n+1)\Delta t$ time levels respectively. Δt represents the time step for computations and n is the time step number. It can be seen by summing the above two equations that the scheme is fully centered in both time and space over the whole time step, indicating second order accuracy.

The non-linear terms in the momentum equations are easy to give rise to

instabilities, even though an implicit scheme has been used. This instability effect may be overcome by time centering the differences using three time levels (Falconer 1977), or a velocity smoothing algorithm. An alternative approach has been used for the non-linear advective acceleration and the eddy viscosity terms by time centered iteration (Roache 1972), except for the cross advective acceleration terms, which are represented using a first order upwind method, thereby including sufficient artificial diffusion to eliminate grid scale oscillations in regions of high velocity gradients.

The x-direction momentum Equation (3-41) can be written in the following manner for the first time step starting from time level n-1/2:

$$\frac{p^{n+\frac{1}{2}}_{i+\frac{1}{2},j} - p^{n-\frac{1}{2}}_{i+\frac{1}{2},j}}{\Delta t} + \beta\left[\frac{\left(\hat{U}\hat{p}\right)^{n}_{i+\frac{3}{2},j} - \left(\hat{U}\hat{p}\right)^{n}_{i-\frac{1}{2},j}}{2\Delta x} + \frac{\left(\overline{\hat{V}}\hat{p}\right)^{n}_{i+\frac{3}{2},j+\frac{1}{2}} - \left(\overline{\hat{V}}\hat{p}\right)^{n}_{i+\frac{3}{2},j-\frac{1}{2}}}{\Delta y}\right]$$

$$= \lambda q^{-n}_{i+\frac{1}{2},j} - \frac{gH^{n}_{i+\frac{1}{2},j}}{2\Delta x}\left(\eta^{n+\frac{1}{2}}_{i+1,j} + \eta^{n-\frac{1}{2}}_{i+1,j} - \eta^{n+\frac{1}{2}}_{i,j}\eta^{n-\frac{1}{2}}_{i,j}\right) + \frac{\rho_a}{\rho}C_*W^2\cos\psi$$

$$- \frac{g\left(p^{n+\frac{1}{2}}_{i+\frac{1}{2},j} + p^{n-\frac{1}{2}}_{i+\frac{1}{2},j}\right)\sqrt{\left(\hat{p}^{n}_{i+\frac{1}{2},j}\right)^2 + \left(q^{-n}_{i+\frac{1}{2},j}\right)^2}}{2\left(H^{n}_{i+\frac{1}{2},j}C^{n}_{i+\frac{1}{2},j}\right)^2} \qquad (3\text{-}48)$$

$$+ \frac{\varepsilon H^{n}_{i+\frac{1}{2},j}}{\Delta x^2}\left[2\left(\hat{U}^{n}_{i+\frac{3}{2},j} + \hat{U}^{n}_{i-\frac{1}{2},j}\right) + \hat{U}^{n}_{i+\frac{1}{2},j+1} + \hat{U}^{n}_{i+\frac{1}{2},j-1}\right.$$

$$\left. - 6\hat{U}^{n}_{i+\frac{1}{2},j} + V^{n}_{i,j-\frac{1}{2}} - V^{n}_{i,j+\frac{1}{2}} - V^{n}_{i+1,j-\frac{1}{2}} + V^{n}_{i+1,j+\frac{1}{2}}\right]$$

where $\hat{U}$ denotes a value corrected by iteration, by setting:

$$\hat{U}^{n} = \begin{cases} U^{n-\frac{1}{2}} & \text{for the first iteration,} \\ \frac{1}{2}\left(U^{n-\frac{1}{2}} + U^{n+\frac{1}{2}}\right) & \text{for the second and remaining iterations,} \end{cases} \qquad (3\text{-}49)$$

$\overline{V}$ denotes a value obtained by averaging corresponding values of surrounding grid points:

$$\overline{V}^{n}_{i+\frac{1}{2},j+\frac{1}{2}} = \frac{1}{2}\left(V^{n}_{i,j+\frac{1}{2}} + V^{n}_{i+1,j+\frac{1}{2}} \right) \tag{3-50}$$

and $\vec{p}$ denotes a value obtained from the upwind algorithm where

$$\vec{p}^{\,n}_{i+\frac{1}{2},j} = \begin{cases} p^{n}_{i+\frac{1}{2},j-1} & if \quad V^{n}_{i+\frac{1}{2},j} > 0, \\ p^{n}_{i+\frac{1}{2},j+1} & if \quad V^{n}_{i+\frac{1}{2},j} > 0, \end{cases} \tag{3-51}$$

Similarly, the y-direction momentum Equation (3-42) can be written for the second time step starting from time level n as:

$$\begin{aligned} &\frac{q^{n+1}_{i,j+\frac{1}{2}} - q^{n}_{i,j+\frac{1}{2}}}{\Delta t} + \beta \left[\frac{\left(\hat{V}\hat{q}\right)^{n+\frac{1}{2}}_{i,j+\frac{3}{2}} - \left(\hat{V}\hat{q}\right)^{n+\frac{1}{2}}_{i,j-\frac{1}{2}}}{2\Delta y} + \frac{\left(\overline{U}\hat{q}\right)^{n+\frac{1}{2}}_{i+\frac{1}{2},j+\frac{1}{2}} - \left(\overline{U}\hat{q}\right)^{n+\frac{1}{2}}_{i-\frac{1}{2},j+\frac{1}{2}}}{2\Delta y} \right] \\ &= \lambda p^{n+1/2}_{i,j+\frac{1}{2}} - \frac{gH^{\,n+1/2}_{i+\frac{1}{2},j}}{2\Delta y}\left(\eta^{n+1}_{i,j+1} + \eta^{n-\frac{1}{2}}_{i,j+1} - \eta^{n+1}_{i,j} - \eta^{n}_{i,j} \right) + \frac{\rho_a}{\rho} C_* W^2 c \sin\psi \\ &\quad - \frac{g\left(q^{n+1}_{i,j+1/2} + q^{n}_{i,j+1/2}\right)\sqrt{\left(q^{n+1/2}_{i,j+1/2}\right)^2 + \left(\overline{p}^{\,n+1/2}_{i,j+1/2}\right)^2}}{2\left(H^{n+1/2}_{i,j+1/2} C^{n+1/2}_{i,j+1/2}\right)^2} \\ &\quad + \frac{\varepsilon H^{n+1/2}_{i,j+1/2}}{\Delta x^2}\left[2\left(\hat{V}^{n+1/2}_{i,j+3/2} + \hat{V}^{n+1/2}_{i,j-1/2}\right) + \hat{V}^{n+1/2}_{i+1,j+1/2} + \hat{V}^{n+1/2}_{i-1,j+1/2} \right. \\ &\quad \left. - 6\hat{V}^{n+1/2}_{i,j+1/2} + U^{n+1/2}_{i-1/2,j} - U^{n+1/2}_{i-1/2,j} - U^{n+1/2}_{i-1/2,j+1} + U^{n+1/2}_{i+1/2,j+1} \right] \end{aligned} \tag{3-52}$$

with the $\hat{V}$, $\overline{U}$ and $\vec{q}$ being similar to those expressions listed in Equations (3-49) - (3-51) at time level $n+\frac{1}{2}$ instead of n.

This scheme is basically second order accurate, both in time and space, with no stability constraints due to the implicit nature of the ADI scheme. However, it has been recognized that the time step needs to be restricted so that a reasonable computational accuracy can be achieved. A maximum Courant number (C_r) has been suggested as:

$$C_r = 2\Delta t \sqrt{gH\left(\frac{1}{\Delta x^2} + \frac{1}{\Delta y^2} \right)} \le 4\sqrt{2} \tag{3-53}$$

with an average depth being used in the estimate.

3.4. TVD-MacCormack model

The ADI method used in DIVAST is suitable to solve the shallow water equations in most of coastal and estuarine waters where the flow varies smoothly. However, it has been generally accepted that the ADI method is not suitable for calculating the super-critical flows, such as dam break, storm surges and flood inundation, hence a TVD-MacCormack (Liang et al., 2007) model has been developed at Cardiff University to simulate such problems.

3.4.1 Hydrodynamic governing equations

The hydrodynamic governing equations used in TVD-MacCormack model are the same as those of DIVAST, i.e., Equations (3-40) to (3-42). Neglecting the turbulence, Coriolis and wind effects, as well as the presence of vegetations, Equations (3-40) to (3-42) can be written in the following general form:

$$\frac{\partial \eta}{\partial t}+\frac{\partial p}{\partial x}+\frac{\partial q}{\partial y}=q_m \tag{3-54}$$

$$\frac{\partial p}{\partial t}+\frac{\partial(\beta p^2/H)}{\partial x}+\frac{\partial(\beta pq/H)}{\partial y}=-gH\frac{\partial \eta}{\partial x}+-\frac{gp\sqrt{p^2+q^2}}{H^2C^2} \tag{3-55}$$

$$\frac{\partial q}{\partial t}+\frac{\partial(\beta pq/H)}{\partial x}+\frac{\partial(\beta q^2/H)}{\partial y}=-gH\frac{\partial \eta}{\partial y}-\frac{gq\sqrt{p^2+q^2}}{H^2C^2} \tag{3-56}$$

where the notations are the same as those for Equations (3-40) to (3-42).

In the TVD-MacCormack model, Equations (3-54) to (3-56) are rearranged into the following conservative form:

$$\frac{\partial \mathbf{X}}{\partial t}+\frac{\partial \mathbf{F}}{\partial x}+\frac{\partial \mathbf{G}}{\partial y}=\mathbf{S}+\mathbf{T} \tag{3-57}$$

where

$$\mathbf{X}=\begin{bmatrix}\eta\\ q_x\\ q_y\end{bmatrix},\quad \mathbf{F}=\begin{bmatrix}q_x\\ \dfrac{\beta q_x^{\,2}}{h+\eta}+\dfrac{g\eta^2}{2}+gh\eta\\ \dfrac{\beta q_x q_y}{h+\eta}\end{bmatrix},\quad \mathbf{G}=\begin{bmatrix}q_y\\ \dfrac{\beta q_x q_y}{h+\eta}\\ \dfrac{\beta q_y^{\,2}}{h+\eta}+\dfrac{g\eta^2}{2}+gh\eta\end{bmatrix} \tag{3-58}$$

$$\mathbf{S}=\begin{bmatrix}0\\ g\eta\dfrac{\partial h}{\partial x}-\dfrac{gq_x\sqrt{q_x^{\,2}+q_y^{\,2}}}{(h+\eta)^2C^2}\\ 0\end{bmatrix},\quad \mathbf{T}=\begin{bmatrix}0\\ 0\\ g\eta\dfrac{\partial h}{\partial y}-\dfrac{gq_y\sqrt{q_x^{\,2}+q_y^{\,2}}}{(h+\eta)^2C^2}\end{bmatrix} \tag{3-59}$$

3.4.2 Numerical schemes

Using the operator-splitting technique, the solution to Equation (3-57) is obtained by solving two 1-D problems in sequence, giving:

$$\frac{\partial \mathbf{X}}{\partial t}+\frac{\partial \mathbf{F}}{\partial x}=\mathbf{S},\quad \frac{\partial \mathbf{X}}{\partial t}+\frac{\partial \mathbf{G}}{\partial y}=\mathbf{T} \tag{3-60}$$

On a uniform rectangular grid system, the explicit discretization of Equations (3-60) can be written as:

$$\mathbf{X}_{i,j}^{n+1}=\mathrm{L}_x\,\mathbf{X}_{i,j}^{n},\quad \mathbf{X}_{i,j}^{n+1}=\mathrm{L}_y\,\mathbf{X}_{i,j}^{n} \tag{3-61}$$

where L_x and L_y are the finite-difference operators, and the subscript and superscript of X represent the spatial and temporal grid levels respectively. The finite difference solution to Equation (3-57) can thus be approximated by:

$$\mathbf{X}_{i,j}^{n+2}=\mathrm{L}_x\mathrm{L}_y\mathrm{L}_y\mathrm{L}_x\,\mathbf{X}_{i,j}^{n} \tag{3-62}$$

The TVD-MacCormack scheme is utilized to solve consecutively the two 1-D hyperbolic equations in each time step. Taking the first operator in Equation (3-61) as an example, the discretization scheme (or the finite-difference operator L_x) is given by:

$$\mathbf{X}_i^p = \mathbf{X}_i^n - \left(\mathbf{F}_i^n - \mathbf{F}_{i-1}^n\right)\cdot \Delta t/\Delta x + \mathbf{S}^n \cdot \Delta t \tag{3-63}$$

$$\mathbf{X}_i^c = \mathbf{X}_i^n - \left(\mathbf{F}_{i+1}^p - \mathbf{F}_i^p\right)\cdot \Delta t/\Delta x + \mathbf{S}^p \cdot \Delta t \tag{3-64}$$

$$\mathbf{X}_i^{n+1} = \left(\mathbf{X}_i^p + \mathbf{X}_i^c\right)/2 + \left[\mathrm{G}(r_i^+) + \mathrm{G}(r_{i+1}^-)\right]\cdot \Delta\mathbf{X}_{i+1/2}^n - \left[\mathrm{G}(r_{i-1}^+) + \mathrm{G}(r_i^-)\right]\cdot \Delta\mathbf{X}_{i-1/2}^n \tag{3-65}$$

where the superscripts p and c denote the predictor and corrector steps respectively, Δx and Δt are the spatial and time steps, G( ) is a function that will be discussed further below and:

$$\Delta\mathbf{X}_{i+1/2}^n = \mathbf{X}_{i+1}^n - \mathbf{X}_i^n, \quad \Delta\mathbf{X}_{i-1/2}^n = \mathbf{X}_i^n - \mathbf{X}_{i-1}^n \tag{3-66}$$

$$r_i^+ = \frac{\left\langle \Delta\mathbf{X}_{i-1/2}^n, \Delta\mathbf{X}_{i+1/2}^n \right\rangle}{\left\langle \Delta\mathbf{X}_{i+1/2}^n, \Delta\mathbf{X}_{i+1/2}^n \right\rangle}, \quad r_i^- = \frac{\left\langle \Delta\mathbf{X}_{i-1/2}^n, \Delta\mathbf{X}_{i+1/2}^n \right\rangle}{\left\langle \Delta\mathbf{X}_{i-1/2}^n, \Delta\mathbf{X}_{i-1/2}^n \right\rangle} \tag{3-67}$$

The angled brackets in the numerator and denominator of Equations (3-67) denote the scalar product of the two vectors within the angled brackets. The function G( ) is defined as:

$$\mathrm{G}(x) = 0.5 \times C \times [1 - \phi(x)] \tag{3-68}$$

in which the flux limiter function is given as:

$$\phi(x) = \max(0, \min(2x, 1)) \tag{3-69}$$

and the variable C as:

$$C = \begin{cases} Cr \times (1 - Cr), & Cr \le 0.5 \\ 0.25, & Cr > 0.5 \end{cases} \tag{3-70}$$

with Cr being the local Courant number, defined as:

$$Cr = \frac{\left(|q_x/H| + \sqrt{gH}\right)\Delta t}{\Delta x} \tag{3-71}$$

3.4.3 Comparison with the ADI scheme

Although the numerical backgrounds of the ADI and the TVD-MacCormack method are very different, the ADI method appears similar to the operator-splitting method in the sense that it breaks up the 2-D problem into 1-D problems. In the present TVD-MacCormack model all of the variables are stored and computed at

the same location, while in the ADI model a staggered computational grid is used, with the water elevations and velocities (or discharges) being located at different grid locations. Nevertheless, the computational grids for both models are uniformly distributed in two orthogonal directions. Therefore, these two methods can be easily incorporated into a single computer model framework. For smooth flows, the two methods produce very similar results, as will be seen in the last section of this chapter. Discrepancies between them are only apparent for rapid flows. The following examples highlight the different results obtained using the two methods when simulating flows with strong water level gradients and regime transitions.

Figure 3-3 illustrates the dam-break problem, which has been chosen for the comparisons between the two methods. This can be considered as a longitudinal profile perpendicular to the dam, with h_1 and h_0 being the water depths at the upstream headwater and downstream tailwater respectively. If the dam collapses all together, then the problem is 1-D. However, if the dam fails only partially, then the problem is 2-D. The bed roughness has practically little influence on this type of flow (e.g. Fraccarollo and Toro 1995, Tseng and Chu 2000), since the acceleration force dominates over the bed friction force in this situation.

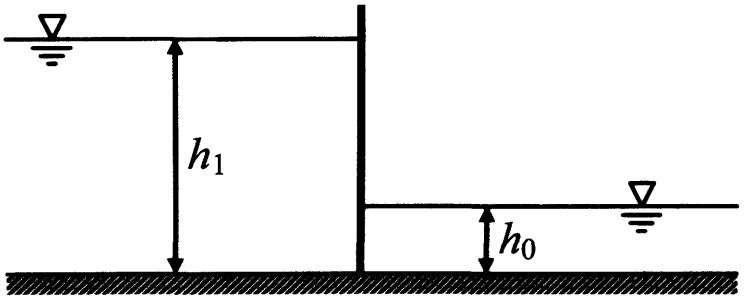

Figure 3-3 Illustration of the dam-break problem

3.4.3.1 1-D dam-break

The scenario considered here was the total and instantaneous dam-failure on a flat and frictionless bed. This provides an ideal benchmark test case for shock-capturing schemes since analytical solution has been known. The present

configuration is the same as that used by Wang et al. (2000), where the initial upstream water depth was 10 m, and the downstream water depth was 2 m and 0.1 m, respectively. The dam was located at x = 500 m, and the grid spacing was 10 m. The time step was 0.5 s, unless otherwise specified. Figure 3-4 shows the water surface positions 30 s after dam failure using the both ADI and TVD-MacCormack methods, where the solid line represents the analytical solution and the circles illustrate the predicted results.

The water level drops due to the propagation of a depression wave upstream are well predicted for both types of the model, since the flow in this region is relatively slow. Better agreement between the analytical and numerical solutions has been observed for the downstream water depths using the TVD-MacCormack model. Negative water depths occurred due to numerical oscillations for the results of ADI method (Figure 3-4).

Figure 3-5 shows the computational results using the ADI model for the same dam-break problem with a large viscosity. In order to remove non-physical oscillations, an exceptionally large viscosity coefficient has to be specified, with the exact value needing to be determined by trial and error. The agreement between the analytical and numerical solutions is satisfactory. But it should be noted that the analytical solutions assume zero viscosity, and the same is true for the TVD-MacCormack model. Consequently the viscosity introduced in the ADI model can only be understood as artificial viscosity.

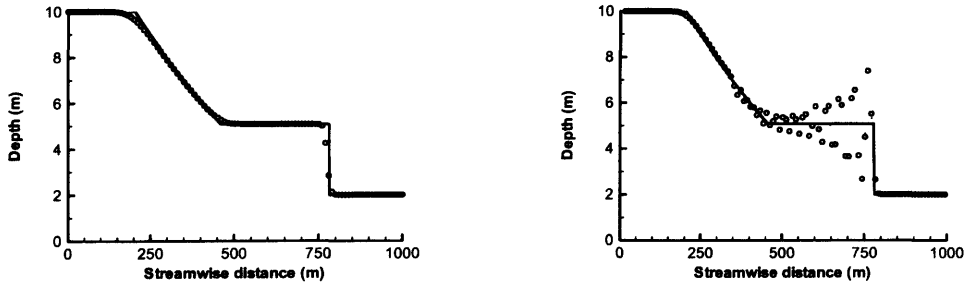

(a) h_0 = 2 m

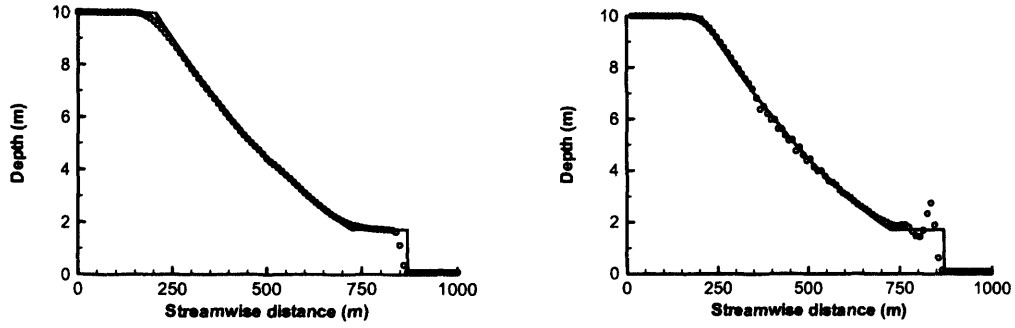

(b) $h_0 = 0.1$ m

Figure 3-4 Comparisons of 1-D dam-break simulations using TVD-MacCormack model (left) and DIVAST(right)

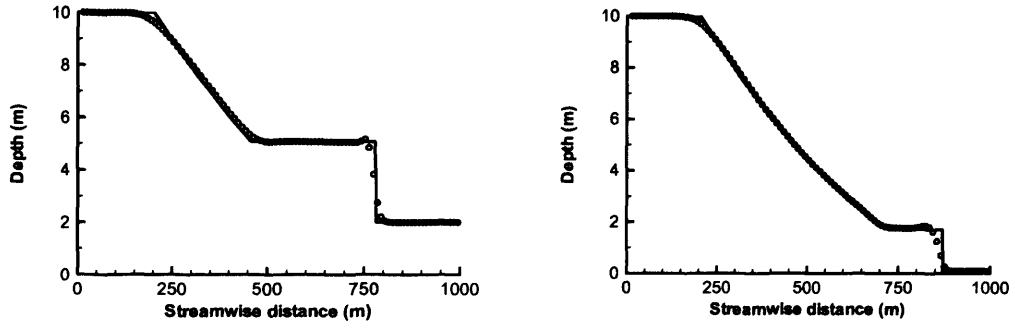

(a) $h_0 = 2$ m, $\varepsilon = 15.0$ m^2/s (b) $h_0 = 0.1$ m, $\varepsilon = 7.0$ m^2/s

Figure 3-5 1-D dam-break simulation using the DIVAST model

3.4.3.2 2-D dam-break

This is another widely used example for benchmarking shock-capturing schemes. In this test case, the computational domain is 200 m wide and 200 m long. A dam with a thickness of 15 m divides the domain into two equal parts at x = 100 m. Initially, the upstream water depth is 10 m, while the downstream water depth is set to 5 m and 0.1 m, respectively. The breach in the dam starts from y = 95 m and ends at y = 170 m. The bed is again flat and frictionless. The water surface at 7.2 s after the breach is examined in detail. Although there are no theoretical solutions available to this problem, there have been a number of numerical simulations reported in the literature (e.g. Mingham and Causon 1998,

Louaked and Hanich 1998, Wang et al. 2000, Tseng and Chu 2000). To be consistent with most of these studies, the grid size is set to be 5 m and the time step is set at 0.2 s.

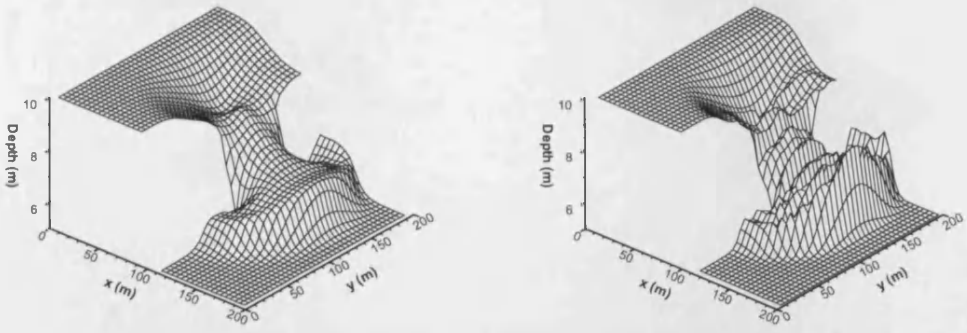

(a) h_0 = 5 m

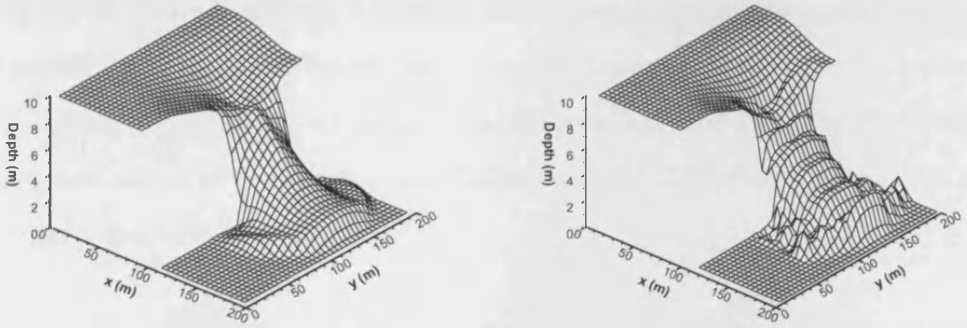

(b) h_0 = 0.1 m

Figure 3-6 Comparisons of 2-D dam-break simulations using TVD-MacCormack model (left) and DIVAST(right)

From Figure 3-6, it can be seen that the results for the TVD-MacCormack model agree well with the results of the other simulations published in the literature, while violent non-physical oscillations are observed in the predicted water surfaces for the computation results of ADI model. Figure 3-7 shows ADI simulations with large viscosity coefficients. It has been found that spurious oscillations cannot be effectively removed by simply increasing the viscosity coefficient when h_0 was set to 0.1 m. Although spurious oscillations still exist near the bore front for a viscosity of 2.0 m^2/s, extra diffusion becomes apparent in the vicinity of the depression wave front when compared with the corresponding result

by the TVD-MacCormack model, as shown in Figure 3-6b.

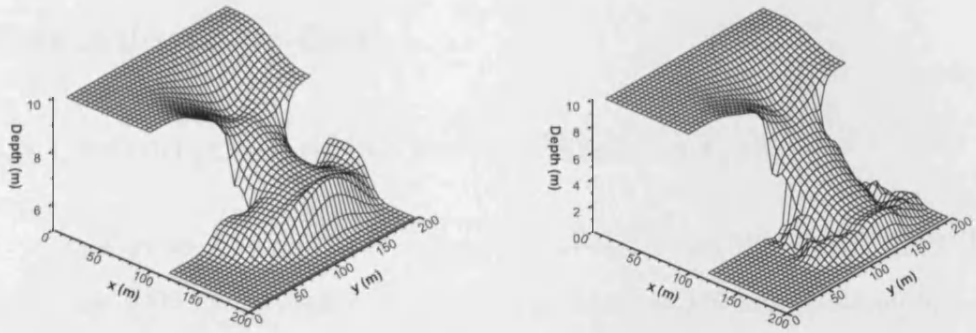

(a) $h_0 = 5$ m, $\varepsilon = 5.0$ m^2/s (b) $h_0 = 0.1$ m, $\varepsilon = 2.0$ m^2/s

Figure 3-7 2-D dam-break simulation using the DIVAST model

Apart from this defect, another problem with the ADI model is that the right amount of artificial viscosity needed is hard to determine without some numerical experiments. It has been found that the results are quite sensitive to the value of the viscosity coefficient. As an example, Figure 3-8 shows the results obtained using two values of the viscosity coefficient, with the difference between both sets of results shown to be quite large.

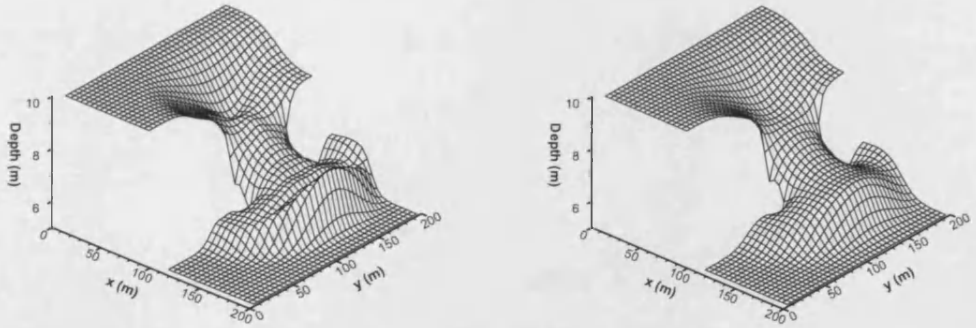

(a) $\varepsilon = 3.0$ m^2/s (b) $\varepsilon = 10.0$ m^2/s

Figure 3-8 Influence of viscosity for a 2-D DIVAST model, $h_0 = 5$ m

3.5 Application of ADI and TVD models to Persian/Arabian Gulf

3.5.1 Introduction of the Persian/Arabian Gulf

The Persian/Arabian Gulf is located between 24° and 30° latitude North. It is more than 1000 km in length. The maximum width is 370 km, spanning between the coasts of United Arab Emirates (UAE) and Iran. It is connected to the Arabian Sea through the Strait of Hormuz - a narrow passage as narrow as 56 km (Elshorbagy et al. 2006; Kampf and Sadrinasab 2005). The Gulf is a large and relatively shallow basin. It covers a surface area of nearly 239,000 km^2 with an average depth of 36 m. Extensive shallow regions, less than 20 m deep, are found along the coast of UAE, around Bahrain, and at the head of the Gulf. Deeper sections of more than 40 m depth are found along the Iranian coast and into the Strait of Hormuz (See Figure 3-9). Four major rivers flow into the Gulf from the northern coast. The southern Gulf is literally rocky, while the northern parts become much smoother as a result of sediment discharges from the rivers.

Figure 3-9 Bathymetry of the Persian/Arabian Gulf

The hydrological, meteorological, and oceanographic forces contribute to the dynamics of the shallow semi-enclosed gulf, and wind, evaporation, and the supply of fresher water from the Arabian Sea maintain a horizontal density gradient with seasonally varying vertical stratifications (Azam et al. 2006). Modelling studies on the tidal dynamics of the Gulf have found that the motion of the water body is complex and mainly related to the tide. The tide-induced flows are the strongest in the Strait of Hormuz (Chu et al. 1988; Lardner et al. 1982; Sabbagh-Yazdi et al. 2007). The following sections show how the hydrodynamic models (both ADI and TVD-MacCormack models) are set up to compute the tidal and wind-induced water level elevations and currents at any prescribed period.

3.5.2 Model setup

The computational domain is limited by the closed boundaries of the Gulf and a cross section at the Strait of Hormuz, which serves as an open boundary. The grid size is set to 10km × 10km for the whole Gulf. The bathymetry of this area is applied to the model using Admiralty Charts published by the United Kingdom Hydrographic Office (UKHO). Since most of the bed materials are very fine sediments, the roughness value (k_s) was set to 5mm for the whole area. The tide at Didamar Island in the Strait of Hormuz is imposed as the open boundary condition. The water elevation variation time series at the open boundary has been calculated by Simplified Harmonic Method (SHM), based on Admiralty Tide Table (ATT) provided by UKHO (UKHO, 2007). The method of tidal prediction will be detailed later. The initial velocities are set to zero, and the initial water elevations are the same as the open boundary value. The simulation time step is set to 240 seconds, and 600 hours of simulation has been conducted.

3.5.3 Tidal predictions based on ATT

The water level fluctuations in the Persian/Arabian Gulf are primarily dominated by the astronomic tide, which can be predicted by harmonic analysis,

which is the superposition of many sinusoidal components with amplitudes and frequencies determined by a local analysis of the measured tidal series. This method is based on long term statistics derived from an empirical method. The Admiralty Tide Table provides the harmonic constants for tidal analysis, as well as the Simplified Harmonic Method (SHM), for tidal predictions at a number of selected ports. A general tidal analysis process is detailed as follows.

The ideal tide curve for any given port is represented as an average height a_0, plus a sum of terms ("constituents"). The water surface elevation η can be expressed as:

$$\eta = a_0 + \sum_{i=1}^{n} a_i \cos(\omega_i t - \delta_i) \tag{3-72}$$

Each of the constituents has the form

$$f_i = a_i \cos(\omega_i t - \delta_i) \tag{3-73}$$

with

$$\omega_i = \frac{2\pi}{T_i} \tag{3-74}$$

The time t is measured in hours, and f_i in metres. T_i is the period for each constituent in hours. a_i, ω_i, δ_i represent the amplitude, the angular speed (or frequency) and the phase of the constituent respectively. Different constituents have different angular speeds, which are complex components of some basic astronomical speed. So for each constituent, the angular speed is fixed and given in radians/hour. The amplitude a_i and phase δ_i for each constituent are determined from the tidal record by a Fourier analysis. The number of constituents needed for accurate predictions varies from port to port.

The SHM is based on Equation (3-72), but only four major constituents are used in the prediction, namely, M2, S2, K1 and O1, which represent the lunar semi-diurnal tide, solar semi-diurnal tide, luni-solar diurnal tide and the lunar declinational tide. The harmonic constants related data can be found in ATT

Volume 3 (UKHO 2007). For each constituent, the preliminary amplitude H and preliminary phase g are given in Part III, and there are daily varied parameters, tidal angle A and factor F, published in Table VII, which can be used to revise the preliminary amplitude and phase of each of the four main constituents for the date concerned. The revision allows for other effects to be taken into account. The relationships between H, g, A, F and a_i, δ_i of Equation (3-72) are as follows:

$$a_i = H \times F \tag{3-75}$$

$$\delta_i = A + g \tag{3-76}$$

This method is able to predict daily tidal levels for a specific port over time. When the Shallow Water Corrections and Seasonal Corrections are introduced, the predictions obtained are equivalent to those containing 36 harmonic constituents. Figure 3-10 shows a SHM prediction based on the ATT for tidal elevation fluctuation in the Port of Didamar Island, which has been designated as the open boundary condition for the hydrodynamic simulation of the Persian/Arabian Gulf.

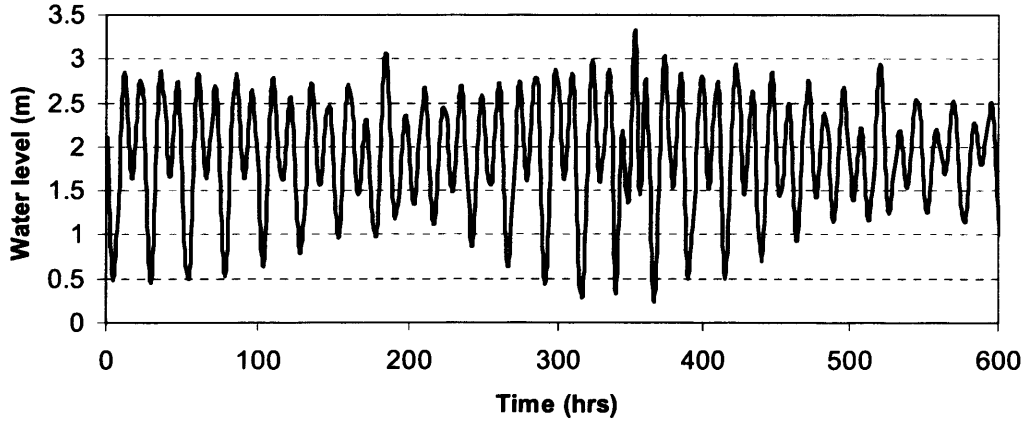

Figure 3-10 Water surface elevation fluctuation at Didamar Island (Strait of Hormuz)

3.5.4 Calibration and verification

The model calibrations were undertaken for both tidal levels and tidal currents. The locations of the calibration points are marked in Figure 3-9, where A, B, and C were calibrated for tidal levels and H and G for tidal currents. Water was considered still at the start of the computation, and after a 100-hour warm-up period, the hydrodynamic model outputs were compared with the ATT predictions (See Table 3-1, 3-2 and Figure 3-11, 3-13).

In order to verify the models' accuracy, four more points were chosen for comparison of the results between the model predictions and the ATT predictions. The locations of these points are also marked in Figure 3-9, with D, E and F for tidal level verifications and F for tidal current verifications (See Table 3-1, 3-2 and Figure 3-12, 3-14).

Table 3-1 Calibration and verification points for tidal levels

Number	Latitude	Longitude	Average error (%) - DIVAST	Average error (%) - TVD
A	28°44′N	48°24′E	-9.11	-4.07
B	29°16′N	50°20′E	6.07	7.47
C	26°12′N	50°37′E	2.29	9.08
D	28°00′N	51°10′E	3.51	1.06
E	25°40′N	52°24′E	-2.11	-2.92
F	25°12′N	54°16′E	-7.81	-5.52

Table 3-2 Calibration and verification points for tidal currents

Number	Latitude	Longitude	Average error (%) - DIVAST	Average error (%) - TVD
H	29°57′N	49°08′E	19.1	20.4
G	28°36′N	49°00′E	21.3	19.1
F	25°12′N	54°16′E	20.7	21.1

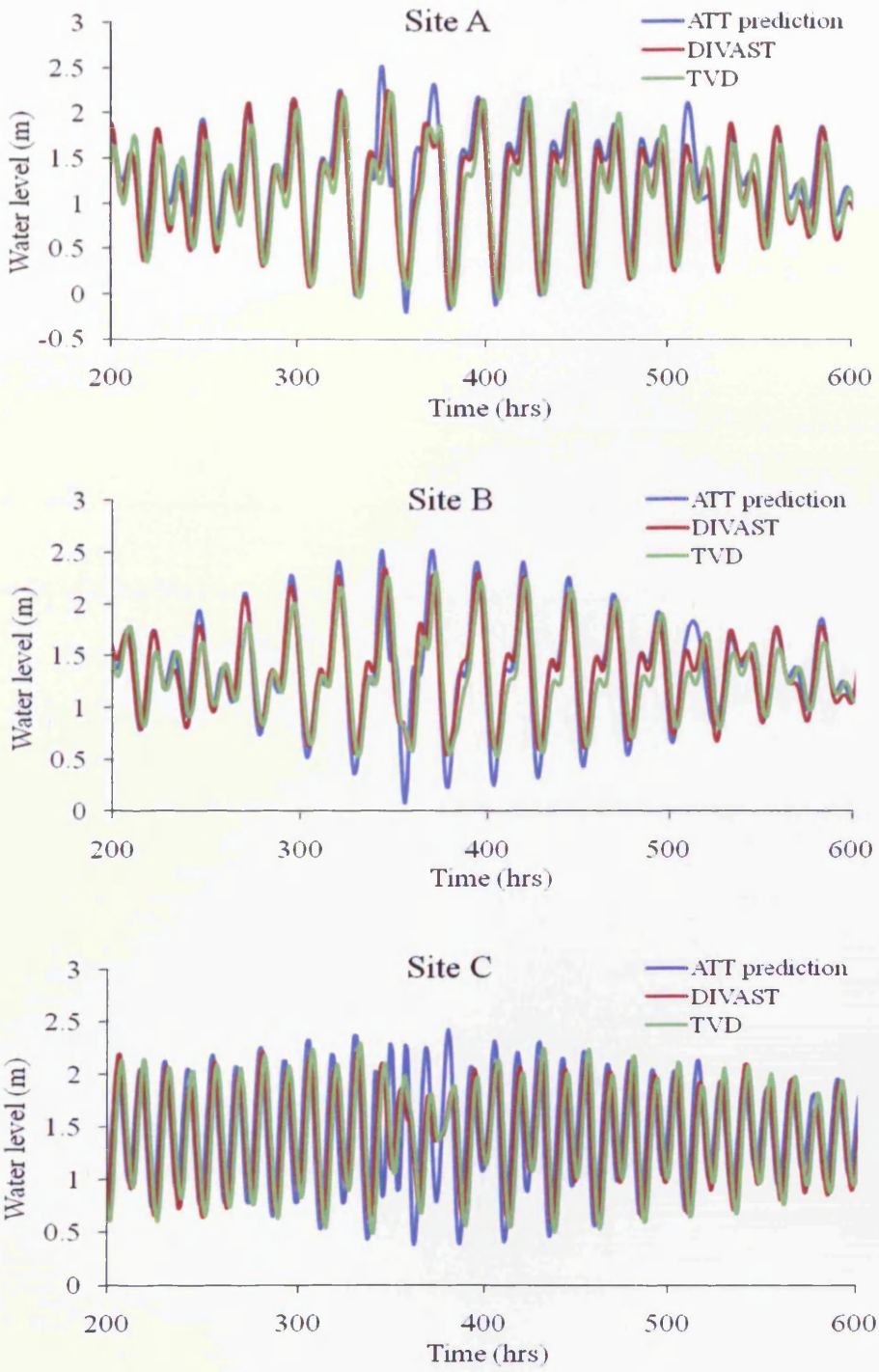

Figure 3-11 Comparison of computed water surface levels with the results of the British Admiralty tide tables at points A, B and C

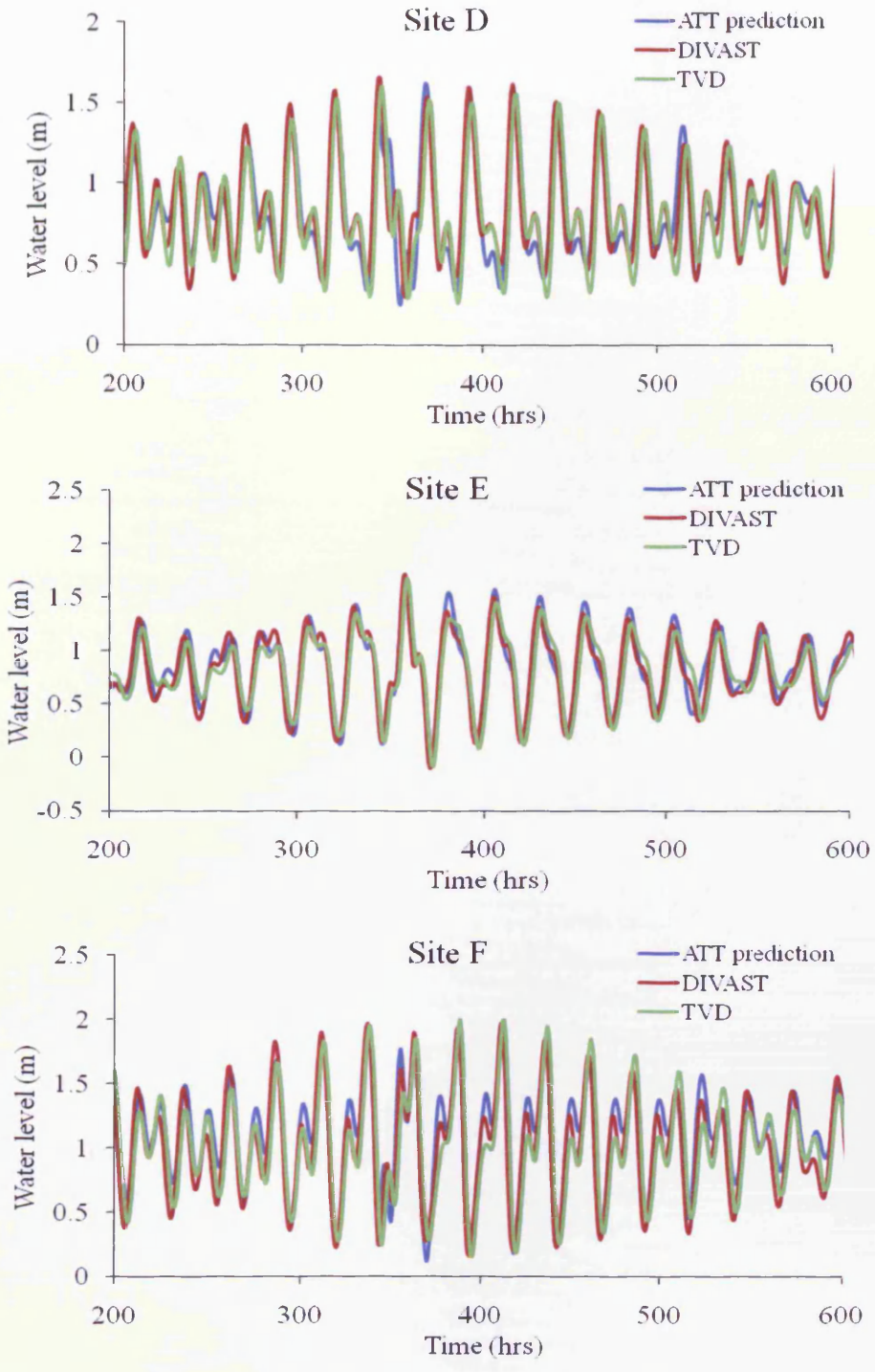

Figure 3-12 Comparison of computed water surface levels with the results of the British Admiralty tide tables at points D, E and F

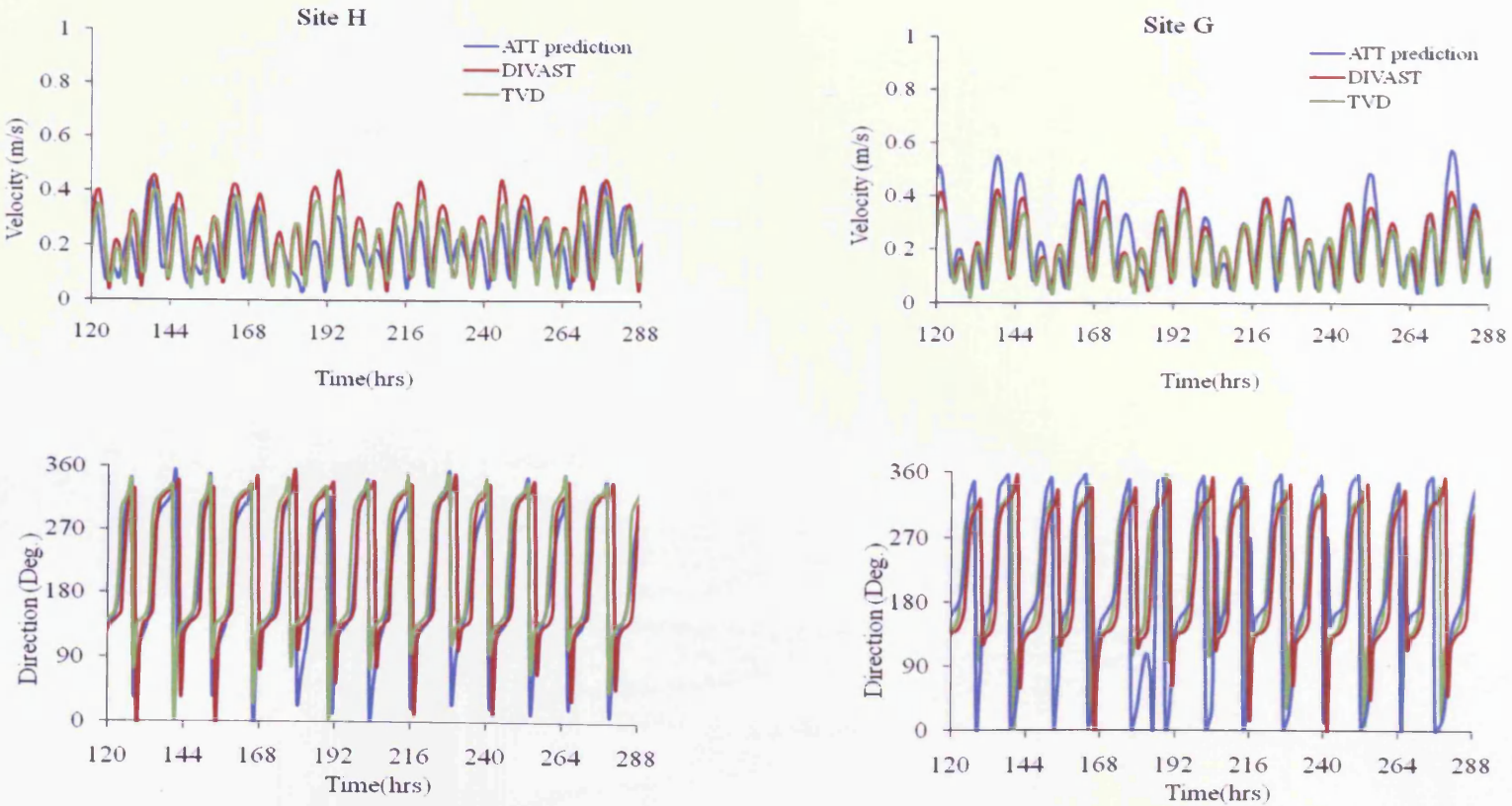

Figure 3-13 Comparison of the computed tidal currents with the results of the British Admiralty tide tables at points H and G

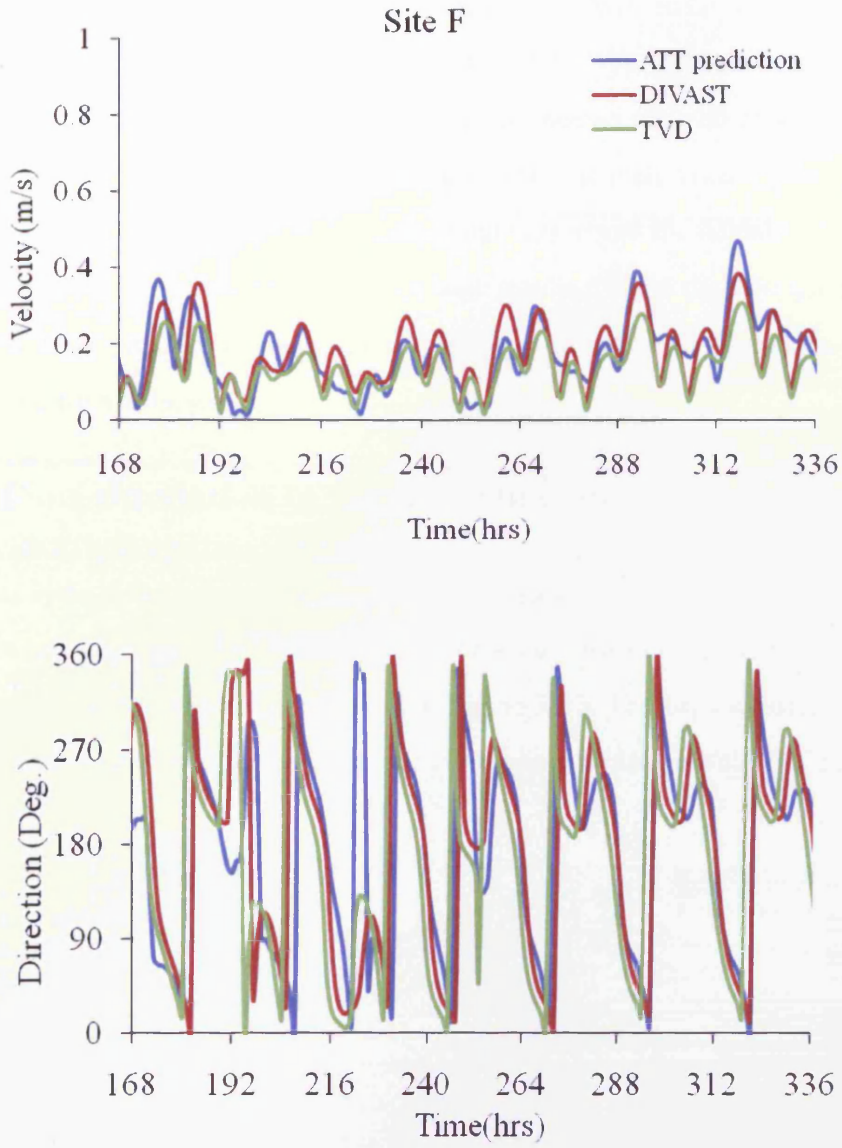

Figure 3-14 Comparison of the computed tidal currents with the results of the British Admiralty tide tables at point F

From the above figures, it can be seen that the water elevations calculated from the hydrodynamic models are in good agreement with the ATT predictions. The results of both the computed velocities and their directions agree in an acceptable extent with the predicted values, although the agreements are not as good as the water elevation comparisons. It is found from the simulation results

that both the ADI model and the TVD-MacCormack model work well in simulating the hydrodynamic processes in the Persian/Arabian Gulf.

The source of errors include imperfect geometric representation (simplification of coastal and bed irregularities as well as removal of several small islands, particularly along the coastal zones), the relatively coarse grid spacing, and the lack of knowledge of the variable roughness across the domain. Therefore, the present model may produce more accurate results if more detailed geometrical data and field parameters, such as the spatial and temporal variations of bed roughness, are available.

3.5.5 Flow simulation in the Arabian Gulf

The hydrodynamic simulation results are visualised at four phases of the tidal cycle: at low tide, high tide, flood tide and ebb tide. Both the velocity vectors and the water surface elevations are plotted in Figure 3-15. The velocity magnitude of the standard arrow is 0.5 m/s, and the water elevation varies between 0 – 2.5m.

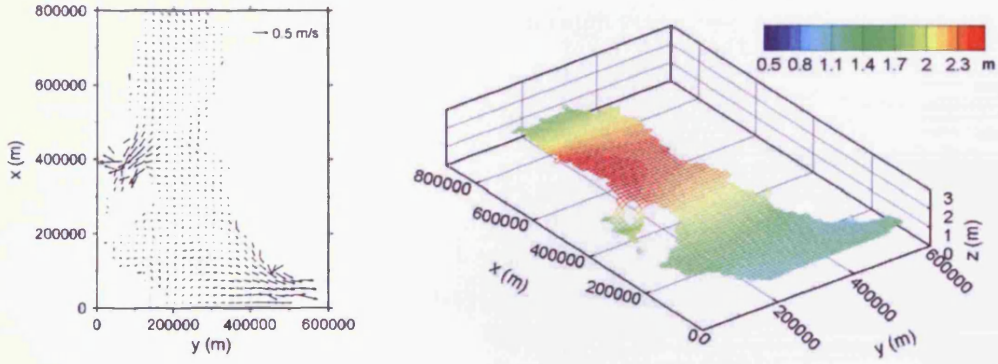

T = 204 hours (low tide)

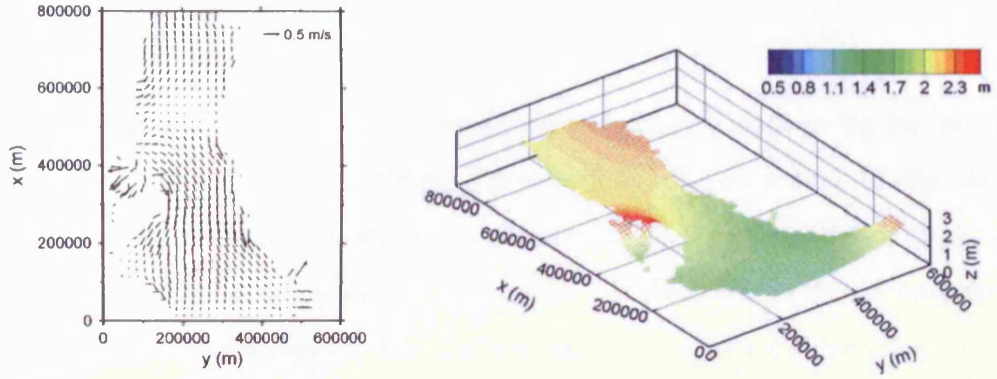

T = 207 hours (flood)

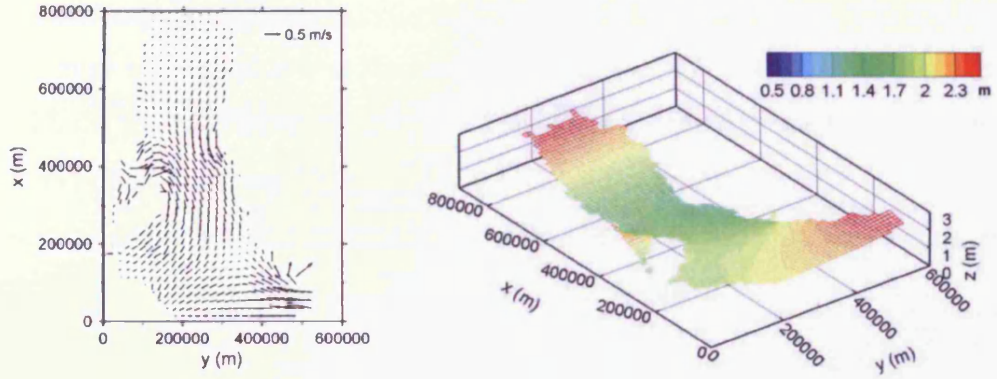

T = 210 hours (high tide)

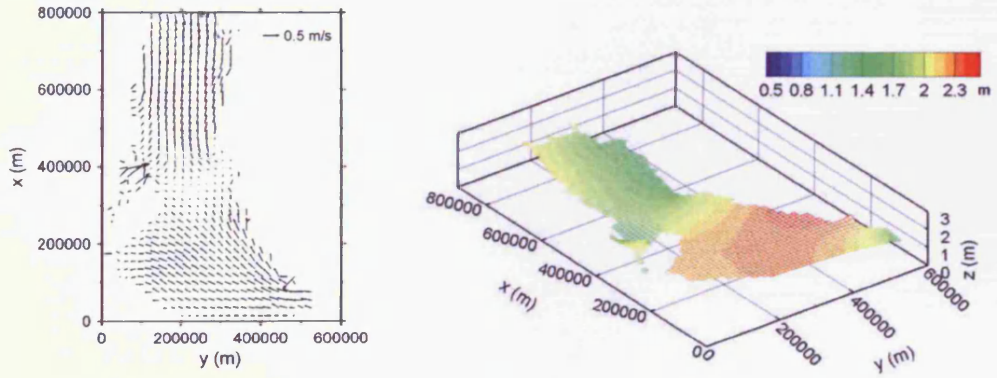

T = 213 hours (ebb)

Figure 3-15 Velocity distributions and water elevations at different times during the tidal cycle (times relative to high water at Strait of Hormuz)

3.6 Summary

In this chapter, the three dimensional governing equations for the general fluid motion have been presented, followed by the derivation of the depth integrated form of the hydrodynamic equations for shallow water flows. The terms and parameters in the mass and momentum conservation equations have been discussed and elaborated on. The shallow water equations are solved numerically using uniform rectangular computational meshes. Two finite difference schemes, ADI and TVD-MacCormack, have been formulated to solve the shallow water equations. After the two hypothetical verification cases, both the ADI and TVD schemes are applied to simulate the tidal oscillations of the Persian/Arabian Gulf, with the results compared with predictions made by the ATT method. It has been found that both the ADI and TVD schemes perform well in simulating hydrodynamic processes that varies smoothly, but only the TVD scheme is capable of predicting rapid hydrodynamic phenomena with shocks.

Chapter 4

The TVD-MacCormack Scheme for Solving the Solute Transport Equation

4.1 Introduction

Increasing environmental awareness demands an increasing level of accuracy in predicting the fate and transport of pollutants in water bodies. In undertaking hydro-environmental impact assessment studies, it is often necessary to simulate flow patterns and monitor pollutant transport processes in inland waters, estuaries and coastal regions, and this need has led to significant advances in numerical model development in water quality predictions and particularly in assessing the quality and health risk assessment of bathing waters. This chapter focuses on the implementation of a TVD-MacCormack model for predicting the solute transport process. Some idealized and practical examples are presented to illustrate the performance of the model.

4.2 TVD-MacCormack model

4.2.1 Governing equation

In modelling the flux of water quality indicators and suspended sediment concentrations within estuaries and coastal waters, when assuming that the solute material exactly follows the flow, the mass conservation equation can be written in general terms for any substance introduced into the water column, as given by Falconer and Chen, (1996):

$$\frac{\partial HS}{\partial t}+\frac{\partial UHS}{\partial x}+\frac{\partial VHS}{\partial y}=\frac{\partial}{\partial x}\left(HD_{xx}\frac{\partial S}{\partial x}+HD_{xy}\frac{\partial S}{\partial y}\right)+\frac{\partial}{\partial y}\left(HD_{yx}\frac{\partial S}{\partial x}+HD_{yy}\frac{\partial S}{\partial y}\right)+q_S \qquad (4\text{-}1)$$

where S is the depth averaged concentration of a solute, which can be used to represent a water quality indicator, H is water depth, t is time, U and V are the depth averaged velocity components along the two Cartesian coordinates, x and y, respectively, and D_{xx}, D_{xy}, D_{yx} and D_{yy} constitute the diffusion tensor of depth-averaged mixing, whose principal direction coincides with the flow direction. Along and perpendicular to the flow, the depth-averaged mixing coefficients are estimated to be

$$D_t=\varepsilon_t H u_*, \quad D_l=\varepsilon_l H u_* \qquad (4\text{-}2)$$

where ε_l and ε_t are dimensionless constants for longitudinal dispersion and turbulent diffusion respectively, and u_* is the shear velocity. For fully-developed boundary layer flows in straight channels, the theoretical values are $\varepsilon_l = 5.86$ and $\varepsilon_t = 0.07$ (Fischer 1973). However, it has been found that these values need to be increased dramatically for open channel flows in natural environments. In the absence of field measurements, Falconer (1991) recommended typical values of $\varepsilon_l = 13.0$ and $\varepsilon_t = 1.2$. The shear velocity can be calculated from the magnitude of the velocity, $\sqrt{U^2+V^2}$, and Chézy coefficient, C.

$$u_*=\frac{\sqrt{g}}{C}\cdot\sqrt{U^2+V^2} \qquad (4\text{-}3)$$

Through tensor rotation, the mixing coefficients in Equation (4-1) can be written as (Preston 1985)

$$D_{xx}=\frac{\sqrt{g}H\left(\varepsilon_l U^2+\varepsilon_t V^2\right)}{C\sqrt{U^2+V^2}} \qquad (4\text{-}4a)$$

$$D_{xy}=D_{yx}=\frac{\sqrt{g}H\left(\varepsilon_l-\varepsilon_t\right)UV}{C\sqrt{U^2+V^2}} \qquad (4\text{-}4b)$$

$$D_{yy} = \frac{\sqrt{g}H\left(\varepsilon_t V^2 + \varepsilon_t U^2\right)}{C\sqrt{U^2 + V^2}} \tag{4-4c}$$

The last term, q_S, on the right hand side of Equation (4-1) represents the source/sink contribution per unit area, which may be due to the wastewater disposal through outfalls, pollutant decay/growth, chemical and biological transformations or a combination of these processes.

4.2.2 Numerical Schemes

A TVD-MacCormack scheme has been used in solving Equation (4-1). Through the operator-splitting technique, the solution to Equation (4-1) can be found by solving two one-dimensional pure advection problems and a pure two-dimensional diffusion problem. Diffusion is a parabolic process and can be solved easily with a central difference scheme. The advection process, however, is a hyperbolic process and admits discontinuities in the solution. The introduction of a non-linear flux limiter to the standard MacCormack scheme can give second-order spatial and temporal accuracy. The flux limiter is designed according to the TVD criterion. An advantage of the operator-splitting technique is that the most suitable numerical schemes can be chosen to address different physical processes separately. In this study, the limiter is applied to the advection process alone, rather than to the combined advection-diffusion processes. Hence, the degree of limiting is independent of the physical dispersion.

Figure 4-1 shows the neighboring grid points used in calculating the value at point (i, j). Five points are used in either x or y direction of the advection calculations, and the nearest nine points are used in the diffusion calculations. Details of the numerical algorithm can be found in Liang et al. (2010).

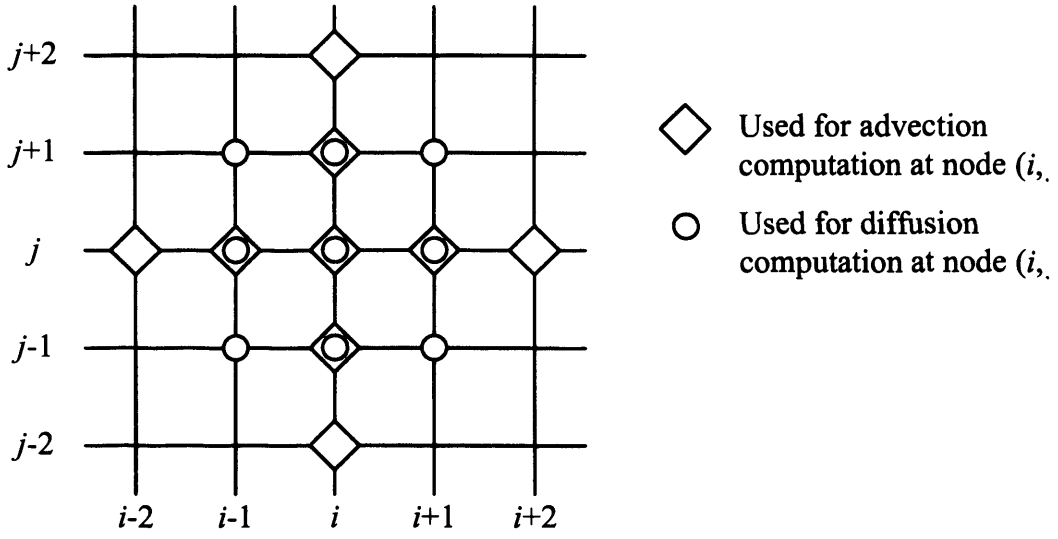

Figure 4-1 Computational stencil of the TVD-MacCormack scheme

4.3 Application to Idealized cases

In this section, the TVD-MacCormack model was applied to some idealized cases. In the pure advection scenario, the movement of a circular patch of a conservative solute in a rotating flow field was simulated, and results by the TVD-MacCormack model, the standard MacCormack model, DIVAST model and HEMAT model were compared with the exact solution. Similar tests were repeated by adding a first-order decay of the solute into the pure advection scenario. The model was also tested for instantaneous release problem in uniform flows, which involve both advection and diffusion phenomena. Then, the model was applied to simulate the solute oscillation along a hypothetical tidal estuary.

4.3.1 Advection and decay in rotating flow

The TVD-MacCormack model was first applied to simulate the movement of a circular patch of solute in a rotating flow field. The computational domain was contained inside a square with a side length of 80 m. The water body had a constant water depth of 1 m, and the velocity field was steady and specified as

follows:

$$U = -(y-40)\times\frac{2\pi}{360} \tag{4-21a}$$

$$V = (x-40)\times\frac{2\pi}{360} \tag{4-21b}$$

Equations (4-21a,b) indicate that the water rotates counter-clockwise about the centre of the domain as a rigid body, and one rotation takes 360 s. The domain was divided into grid cells with equal spacing of 1 m. Initially, the concentration within a circle, which had a radius of 7 m and was centred at x = 20 m and y = 40 m, was unity, while the concentration elsewhere was zero, as illustrated in Figure 4-2.

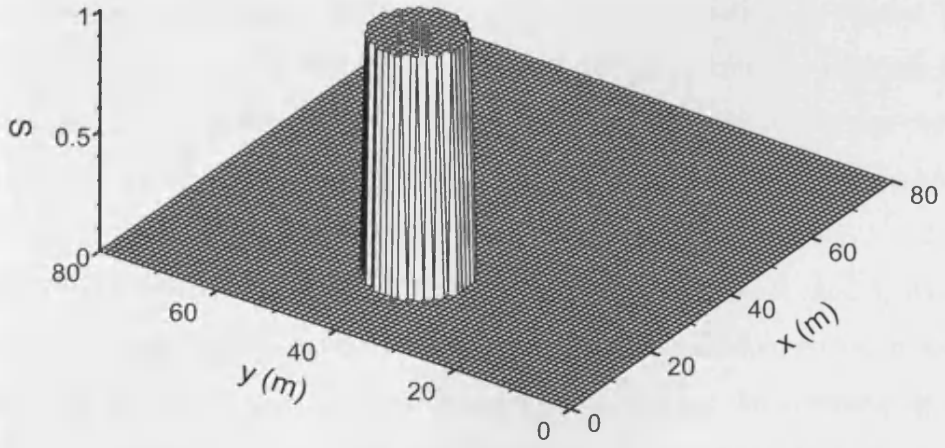

Figure 4-2 Initial concentration in a rotating flow

The diffusion terms in Equation (4-1) are not included in this example. The time step for all of the calculations was set to 1 s. The predicted concentration distributions after half a rotation and one rotation by the TVD-MacCormack scheme are shown in Figure 4-3. It can be seen that the TVD-MacCormack scheme exhibits a certain degree of excessive numerical damping, but it avoids the numerical oscillations which is seen in the standard MacCormack scheme (Liang et al., 2010). In this pure advection scenario, the circular column should theoretically return to its original position, with its original shape. However, it is extremely difficult to maintain numerically the vertical change of concentration at

the edge of the column.

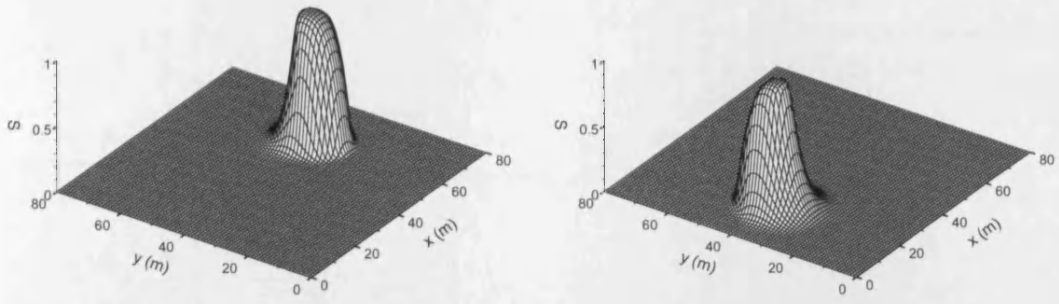

(a) $t = 180$ s (b) $t = 360$ s

Figure 4-3 TVD-MacCormack results after half and one rotation

Figure 4-4 compares the numerical predictions with the theoretical solutions along two directions after one complete rotation. It is seen that the TVD-MacCormack scheme undershoots the peak concentration by around 6% after one rotation, but is free of any negative concentrations. To compare the performance of the present model with some other models, Figure 4-4 also shows the predictions made by the DIVAST model, which solves the solute transport equation by the ULTIMATE QUICKEST scheme (Lin and Falconer 1997), and the HEMAT (Hydro-Environmental Modelling and Analysing Tool) model, which solves the solute transport equation by a second order Godunov-type scheme (Namin et al. 2004). The DIVAST model also carries out the computation on regular rectangular meshes, so it shared the same computational mesh as the MacCormack and TVD-MacCormack models. The HEMAT model uses unstructured triangular mesh, and 8010 vertices and 15698 triangles were deployed in this example so that the side length of each triangle is slightly smaller than 1 m. As can be seen in Figure 4-4, the TVD-MacCormack scheme is much more accurate than the HEMAT model, but is less accurate than the DIVAST model. The HEMAT model severely undershoots the peak concentration. The DIVAST model is least diffusive among all three shock-capturing models compared, although some slight overshooting is noticed. These observations are consistent with the previous results (Lin and Falconer 1997, Namin et al. 2004).

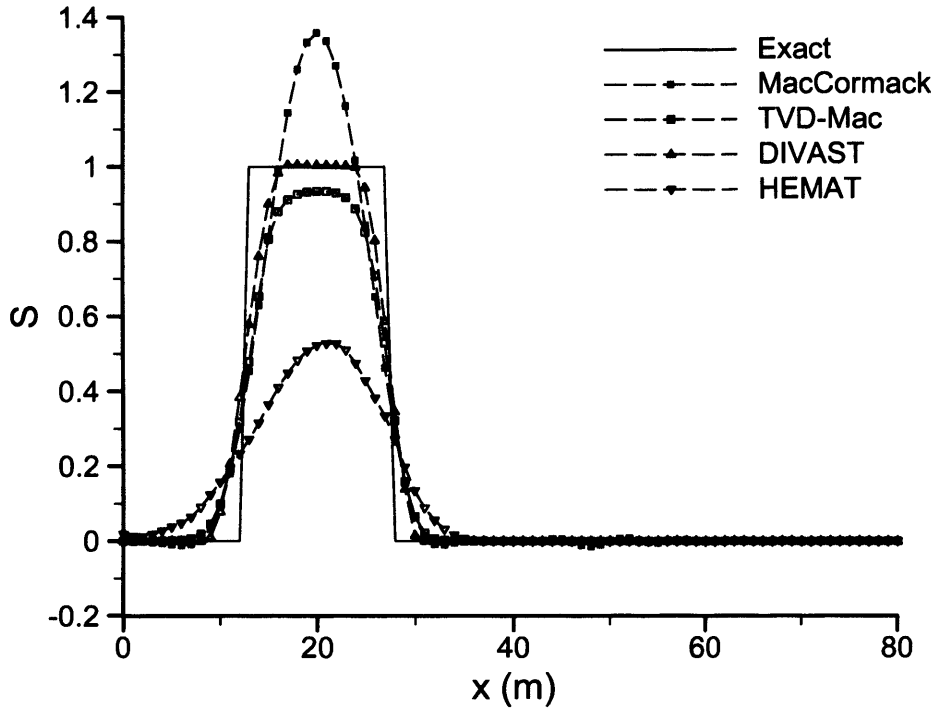

(a) Along line $y = 40$ m

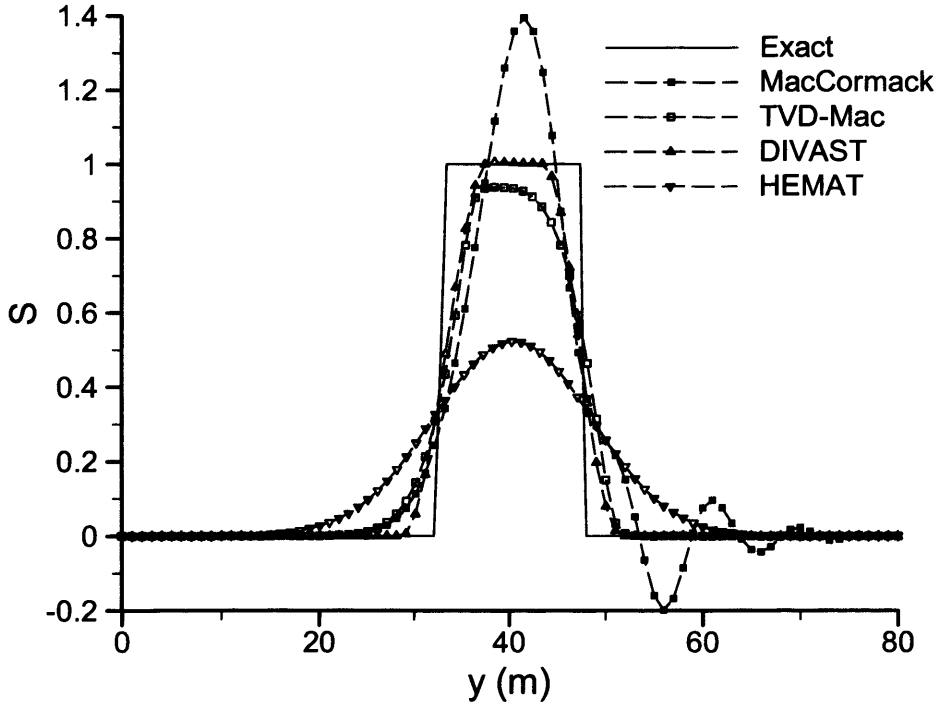

(b) Along line $x = 20$ m

Figure 4-4 Concentration variations after one rotation, $t = 360$s

In terms of the computational speed, the TVD-MacCormack model is fastest. The case study above took the TVD-MacCormack, DIVAST and HEMAT models 5 s, 12 s and 142 s respectively on a standard IBM ThinkPad laptop computer.

With the flow field and initial concentration distribution unchanged, the first-order decay of the contaminant is introduced by setting the source term in Equation (4-1) to be:

$$q_S = -0.00447 \cdot S \tag{4-22}$$

Theoretically, the concentration column should maintain its shape, but exponentially decrease its height. In equation (4-22), coefficient 0.00447 is chosen so that the maximum concentration will decrease from 1 unit at the beginning to 0.2 units at t = 360 s. The quantitative comparisons of the simulations after one complete rotation are shown in Figure 4-5. It is seen that the previous conclusions still apply to this problem comprising both advection and decay, with the percentages of over- and under-shoot remaining similar.

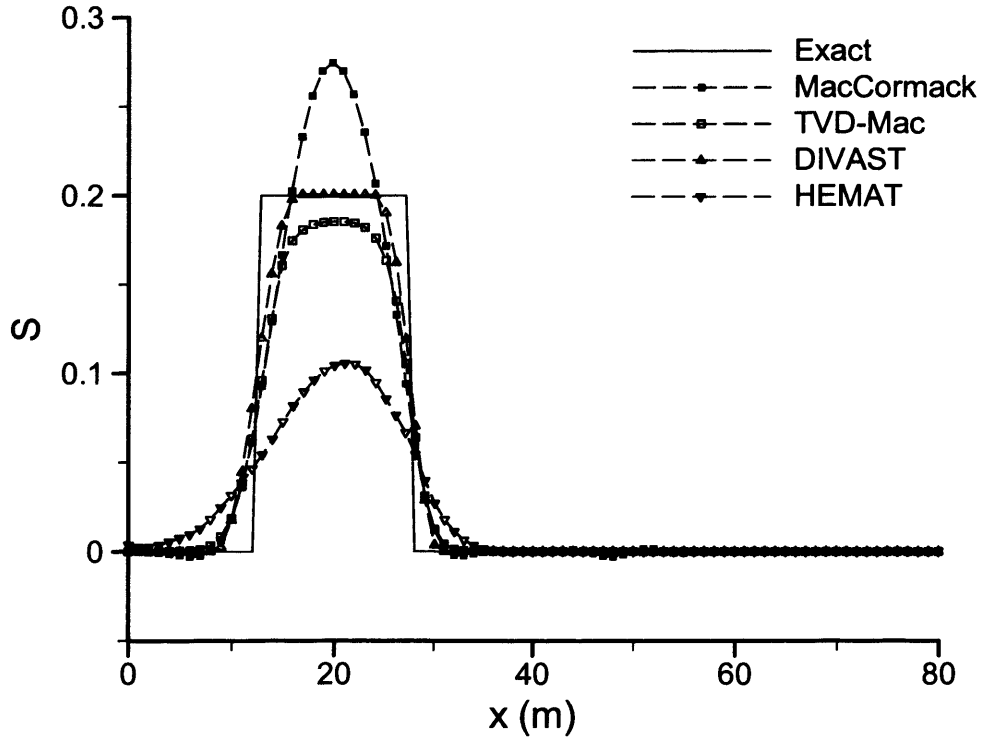

(a) Along line y = 40 m

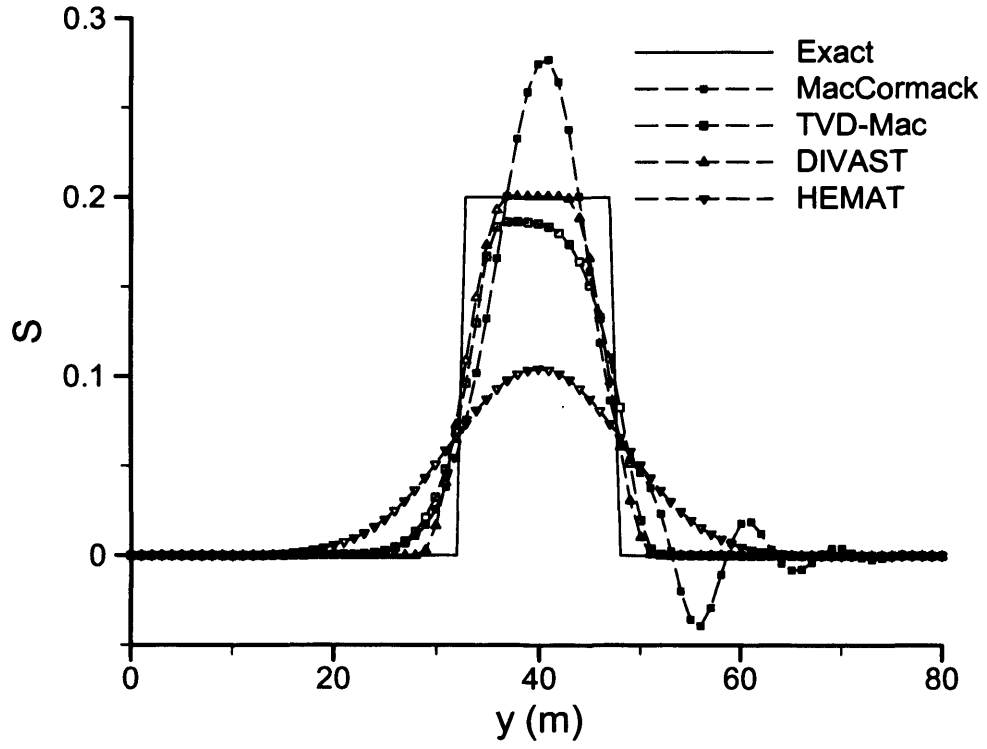

(b) Along line x = 20 m

Figure 4-5 Concentration variations after one rotation with decay

It should be noted that the contact discontinuity is more difficult to predict accurately than shockwaves in hydrodynamics. Fortunately, solutes or pollutants are also transported through diffusion and dispersion, along with advection, which helps relax the requirement on numerical schemes. The simulations can tolerate some degree of numerical diffusion, as long as its magnitude is much smaller than the physical dispersion and diffusion. Of course, numerical simulations should always be viewed with caution until the influence of numerical diffusion is confirmed to be insignificant.

4.3.2 Advection and diffusion in a uniform flow

The instantaneous release problem in uniform flows was tested in this section, which involve both advection and diffusion phenomena. The basic solution for this problem is acquired in an infinite domain. To eliminate boundary effects, the test domain extends from 0 to 800 m in both the x and y directions. When the flow is

along the x axis, *i.e.* $V = 0$ and $D_{xy} = 0$, the analytical solution can be formulated as (Chapra, 1997)

$$S(x,y,t) = \frac{M/H}{4\pi t\sqrt{D_{xx}D_{yy}}} \exp\left(-\frac{(x-x_0-Ut)^2}{4D_{xx}t} - \frac{(y-y_0)^2}{4D_{yy}t}\right) \tag{4-23}$$

where $M = 233.06$ is the total amount of solute or pollutant, the water depth is $H =$ 1 m, the velocity is set to $U =$ 1 m/s, and $(x_0, y_0) = (0, 400$ m) is the location at which the sudden influx of mass takes place at $t = 0$. Across the domain, the Chezy roughness value is fixed at 40 $m^{1/2}/s$, and the longitudinal dispersion and lateral diffusion constants are specified at 13.0 and 1.2 respectively. For all computations in this section, the grid size is 1 m and time step 0.5 s.

To verify whether the cross-diffusion terms are treated correctly in the model, this phenomenon was simulated three times, with the flow aligned in different directions: along the x direction, 45° direction, and 135° direction. The concentration contours are predicted to evolve as shown in Figure 4-6. As the magnitude of longitudinal dispersion is more than ten times larger than that of lateral diffusion, the cloud experienced rapid elongation in the flow direction. Visual inspection of the elliptical patches of solute distribution reviews a fairly good match between the three sets of results, with the major axis of the ellipses always in line with the flow direction.

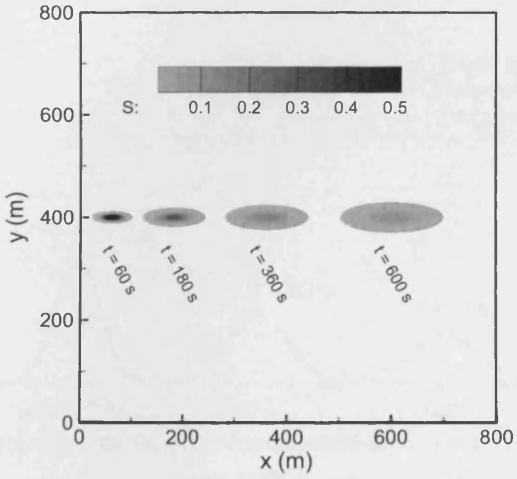

(a) Flow in x direction

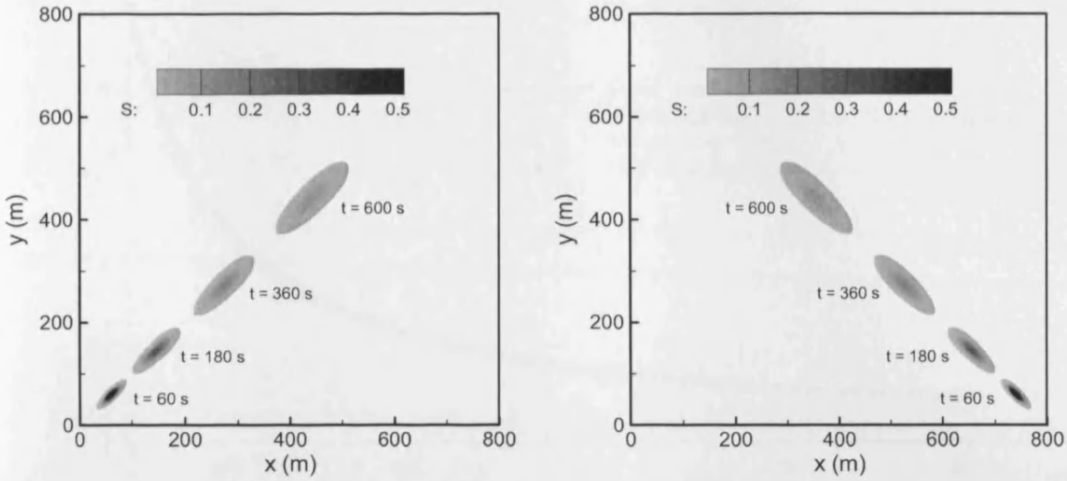

(b) Flow in the 45° direction (c) Flow in the 135° direction

Figure 4-6 Evolution of the pollutant cloud with time

Quantitative comparisons between the predicted and analytical results are shown in Figures 4-7 and 4-8. Figure 4-7 plots the concentration profiles in the streamwise direction at several instants. Figure 4-8 illustrates the decrease in the peak concentration with time. When the flow is aligned in the x direction, the simulation results are in perfect agreement with the analytical solution. When the flow is oriented in the diagonal direction, the peak concentration is slightly underpredicted, especially at an early stage of transport.

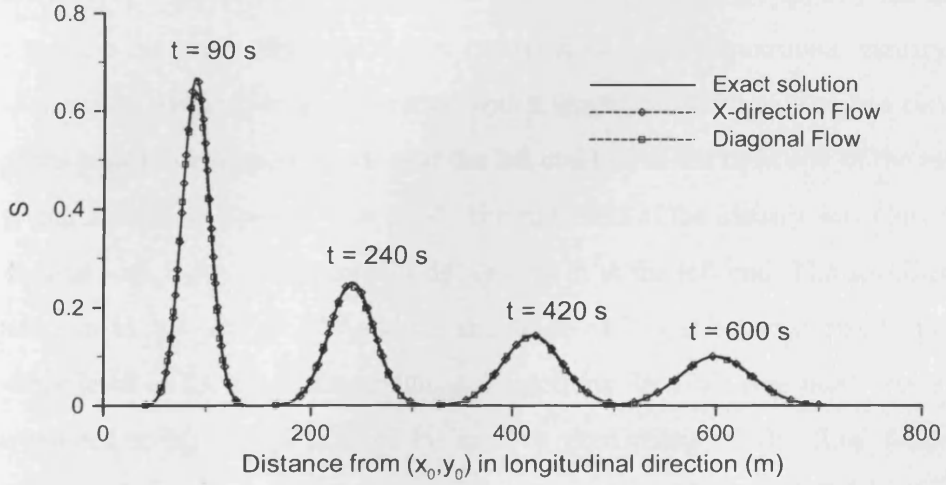

Figure 4-7 Longitudinal concentration profile development

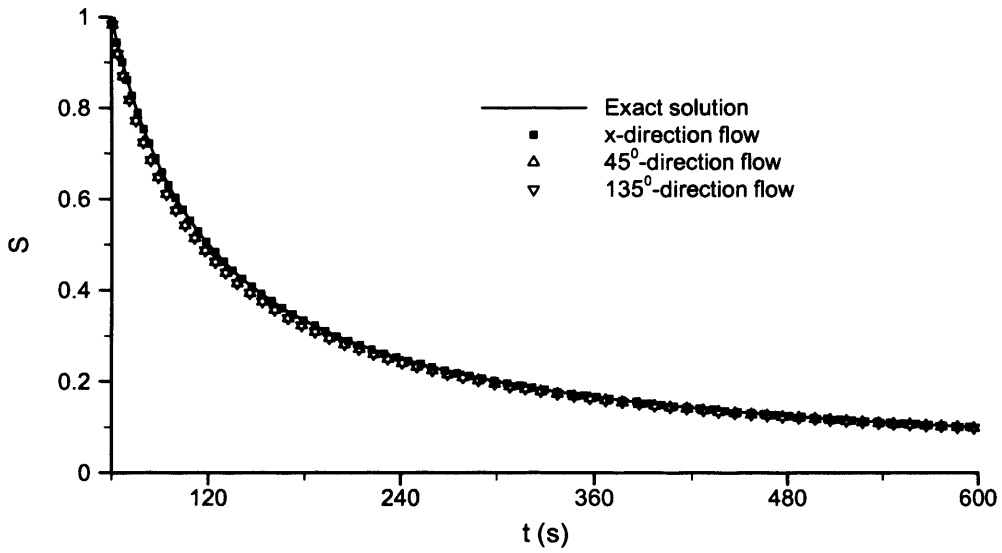

Figure 4-8 Variations of the peak concentration with time

Overall, the results for both computations are satisfactory. The predictions for the x-direction flow case are more accurate, the reason for the less satisfactory predictions in the diagonal-flow case is that the grid resolution in the cross-flow direction is poorer than that in the x-direction flow case.

4.3.3 Solute oscillation along a hypothetical tidal estuary

In order to examine the ability of the TVD-MacCormack model in handling the moving boundaries, and further compare with the DIVAST model, this section considers the water flow and solute transport in a one-dimensional estuary. The estuary was aligned in the x direction with a length of 13800 m. The bed elevation of the estuary changed from -5 m at the left end to 0 at the right end of the estuary, giving a uniform slope of 1 in 2760. The right end of the estuary was closed by a vertical wall, while a sinusoidal tide was fed in at the left end. The specified tide had a mean water level of 0 and the amplitude of 2 m; it began to rise from mean water level at the beginning of the computations. In total, five tidal cycles were simulated using a grid size of 80 m. The predictions of the flow field were achieved by solving the shallow water equations with the TVD-MacCormack scheme, details of which can be found in Liang et al. (2007). The time step for the

flow simulation was 8 s. Figures 4-9(a) and 4-9(b) show the water surface profile variations for every 20 min during an ebb tide (39 hours – 45 hours) and a flood tide (45 hours – 51 hours) respectively. Corresponding to the ebbing and flooding tide, the right part of the computational domain underwent repetitive drying and wetting. These results are in agreement with those presented by Falconer and Chen (1991), and Balzano (1998), where the shallow water equations were solved using the ADI scheme, as in the DIVAST model.

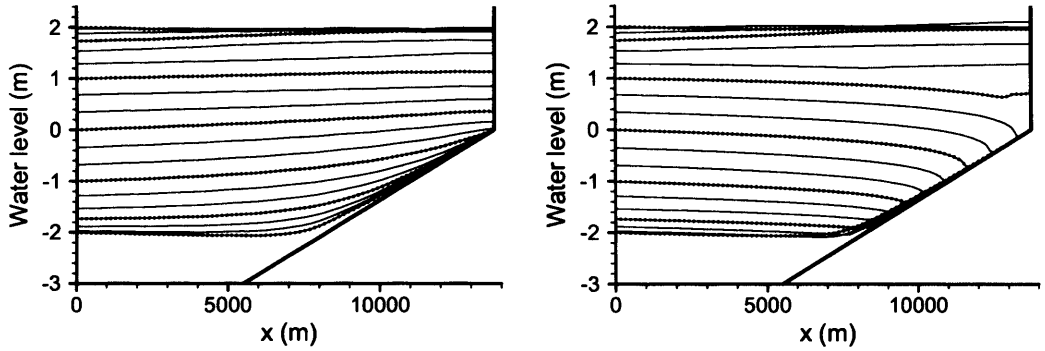

(a) Ebb tide (b) Flood tide

Figure 4-9 Water surface profiles along a hypothetical tidal estuary

At the start of the simulation, the concentration all over the domain was set to zero except for one grid cell, centred at x = 10 km, where the concentration was equated to 100 units. The dispersion constant was taken to be 13.0 and the time step for the solute transport computation was 80 s. Under the action of the tidal flows, this instantaneously released solute travels to the closed wall with the rising water and to the open boundary with the receding water. At the same time, the solute is dispersed to a larger region. A series of concentration distributions at high and low water are plotted in Figure 4-10, which clearly illustrates the scattering of the solute with time. Owing to the sharp concentration gradient, the numerical diffusion can be quite large at the beginning. As demonstrated above, the DIVAST model is less diffusive, so it predicts a narrower distribution with a higher peak concentration. However the difference between the DIVAST and TVD-MacCormack models gets smaller and smaller as time progresses and it almost diminishes in the fifth tide.

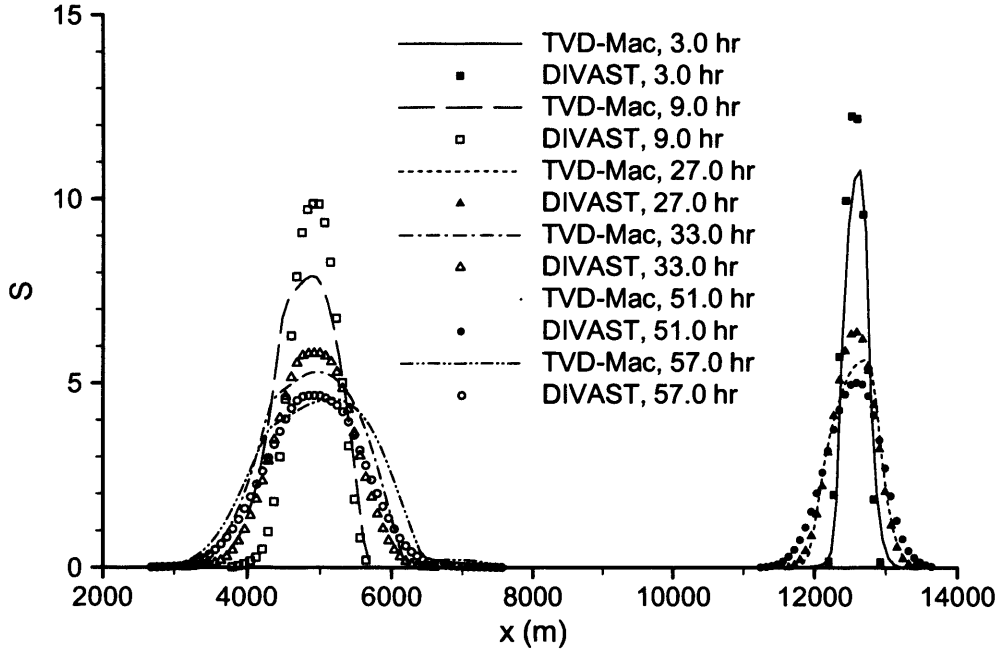

Figure 4-10 Development of the concentration distribution along the hypothetical estuary

Figure 4-10 shows that the solute cloud was still of some distance away from the open boundary on the left, even towards the end of the simulation. As no solute had escaped, the total amount of the solute within the domain should maintain the initially released value throughout the simulation. As shown in Figure 4-11, the TVD-MacCormack model conserved the mass perfectly. The total amount of the solute simulated by the DIVAST model was higher than the exact value and exhibited the oscillation with a same period as the tide, although the deviation was within 1%. The TVD-MacCormack model solves Equation (4-1) for the solute concentration, while the DIVAST and some other models (e.g. Holly and Usseglio-Polatera 1982, Lin and Falconer 1995) adopt the following non-conservative equation for the solute concentration *S*.

$$\frac{\partial S}{\partial t}+\frac{\partial US}{\partial x}+\frac{\partial VS}{\partial y}=\frac{1}{H}\frac{\partial}{\partial x}\left(HD_{xx}\frac{\partial S}{\partial x}+HD_{xy}\frac{\partial S}{\partial y}\right)+\frac{1}{H}\frac{\partial}{\partial y}\left(HD_{yx}\frac{\partial S}{\partial x}+HD_{yy}\frac{\partial S}{\partial y}\right)+\frac{q_s}{H} \qquad (4\text{-}24)$$

which is converted from Equation (4-1) by incorporating the water mass conservation relationship

$$\frac{\partial H}{\partial t}+\frac{\partial HU}{\partial x}+\frac{\partial HV}{\partial y}=0 \tag{4-25}$$

However, the discretised form of Equation (4-25) may not always hold exactly true, especially when the solute computation and flow computation deploy different discretisation schemes, as in the DIVAST model, and use of different time steps. In the current study, the original conservative equation for *HS* is solved directly. In this way, the mass of the solute is strictly conserved, regardless of whether *H*, *U* and *V* satisfy the conservation law or not. Hence it is not surprising that the present model conserves mass better than the DIVAST model.

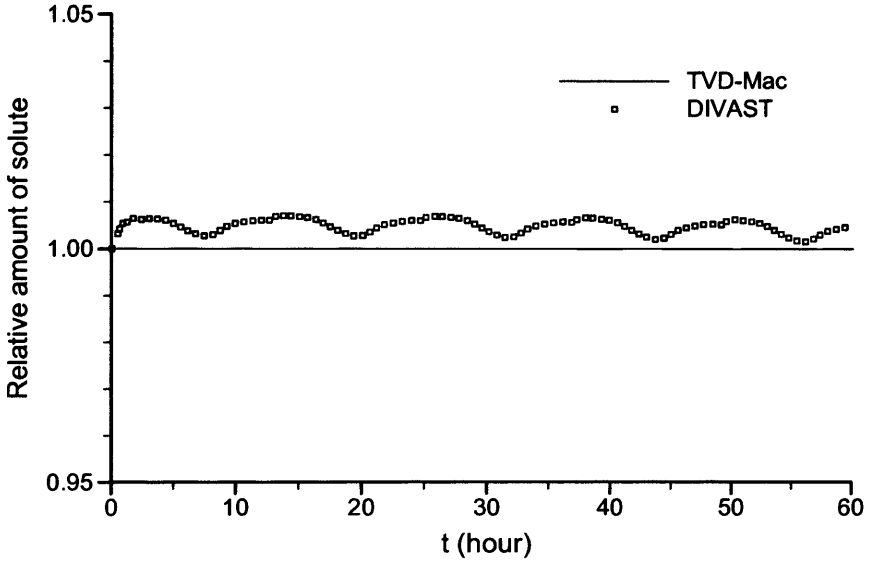

Figure 4-11 Variation of the normalised total pollutant amount

4.5 Summary

A TVD-MacCormack scheme has been discussed in solving the solute transport problems in shallow water flows. The model has been tested against idealized cases, with encouraging results having been obtained, which were not plagued by negative concentrations and numerical oscillations and compared favourably with analytical solutions. Small amounts of numerical dissipation are observed where the concentration changes abruptly, especially under the

circumstances of low resolution and disalignment between the flow direction and grid orientation. Through a test on the solute oscillation along a one-dimensional hypothetical estuary, the model was demonstrated to have the advantage of accurately conserving mass as the solute moved back and forth with the tide.

Chapter5

Interaction systems within the water quality model

5.1 Introduction

The water quality process can be described based on the solute transport model, which includes terms for dispersive and/or advective transport depending on the hydrodynamic characteristics of the water body, and the terms of the biological, chemical and physical reactions among constituents. The advection and dispersion terms have been discussed in previous chapter. Therefore, this chapter will focus on the biological, chemical and physical reactions among water quality constituents and how they are represented in computer model.

One of the most important considerations in determining a healthy state of an aquatic system is its ability to maintain an adequate dissolved oxygen (DO) concentration. Dissolved oxygen concentrations in aquatic systems are controlled by atmospheric reaeration, photosynthesis, plant and animal respiration, benthal demand, biochemical oxygen demand, nitrification, salinity, and temperature, among other factors.

DO was originally modeled in the Ohio River (US) by Streeter and Phelps (1925). Since then a number of modifications and extensions of the model have been made relating to the number of sinks and sources of DO being considered, and how processes involving the nutrients and phytoplankton cycles are being modeled, as illustrated in QUAL2E. This model includes the major interactions of the nutrient cycles, algal production, benthic oxygen demand, carbonaceous oxygen uptake, atmospheric reaeration and their effect on the behavior of

dissolved oxygen, as shown in Figure 5-1. The arrows on the figure indicate the direction of normal system progression in a moderately polluted environment; the directions may be reversed in some circumstances for some constituents.

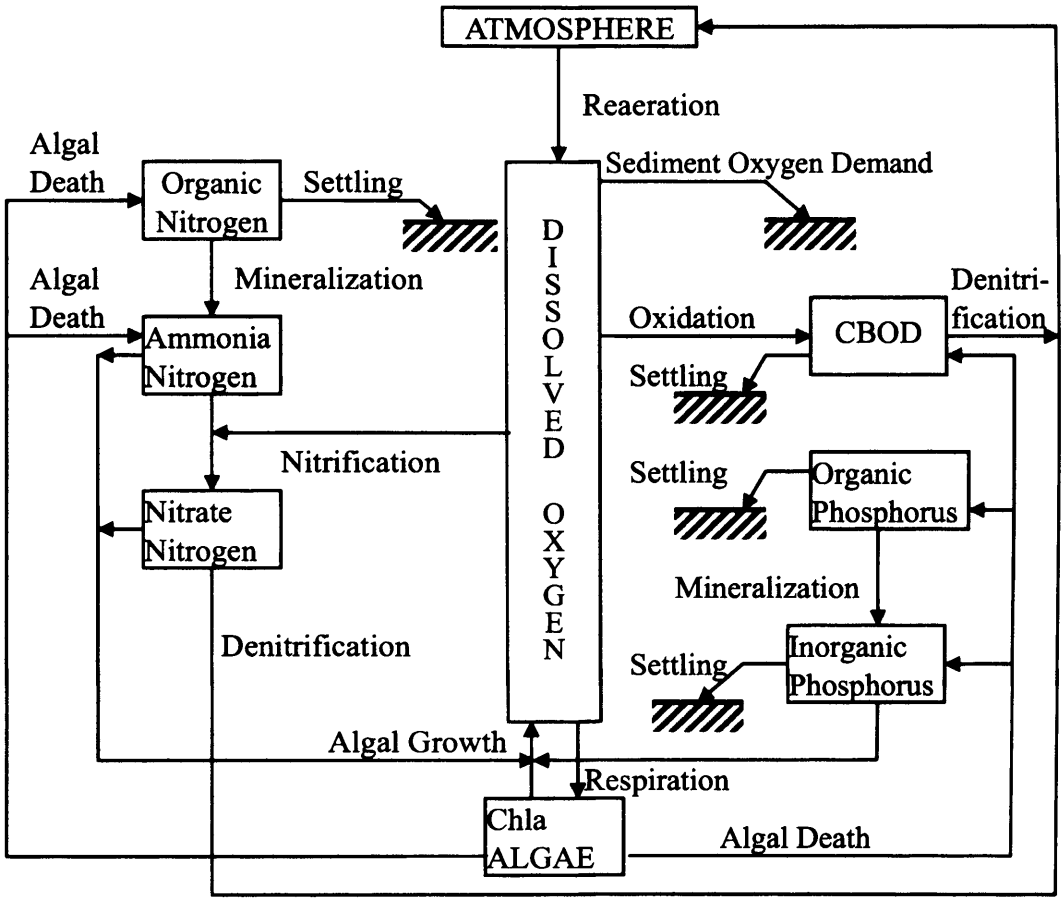

Figure 5-1 Conceptual model of constituent interactions

This model simulates the transport and transformation reactions of up to ten state variables. They can be considered as four interacting systems: phytoplankton kinetics, the phosphorus cycle, the nitrogen cycle, and the dissolved oxygen balance. The general solute and mass transport equation is solved for each state variable. To this general equation, the water quality subroutines add specific transformation processes to customize the general mass balance for these state variables in the water column. The mathematical relationships that describe the individual reactions and interacting systems are presented in the following sections.

5.2 Phytoplankton kinetics

Chlorophyll a concentration is considered to be directly proportional to the concentration of phytoplanktonic algal biomass. For the purposes of this model, algal biomass is converted to chlorophyll a by the simple relationship:

$$Chla = \alpha_0 A \tag{5-1}$$

where *Chla* and *A* are concentrations of the chlorophyll a (μg/L) and algal biomass (mg/L), and α_0 is a conversion factor between chlorophyll a and algal biomass.

The differential equation that governs the growth and production of algae (chlorophyll a) is formulated according to the following relationship.

$$\frac{dA}{dt} = \mu A - D_{loss} A - \frac{\sigma_1}{d} A \tag{5-2}$$

where *t* is the time (day) and *d* is the average depth (m). μ, D_{loss} and σ_1 represent the algal growth rate (day^{-1}), death rate (day^{-1}), and settling rate (m/day), respectively, which are all temperature dependent.

5.2.1 Algal growth rate

The local specific growth rate of algae, μ, is known to be coupled to the availability of required nutrients (nitrogen and phosphorus) and light. A variety of mathematical expressions for expressing multiple nutrient-light limitations on algal growth rate have been reported (De Groot, 1983; Scavia and Park, 1976; Swartzman and Bentley, 1979). The limiting nutrient formulation represents the local algal growth rate as limited by light and either nitrogen or phosphorus, but not both. The formulation mimics Liebig's law of the minimum:

$$\mu = \mu_{\max} \theta_{\mu \max} (FL) Min(FN, FP) \tag{5-3}$$

In which μ_{max} is the maximum algal growth rate (day^{-1}) which is dependent on temperature. *FL*, *FN* and *FP* are the limitations due to light intensity or nitrogen and phosphorus availability, respectively.

5.2.1.1 Temperature dependence of rate coefficient

The temperature values are used to correct the rate coefficients in the source/sink terms for the water quality variables. These coefficients are input at 20°C and are then corrected to temperature using a Streeter-Phelps (Streeter and Phelps, 1925) type formulation:

$$X_T = X_{20}\theta^{(T-20^\circ)} \tag{5-4}$$

where X_T and X_{20} are the values of the coefficient at the local temperature (T) and the standard temperature (20°C), respectively, and θ is an empirical constant for each reaction coefficient. For example, the temperature corrected maximum algal growth rate is:

$$u_{\max,T} = u_{\max,20}\theta^{(T-20^\circ)} \tag{5-5}$$

The temperature dependent coefficient mentioned hereafter is described in the same way as in equation (5-5).

5.2.1.2 Light limitation factor

In the natural environment, the light intensity to which the phytoplankton is exposed will be attenuated due to the effects of water, phytoplankton algae, and other suspended and dissolved substances. At the surface and near-surface of the air-water interface, photo inhibition can occur at high light intensities, whereas at depths below the euphotic zone light is not available for photosynthesis due to natural and algal-related turbidity.

QUAL2E provides three options for computing light attenuation effects on the algal growth rate, namely Monod half saturation method, Smith's function (Smith, 1936) or Steele's equation (Steele, 1962). WASP6 includes equations developed by Di Toro et al. (1971) and by Smith (1980), extending upon a light curve analysis formulated by Steele (1962), which account for both, the effects of supersaturating light intensities and light attenuation through the water column.

This study chose the Monod half saturation for simulating light limitation factor *FL*, which is obtained by depth integrating and time averaging as:

$$FL = \frac{AFACT * f}{\lambda d} \ln[\frac{K_L + I}{K_L + Ie^{-\lambda d}}] \quad (5\text{-}6)$$

where *FL* is the depth-averaged algal growth attenuation factor for light, K_L is the half saturation coefficient for light (Btu/ft^2-hr), i.e., light intensity at which growth rate is 50% of the maximum growth rate. *I* is the daylight average light intensity (Btu/ft^2-hr). *f* is the fraction of daylight hours, *AFACT* is a light averaging factor, used to provide similarity between calculations using a single average value of solar radiation and computations using the average of hourly values of *FL*, and λ is the light extinction coefficient (ft^{-1}), which is coupled to the algal density using the nonlinear equation:

$$\lambda = \lambda_0 + \lambda_1 \alpha_0 A + \lambda_2 (\alpha_0 A)^{2/3} \quad (5\text{-}7)$$

where λ_0, λ_1, λ_2 represent non-algal portion of the light extinction coefficient (ft^{-1}), linear algal self shading coefficient (ft^{-1}(ug Chl a/l)$^{-1}$) and nonlinear algal self shading coefficient (ft^{-1}(ug Chl a /l)$^{-2/3}$).

5.2.1.3 Nutrient limitation factor

The algal growth limitation factors for nitrogen (*FN*) and phosphorus (*FP*) are defined by the Monod expressions:

$$FN = \frac{N_2 + N_3}{N_2 + N_3 + K_N} \quad (5\text{-}8)$$

$$FP = \frac{P_2}{P_2 + K_P} \quad (5\text{-}9)$$

where N_2, N_3 and P_2 are the concentrations of ammonia nitrogen, nitrate nitrogen and inorganic phosphorus (mg/l), respectively, and K_N and K_P are the Michaelis-Menton half-saturation constants for nitrogen and phosphorus (mg/l), respectively.

5.2.2 Algal death rate

Algal biomass losses mainly include endogenous respiration, mortality and grazing by zooplankton. The death rate of algal biomass is given as follows:

$$D_{loss} = \rho\theta_{\rho} + D_m + D_g \tag{5-10}$$

where ρ, D_m and D_g are the rates for endogenous respiration, mortality and grazing (day^{-1}). The endogenous respiration rate is temperature dependent (Riley et al., 1949) and is determined as in the format of equation (5-4). The typical values for the rate coefficients and temperature coefficients related to phytoplankton cycle are listed below.

Table 5-1 Reference values for algae reaction coefficients

Notation	Description	Value	Unit
α_0	Ratio of chlorophyll-a (Chl a) to algal biomass (A)	10-100 [a] 20-50	μg Chl a/mg A μg Chl a/mg A
K_L	Half saturation constant for light	0.02-0.1 [a]	Btu/ft^2-min
λ	Extinction coefficient	0.1-5 Eq.(5-7) [a]	m^{-1}
λ_0	Non-algal light extinction coefficient	Variable	ft^{-1}
λ_1	Linear algal self-shading coefficient	0.002-0.02 [a]	ft^{-1}(μg Chl a /l)$^{-1}$
λ_2	Nonlinear algal self-shading coefficient	0.0165 [a]	ft^{-1}(μgChl a /l)$^{-2/3}$
f	Fraction of day that is daylight	0.3-0.7	
I	Average daily surface solar radiation	200-750	Langley
μ_{max}	Maximum growth rate at 20 °C	2.0 1.0-3.0 [a]	day^{-1} day^{-1}
$\theta_{\mu max}$	Temperature coefficient for	1.068	

	maximum growth rate	1.047 [a]	
K_N	Half saturation constant for nitrogen (N)	25.0 10-300 [a] 10-20 [b] 50-200 [c]	μg N/L μg N/L μg N/L μg NO_3/L
K_P	Half saturation constant for phosphorus (P)	1.0 1-50 [a] 1-5 [b] 20-70 [c]	μg P/L μg P/L μg P/L μg P/L
ρ_{20}	Endogenous respiration at 20 °C	0.125 0.05-0.5 [a]	day^{-1} day^{-1}
θ_ρ	Temperature coefficient for ρ	1.045 1.047 [a]	
σ_1	Algal settling velocity	0.1 0.15-1.8 [a]	m/day m/day
D_m	Algal death rate	0.02 0.2-8 [c]	day^{-1} day^{-1}
D_g	Algal grazing rate	0	L/mgC-day

Note: The superscript "a" represents sources from QUAL2E, superscript "b" represents source Thomann and Mueller (1987), superscript "c" represents source Bowie et al. (1985), and contents without superscript are from WASP6.

5.3 Nitrogen cycle

Ammonia and nitrate are consumed by algae for growth. For physiological reasons, ammonia is the preferred form of inorganic nitrogen for algae. Nitrogen is returned from the algal biomass pool to organic nitrogen pool as a result of algal death and endogenous respiration and zooplankton grazing and mortality. Organic nitrogen is converted to ammonia nitrogen at a temperature dependent mineralization rate, and ammonia nitrogen is then converted to nitrate at a

temperature and oxygen dependent nitrification rate. In the absence of oxygen, nitrate can be converted to nitrogen gas through denitrification at a temperature dependent rate. The governing equations for nitrogen cycle can be expressed as:

(1) Organic nitrogen:

$$\frac{dN_1}{dt} = \alpha_1 f_{on} D_{loss} A - \beta_1 \theta_1 \left(\frac{A}{K_{mpc} + A}\right) N_1 - \sigma_2 (1 - f_{D2}) N_1 \tag{5-11}$$

Death Mineralization Settling

(2) Ammonia nitrogen:

$$\frac{dN_2}{dt} = \alpha_1 (1 - f_{on}) D_{loss} A + \beta_1 \theta_1 \left(\frac{A}{K_{mpc} + A}\right) N_1 - \beta_2 \theta_2 \left(\frac{O}{K_{NIT} + O}\right) N_2 - F \alpha_1 \mu A \tag{5-12}$$

Death Mineralization Nitrification Growth

(3) Nitrate nitrogen:

$$\frac{dN_3}{dt} = \beta_2 \theta_2 \left(\frac{O}{K_{NIT} + O}\right) N_2 - (1 - F) \alpha_1 \mu A - \beta_3 \theta_3 \left(\frac{O}{K_{NO3} + O}\right) N_3 \tag{5-13}$$

Nitrification Growth Denitrification

where N_1, N_2, N_3 are the concentrations for organic nitrogen, ammonia nitrogen and nitrate nitrogen (mg/l), respectively. A and O represent the concentrations of algal biomass and dissolved oxygen (mg/l). F is the fraction of algal nitrogen taken from ammonia pool, which is expressed as:

$$F = P_N N_2 / (P_N N_2 + (1 - P_N) N_3) \tag{5-14}$$

where P_N is the preference factor for ammonia nitrogen. Other coefficients are explained in Table 5-2, with their reference values being listed as well.

Table 5-2 Reference values for nitrogen reaction coefficients

Notation	Description	Value	Unit
α_1	Fraction of algal biomass (A) that is nitrogen (N)	0.25 0.07-0.09 [a] 0.08-0.09 [c]	mgN/mgA mgN/mgA $mgNO_3$/mgA
β_1	Organic nitrogen mineralization rate at 20 °C	0.075 0.02-0.4 [a]	day^{-1} day^{-1}

θ_1	Temperature coefficient for β_1	1.08	
β_2	Nitrification rate at 20 °C	0.09-0.13	day^{-1}
θ_2	Temperature coefficient for β_2	1.08 1.047 [a]	
K_{mpc}	Half saturation constant for algae (A) limitation of nitrogen recycle	1.0	mg A/L
K_{NIT}	Half saturation constant for oxygen (O_2) limitation of nitrification	2.0	mg O_2/L
β_3	Denitrification rate at 20 °C	0.09	day^{-1}
θ_3	Temperature coefficient β_3	1.045	
K_{NO3}	Michaelis constant for denitrification	0.1	mg O_2/L
f_{ON}	Fraction of dead and respired algae recycled to the organic nitrogen pool	0.5 0.5 [a]	
$(1-f_{ON})$	Fraction of dead and respired algae recycled to the ammonia nitrogen pool	0.5 0.5 [a]	
P_N	Preference for ammonia uptake term	0-1.0 0-1.0 [a]	
f_{D2}	Fraction of dissolved organic nitrogen	1.0	
σ_2	Organic nitrogen settling rate	0.001-0.1 [a]	day^{-1}

Note: The superscript "a" represents sources from QUAL2E, superscript "c" represents source Bowie et al. (1985), and contents without superscript are from WASP6.

5.3.1 Organic nitrogen mineralization

Nonliving organic nitrogen must undergo mineralization or bacterial decomposition into ammonia nitrogen before utilization by phytoplankton. In their work on Lake Huron and Saginaw Bay, Di Toro and Matystik (1980) proposed a nutrient recycle formulation that was a function of the localized phytoplankton population. This proposal was based on both an analysis of available field data and

the work of others (Hendry, 1977; Lowe, 1976; Henrici, 1938; Menon, 1972; and Rao, 1976) that indicated bacterial biomass increases as phytoplankton biomass increases. QUAL2E doesn't consider this factor, while WASP6 uses a saturating recycle mechanism, a compromise between conventional first-order kinetics and a second order recycle mechanism wherein the recycle rate is directly proportional to the phytoplankton biomass present.

Saturating recycle permits second order dependency at low phytoplankton concentrations, and permits first order recycle when the phytoplankton concentration greatly exceed the half-saturation constant K_{mpc}. Basically, this mechanism slows the recycle rate if the phytoplankton population is small, but does not permit the rate to increase continuously as phytoplankton increase. The assumption is that at higher population levels, recycle kinetics proceed at the maximum first order rate.

5.3.2 Nitrification

Ammonia nitrogen, in the presence of nitrifying bacteria (Nitrosomonas and Nitrobacter) and oxygen, is converted to nitrate nitrogen (nitrification). The process of nitrification in natural waters is carried out by aerobic autotrophs. It is a two-step process with Nitrosomonas bacteria responsible for the conversion of ammonia to nitrite and Nitrobacter responsible for the conversion of nitrite to nitrate. This process is complex, depending on dissolved oxygen, pH, and flow conditions, which in turn leads to spatially and temporally varying rates of nitrification. Properly accounting for this complex phenomenon in the modeling framework would be difficult and would require a database that is usually unavailable. QUAL2E uses a temperature dependent, first order rate for nitrification. In WASP6, the kinetic expression for nitrification contains three terms -- a first order rate constant (β_2), a temperature correction term (θ_2), and a low dissolved oxygen (DO) correction term (K_{NIT}). The first two terms are standard. The third term represents the decline of the nitrification rate as DO levels

approach 0. K_{NIT} can be specified as the half-saturation constant, which represents the DO level at which the nitrification rate is reduced by half.

5.3.3 Denitrification

Denitrification refers to the reduction of nitrate nitrogen (NO_3) or nitrite nitrogen (NO_2) to nitrogen gas (N_2) and other gaseous products such as N_2O and NO. This process is carried out by a large number of heterotrophic, facultative anaerobes. Under normal aerobic conditions found in the water column, these organisms use oxygen to oxidize organic material. Under the anaerobic conditions found in the sediment bed or during extremely low oxygen conditions in the water column, however, these organisms are able to use NO_3 as the electron acceptor.
The process of denitrification is included in the modeling framework of WASP6 simply as a sink of nitrate. The kinetic expression for denitrification contains three terms -- a first order rate constant (β_3), a temperature correction term (θ_3), and a DO correction term (K_{NO3}). The first two terms are standard. The third term represents the decline of the denitrification rate as DO levels rise above 0. K_{NO3} can be specified as the half-saturation constant, which represents the DO level at which the denitrification rate is reduced by half.

5.4 Phosphorus cycle

Phosphorus kinetics are similar to the nitrogen kinetics except there are no processes analogous to nitrification and denitrification. Inorganic phosphorus, mainly existing as orthophosphate (PO_4^{3-}) in water, is utilized by algae for growth and is incorporated into algal biomass. Phosphorus is returned to the water column from dead or decaying algal biomass in the bed. The various forms of organic phosphorus undergo settling and mineralization, and are converted to inorganic phosphorus at temperature dependent rates. The governing equations for the phosphorus cycle can be expressed as:
(1) Organic phosphorus:

$$\frac{dP_1}{dt} = \alpha_2 f_{op} D_{loss} A - \beta_4 \theta_4 (\frac{A}{K_{mpc} + A}) P_1 - \sigma_3 (1 - f_{D3}) P_1 \quad (5\text{-}15)$$

Death Mineralization Settling

(2) Inorganic phosphorus:

$$\frac{dP_2}{dt} = \alpha_2 (1 - f_{op}) D_{loss} A + \beta_4 \theta_4 (\frac{A}{K_{mpc} + A}) P_1 - \sigma_4 (1 - f_{D4}) P_2 - \alpha_2 \mu A \quad (5\text{-}16)$$

Death Mineralization Settling Growth

where P_1 and P_2 are the concentrations for organic and inorganic phosphorus respectively (mg/l). Other coefficients are explained in Table 5-3, with their reference values being listed as well.

Table 5-3 Reference values for phosphorus reaction coefficients

Notation	Description	Value	Unit
α_2	Fraction of algal biomass (A) that is phosphorus (P)	0.025 0.01-0.02 [a] 0.012-0.015 [c]	mg P/mg A mg P/mg A mg P/mg A
β_4	Dissolved organic phosphorus mineralization at 20 °C	0.22 0.01-0.7 [a]	day^{-1} day^{-1}
θ_4	Temperature coefficient for β_4	1.08	
f_{op}	Fraction of dead and respired algae recycled to the organic phosphorus pool	0.5	
$(1-f_{op})$	Fraction of dead and respired algae recycled to the phosphate phosphorus pool	0.5	
f_{D3}	Fraction of dissolved organic phosphorus in the water column	0.85	
f_{D4}	Fraction of dissolved inorganic phosphorus in the water column	0.70	
σ_3	Organic phosphorus settling rate	0.001-0.1[a]	day^{-1}

σ_4	Inorganic phosphorus settling rate	0.001-0.1[a]	day^{-1}

Note: The superscript "a" represents sources from QUAL2E, superscript "c" represents source Bowie et al. (1985), and contents without superscript are from WASP6.

5.4.1 Organic phosphorus mineralization

Nonliving organic phosphorus must undergo mineralization or bacterial decomposition into inorganic phosphorus before utilization by phytoplankton. The first order, temperature corrected rate constant is modified by a saturated recycle term, equivalent to the one explained in the organic nitrogen mineralization section. This mechanism slows the mineralization rate if the phytoplankton population is small, but does not permit the rate to increase continuously as phytoplankton concentrations increase.

5.4.2 Settling

Particulate organic and inorganic phosphorus settle according to the specified velocities and particulate fractions. The settling velocities can either be input with the initial conditions, or calculated by sediment falling equations, based on the solid types of the particulate matter. The particulate fractions can also be obtained from two methods, namely, input with the initial conditions, and calculations which will be detailed in Chapter 6.

5.5 Dissolved oxygen balance

Dissolved oxygen (DO) is one of the most important variables in water quality analysis. The sources of DO included in the model are reaeration from the atmosphere, photosynthetic oxygen production from aquatic plants occurring during day light, and DO inputs. The sinks of DO include phytoplankton respiration, oxidation of BOD, nitrification and sediment oxygen demand. The

differential equation used in the model to describe the rate of change of oxygen is:

$$\frac{dO}{dt} = K_2(O^* - O) + \alpha_3 \mu A - \alpha_4 \rho \theta_\rho A - K_1\left(\frac{O}{K_{BOD}+O}\right)\theta_{K1} L - K_4 \theta_{K4}/d - \alpha_5 \beta_2 \theta_2 \left(\frac{O}{K_{NIT}+O}\right) N_2 \quad (5\text{-}17)$$

Rearation Photosynthesis Respiration Oxidation Sediment demand Nitrification

where O is the concentration of dissolved oxygen (mg/l), α_3, α_4, and α_5 are the rates of oxygen production from algal photosynthesis, algae respiration, and ammonia nitrogen oxidation (mg/mg), L is the concentration of ultimate carbonaceous BOD (mg/l), K_1, K_2 and K_4 are the temperature dependent rate of carbonaceous BOD deoxygenation, oxygen reaeration and sediment oxygen demand (day^{-1}). O^* is the dissolved oxygen saturation concentration (mg/l), which is dependent on the temperature, atmospheric pressure and salinity. At standard atmospheric pressure (1 atm), the predictive equation used in this model is (APHA, 1992):

$$\ln O^* = -139.34410 + \frac{1.575701\times10^5}{T_a} - \frac{6.642308\times10^7}{T_a^2} + \frac{1.243800\times10^{10}}{T_a^3} - \frac{8.621949\times10^{11}}{T_a^4} - C_{SAL}\left(1.7674\times10^{-2} - \frac{1.0754\times10}{T_a} + \frac{2.1407\times10^3}{T_a^2}\right) \quad (5\text{-}18)$$

where C_{SAL} is the salinity level (ppt), and T_a is the absolute temperature which is given as:

$$T_a = T + 273.15 \quad (5\text{-}19)$$

In which T is the temperature (°C).

Other coefficients are explained in Table 5-4, with their reference values being listed as well.

Table 5-4 Reference values for DO and CBOD reaction coefficients

Notation	Description	Value	Units

α_3	Oxygen (O_2) production per unit of algae (A) growth	2.67-5.67 1.4-1.8 [a]	mg O_2/mg A mg O_2/mg A
α_4	Oxygen (O_2) uptake per unit of algae (A) respired	2.67 1.6-2.3 [a]	mg O_2/mg A mg O_2/mg A
K_3	CBOD settling rate at 20 °C	-0.36-(+0.36) [a]	day^{-1}
θ_{K3}	Temperature coefficient for K_3	1.024 [a]	
K_1	Carbonaceous De-oxygenation rate at 20 °C	0.21-0.16 0.02-3.4 [a]	day^{-1} day^{-1}
θ_{K1}	Temperature coefficient for K_1	1.047 1.047 [a]	
K_{BOD}	Half saturation constant for oxygen (O_2) limitation	0.5	mg O_2/L
K_4	Sediment oxygen (O_2) demand rate coefficient	0.2-4.0	g O_2/m^2/day
θ_{K4}	Temperature coefficient for K_4	1.08 1.06 [a]	
α_5	Oxygen (O_2) uptake per unit of ammonia nitrogen oxidation	4.57 3.0-4.0 [a]	mg O_2/mg A mg O_2/mg A

Note: The superscript "a" represents sources from QUAL2E, and contents without superscript are from WASP6.

5.5.1 Reaeration

When the dissolved oxygen level is below saturation, waters are replenished via atmospheric reaeration. The reaeration rate coefficient is a function of the average water velocity (v), depth (d), wind (w), and temperature (T). There have been numerous equations developed to define this rate constant (K_2) at standard temperature (20°C). Table 5-5 lists some of them.

Table 5-5 Equations for defining the reaeration rate constant K_2

Equations	Employing conditions	References
$K_2 = 5.026v^{0.969}d^{-1.673}$	Moderately shallow, faster moving streams	Churchill et al., 1962
$K_2 = 3.93v^{0.5}d^{-1.5}$	Deeper, slowly moving waters	O'Connor and Dobbins, 1958
$K_2 = 5.344v^{0.67}d^{-1.85}$	Shallow water $d < 2$ feet	Owens et al., 1964
$K_2 = \frac{0.065w^2 + 3.86(v/d)^{0.5}}{d}$	Wind induced reaeration	van Pagee, 1978 Delvigne, 1980

Schnoor (1996) suggested some reference value ranges of the reaeration rate constant at standard temperature (20°C) as: K_2 = 0.1-0.4 for slow, deep rivers, K_2 = 0.4-1.0 for typical conditions, K_2 = 1.5-4.0 for swift, deep rivers and K_2 = 4.0-10.0 for swift, shallow rivers. In the water quality model of this study, the reaeration rate can either be specified as a constant from input, or calculated following either the flow-induced rate or the wind induced rate, whichever is larger.

5.5.2 Carbonaceous oxidation

The long history of applications has focused primarily on the use of BOD as the measure of the quantity of oxygen demanding material and its rate of oxidation as the controlling kinetic reaction. This has proven to be appropriate for waters receiving a heterogeneous combination of organic wastes of municipal and industrial origin since an aggregate measure of their potential effect is a great simplification that reduces a complex problem to one of tractable dimensions.

The oxidation of carbonaceous material is the classical BOD reaction. Internally, the water quality model in this study uses ultimate carbonaceous biochemical oxygen demand (CBOD) as the indicator of equivalent oxygen demand for the carbonaceous material. A principal source of CBOD, other than man-made sources and natural runoff, is detrital phytoplankton carbon, produced as a result of algal death. The primary loss mechanism associated with CBOD is

oxidation, settling and denitrification. The BOD function in this model can be expressed as:

$$\frac{dL}{dt} = \alpha_3 D_m \mathrm{A} - K_1\left(\frac{O}{K_{BOD}+O}\right)\theta_{K1}L \; - K_3 L \; - \frac{5}{4}\frac{32}{14}\beta_3\theta_3\left(\frac{O}{K_{NO3}+O}\right)N_3 \qquad (5\text{-}20)$$

Death Oxidation Settling Denitrification

The kinetic expression for carbonaceous oxidation contains three terms -- a first order rate constant (K_1), a temperature correction term (θ_{K1}), and a low DO correction term (K_{BOD}). The first two terms are standard. The third term represents the decline of the aerobic oxidation rate as DO levels approach 0. K_{BOD} can be specified as the half-saturation constant, which represents the DO level at which the oxidation rate is reduced by half.

5.5.3 Sediment oxygen demand

The decomposition of organic material in benthic sediment can have profound effects on the concentrations of oxygen in the overlying waters. The decomposition of organic material results in the exertion of an oxygen demand at the sediment-water interface. As a result, the areal fluxes from the sediment can be substantial oxygen sinks to the overlying water column.

This model assumed the sediment oxygen demand rate (K_4) as a constant at standard temperature (20°C). Reference value ranges are given in Table 5-6 (Thomann and Muller, 1987; Bowie et al., 1985).

Table 5-6 Typical value ranges for sediment oxygen demand rate

Sediment oxygen demand rate	Value range	Unit
Municipal sludge (outfall vicinity)	2-10	g O_2/m^2/day
Municipal sewage sludge	1-2	g O_2/m^2/day
Sandy bottom	0.2-1.0	g O_2/m^2/day
Mineral soils	0.05-0.1	g O_2/m^2/day

5.6 Numerical tests for the reaction system

The solute transport model has been tested in chapter 4, for the numerical effects of advection and diffusion. In this section, the numerical solutions for coupled reactors with feedbacks are tested in a completely mixed system with time variation.

There are about ten reactors representing the major interactions of the nutrient cycles, algal production, benthic and carbonaceous oxygen demand, and atmospheric reaeration connected with the dissolved oxygen balance. Theoretically, the analytical solution for each reactor can be obtained by solving the interaction equations simultaneously, while in practice, these equations could only be solved numerically by computational models.

To test the accuracy of the numerical model set up in this study, a simplified case for a two reactors system will be used with first order reaction. For a time-variable reaction system, the interaction equations for two reactors can be written as (Chapra, 1997):

$$\begin{cases} \dfrac{dc_1}{dt} = -\alpha_{11}c_1 + \alpha_{12}c_2 \\ \dfrac{dc_2}{dt} = \alpha_{21}c_1 - \alpha_{22}c_2 \end{cases} \tag{5-21}$$

where c_1 and c_2 are the concentrations of the two reactors. Coefficients α_{11}, α_{12}, α_{21} and α_{22} define the interactions between the two reactors. The coefficient matrix can be written as:

$$A = \begin{bmatrix} -\alpha_{11} & \alpha_{12} \\ \alpha_{21} & -\alpha_{22} \end{bmatrix} \tag{5-22}$$

The characteristic polynomial is given by:

$$|A - \lambda E| = \begin{vmatrix} -\alpha_{11} - \lambda & \alpha_{12} \\ \alpha_{21} & -\alpha_{22} - \lambda \end{vmatrix} = \lambda^2 + (\alpha_{11} + \alpha_{22})\lambda + \alpha_{11}\alpha_{22} - \alpha_{12}\alpha_{21} = 0 \tag{5-23}$$

This is a quadratic equation which has two roots in the form:

$$\begin{matrix}\lambda_f \\ \lambda_s\end{matrix} = \frac{(\alpha_{11}+\alpha_{22}) \pm \sqrt{(\alpha_{11}+\alpha_{22})^2 - 4(\alpha_{11}\alpha_{22} - \alpha_{12}\alpha_{21})}}{2} \tag{5-24}$$

where the λ's are eigenvalues for the coefficient matrix, and E is an identity matrix defined as:

$$E = \begin{bmatrix} 1 & 0 \\ 0 & 1 \end{bmatrix} \tag{5-25}$$

If the initial condition is $c_1=c_{10}$ and $c_2=c_{20}$, then the general solution can be developed as:

$$c_1 = c_{1f}e^{-\lambda_f t} + c_{1s}e^{-\lambda_s t} \tag{5-26}$$

$$c_2 = c_{2f}e^{-\lambda_f t} + c_{2s}e^{-\lambda_s t} \tag{5-27}$$

and the coefficients are

$$c_{1f} = \frac{(\lambda_f - \alpha_{22})c_{10} - \alpha_{12}c_{20}}{\lambda_f - \lambda_s} \tag{5-28}$$

$$c_{1s} = \frac{\alpha_{12}c_{20} - (\lambda_s - \alpha_{22})c_{10}}{\lambda_f - \lambda_s} \tag{5-29}$$

$$c_{2f} = \frac{-\alpha_{21}c_{10} + (\lambda_f - \alpha_{11})c_{20}}{\lambda_f - \lambda_s} \tag{5-30}$$

$$c_{2s} = \frac{-(\lambda_s - \alpha_{11})c_{20} + \alpha_{21}c_{10}}{\lambda_f - \lambda_s} \tag{5-31}$$

The system recovery (process of approaching the steady state) depends on the relative magnitudes of the eigenvalues. Note that λ_f will always be greater than λ_s. Consequently λ_f and λ_s are often referred to as the "fast" and "slow" eigenvalues, respectively. This nomenclature derives from the rate at which they approach zero as time progresses.

5.6.1 Case 1: System with monotonous solutions

The two reactors system can be described as:

$$\begin{cases} \dfrac{dc_1}{dt} = -3c_1 + 2c_2 \\ \dfrac{dc_2}{dt} = 2c_1 - 3c_2 \end{cases} \tag{5-32}$$

The two eigenvalues can be obtained as $\lambda_f = 5$ and $\lambda_s = 1$, according to equation (5-24). Assume the initial conditions as $c_{10} = 1$ and $c_{20} = 2$, the analytical solutions for this reaction system are:

$$c_1 = 1.5e^{-t} - 0.5e^{-5t} \tag{5-33}$$

$$c_2 = 1.5e^{-t} + 0.5e^{-5t} \tag{5-34}$$

The numerical solutions from the model compared with the analytical solutions are plotted in Figure 5-2. It can be seen that the results of the numerical simulation match exactly with the analytical solutions, thus the correctness of the numerical model can be validated.

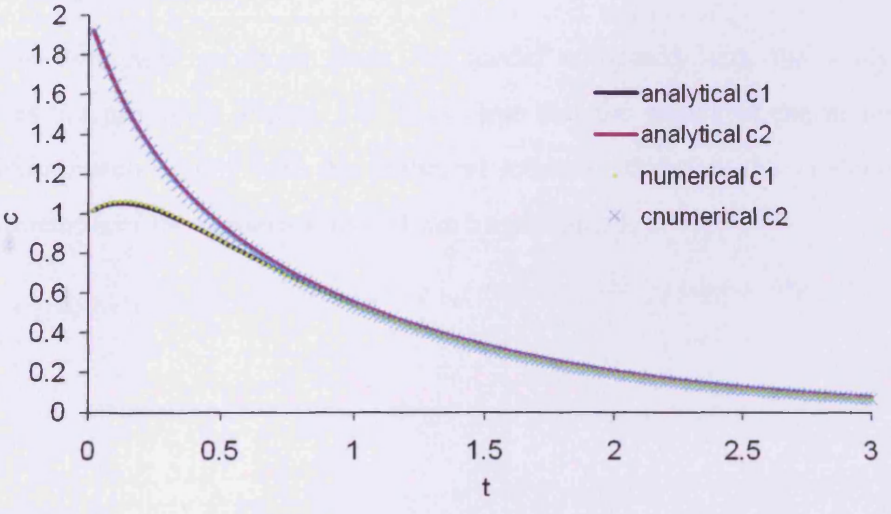

Figure 5-2 Comparison of numerical and analytical solutions for case 1

5.6.2 Case 2: System with fluctuating solutions

The two reactors system can be described as:

$$\begin{cases} \dfrac{dc_1}{dt} = -c_1 - 10c_2 \\ \dfrac{dc_2}{dt} = 10c_1 - c_2 \end{cases} \tag{5-35}$$

The two eigenvalues can be obtained as λ_f = -1+10i and λ_s = -1-10i, according to equation (5-24). Therefore, the general solutions can be found as:

$$c_1 = e^{-t}[c_{01}\cos 10t - c_{02}\sin 10t] \tag{5-36}$$

$$c_2 = e^{-t}[C_{01}\sin 10t + C_{02}\cos 10t] \tag{5-37}$$

Assume the initial condition as:

$$\begin{cases} c_{01} = 1 \\ c_{02} = 2 \end{cases} \tag{5-38}$$

Then the analytical solutions can be written as:

$$c_1 = e^{-t}[\cos 10t - 2\sin 10t] \tag{5-39}$$

$$c_2 = e^{-t}[2\cos 10t + \sin 10t] \tag{5-40}$$

The numerical solutions from the model compared with the analytical solutions are plotted in Figure 5-3. It is clear that the results of the numerical simulation match exactly with the analytical solutions, therefore the validation of the correctness of the numerical model can be reinforced.

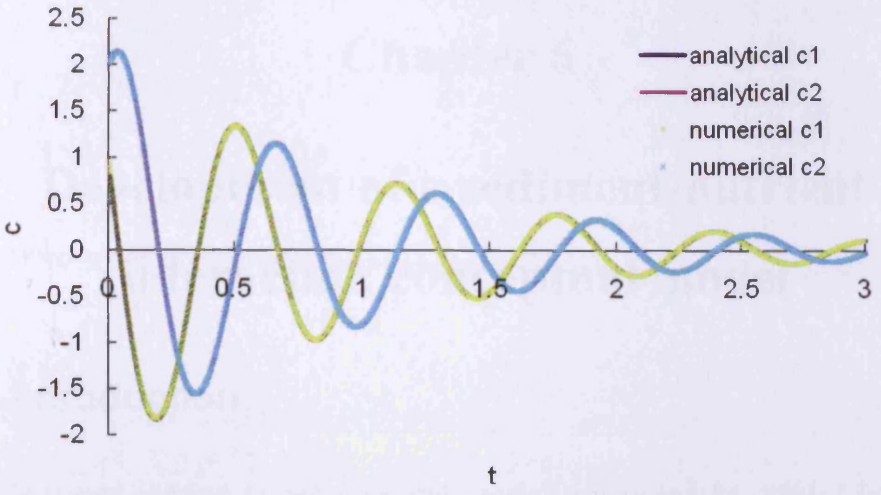

Figure 5-3 Comparison of numerical and analytical solutions for case 2

5.7 Summary

This chapter described the biological, chemical and physical processes of the water quality constituents. The transport and transformation reactions of up to ten state variables were considered as four interacting systems, namely, phytoplankton kinetics, nitrogen and phosphorus cycles and dissolved oxygen balance. The model framework was established based on QUAL2E, which has the advantage of simplicity and clarity. New formulae and coefficients have been introduced, based on WASP6, to consider more factors in various conditions. The relationships between individual reaction and interacting systems were also addressed mathematically. Finally, the numerical model has been tested for a simple two-reactor system.

Chapter 6

Development of a sediment-nutrient interaction conceptual model

6.1 Introduction

Nutrients existing in estuaries and coastal waters can be divided into two forms, either dissolved in the water column or attached to suspended particles. Dissolved nutrients may be transported and diffused as solute within the water column, or they may adsorb onto the sediments, transforming to particulate phase, and then be transported with the sediments. Deposition of the sediments can take particulate nutrients out of the water column and onto the bed. The sediments can subsequently be re-suspended to the water column, which can then lead to re-suspension of the nutrients of the attached forms back into the water column. In this chapter, a conceptual model is established to describe the interaction between the sediments and nutrient concentrations, which is verified by idealized cases through comparison of analytical and computational solutions. Before going into further details, it is necessary to consider the sediment transport for both non-cohesive and cohesive sediment particles.

6.2 Sediment transport model

6.2.1 Suspended sediment transport

The governing equation for suspended sediment transport in estuaries and coastal waters is usually based on the depth integrated two-dimensional advection-diffusion equation, and can be written as:

$$\frac{\partial HS}{\partial t}+\frac{\partial HUS}{\partial t}+\frac{\partial HVS}{\partial t}-\frac{\partial}{\partial x}(HD_{xx}\frac{\partial S}{\partial x}+HD_{xy}\frac{\partial S}{\partial y})$$
$$-\frac{\partial}{\partial y}(HD_{yx}\frac{\partial S}{\partial x}+HD_{yy}\frac{\partial S}{\partial y})=\phi \tag{6-1}$$

where S is the depth averaged suspended sediment concentration, and ϕ is the source or sink term, which can also be expressed as a net sediment flux, in the form (Van Rijn, 1993):

$$\phi = E - D = w_s(S_{a,e} - S_a) \tag{6-2}$$

where E and D are the sediment erosion and deposition rates, respectively. S_a is the sediment concentration at a reference level (i.e. the concentration at an elevation "a" above the bed), and $S_{a,e}$ is the equilibrium sediment concentration at reference level a. The equilibrium concentration is the value that occurs when the re-suspended sediment flux from the bed is in equilibrium with the deposited sediment flux to the bed.

The equilibrium reference concentration used in this study was proposed by Van Rijn, (1993), and given as:

$$S_{a,e} = 0.015\frac{D_{50}T^{1.5}}{aD_*^{0.3}} \tag{6-3}$$

where D_{50} is the sediment medium grain size, T is the transport stage parameter, a is the reference elevation above the bed , and D_* is the particle parameter.

For non-cohesive sediment transport, the net sediment flux rate in equation (6-2) can be written in the form (Yuan, 2007):

$$E - D = \gamma w_s(S_e - \alpha S) \tag{6-4}$$

where w_s is the particle falling velocity, γ is a profile factor given by the ratio of the equilibrium bed concentration $S_{a,e}$, to the depth averaged equilibrium sediment concentration S_e, $\alpha$is the sediment concentration profile parameter. The depth averaged equilibrium sediment concentration evaluated using Van Rijn (1984b) and the procedures were also detailed in Falconer and Chen (1996).

For cohesive sediment transport, the deposition and erosion flux rates can be expressed as in the Equations (6-5) and (6-6).

$$D = \begin{cases} w_s S_b (1 - \dfrac{\tau_b}{\tau_{c,d}}) & for\ \tau_b < \tau_{c,d} \\ 0 & for\ \tau_b \geq \tau_{c,d} \end{cases} \tag{6-5}$$

$$E = \begin{cases} M\left[(\dfrac{\tau_b}{\tau_{c,e}(z,t)} - 1) \right]^{n_0} & for\ \tau_b > \tau_{c,e}(z,t) \\ 0 & for\ \tau_b \leq \tau_{c,e}(z,t) \end{cases} \tag{6-6}$$

In this study, Equations (6-5) and (6-6) being rewritten in a simplified form (Falconer and Chen, 1996) are used to model the cohesive sediment transport.

$$D = \begin{cases} w_s S (1 - \dfrac{\tau_b}{\tau_{c,d}}) & for\ \tau_b < \tau_{c,d} \\ 0 & for\ \tau_b \geq \tau_{c,d} \end{cases} \tag{6-7}$$

$$E = \begin{cases} M(\dfrac{\tau_b}{\tau_{c,e}} - 1) & for\ \tau_b > \tau_{c,e} \\ 0 & for\ \tau_b \leq \tau_{c,e} \end{cases} \tag{6-8}$$

where τ_b is the bed shear stress, $\tau_{c,d}$ and $\tau_{c,e}$ are the critical shear stress for deposition and erosion respectively, and M is the empirical erosion constant.
Most of the parameters included in the above formulations are sensitive to the sediment characteristics locally. During numerical modelling studies of estuarine flows the value used must be chosen with extreme care. Typical values of the critical stress for erosion and deposition are given in Van Rijn (1993) for a range of different mud types. For the empirical erosion coefficient M, reported values are typically in the range of 0.00001 to 0.0005 for soft natural mud (Falconer and Chen, 1996).

6.2.2 Bed load transport

The bed load sediment transport rate can be expressed in the form of the product of particle concentration, particle velocity and bed layer thickness, as

following:

$$q_b = c_b u_b \delta_b \tag{6-9}$$

where q_b is the volumetric bed-load transport rate, c_b is the volumetric concentration , u_b is the particle velocity, and δ_b is the thickness of bed load layer. The thickness of bed load layer (δ_b) is defined as the saltation height of the bed particles. Van Rijn (1993) found that the saltation height was related to a dimensionless bed-shear stress parameter (or the transport stage parameter) T and a dimensionless particle parameter D_* (Equation (2-7)), given as follows:

$$\frac{\delta_b}{D} = 0.3 D_*^{0.7} T^{0.5} \tag{6-10}$$

in which D is particle grain size.

The particle velocity and the bed load concentration are given by Van Rijn (1984a) as follows:

$$u_b = 1.5 T^{0.6} [(s-1) g D]^{0.5} \tag{6-11}$$

$$c_b = 0.18 c_o \frac{T}{D_*} \tag{6-12}$$

where $c_o = 0.65$ is the maximum volumetric concentration.

Substituting Equations (6-10), (6-11) and (6-12) into Equation (6-9) gives the formulation for calculating bed load transport as follows (Van Rijn, 1984a):

$$q_b = \frac{0.053 T^{2.1} [g(s-1)]^{0.5} D_{50}^{1.5}}{D_*^{0.3}} \qquad 0 < T < 3 \tag{6-13}$$

Equation (6-13) was found to over-predict the transport rate when T≥3, therefore, a modified expression is proposed for this range as follows (van Rijn, 1993):

$$q_b = \frac{0.1 T^{1.5} [g(s-1)]^{0.5} D_{50}^{1.5}}{D_*^{0.3}} \qquad T \geq 3 \tag{6-14}$$

6.3 Sediment-nutrient interaction conceptual model

6.3.1 Partitioning of nutrients between sediment and water

Nutrients in the water can be classified as dissolved phase and particulate phase. There is an adsorption-desorption interaction between these two phases, as the suspended sediment settling together with the adsorbed nutrients can act as a significant loss in the water column and as a source for the bed sediment. Because the rates of reaction for adsorption-desorption are in the order of minutes versus reaction rates in the order of days for the biological kinetics, an equilibrium assumption can be made. This equilibrium reaction implies that the dissolved and particulate phases "instantaneously" react to any discharge sources or runoff so as to redistribute the nutrients to its "equilibrium" dissolved and particulate phase concentrations. At equilibrium, the nutrient concentration distribution between dissolved and particulate phases can be defined by a partition coefficient, which is the ratio of concentrations in these two phases. Chapra (1997) expressed the partition coefficient, K_D, in the form:

$$K_D = \frac{P}{C_d} \tag{6-15}$$

where C_d is the dissolved nutrient concentration, and P is the mass of nutrient attached to the suspended sediment, which is calculated as:

$$P = \frac{C_p}{S} \tag{6-16}$$

where S is the suspended sediment concentration, and C_p is the particulate nutrient concentration.

Substituting Equation (6-16) into Equation (6-15) gives:

$$C_p = K_D S C_d \tag{6-17}$$

In equilibrium, the total concentration can be expressed as the sum of dissolved and particulate concentration.

$$C_T = C_d + C_p = C_d + C_d K_D S = (1 + K_D S) C_d \tag{6-18}$$

which can be written as:

$$C_d = f_d C_T \tag{6-19}$$

with

$$f_d = \frac{1}{1 + K_D S} \tag{6-20}$$

f_d is the fraction of nutrient dissolved in the water column. The fraction of nutrient attached to the suspended sediment f_p can be calculated from Equations (6-17) and (6-18) as

$$f_p = \frac{K_D S}{1 + K_D S} \tag{6-21}$$

and

$$f_d + f_p = 1 \tag{6-22}$$

The distribution of dissolved and particulate concentrations therefore depends on the partition coefficient (K_D) and the suspended sediment concentration.

The partition coefficient can be determined through experiment, when the dissolved concentration and particulate mass can both be measured at equilibrium. There are some factors affecting the value of the partition coefficient, such as the physical and chemical characteristics of the sediment particles, and the ambient conditions, i.e., salinity. Details are discussed in Chapter 7.

6.3.2 Nutrient exchange between sediment-water interface

Figure 6-1 illustrates the interaction of nutrients and sediment particles on the interface of the water column and bed sediment. Particulate nutrients settle to or re-suspend from bed sediment via deposition and erosion processes. While the exchange of dissolved nutrients between the surface water and the interstitial

water is via diffusive processes. This means the mass exchange between water body and bed sediment is mainly due to the settling and re-suspension of sediments. It is reasonable to ignore the mass exchange of the dissolved nutrients between the water body and the interstitial water due to diffusive processes. Thus, only the mass exchange due to settling and re-suspension of particulates will be taken into account in this study.

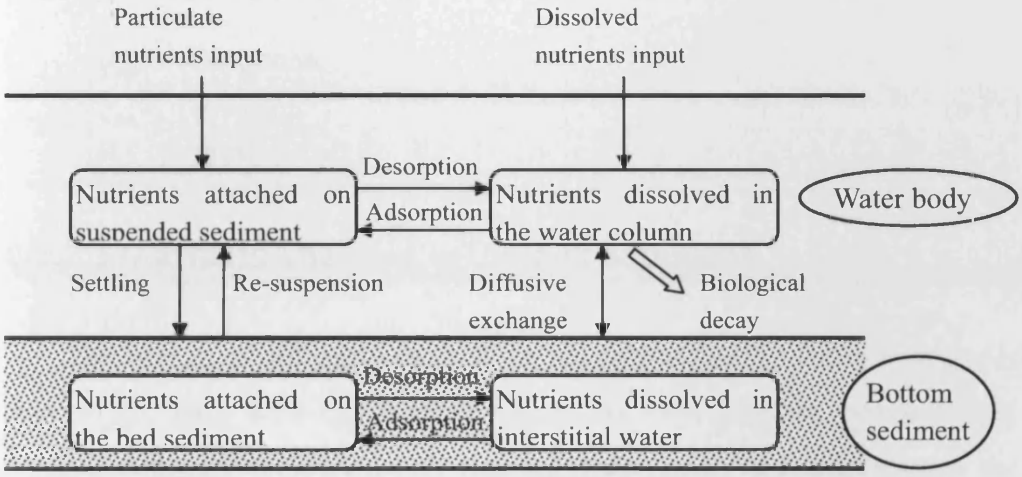

Figure 6-1 Illustration of nutrient transport between water and sediment

6.3.2.1 Nutrient settlement flux

Particulate nutrient can be taken out of the water column to the bed sediment with the suspended sediment settling. The settlement flux from the water column to the bed sediment F_{dep}, can be expressed as:

$$F_{dep} = q_{dep} P \tag{6-23}$$

where q_{dep} is the sediment deposition rate (kg/m^2/s), and P is the amount of nutrient attached to the suspended sediment (mg/g).

6.3.2.2 Nutrient re-suspension flux

The re-suspension flux of nutrients from the bed sediment to the water

column, F_{ero}, can be expressed as:

$$F_{ero} = q_{ero} P_b \tag{6-24}$$

where q_{ero} is the sediment erosion rate (kg/m^2/s), and P_b is the amount of nutrient attached to the bed sediment (mg/g).

To summarize the sediment settling and re-suspension effects, the net nutrient flux F_{net}, can be expressed as:

$$F_{net} = \begin{cases} q_{dep} P & \text{Deposition} \\ q_{ero} P_b & \text{Erosion} \\ 0 & \text{Rest} \end{cases} \tag{6-25}$$

6.3.2.3 Nutrients attached in the bed sediment

The amount of nutrients adsorbed on bed sediments (P_b) varies temporarily due to the mass exchange between the water body and the bed sediment. Assuming that the diffusive coefficient is infinite in the bed sediment (i.e. the deposited sediment and the bed sediment mix well immediately once the deposit sediment touches the bottom), the change rate of P_b can be expressed as follows:

$$\frac{dP_b}{dt} = \frac{q_{dep}}{M_b}(P - P_b) \tag{6-26}$$

where M_b is the mass of the bed sediment per unit area. Equation (6-26) shows that if the concentration of the particulate nutrient adsorbed on the suspended sediment (P) is greater than that on the bed sediment (P_b), then P_b will increase with time, and vice versa.

The mass of the bed sediment per unit area (M_b) also varies temporarily and is calculated with the following formula:

$$\frac{dM_b}{dt} = q_{dep} - q_{ero} \tag{6-27}$$

6.3.3 Governing equations for nutrient transport processes

6.3.3.1 Governing equations for dissolved and particulate nutrient transport

The transport in the dissolved phase can be described by the following two-dimensional advection-diffusion equation:

$$\frac{\partial HC_d}{\partial t}+\frac{\partial HUC_d}{\partial t}+\frac{\partial HVC_d}{\partial t}-\frac{\partial}{\partial x}(HD_{xx}\frac{\partial C_d}{\partial x}+HD_{xy}\frac{\partial C_d}{\partial y}) \\ -\frac{\partial}{\partial y}(HD_{yx}\frac{\partial C_d}{\partial x}+HD_{yy}\frac{\partial C_d}{\partial y})=H(S_o^d+S_t^d) \tag{6-28}$$

where $S_o{}^d$ is the source or sink of dissolved nutrients; and S_t^d is the transformation term defining adsorbed or desorbed particulate fluxes to or from the suspended sediments.

The adsorbed particulate phase is transported with the sediments, and this process may be described by the following equation:

$$\frac{\partial HC_p}{\partial t}+\frac{\partial HUC_p}{\partial t}+\frac{\partial HVC_p}{\partial t}-\frac{\partial}{\partial x}(HD_{xx}\frac{\partial C_p}{\partial x}+HD_{xy}\frac{\partial C_p}{\partial y}) \\ -\frac{\partial}{\partial y}(HD_{yx}\frac{\partial C_p}{\partial x}+HD_{yy}\frac{\partial C_p}{\partial y})=H(S_o^p+S_t^p)+S_b^p \tag{6-29}$$

where S_o^p is the source or sink of particulate nutrients; and $S_t{}^p$ is the transformation term defining adsorbed or desorbed particulate fluxes to or from the suspended sediments. $S_b{}^p$ represents the source term defining particulate flux from or to the bed, for sediment erosion or deposition, respectively.

6.3.3.2 Governing equations for total nutrient load

The transformation processes between the dissolved and adsorbed particulate phases are very complex. However, noting that $S_t^d = -S_t^p$, Wu et al (2005) introduced a new method to avoid calculating the transformation rate of trace metals between the dissolved and adsorbed particulate phases by first calculating

the total trace metal concentration distributions, and then dividing the dissolved and adsorbed particulate phases using a partitioning relationship of the form given in Equations (6-17) and (6-18). The evaluation of the total nutrients concentrations in this form is thought to be novel, with the corresponding equation derived by summing Equations (6-28) and (6-29), and re-arranging the diffusion terms to give:

$$\frac{\partial HC_T}{\partial t}+\frac{\partial HUC_T}{\partial t}+\frac{\partial HVC_T}{\partial t}-\frac{\partial}{\partial x}(HD_{xx}\frac{\partial C_T}{\partial x}+HD_{xy}\frac{\partial C_T}{\partial y}) \\ -\frac{\partial}{\partial y}(HD_{yx}\frac{\partial C_T}{\partial x}+HD_{yy}\frac{\partial C_T}{\partial y})=H(S_o^d+S_o^p)+S_b^p \tag{6-30}$$

where C_T = concentration of total nutrients, i.e.:

$$C_T=C_d+C_p \tag{6-31}$$

Equation (6-30) can be solved by using the numerical method introduced in Chapter 4 with suitable initial and boundary conditions. Then the values of C_d and C_p can be evaluated using Equations (6-17) and Equation (6-18).

6.4 Idealized test cases

In this section two analytical solutions for sediment-nutrient interaction case studies have been investigated, namely for a deposition and re-suspension test. These solutions were first derived and the numerical model was then set up for validation cases. The numerically predicted results were compared with the analytical results in order to validate the sediment-nutrient interaction properties of the numerical model. After validating the numerical model against these analytical solutions, the numerical model was then tested for the sensitivities of some coefficients.

6.4.1 Deposition and re-suspension test

6.4.1.1 Derivation of analytical solutions

To derive the analytical solutions for sediment-nutrient interaction with sediment deposition and re-suspension processes, it is necessary to make the hydrodynamic process, the advection-diffusion process and the sediment properties as simple as possible. Figure 6-2 illustrates a simple process with sediment deposition. K_D is the partition coefficient, P and P_b represent the amount of nutrients attached to suspended and bed sediment, respectively, S_0 and C_T^0 are the initial concentrations of suspended sediment and total nutrient concentration in the water column, and w_s is the suspended sediment settling velocity. H and h_b represent the water depth and the thickness of the bed sediment. The assumptions are indicated as follows:

(1) The flow is one-dimensional uniform and steady.

(2) The sediment has a uniform particle size across the domain, and has a constant settling velocity w_s.

(3) The initial sediment concentration S_0 and the equilibrium sediment concentration S_e have the relationship of : $S_0 > S_e$ for the deposition process and $S_0 < S_e$ for the re-suspension process, which makes the sediment and the movement of the attached nutrients always go one way, either settling down onto the bed or re-suspending from the bed. Thus the concentrations of the sediment and the nutrients will decrease or increase monotonically until they reach equilibrium.

(4) The change of bed elevation due to deposition or re-suspension of sediment is far less than the water depth and can be ignored.

(5) The nutrients' decay rates can be neglected because the biological or chemical reaction will take much more time than the sediment-nutrient interaction to reach their equilibrium (in the order of days versus minutes).

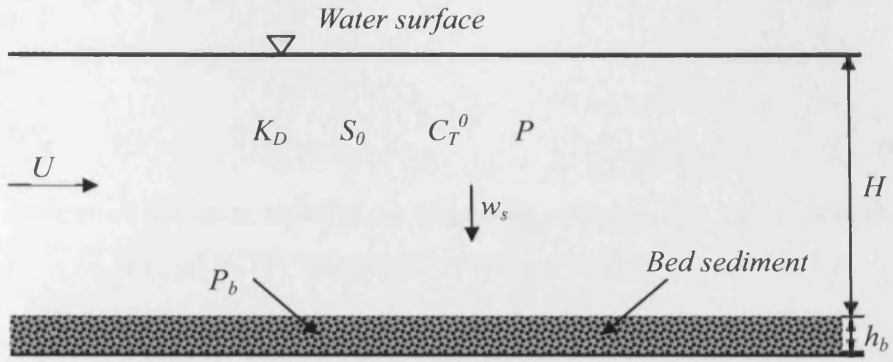

Figure 6-2 Schematic illustration of test cases

Based on the above assumptions, the governing equation for total nutrient transport (Equation (6-30)) can be simplified as:

$$\frac{dC_T}{dt} = \frac{1}{H} S_b^P \tag{6-32}$$

where $S_b{}^P$ represents source or sink term due to particulate nutrient flux from or to the bed, for sediment erosion or deposition. Since there is no decay of the dissolved nutrients, $S_b{}^P$ can also be expressed as net nutrient flux F_{net} in Equation (6-25). Thus, we have

$$S_b^P = \begin{cases} q_{dep} P = \dfrac{dHS}{dt} P & \textit{for deposition} \\ q_{ero} P_b = \dfrac{dHS}{dt} P_b & \textit{for resuspension} \end{cases} \tag{6-33}$$

The sediment transport model gives

$$\frac{dS}{dt} = \frac{\gamma w_s}{H}(S_e - \alpha S) \tag{6-34}$$

Combining Equations (6-33) and (6-34), the nutrient transport equation (6-32) can be expressed as:

$$\frac{dC_T}{dt} = \begin{cases} \dfrac{\gamma w_s}{H}(S_e - \alpha S) P & \textit{for deposition} \\ \dfrac{\gamma w_s}{H}(S_e - \alpha S) P_b & \textit{for resuspension} \end{cases} \tag{6-35}$$

The analytical solution for sediment transport in Equation (6-34) is derived as (Yuan, 2007):

$$S = \frac{1}{\alpha} S_e + (S_0 - \frac{1}{\alpha} S_e) e^{-\lambda t} \tag{6-36}$$

where

$$\lambda = \frac{\alpha \gamma w_s}{H} \tag{6-37}$$

The amount of nutrients attached to suspended sediment can be calculated from Equations (6-16) and (6-19), given as:

$$P = \frac{K_D C_T}{1 + K_D S} \tag{6-38}$$

Substituting Equations (6-38) and (6-36) into Equation (6-35), gives:

$$\frac{dC_T}{dt} = \frac{\lambda K_D C_T}{1 + K_D C_T} (\frac{1}{\alpha} S_e - S) \tag{6-39}$$

Yuan (2007) solved the Equation (6-39) and got the analytical solution for the nutrient transport with sediment deposition as:

$$C_T = \frac{\alpha + K_D [S_e + (\alpha S_0 - S_e) e^{-\lambda t}]}{\alpha (1 + K_D S_0)} C_T^0 \tag{6-40}$$

The analytical solution for nutrient transport with the sediment suspension was also solved and given as:

$$C_T = C_T^0 + \frac{P_b^0}{\alpha} (S_e - \alpha S_0)(1 - e^{-\lambda t}) \tag{6-40}$$

where P_b is designated as a constant P_b^0.

6.4.1.2 Numerical model validation against analytical solutions

In this section, the sediment-nutrient interaction model is verified against the analytical solutions for sediment deposition and erosion processes derived in the previous section.

Case 1: Deposition

The computational parameters are set as follows:

(1) The depth of the water column (H) and the thickness of the bed sediment layer

(h_b) are set as $1m$ and $0.2m$, respectively. The grid size and the time step used in this simulation are $\Delta x=1m$ and $\Delta t=10s$, respectively.

(2) The initial suspended sediment concentration (S_0) and the equilibrium sediment concentration (S_e) are set as $2kg/m^3$ and $1kg/m^3$, respectively. The initial bed sediment concentration is set to be zero.

(3) Parameters for sediment transport are set as follows: α =1, γ =1, and the settling velocity $w_s=0.001m/s$. The value of the partition coefficient K_D is set to $0.5L/g$, which is a little larger but in the same order as the experimental results (Abdulgawad, 2010). This value gives the particulate nutrient concentration being 50 percent of the total nutrient concentration in the water column, using Equation (6-21).

(4) The initial nutrient concentration in the water column (C_T^0) is set to $10mg/l$, and it is assumed that the nutrient level in the bed sediment is zero at the initial stage.

The comparisons between the model simulation of Equation (6-30) and the analytical solutions are shown in Figures 6-3a, 6-3b, 6-3c and 6-3d. It can be seen from the graphs, that the numerical model produces very accurate results in predicting the sediment and nutrient concentrations. It takes about 60 minutes for the reaction system to reach its equilibrium condition, with the reduced particulate nutrient concentration taken out of the water column by the deposited sediment being the same as the total nutrient concentration reduction, which is 25 percent of the total nutrient concentration. It is clear that the suspended sediment can be a non-negligible fraction in the nutrient storage.

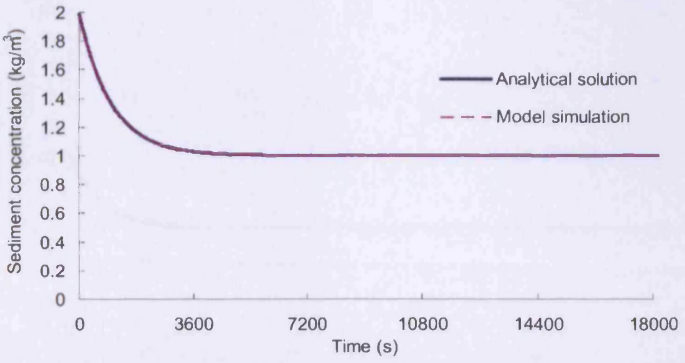

Figure 6-3a Comparison of sediment concentration for deposition test

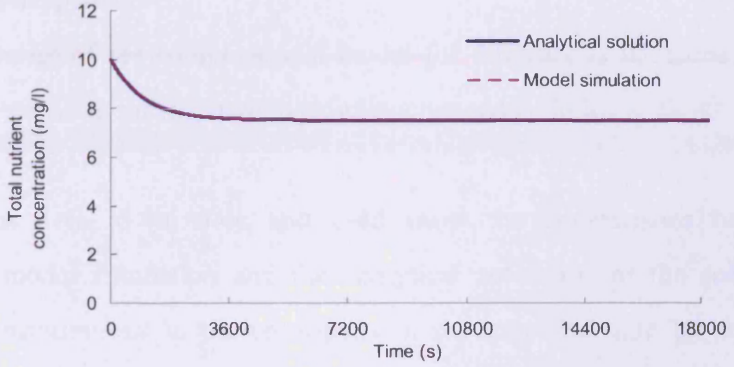

Figure 6-3b Comparison of total nutrient concentration for deposition test

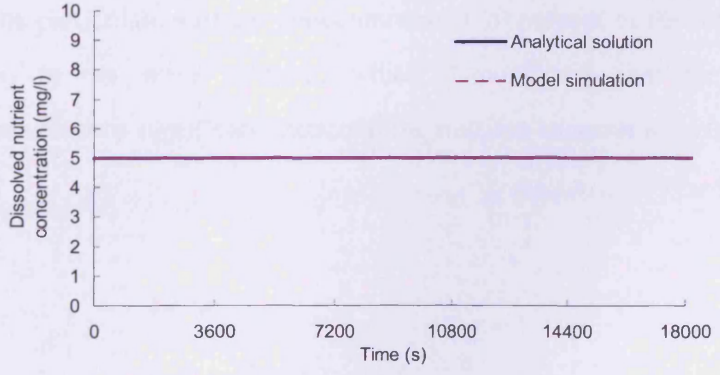

Figure 6-3c Comparison of dissolved nutrient concentration for deposition test

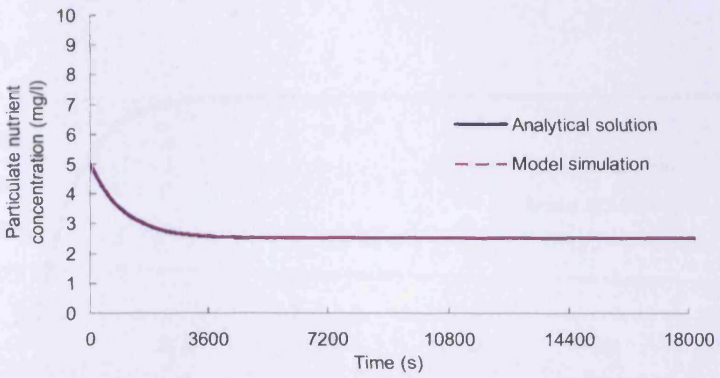

Figure 6-3d Comparison of particulate nutrient concentration for deposition test

Case 2: Re-suspension

The set up of the computational model for this case is the same as that for case 1, except some initial conditions being changed as follows: S_0 =0, C_T^0=0, and P_b^0=1mg/g.

Figures 6-4a, 6-4b, 6-4c and 6-4d show the comparisons between the numerical model simulation and the analytical solutions for the sediment and nutrient concentrations in the re-suspension process. The time for the reaction system to reach its equilibrium concentration is about 60 minutes. Both the dissolved and particulate nutrient concentrations increase simultaneously with the sediment re-suspension. After the equilibrium condition has been achieved, the fraction of the particulate nutrient concentration is 70 percent of the total nutrient concentration in the water column, which demonstrates that the sediment re-suspension can be a significant source to the nutrient concentration in the water body.

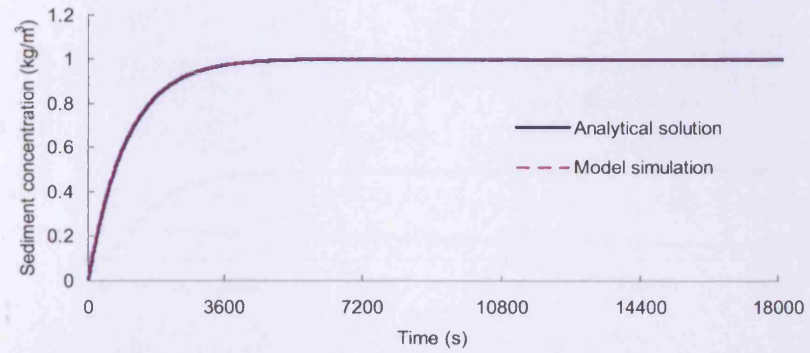

Figure 6-4a Comparison of sediment concentration for re-suspension test

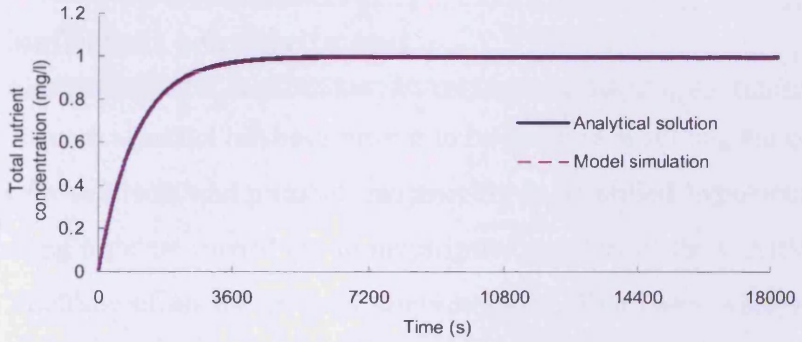

Figure 6-4b Comparison of total nutrient concentration for re-suspension test

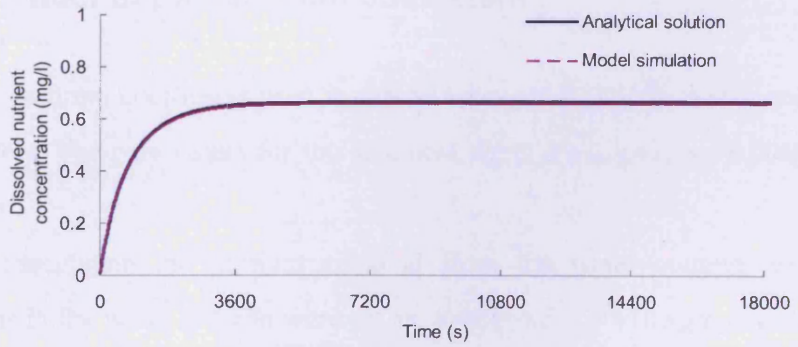

Figure 6-4c Comparison of dissolved nutrient concentration for re-suspension test

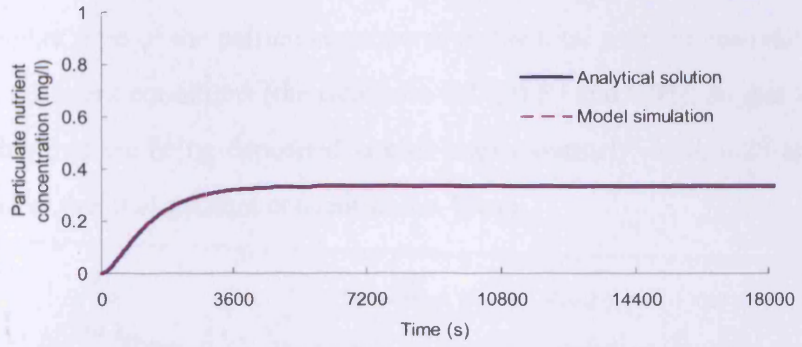

Figure 6-4d Comparison of particulate nutrient concentration for re-suspension test

6.4.2 Coefficient sensitivity test

The numerical model has been proven to be accurate in solving the governing equations for sediment and nutrient transport for a simplified hypothetical case. The following tests are carried out to investigate the effect of the variation of the different coefficients on the nutrient concentrations. Two cases were set up to study the nutrient removal from the water column and the subsequent re-entering to the water column.

6.4.2.1 Effect of the partition coefficient

The partition coefficient used in this test was set as $0.1L/g$, $0.5L/g$ and $10L/g$, respectively. The parameters for the sediment were: α =1, γ =1, w_s=$0.001m/s$, and S_e=$1kg/m^3$.

To investigate the nutrient removal from the water column, the initial conditions in the water column were set as: S_0=$2kg/m^3$, C_T^0=$10mg/l$, and the initial bed sediment was set to be zero. The numerical model results for the changing process of the nutrient levels are shown in Figures 6-5a, 6-5b and 6-5c. The graphs clearly show that with increasing values of the partition coefficient, the total nutrient concentrations will decrease, as well as the dissolved nutrient

concentrations. The reason for this finding is that the higher partition coefficient gives a higher ratio of the particulate nutrient to the total nutrient coagulations for the same sediment conditions (the ratios are 0.17, 0.50 and 0.95), so that the ratio of nutrients that are being deposited is also higher (namely, 0.08, 0.25 and 0.48) which makes the total nutrient concentrations lower.

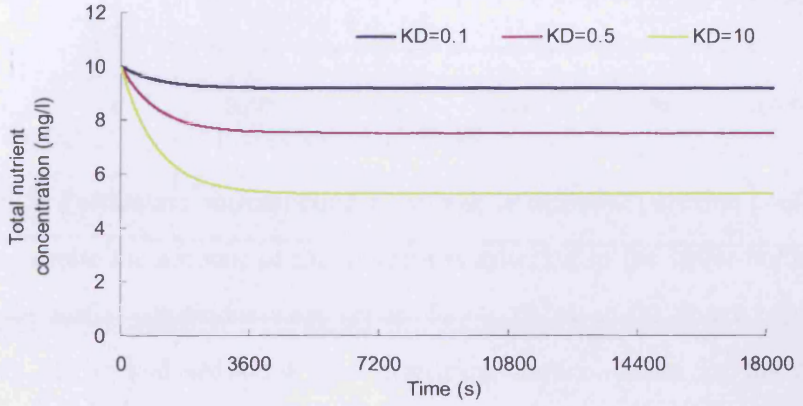

Figure 6-5a Total nutrient concentration for different partition coefficients

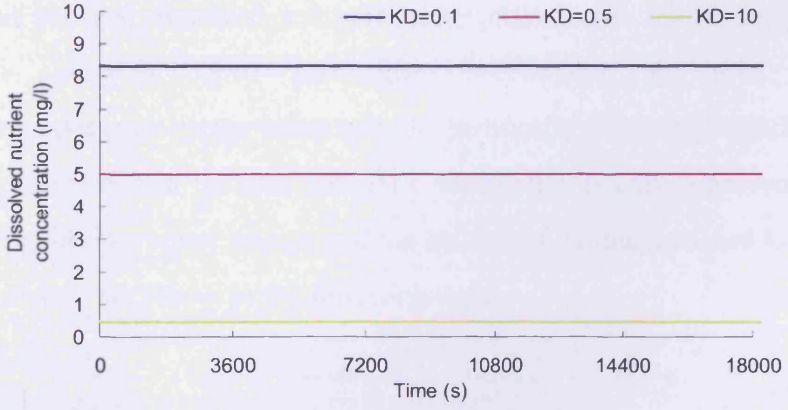

Figure 6-5b Dissolved nutrient concentrations for different partition coefficients

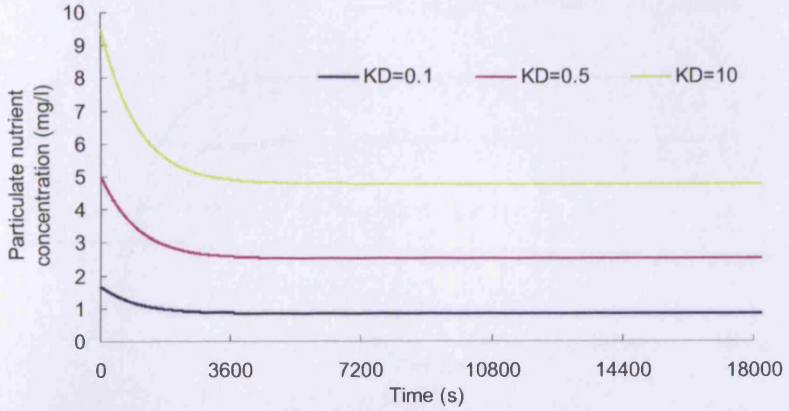

Figure 6-5c Particulate nutrient concentrations for different partition coefficients

To examine the amount of the nutrient re-entering to the water column from the bed, the initial conditions were set as: S_0 =0, C_T^0=0 in the water column, and P_b^0=1mg/g in the bed sediment. The numerical model results for the changing process of nutrient levels are shown in Figures 6-6a, 6-6b and 6-6c. It can be seen from the graphs that although the partition coefficient affects the concentration distribution between dissolved and particulate phases, with the higher partition coefficient giving a higher particulate concentration, the total nutrient concentration does not change much with the partition coefficient's variation. This can be explained as that the total nutrient concentration is only dependent on the sediment equilibrium concentration and the amount of nutrient attached to the bed sediment. Details are shown in the following tests.

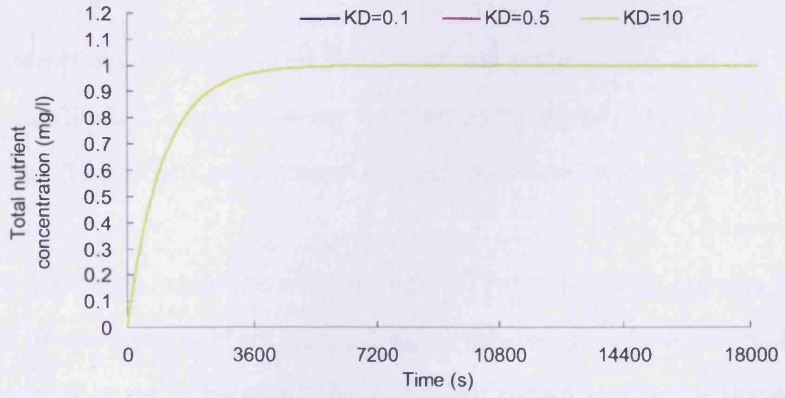

Figure 6-6a Total nutrient concentrations for different partition coefficients

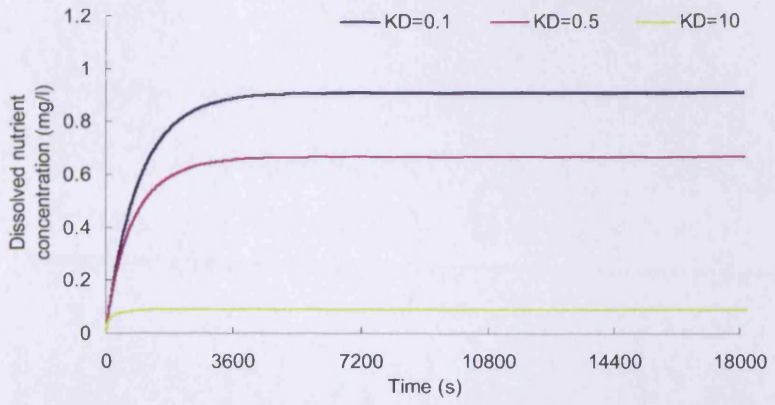

Figure 6-6b Dissolved nutrient concentrations for different partition coefficients

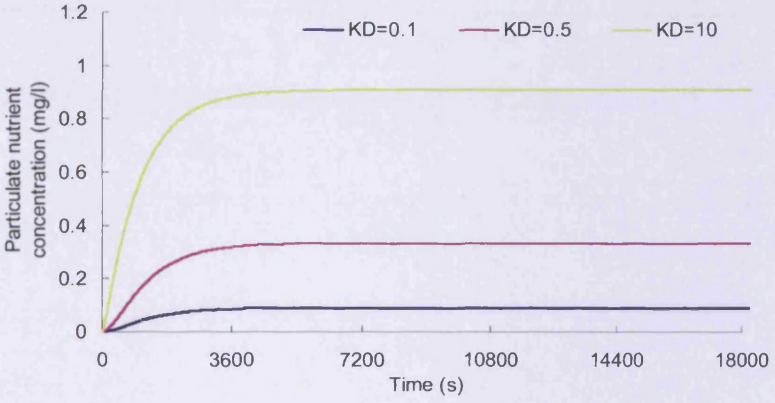

Figure 6-6c Particulate nutrient concentrations for different partition coefficients

6.4.2.2 Effect of suspended sediment equilibrium concentration

The partition coefficient used in this test was set to $0.5L/g$, and the suspended sediment equilibrium concentrations were set as 0.5 kg/m^3, $1kg/m^3$ and 1.5 kg/m^3, respectively. The other parameters for the sediment were: α =1, γ =1, and w_s=$0.001m/s$.

In the investigation of the nutrient removal from the water column, the initial conditions in the water column were set as: S_0=$2kg/m^3$, C_T^0=$10mg/l$, and the initial bed sediment was set to be zero. The numerical model results for the process of the nutrient level changes are shown in Figures 6-7a, 6-7b, 6-7c and 6-7d. It can be

observed that higher sediment equilibrium concentrations give higher total nutrient concentrations because of more nutrient attaching on the suspended sediment (Figure 6-7d).

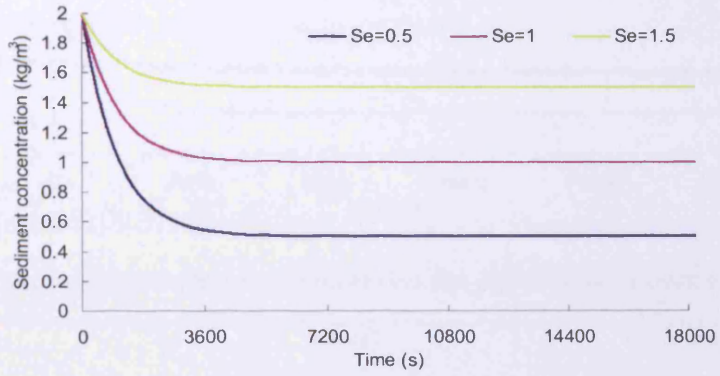

Figure 6-7a Concentrations of sediment for different sediment equilibrium values

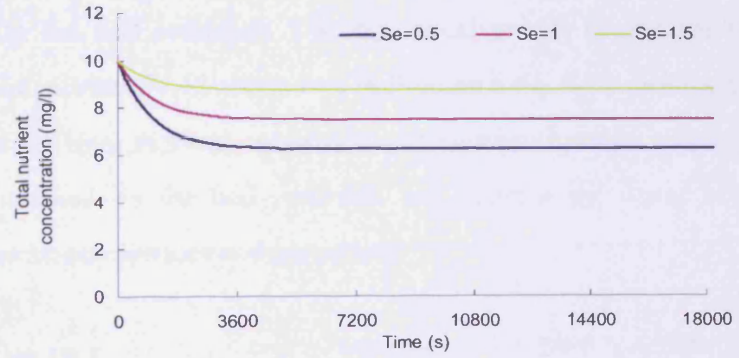

Figure 6-7b Total nutrient concentrations for different sediment equilibrium values

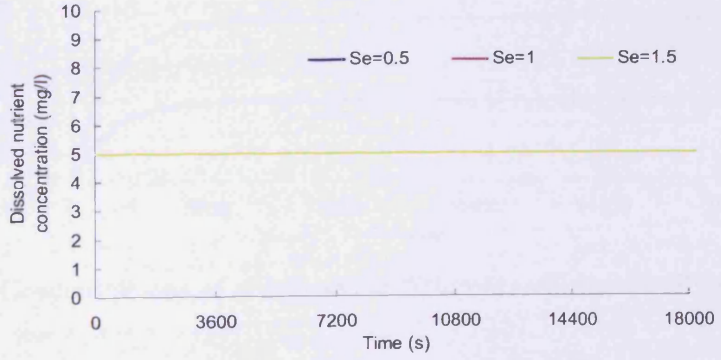

Figure 6-7c Dissolved nutrient concentrations for different sediment equilibrium values

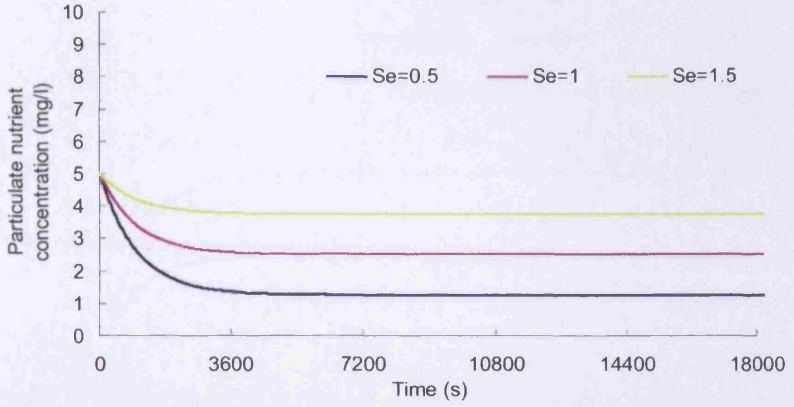

Figure 6-7d Particulate nutrient concentrations for different sediment equilibrium values

For testing the amount of the nutrients re-entering the water column from the bed, the initial conditions were set as: S_0 =0, C_T^0=0 in the water column, and P_b^0=1mg/g in the bed sediment. The numerical model results for the changing process of the nutrient level are shown in Figures 6-8a, 6-8b, 6-8c and 6-8d. It can be seen that the total nutrient concentrations increase because more nutrients that are being attached on the bed sediment are entering the water column with a higher sediment equilibrium concentration.

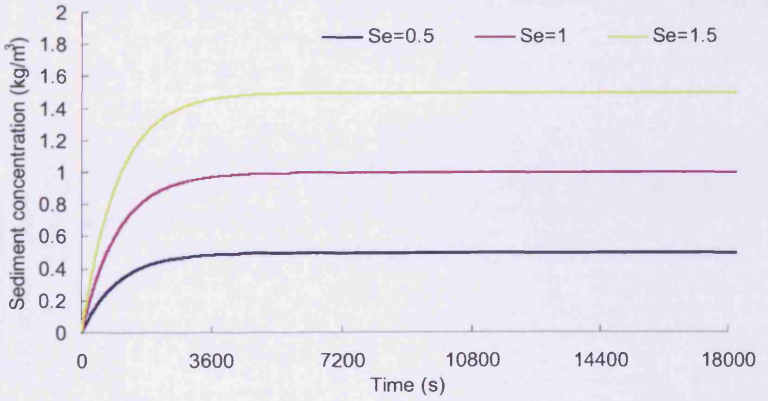

Figure 6-8a Concentrations of sediment for different sediment equilibrium values

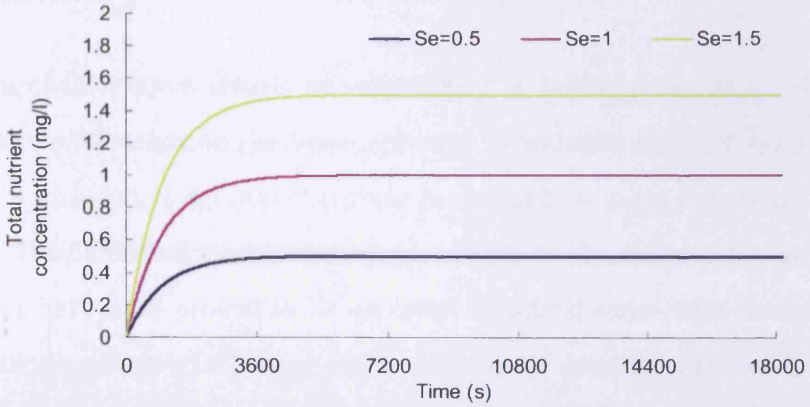

Figure 6-8b Total nutrient concentrations for different sediment equilibrium values

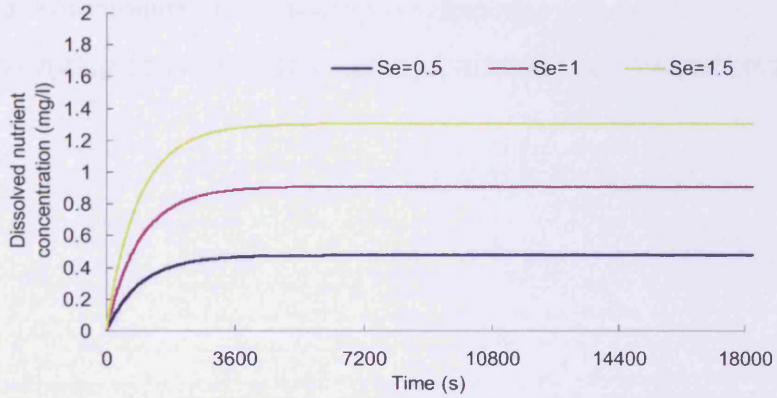

Figure 6-8c Dissolved nutrient concentrations for different sediment equilibrium values

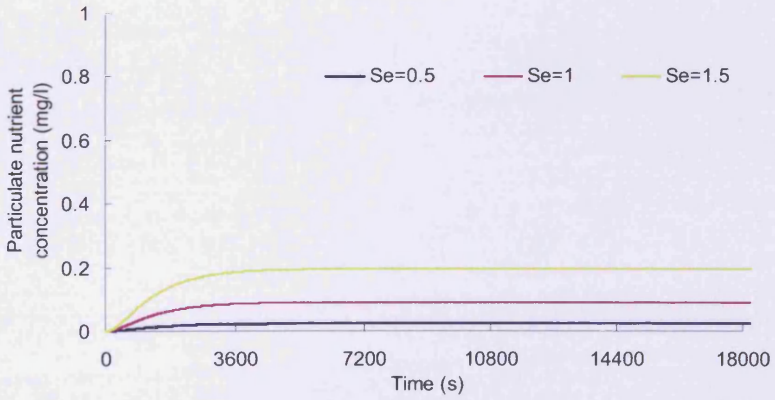

Figure 6-8d Particulate nutrient concentrations for different sediment equilibrium values

6.5 Summary

This chapter gave details of establishing a sediment-nutrients interaction model, where the deposition and re-suspension of nutrients attached with sediment have been included. Total nutrients were partitioned by using a dynamic fraction ratio K_D. The numerical model has been tested against the analytical solutions, and the results have been proved to be accurate. Idealized cases were then set up to investigate the effects of different coefficients on the deposition and re-suspension of nutrients. It was found that the concentrations of nutrients adsorbed by the sediments were dependent on the values of the partition coefficients and the equilibrium concentration of the suspended sediments.

Chapter 7

Data analysis on the nutrient adsorption experiments

7.1 Introduction

To study the sediment transport effect on the nutrient concentration distributions in the water body, the sediment-nutrient adsorption/desorption mechanisms were be investigated through controlled laboratory experiments. A series of adsorption/desorption experiments for ammonium ion (NH_4^+) were undertaken in the laboratory at Cardiff University. The details of these experiments can be found in the PhD thesis of Abdulgawad (2010). This chapter analyzes the experimental results, uses theoretical derivations to validate the experiments, and summarizes the factors that have effects on the adsorption processes.

7.2 Ammonium adsorption-desorption experiments

7.2.1 Sediment particle sizes

Four commercial types of clay and sand, namely Montmorillonite, Kaolinite and fine and coarse sand were used in the laboratory experiments, with their median grain size being 3.5μm, 6.75μm, 30μm and 270μm. The particle size distribution was determined by using a Laser particle size instrument (Malvern Master Sizer). Figure 7-1 shows a comparison of the particle size and accumulative percent distributions of mass for all of the four sediment samples.

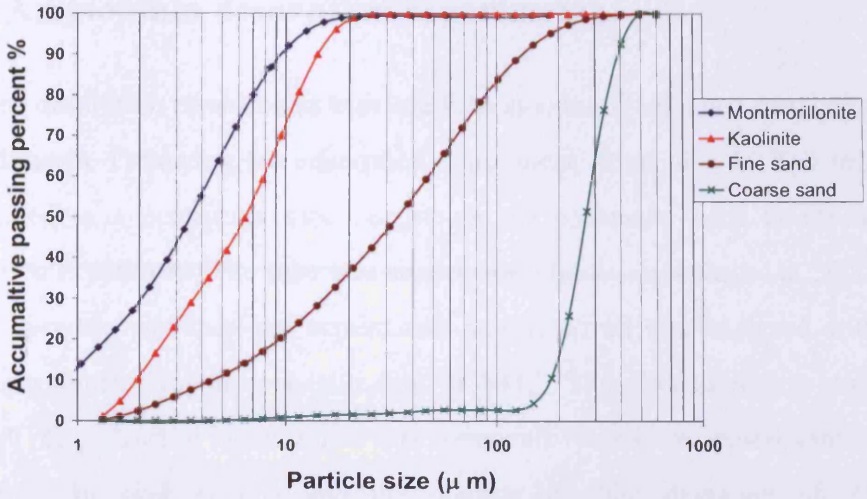

Figure 7-1 Particle size distributions for sediment samples (Abdulgawad, 2010)

7.2.2 Ammonium adsorption experiments

The sediment samples were washed to eliminate all attached chemicals. Different concentrations of ammonium chloride (NH_4CL) were prepared, at 2, 4, 6, 8, 10, 20 and 30 mg/l NH_4^+. Samples of 0.8g dried sediment sample were placed in a series of centrifuge tubes, and then 40 ml of ammonium solutions (containing NH_4CL) of various concentrations from 2 to 30 mg/l was added. The centrifuge tube was placed on a shaker with continuous agitation for 24 hours, at standard room temperature. The sample solutions were then centrifuged at 3000 rpm for 20 minutes. The supernatant was then collected, filtered through a 2 μm cellulose filter paper and analyzed for ammonium (NH_4^+) concentration using a Lambda EZ150 Spectrophotometer in conjunction with HACH reagent. The quantity of adsorbed ammonium was calculated through the decrease of the ammonium concentration in the solution. The ammonium concentration in the supernatant was considered as an equilibrium concentration of ammonium in the water. For all samples, triplicate experiments were performed, and data were reported as their average. The results show that standard error deviation was within 5%.

7.2.3 Ammonium desorption experiments

The desorption experiments measured the amount of adsorbed ammonium on the sediments. Following the adsorption experiment, 40ml of 2 M KCl solution was added to a centrifuge tube containing the sediments used in the above adsorption experiment. The tube was shaken for 2 hours, centrifuged at 3000 rpm for 20 minutes, and then the supernatant was removed and analyzed with the spectrophotometer for the concentration of NH_4^+. This procedure was repeated until all the adsorbed ammonium was removed. Triplicate experiments were conducted for each sample and the relative standard deviation of all the experiments was between 0 and 10%.

7.3 Adsorption models

7.3.1 Theoretical solutions of dissolved and particulate concentration

The widely used models that can describe adsorption process have been introduced in Chapter 2. The adsorption process can be expressed in different formats, the equations and their correlation coefficients are listed below:

1. Linear adsorption isotherm:

According to the linear adsorption model, in an equilibrium water column, the amount of the ammonium adsorbed on the sediment q_e (mg/g) can be expressed as the product of the partition coefficient K_d (l/g) and the equilibrium concentration C_e (mg/l).

$$q_e = K_d C_e \tag{7-1}$$

Herein C_e (mg/l) is also the dissolved ammonium concentration. The particulate ammonium concentration C_p (mg/l) can be expressed as:

$$C_p = q_e S \tag{7-2}$$

where S (g/L) is the suspended sediment concentration. Substitute equation (7-1) into equation (7-2), given:

$$C_p = K_d C_e S \tag{7-3}$$

Under the controlled laboratory conditions, the total ammonium concentration (C_T) is constant, which is the same as the initial concentration C_0 (mg/l):

$$C_0 = C_T = C_e + C_p \tag{7-4}$$

Substitute equation (7-3) into equation (7-4), gives:

$$C_0 = (1 + K_d S) C_e \tag{7-5}$$

So the derived expression of both dissolved concentration and particulate concentrations are:

$$C_e = \frac{C_0}{1 + K_d S} \tag{7-6}$$

$$C_p = \frac{C_0 K_d S}{1 + K_d S} \tag{7-7}$$

Equations (7-6) and (7-7) can be taken as theoretical solutions of the linear adsorption model for the dissolved and particulate ammonium concentrations, which are determined by the initial ammonium concentration C_0 at each time step, the partition coefficient K_d and the suspended sediment concentration S. In this study, C_0 is dependent on the external loadings, biochemical processes, etc., S is calculated from the sediment transport model, and K_d is a constant found in the laboratory experiments.

2. Langmuir adsorption isotherm:

The Langmuir adsorption equation is written as:

$$q_e = \frac{q_m K_a C_e}{1 + K_a C_e} \tag{7-8}$$

where the maximum adsorption capacity q_m (mg/g) and Langmuir adsorption constant K_a (l/mg) are determined from the experiment. The particulate

concentration C_p (mg/l) and the dissolved concentration C_e (mg/l) can be calculated from equations (7-3) and (7-4):

$$C_p = q_e S = \frac{q_m K_a C_e}{1 + K_a C_e} S \tag{7-9}$$

$$C_e = C_0 - C_p = C_0 - \frac{q_m K_a C_e}{1 + K_a C_e} S \tag{7-10}$$

By substituting equations (7-9) and (7-10) into equation (7-8) and simplifying, a quadratic equation can be obtained:

$$C_p^{\,2} - (\frac{1}{K} + C_0 + Sq_m)C_p + C_0 Sq_m = 0 \tag{7-11}$$

By using the quadratic formula, C_p can be solved as:

$$C_p = \frac{1}{2}\left[(\frac{1}{K} + C_0 + Sq_m) \pm \sqrt{(\frac{1}{K} + C_0 + Sq_m)^2 - 4C_0 Sq_m}\right] \tag{7-12}$$

In order to determine the sign to be used before the radical in equation (7-12), this equation is rewritten as:

$$C_p = \frac{1}{2}\left[(\frac{1}{K} + C_0 + Sq_m) \pm \sqrt{(\frac{1}{K} + C_0 - Sq_m)^2 + \frac{4Sq_m}{K}}\right] \tag{7-13}$$

In equation (7-12),

$$\sqrt{(\frac{1}{K} + C_0 - Sq_m)^2 + \frac{4Sq_m}{K}} > (\frac{1}{K} + C_0 - Sq_m)$$

If the "+" is adopted, then

$$C_p > C_0$$

Based on equation (7-4), it is known that C_p is less than C_0, thus, in equation (7-12), only "-" is possible, and it becomes:

$$C_p = \frac{1}{2}\left[(\frac{1}{K} + C_0 + Sq_m) - \sqrt{(\frac{1}{K} + C_0 + Sq_m)^2 - 4C_0 Sq_m}\right] \tag{7-14}$$

Based on equation (7-10), C_e is expressed as:

$$C_e = \frac{1}{2}\left[(\frac{1}{K} - C_0 - Sq_m) + \sqrt{(\frac{1}{K} + C_0 + Sq_m)^2 - 4C_0Sq_m}\right] \quad (7\text{-}15)$$

In this study, C_0 and S are calculated from the solute and sediment transport model for each time step, followed by the sediment adsorption model to solve the dissolved concentration C_e and particulate concentration C_p.

7.3.2 Adsorption isotherm regression from the experiments

The laboratory experiments tested 4 types of sediment, namely Montmorillonite, Kaolinite and fine sand and coarse sand, with median grain sizes of 3.5μm, 6.75μm, 30μm and 270μm. The first three can be categorized as cohesive sediment, and the last one is non-cohesive sediment, according to the standard of the classification of cohesive and non-cohesive sediment (van Rijn, 1993).

The coefficients in the linear adsorption equation and Langmuir adsorption equation can be derived from the experiment data by linear regression. Figure 7-2 shows the relationship between the equilibrium concentration and the ammonium adsorption on the sediment, wherein the slope of the regression line is the partition coefficient K_d, based on equation (7-1). For Langmuir adsorption description, equation (7-8) can be written as:

$$\frac{C_e}{q_e} = \frac{C_e}{q_m} + \frac{1}{q_m K_a} \quad (7\text{-}16)$$

Figure 7-3 shows a plot of Langmuir adsorption regression, where the slope of the regression line is $1/q_m$ and the intercept should be $1/q_mK_a$.

Table 7-1 demonstrates the related coefficients for both linear and Langmuir adsorption isotherms in the experiments using four sediment types. The correlation coefficients R^2 indicates that the regression for Langmuir adsorption isotherm is more accurate than the regression for linear adsorption isotherm. The coefficient K_d for the linear adsorption isotherm has the largest value for Montmorillonite, and smallest value for coarse sand, which means that the adsorption capacity decreases

with the increase of sediment particle size. This can be explained theoretically as the small particles having lager specific surface area than large particles, which makes them more easily to adsorb ammonium ion. The maximum adsorption capacity q_m for Langmuir adsorption isotherm has the same tendency, decreasing with the particle size increasing, which gives another support for the aforementioned theoretical explanation, and also prove the correctness of the experimental results.

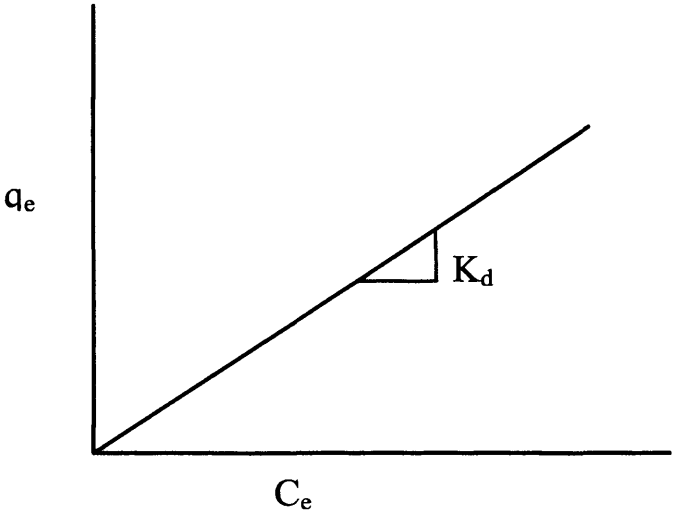

Figure 7-2 Linear adsorption isotherm

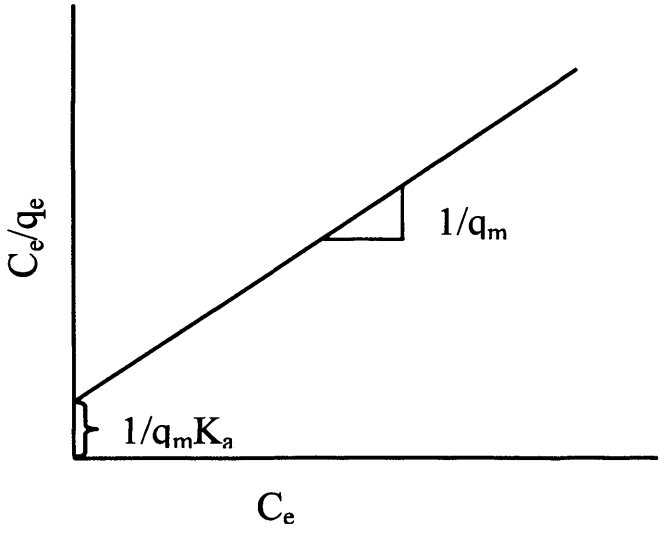

Figure 7-3 Linear regression of Langmuir adsorption isotherm

Table 7-1 The adsorption isotherm regressions with the correlation coefficients

	Linear		Langmuir		
Sediment type	K_d (l/g)	R^2	q_m (mg/g)	K_a (l/mg)	R^2
Montmorillonite	0.202	0.923	1.667	0.167	0.994
Kaolinite	0.025	0.839	0.769	0.045	0.949
Fine sand	0.016	0.842	0.556	0.037	0.921
Coarse sand	0.008	0.889	0. 217	0.054	0.956

7.3.3 Comparisons of the experimental and theoretical results using different models

Once the adsorption related coefficients have been found through the experiments, they can be substituted into the adsorption equations to give an adsorption isotherm for a specific sediment type. Applying the coefficients in Table 7-1 to equations (7-6) and (7-7) for linear adsorption, and equations (7-14) and (7-15) for Langmuir adsorption, the theoretical solutions for dissolved and particulate concentrations for ammonium can be obtained. Comparisons between these concentrations and the experimental results have been plotted in the following figures. The initial concentration C_0 are set as 2, 4, 6, 8, 10, 20, 30, 40, 50 and 60 mg/l NH_4^+ for each type of sediment in the experiments, and the sediment concentration S is given as 20g/l (0.8g dried sediment sample in 40ml NH_4^+ solutions) for each experiment.

Figures (7-4a) and (7-4b) show the comparisons between the results for Montmorillonite experiments and theoretical concentrations from different adsorption models, namely, linear adsorption model and Langmuir adsorption model. It can be seen that Langmuir adsorption model fits the experiment data very well, for both particulate and dissolved concentrations, while the linear adsorption model is far less accurate in predicting the particulate and dissolved concentrations at high level of the initial concentration. The linear adsorption

model results only fit the experimental data at a lower initial concentration, namely, at less than 10mg/l. Similar phenomena can be observed in the comparison figures for Kaolinite, fine sand and coarse sand (Figures 7-5 to 7-7).

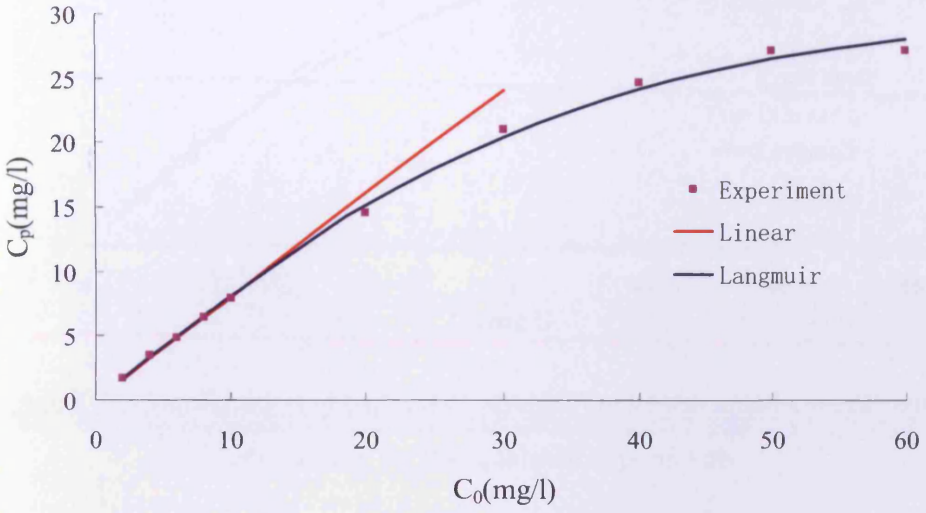

Figure 7-4a Concentration of particulate ammonium versus initial concentration at equilibrium for the Montmorillonite experiments

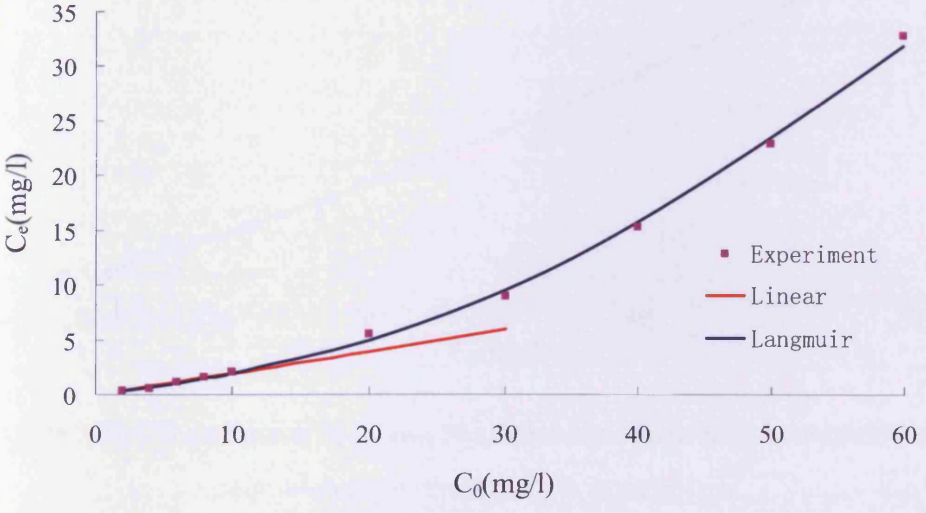

Figure 7-4b Concentration of dissolved ammonium versus initial concentration at equilibrium for the Montmorillonite experiments

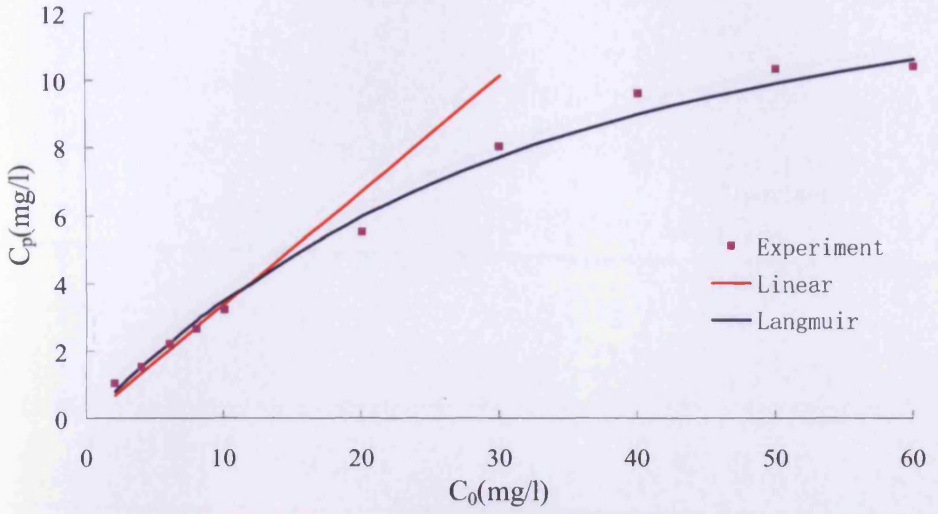

Figure 7-5a Concentration of particulate ammonium versus initial concentration at equilibrium for the Kaolinite experiments

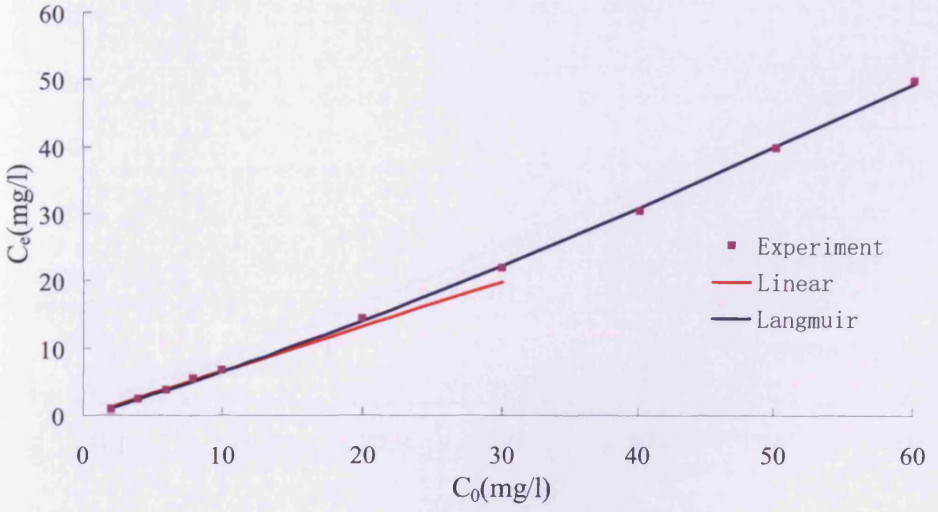

Figure 7-5b Concentration of dissolved ammonium versus initial concentration at equilibrium for the Kaolinite experiments

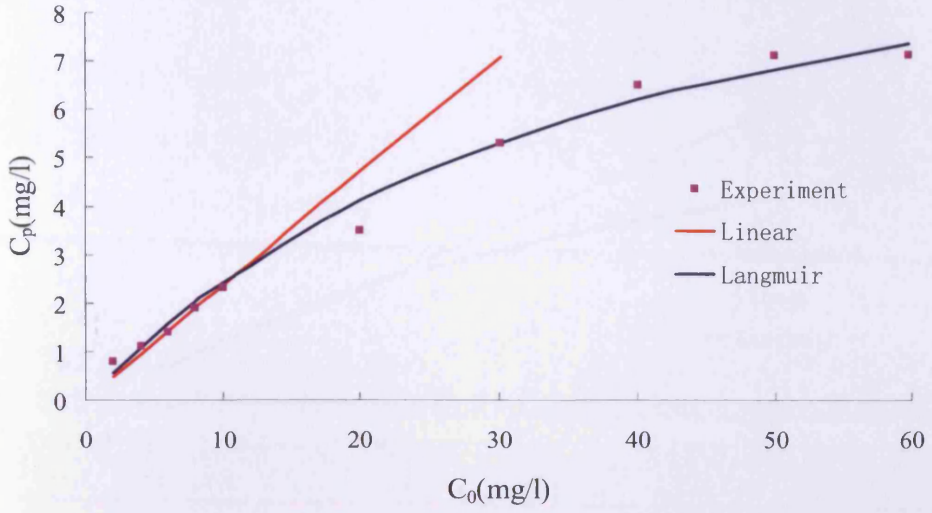

Figure 7-6a Concentration of particulate ammonium versus initial concentration at equilibrium for the fine sand experiments

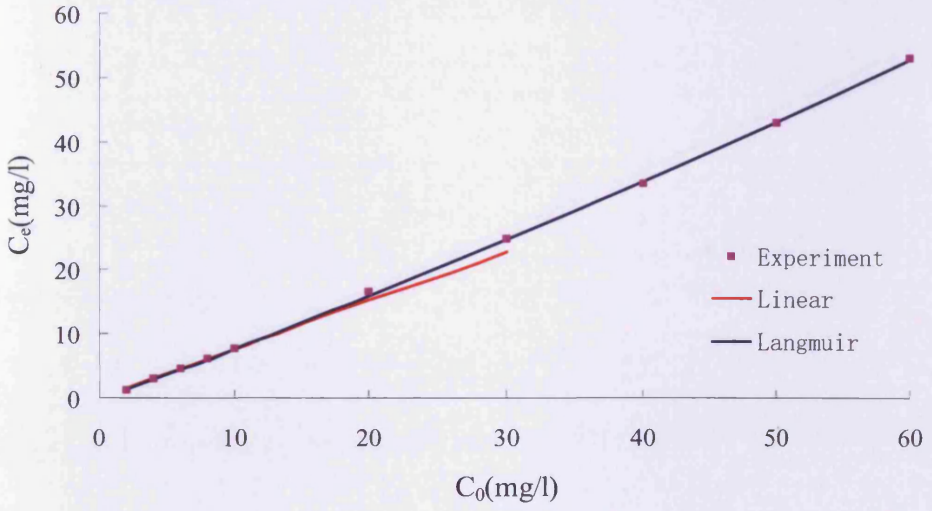

Figure 7-6b Concentration of dissolved ammonium versus initial concentration at equilibrium for the fine sand experiments

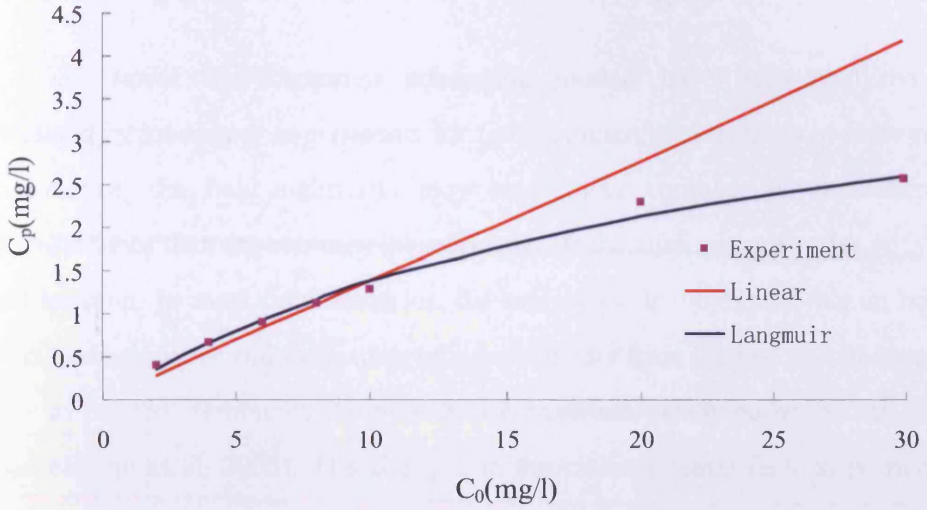

Figure 7-7a Concentration of particulate ammonium versus initial concentration at equilibrium for the coarse sand experiments

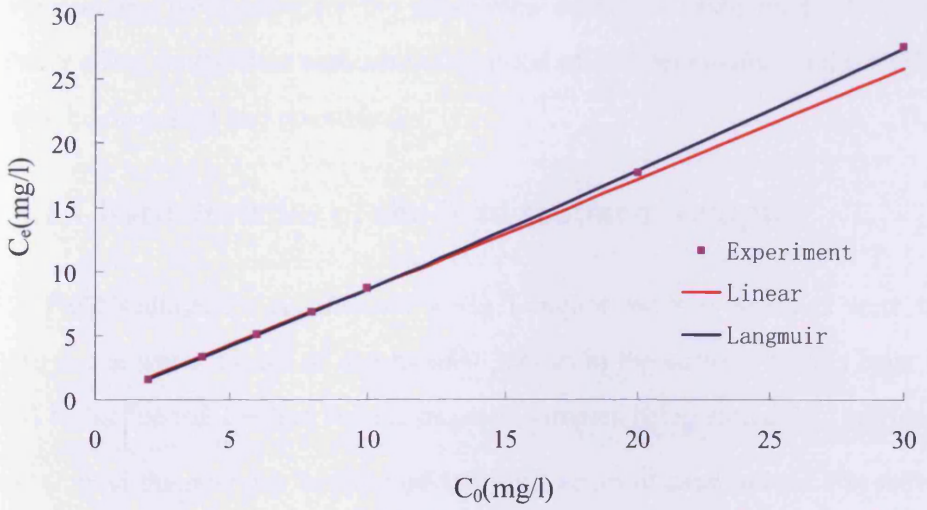

Figure 7-7b Concentration of dissolved ammonium versus initial concentration at equilibrium for the coarse sand experiments

It can be concluded from the above figures, that both linear and Langmuir adsorption models are suitable for the ammonium adsorption at low concentrations, but for high concentrations, the Langmuir adsorption model is more accurate in simulating the ammonium adsorption process.

7.4 Adsorption analysis for field samples

The linear and Langmuir adsorption models have been analyzed and validated by laboratory experiments for four commercial sediments in section 7.3. In practice, the field sediments may have more complex physical-chemical characteristics than the commercial sediments, as the environment varies with time and location. In most tidal estuaries, the tide plays an important role in mixing fresh and salt water and in re-suspending sediments from the bed and transporting the suspended sediments landwards or seawards (Schnauder et al, 2007; Bockelmann et al, 2008). The changes in the environmental factors, particularly salinity, are very intense and can influence the nutrient adsorption and their concentration distributions as a result of the interaction between the riverine fresh water and the sea water (Hou et al., 2003; Abdulgawad, 2010). This section applies the adsorption models to the analysis of the field sediment samples, and derive the corresponding parameters for the adsorption equations based on field data. The salinity effect on the field sediment adsorption of both ammonium and phosphorus is also be discussed and quantified.

7.4.1 Characteristics of the field sediment samples

Field sediment was collected along Loughor Estuary. Samples were taken close to the water's edge at depths of 0-3cm from the surface. Plastic bags were used for collecting the bed sediments, with samples being stored in a refrigerator at 4° C over the next day before undertaking a series of experiments. Six sediment samples taken on 14th December 2007 were analyzed, and their characteristics are listed below (Abdulgawad, 2010), in which the sample number represents the location where the sediments were collected (details of the locations can be found in Chapter 8), and the subscript number indicates the sampling time (within 3 hours at one hour intervals).

Table 7-2 Sediment characteristics of field samples

Sample number	$1b_1$	$1b_2$	$1b_3$	2_1	2_2	2_3
Bulk density (Mg/m^3)	1.10	1.30	1.30	1.50	1.30	1.20
Particle density(Mg/m^3)	2.65	2.67	2.69	2.65	2.68	2.63
Porosity (%)	0.58	0.51	0.52	0.43	0.51	0.54
Total carbon (%)	4.1	2.92	2.31	5.19	1.60	1.33
Inorganic carbon (%)	0.36	0.1	0.78	0.38	0.21	0.04
Organic carbon (%)	3.74	2.82	1.53	4.81	1.39	1.29

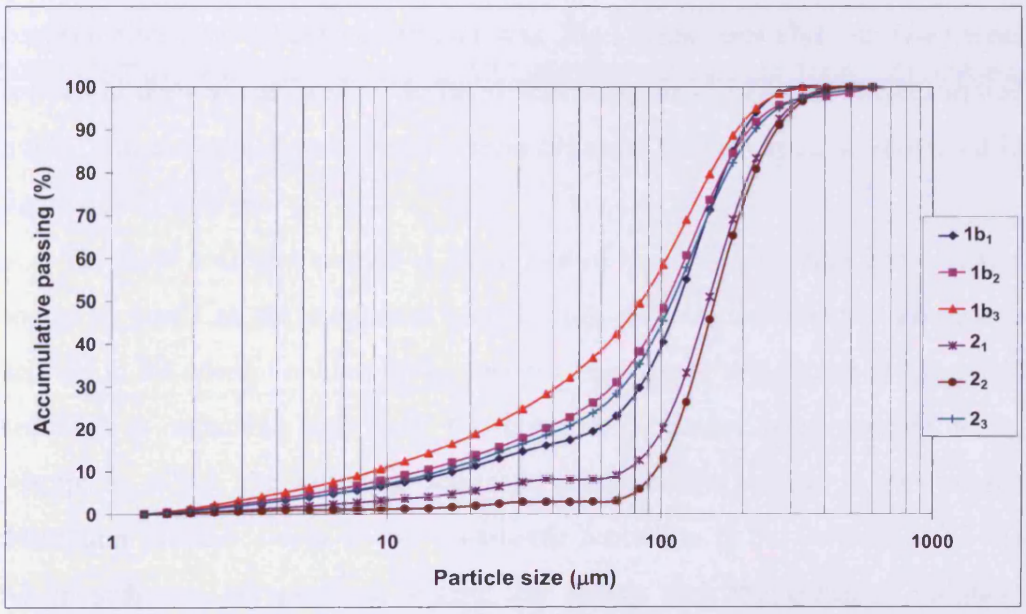

Figure 7-8 Particle size distributions of 6 field sediment samples

Table 7-2 and Figure 7-8 show that the sediment samples collected in close proximity and within three consecutive hours have no significant variations in the median grain size, density and porosity, so that they could have similar behaviors during the adsorption processes. The only factor that might make their adsorption characteristics different could be the different organic carbon content of each sample. Compared to the commercial sediments, the field sediments have a wider range of particle size distribution, and their grain sizes are in the range of

80-170μm which defines them as fine sand.

7.4.2 Adsorption isotherms for field sediments

Since the characteristics of the collected six sediment samples show not much difference, to simplify the analysis, the sediment sample $1b_2$ is designated as a representative sample for the later discussions.

The collected sample was used in the ammonium adsorption and desorption experiments described in sections 7.2.2. and 7.2.3. The initial concentration and the equilibrium concentration for ammonium were measured in the experiment, and their difference was the adsorbed concentration on the sediment. The sediment concentration used in the experiment was 20g/l. Equations (7-1) or (7-8) were applied to draw an adsorption isotherm depending on the type of the adsorption model, and the related parameters can be obtained by regression as described in Figures (7-2) or (7-3).

The field sediment sample is composed of both cohesive and non-cohesive sediment, while in the numerical model, only cohesive sediment is taken into account in the adsorption/desorption process. It is therefore assumed that the field sediment is separated and only the cohesive sediment is considered to be adsorptive. Thus, the cohesive sediment concentration, which is part of the adsorption process, needs to be calculated, according to its percentage of the whole sediment composition. Figure 7-9 shows that the cohesive sediment (particle size less than 63μm) makes up about 30 percent of weight in sample $1b_2$, and the half of this ratio is 15%. This number is used to find out the median grain size, which is approximately 26μm, and which is similar to one of the commercial sediments (namely, fine sand) used in previous experiments. The concentration of cohesive sediment is calculated as 30% of 20g/l, this being 6g/l, which should be used in the adsorption equations for calculation of the adsorption parameters.

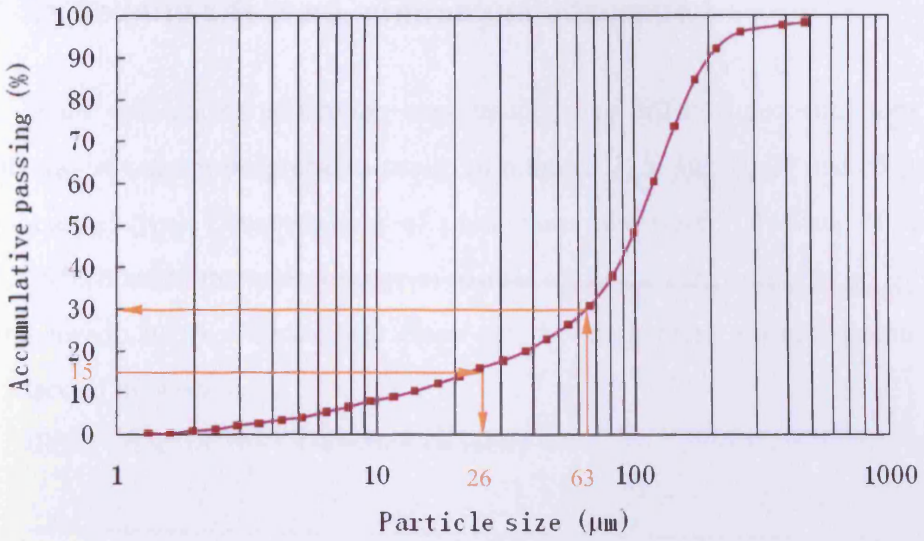

Figure 7-9 Particle size distributions and the cohesive sediment percentage for sediment sample $1b_2$

Table 7-3 shows a comparison of the adsorption parameters if the Langmuir adsorption isotherm is applied. It can be observed that the maximum adsorption capacity for the field sediment is significantly increased when only considering the cohesive part, and the value is comparable with the commercial sediment as the cohesive part has similar characteristics with the commercial sediment.

Table 7-3 Adsorption parameters for different sediment types

Sediment type / Parameters	Field sediment		Commercial sediment
	$1b_2$	$1b_2$ cohesive part	Fine sand
q_m (mg/g)	0.161	0.526	0.556
K_a (l/mg)	0.104	0.106	0.037
R^2	0.967	0.967	0.921

7.4.3 Salinity effect on field sediment adsorption

The investigations carried out in this study were to find out how the saline water will affect the sediment adsorptions of the ammonium nitrogen and orthophosphate.

7.4.3.1 Salinity effect on ammonium adsorption

In the ammonium adsorption experiments, five different concentrations of artificial sea water were prepared using salinities of 2, 5, 10, 15, 20 and 25 parts per thousand (ppt). Concentrations of ammonium used were 2, 4, 6 and 10 mg/l NH_4^+, which are in the typical range of natural estuarine waters (Hou et al., 2003; Abdulgawad, 2010). The salinity effect on the ammonium adsorption can be summarized in two ways:

(1) Salinity effect on the adsorption capacity

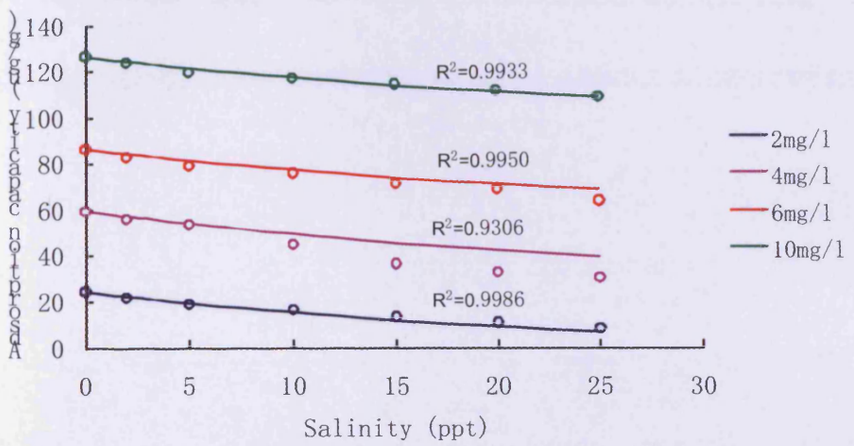

Figure 7-10 Ammonium adsorption for various salinities

Different ammonium adsorption quantities changing with salinity at four initial concentrations of 2, 4, 6 and 10 mg/l are plotted in Figure 7-10. A general equation is derived from the graph as follows:

$$q = q_0 + 0.0144 C_{SAL}^{\ 2} - 1.06 C_{SAL} \tag{7-17}$$

where q_0 is the ammonium adsorption (μg/g) in fresh water and C_{SAL} is the salinity level (ppt).

(2) Salinity effect on the partition coefficient

The partition coefficients, derived from the regression of the linear adsorption

isotherm (Figure 7-2) using the initial ammonium concentrations at 2, 4, 6 and 10 mg/l NH_4^+, respectively, changed with different salinity, and these changes are plotted in figure 7-10. A general equation is also derived as shown in Equation (7-18).

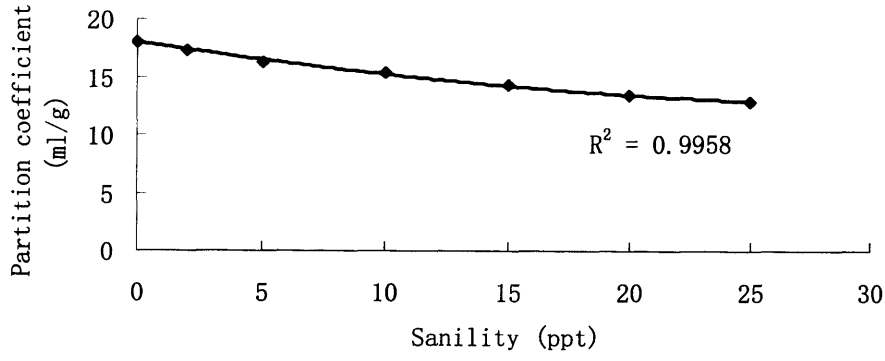

Figure 7-11 Ammonium partition coefficient for various salinities

$$k = k_0 + 0.0048C_{SAL}^{\ 2} - 0.3223C_{SAL} \tag{7-18}$$

where k_0 is the ammonium partition coefficient (ml/g) in fresh water and C_{SAL} is the salinity level (ppt).

7.4.3.2 Salinity effect on phosphorus adsorption

The phosphorus adsorption experiments were conducted for five different concentrations of artificial sea water, using salinities of 1, 2, 5, 10, 20 and 35 parts per thousand (ppt). Concentrations of orthophosphate used were 0.4, 0.6, 0.8 and 1.0 mg/l, which are in the typical range found in natural estuarine waters (Chao et al. 2006). The salinity effect on the phosphorus adsorption can be summarized in the following two ways:

(1) Salinity effect on the adsorption capacity

Different phosphorus adsorption quantities changing with salinity at four initial concentrations of 0.4, 0.6, 0.8 and 1.0 mg/l are plotted in figure 7-12. A general equation is derived from the graph as follows:

$$q = q_0 + 0.0016C_{SAL}^{\ 2} - 0.1655C_{SAL} \tag{7-19}$$

where q_0 is the phosphorus adsorption (μg/g) in fresh water and C_{SAL} is the salinity level (ppt).

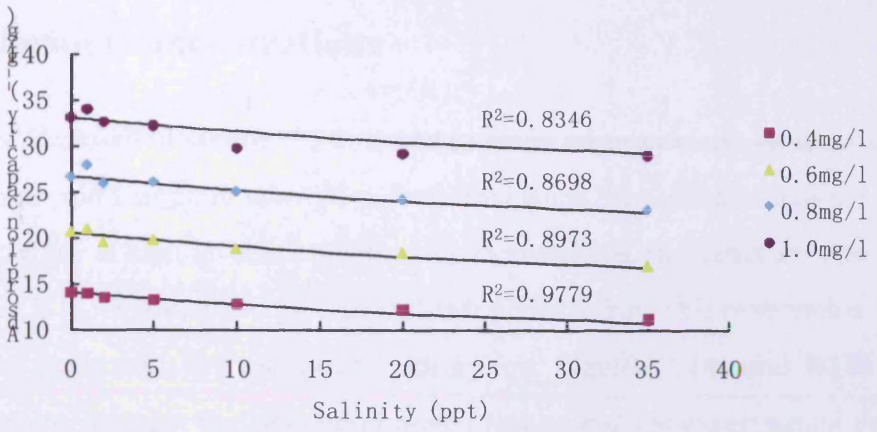

Figure 7-12 Phosphorus adsorption for various salinities

(2) Salinity effect on the partition coefficient

Different partition coefficients changing with salinity (derived in the same way as that for ammonium) are plotted in figure 7-13. A general equation is also derived as shown in equation (7-20).

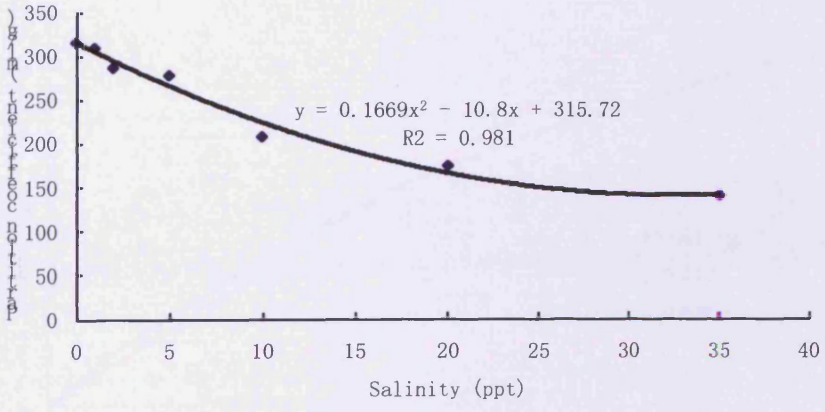

Figure 7-13 Phosphorus partition coefficient for various salinities

$$k = k_0 + 0.1677 C_{SAL}^{\ 2} - 10.828 C_{SAL} \qquad (7\text{-}20)$$

where k_0 is the phosphorus partition coefficient (ml/g) in fresh water and C_{SAL} is the salinity level (ppt).

7.5 Discussion

7.5.1 Sediment adsorption isotherms for different equilibrium concentrations

As discussed in section 7.3.3, the ammonium adsorption can be described by both linear and Langmuir adsorption isotherms when the concentrations are below 10mg/l, while at high level of ammonium concentrations, the Langmuir adsorption isotherm is more suitable to give an accurate presentation. This observation is also found to agree with the phosphorus adsorption. Figures 7-14a and 7-14b show comparisons between the adsorption model results and the experimental data for dissolved and particulate concentrations of phosphorus. Although the experimental data for phosphorus is not enough to lead to a clear conclusion, the tendency of the data can reveal that the linear adsorption isotherm can be used to fit the data at concentrations of less than 5mg/l, and Langmuir adsorption isotherm fit a wider range of experimental data.

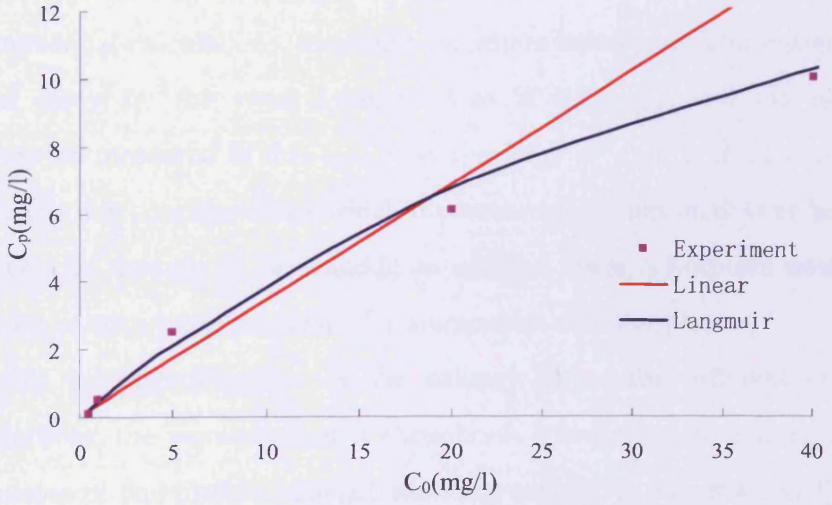

Figure 7-14a Concentration of particulate phosphorus versus initial concentration at equilibrium for field data experiment

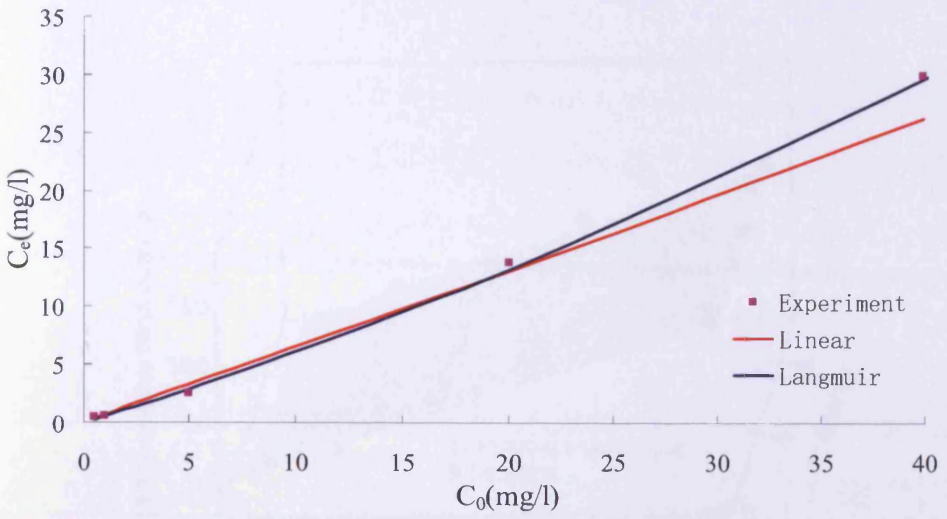

Figure 7-14b Concentration of dissolved phosphorus versus initial concentration at equilibrium for field data experiment

The linear adsorption model is simpler than the Langmuir adsorption model, as it only needs one parameter to be determined from the experimental data, which might avoid introducing more error in regression analysis. Also, the calculation for dissolved and particulate concentrations is not as complex as that of the Langmuir adsorption model. This advantage can make linear adsorption model more efficient in the numerical calculations. Since the maximum ammonium concentration found in field study for the river Loughor area is 4.25mg/l, and the phosphorus concentration measured in this area is in the order of μg/l, both of which can be classified as low concentrations which the linear adsorption model can be matched. It is therefore thought to be suitable to use the linear adsorption model in the simulation of adsorption processes for ammonium and phosphorus.

To clarify the quantification of the salinity effect for different equilibrium concentrations, the ammonium and phosphorus adsorption can also be expressed as a function of equilibrium concentration and salinity, in which X and Y represent the nutrient (ammonium or orthophosphate) equilibrium concentration and salinity, respectively, and Z represents the nutrient adsorption on the suspended sediment. The formulation contours are shown as follows.

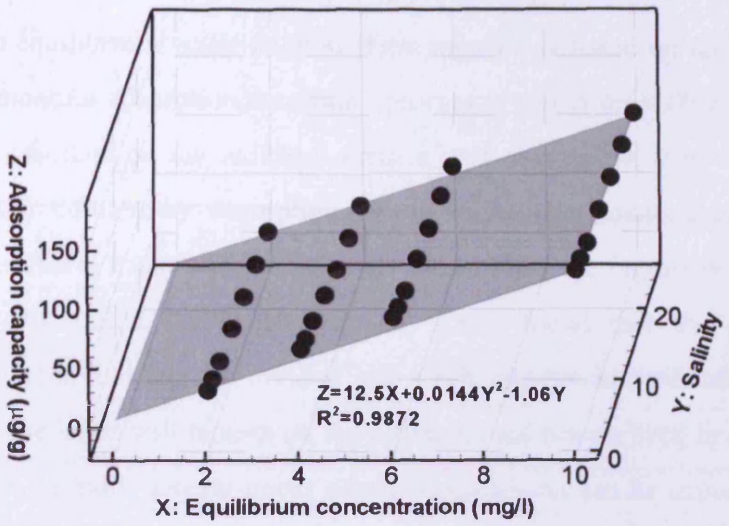

Figure 7-15 Ammonium adsorption contour

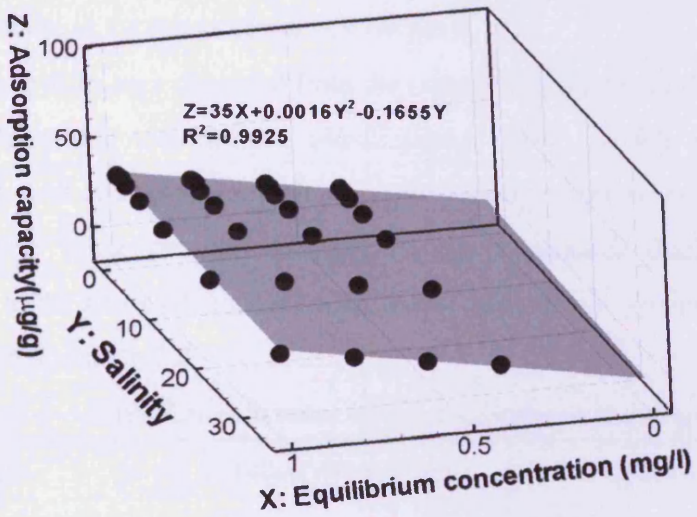

Figure 7-16 Orthophosphate adsorption contour

7.5.2 Fixed ammonium on sediment

Equation (7-1) described a linear adsorption isotherm, where the amount of

the ammonium adsorbed on the sediment q_e (mg/g) can be expressed as the product of the partition coefficient K_d (l/g) and the equilibrium concentration C_e (mg/l) in an equilibrium water column. This equation is based on an assumption that the ammonium adsorption/desorption process is totally reversible, i.e., all the ammonium adsorbed on the sediment surface is exchangeable; they can go back into the water column by desorption. Some researchers found that the linear adsorption isotherm has a positive intercept when doing the regression, and some researchers (Rosenfeld, 1979; Hou et. al, 2003) found that the ammonium adsorbed by sediment can be divided into exchangeable ammonium and fixed ammonium, the latter will remain on the sediment and not go back into the water by desorption. A more general linear adsorption isotherm can be expressed based on equation (7-21).

$$q_e = K_d C_e + \mathrm{q} \tag{7-21}$$

where q is the amount of fixed ammonium (mg/g) which is represented by the positive intercept of the linear adsorption isotherm.

There is a difference observed from the comparison figures of the ammonium adsorption/desorption experiments (Abdulgawad, 2010), which means that a certain amount of ammonium remained on the sediment surface instead of going back into the water column through desorption process. Such amount is comparable to the non-exchangeable ammonium or fixed ammonium. The details are summarized in table 7-4.

Table 7-4 Ammonium difference between adsorption and desorption

Sediment type	Distilled water (mg/g)	Artificial sea water (mg/g) (salinity = 35ppt)
Montmorillonite	13.29	10.07
Kaolinite	10.71	7.92
Find sand	4.79	4.36
Coarse sand	3.00	2.64

It can be seen that after an adsorption/desorption cycle, the amount of

ammonium fixed on the sediment surface decreases with the sediment size increasing, and the amount is higher in fresh water (distilled water) than in saline water (artificial sea water).

7.6 Summary

In this chapter, two types of adsorption models have been discussed. Theoretical formats of dissolved and particulate concentrations derived from these models have been compared with the experimental data which were published in the thesis of Abdulgawad, (2010), and the results showed that both linear and Langmuir adsorption model can well describe the ammonium and orthophosphate adsorption processes, with the former being recommended to be used at low nutrients concentrations for its simplicity and efficiency, and the latter being recommended to be used at high nutrient concentrations for its accuracy. The salinity effects on the adsorption processes of ammonium and orthophosphate have been quantified for field sediments. Other factors, such as equilibrium concentration and particle size in sediment have also been discussed for their influences on the adsorption processes.

Chapter 8

Simulations of hydrodynamic and water quality processes in River Loughor Estuary

8.1 Introduction

The River Loughor sources from an underground lake in the Black Mountains, in Carmarthenshire, south west Wales. It flows southwards to the Loughor Estuary, and is often also known as as Burry Inlet or Burry Estuary, covering the region to the west of the road and rail bridges at Loughor, where the waterway turns abruptly from a southerly direction to a westerly direction, towards Carmarthen Bay (see Figure 8-1).

The Loughor Estuary is a shallow and muddy estuary, with strong tidal streams and frequently shifting sandbanks. At high water on an average spring tide, the estuarine area covered by the tide is approximately 45 km^2, with a width of 6.6 km at the widest section. At low water, the main channel of the River Loughor winds across the bed of the estuary through an expanse of sandflats. The estuary has a tidal range of around 8 m, and the tidal influence extends upstream to Pontardulais, a distance from the estuary mouth of 16 km or so. The tidal current is up to 1.5m/s during peak spring tides in the deepest channels (DTI 2004). The sediment grain size generally increases from the head to the mouth of the estuary and varies from mud to medium-sized sand. The southern shore has the largest continuous area of saltmarsh in Wales (22 km^2), which supports one of the largest cockle fisheries in Britain. Large numbers of over wintering wildfowl and waders feed in the intertidal and saltmarsh area (Craig et al. 2007). This area was designated both as Special Protection Area (SPA) for the wildlife and a Sensitive Area for Eutrophic (SAE) under the Urban Waste Water Treatment Directive in

2001.

The Loughor Estuary suffers from eutrophication, which causes serious changes in the stability and diversity of the ecosystem, such as the decrease of fish populations and species. Eutrophication can also bring negative economical impacts on tourism and aquaculture industries (Bockelmann-Evans et al. 2007). Therefore, there is an urgent need for a better understanding of the nutrient cycle in the estuary and to find out the best ways of nutrient removal.

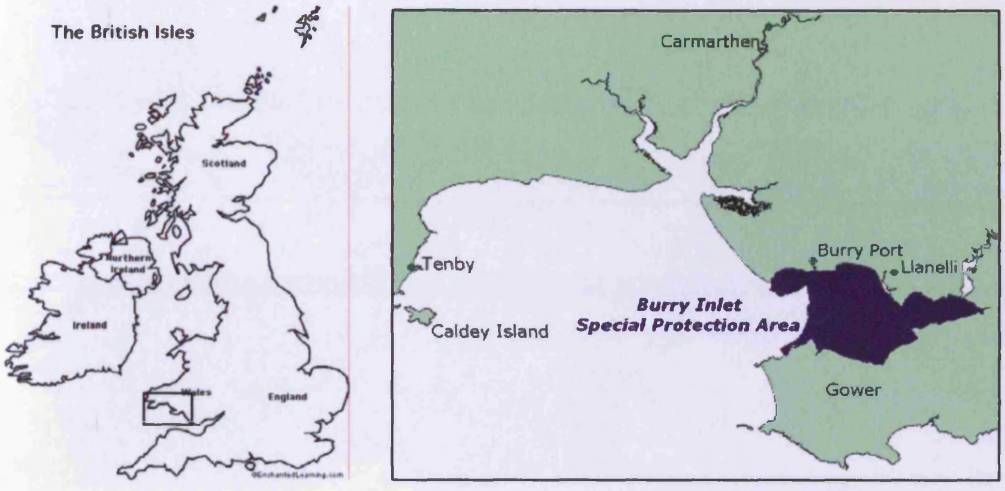

Figure 8-1 Location of the Loughor Estuary and Carmarthen Bay

Nutrients (nitrogen and phosphorus) enter the water body mainly through two routes: diffuse sources from upstream river catchments and discharges from the nearby sewage treatment works (STWs).

All the river discharges within the Burry Inlet catchment area have been plotted in ArcMap and grouped by the hydrological sub-catchment areas in Figure 8-2. Each of the hydrological sub-catchment has been plotted with an Environment Agency Wales (EAW) water quality sampling point at its outlet, from where water runoff and nutrients runoff are introduced to the estuary.

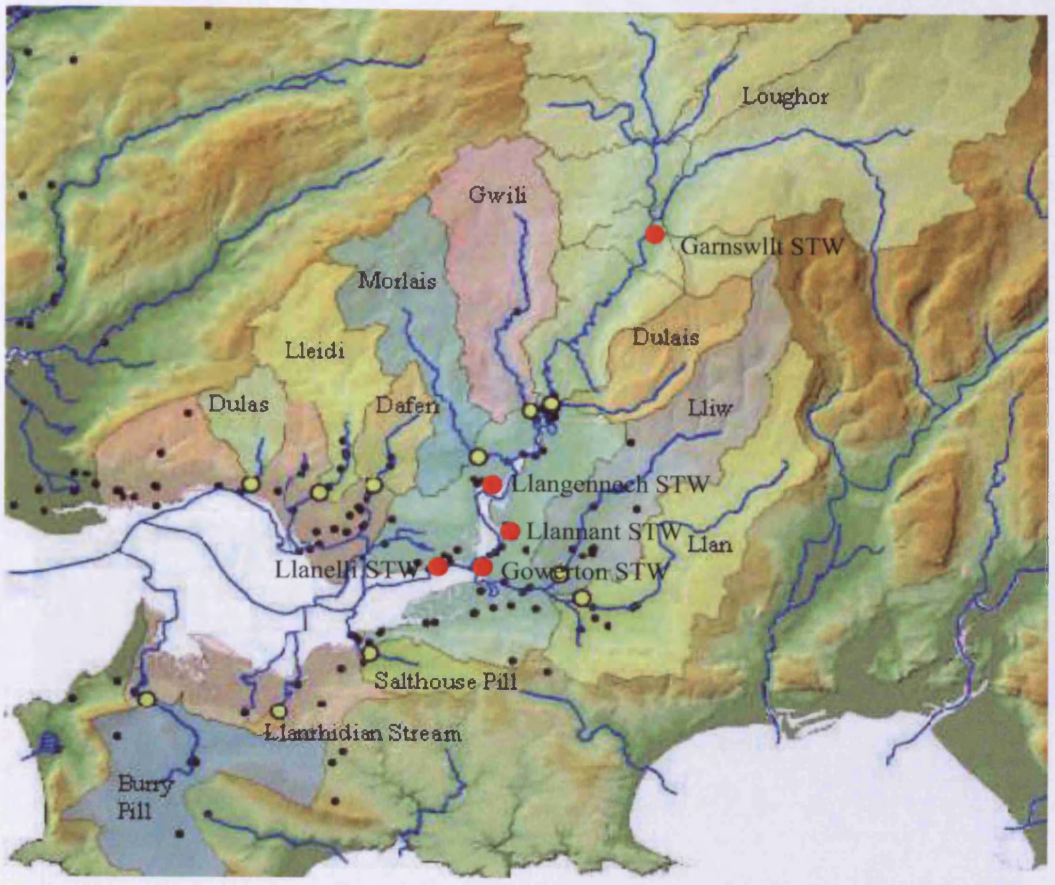

Figure 8-2 Hydrological catchment areas, river discharges (blue lines), STWs (red points) and key sample points (yellow spots) (Edwards, 2007)

8.2 Data processing

8.2.1 Topography and bathymetry data

The topography of the river Loughor area has been obtained from LiDAR (**Li**ght **D**etection **A**nd **R**anging) data provided by Environment Agency Wales. The data are supplied in an ASCII raster file format, which is a simple format that can be easily converted into other formats for various applications. The LiDAR data have been classified and filtered to produce Digital Terrain Models (DTM) from the Digital Surface Models (DSM). The Digital Surface Models contain objects

such as buildings and vegetation, as well as open ground, while Digital Terrain Models ("bare-earth" elevation models) contain data that have been passed through classification and filtering routines that attempt to strip out vegetation and buildings from LiDAR derived surface models. This produces more accurate and representative bare-earth DTMs for hydrodynamic simulations.

The LiDAR data include a series of data files at 2 m resolution in 2 km × 2 km tiles. These data files are imported and processed by ArcGIS Spatial Analyst software, MapInfo GIS, to produce the topography of the river Loughor as shown in Figure 8-3, where the black area indicates regions where no data exist.

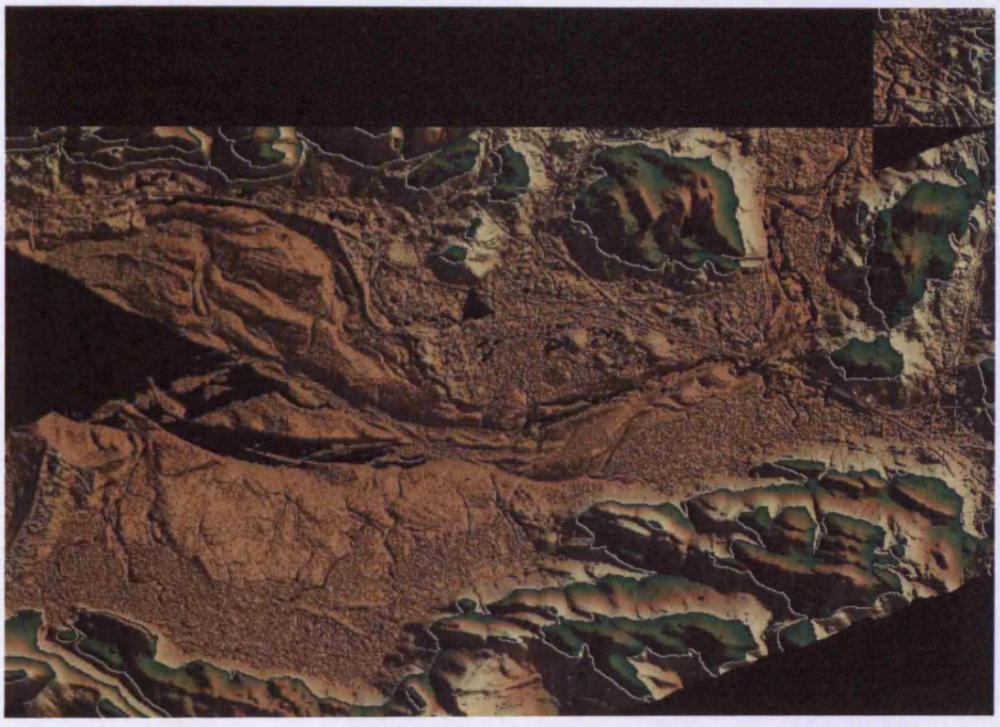

Figure 8-3 LiDAR Topography of river Loughor area

From Figure 8-3, it is known that LiDAR data can provide most of the topography in the Loughor area, except the main river channel, which is under water and cannot be detected by airborne LiDAR. The Admiralty Chart map (No. 1167) for Burry Inlet has been used to extract the information complementary to that provided by LiDAR. The map was published by the UKHO in 2001, which was the second edition with a scale of 1:25000. The overall bathymetry data have

been obtained by integrating the map and LiDAR information. It should be noted that the Admiralty Chart data are based on Chart Datum (CD), which approximately corresponds to the lowest astronomical tidal level, while the LiDAR data are based on Ordnance Datum (OD), which is defined as Mean Sea Level (MSL) at Newlyn in Cornwall, between 1915 and 1921. Therefore, a transformation is needed to unify the data to the same datum. The elevation of CD relative to OD in the UK is provided by the National Oceanography Centre (NOC) on their website (http://www.pol.ac.uk/ntslf/tides/datum.html). Figure 8-4 shows the final bathymetry used in this simulation exercise, which has a horizontal resolution of 50 m, and the bed elevation is relative to Ordnance Datum.

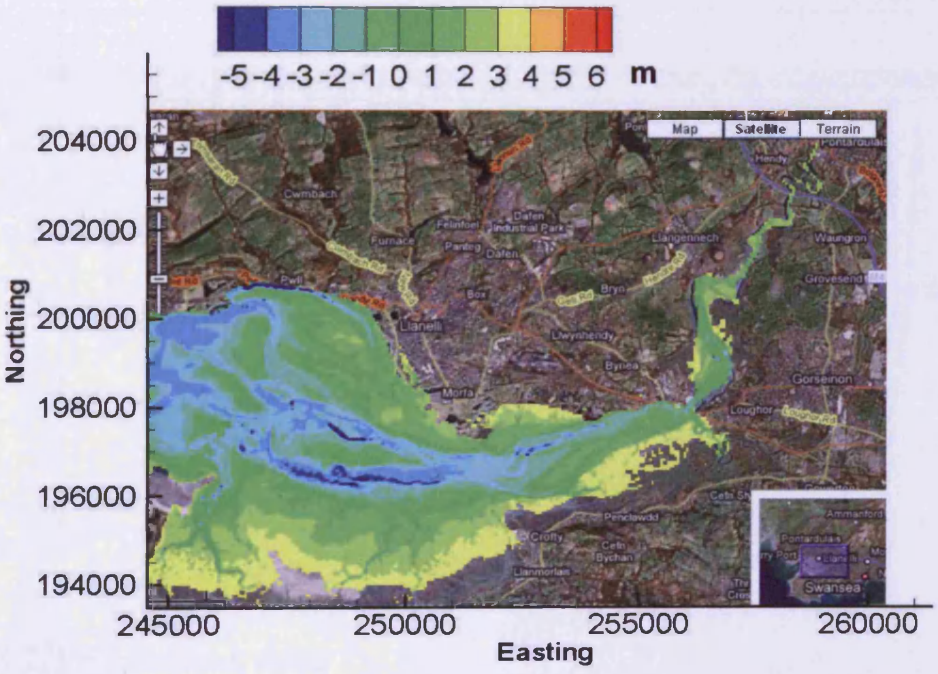

Figure 8-4 Bathymetry of the River Loughor and its estuary

8.2.2 Tidal level data

The tide measured at Burry Port is used to define the water surface level variations at the open boundary, which is the driving force for the water motion

inside the estuary. The Admiralty Chart map gives the tidal levels between 8.6m and 1.1m for spring tides, and between 6.6m and 3.0m for neap tides, respectively, relative to the Chart Datum, which is 4.70m below Ordnance Datum. Since the tide at Burry Port is an astronomic tide, which can be accurately predicted based on long term statistics, the UKHO also provide an online tidal prediction tool on their website (http://easytide.ukho.gov.uk/EasyTide/EasyTide/index.aspx), which offers an accurate and updated source of information for the tidal level data in the numerical simulations. Figure 8-5 shows a typical tidal period predicted by UKHO for Burry Inlet, which covers a cycle of evolutions between spring tide, neap tide and mid-tide.

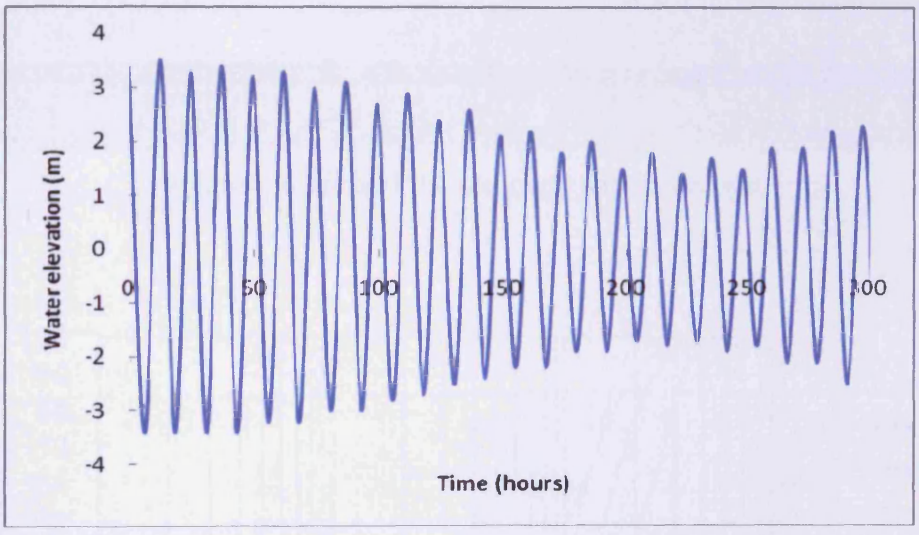

Figure 8-5 Water elevations at Burry Port

8.2.3 Sediment data

Sediments in the Loughor Estuary consist mainly of mobile fine and medium sands. This study has considered the sediment data at four sites as shown in Figure 8-6. Field sampling and laboratory analysis of the sediment particle size distribution have been conducted for sites 1b and site 2, and published data have been obtained for sites A1 and A2 (Collins et al. 1998). Figure 8-7 shows the sediment compositions at these four sites.

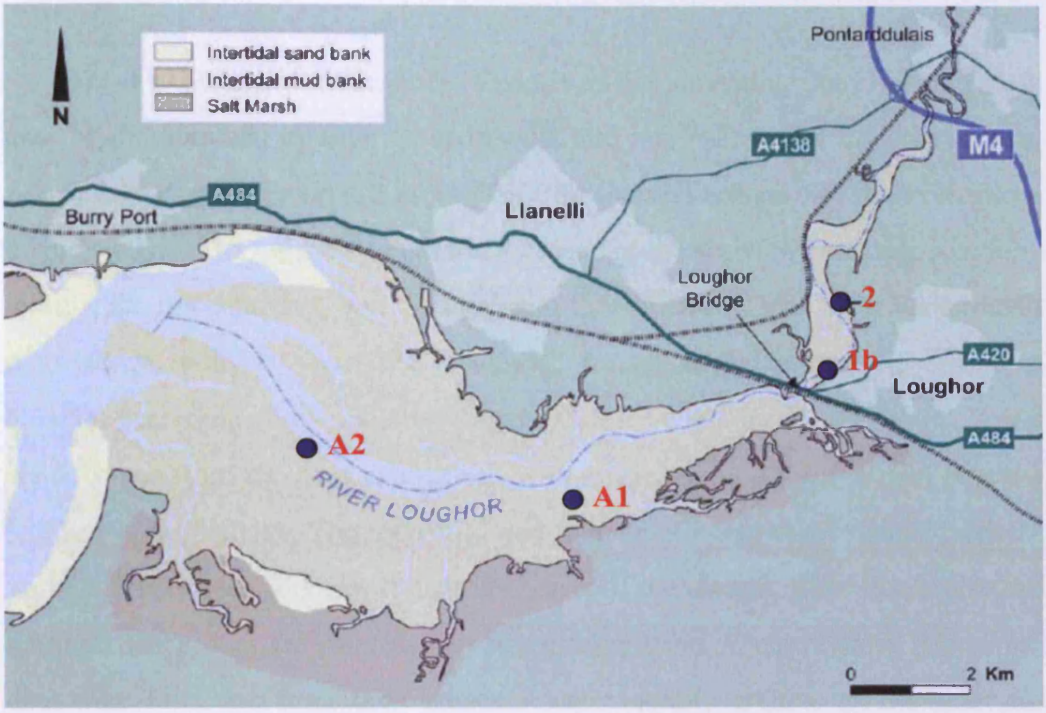

Figure 8-6 Sites of the sediment data collection

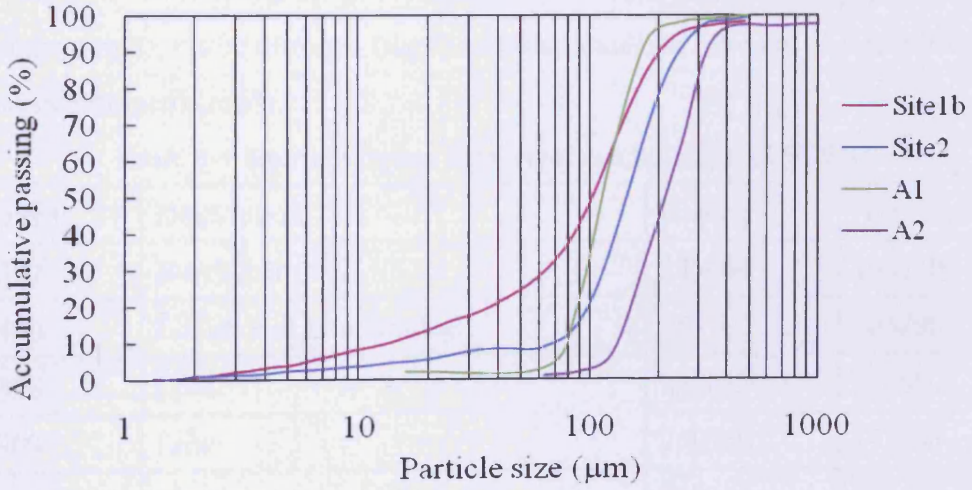

Figure 8-7 Sediment particle size distributions at four sites

8.3 Model setup

The TVD-MacCormack model was set up for simulating the tidal flow field and the distributions of salinity, sediments and nutrients in the Loughor estuary from Burry Port to the tidal limit at Pontardulais road bridge. The tidal elevations predicted by UKHO at Burry Port were chosen as the seaward boundary condition to drive the tidal currents, and the upstream flow boundary was set at Pontardulais road bridge, with the flow rate evaluated for an annual average discharge of $5.6m^3/s$, according to a report by Countryside Council for Wales (2005). Fresh water comes from the river catchments with nutrients due to agricultural land use within sub-catchments. The industrial and municipal waste water comes from the Sewage Treatment Works built near the banks of the estuary. Flow discharges and nutrients loads data are provided by the Environment Agency Wales. Moreover, data were retrieved from the Agency's water quality archive (WIMS) for the period between April 2000 and March 2005 for the following determinants at the discharge locations and main-river sample points (as shown in Figure 8-2): flow (m^3/sec), dissolved inorganic phosphorus (mg/l), ammonia nitrogen (mg/l), nitrate nitrogen (mg/l), nitrite nitrogen (mg/l) and total oxidized nitrogen (nitrate nitrogen + nitrite nitrogen) (mg/l).

Table 8-1 Nutrient inputs from river catchments and STWs

Site No.	Description	Easting	Northing
30392	Burry Pill	245060	193130
30406	Loughor at Pontardulais	258760	203890
30408	Llan	259812	196880
30409	Lliw	259060	197705
30410	Gwili	258040	203600
30461	Dulais	258800	203785
30470	Gowerton STW	256110	197900
30471	Llannant STW	257200	199500

30874	Dafen	252497	200380
72796	Llanelli STW	254600	197840
72799	Afon Morlais	256285	201945
72946	Salthouse Pill	254600	198740
72947	Dulas at pwll	248570	200870
72948	Llanrhidian Stream	249530	192715
75512	Lleidi	250900	200600
100333	Garnswllt STW	262100	209900
100345	Llangennech STW	256700	200900

The uniform grid size was set to 50m×50m, which was the same as the resolution of the digitized topography. The hydrodynamic model was firstly solved separately, followed by simulations of water quality processes, which used the flow field results from the hydrodynamic model. The time step was set to 4.5s for the hydrodynamic model, based on the maximum shallow wave speed across the estuary, and 15s for the water quality model based on the maximum flow velocity in the estuary.

8.4 Model calibration and verification

The numerical model needs to be calibrated in order to determine the computational parameters that produce the best possible match between model predictions and measured data. In this study, the water level was calibrated against published data at sites S_2m and S_3m, and the current speeds were calibrated against published data at sites A1 and A2 (Figure 8-8). After calibration the hydrodynamic model was validated against measured data at site 1b for water levels, and the Admiralty Chart data at site B for current speeds. The sediment transport and water quality constituent predictions were calibrated against measured data at sites 1a and 1b.

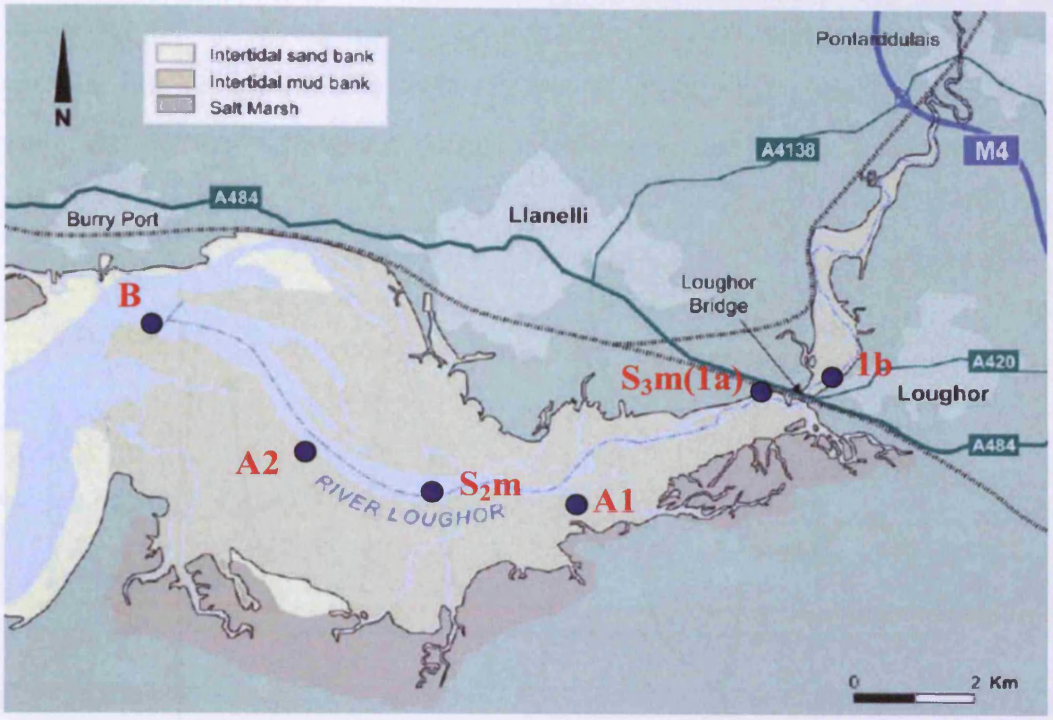

Figure 8-8 Location of the calibration and validation sites

8.4.1 Hydrodynamic model

The main parameter used for the hydrodynamic calibration was the bed roughness. In the Colebrook-White formula, the bed roughness is represented as an equivalent roughness height k_s, which has been calibrated by trial and error via a number of simulations. The best results were obtained with the roughness height taken to be 40mm in this model. The eddy viscosity coefficient c_e is set as 1.5, and the minimum depth for flooding/drying calculation is set at 0.05m. The computation starts with still water at the mean water level acorss the domain, and calculates for 4 tidal cycles before calibration begins. Water elevations were compared at two sites: Llaneli (S_2m) and Loughor bridge (S_3m), for spring tide on the 20th August 1978, and neap tide on the 8th May 1978. The measured data were obtained from a technical report (No. 261) of MAFF Commission (Swarbrick, 1984). Figures 8-9 to 8-12 show that the model predicted water elevations to give good agreement with the measured data. The current speeds were calibrated against published data

at site A1 for the spring tide on the 4th February 1977, and at site A2 for the medium tide on the 5th July 1981 (Collins et al. 1998). Figures 8-13 and 8-14 show that the model predicted current speeds compared well with the measured data.

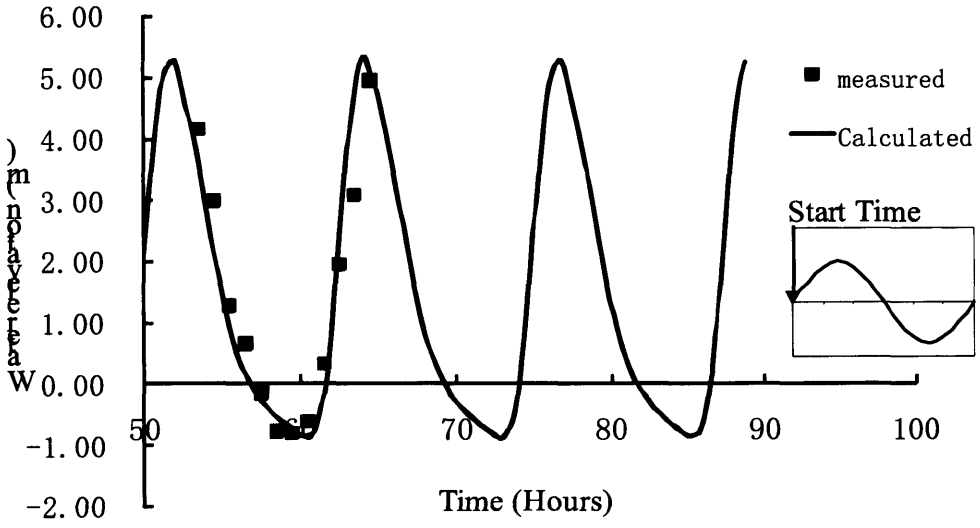

Figure 8-9 Calibration of predicted water elevations at Llanelli for spring tide

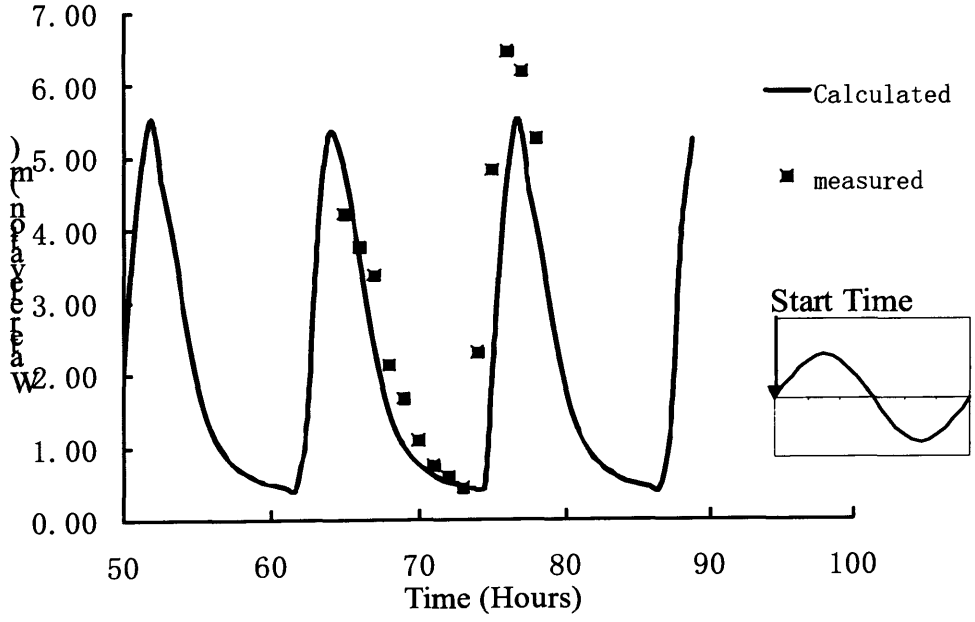

Figure 8-10 Calibration of predicted water elevations at Loughor Bridge for spring tide

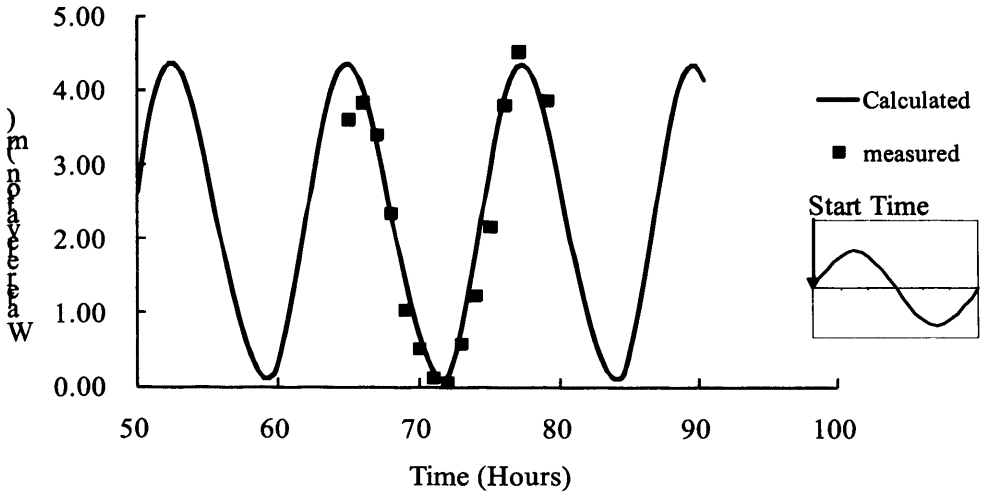

Figure 8-11 Calibration of predicted water elevations at Llanelli for neap tide

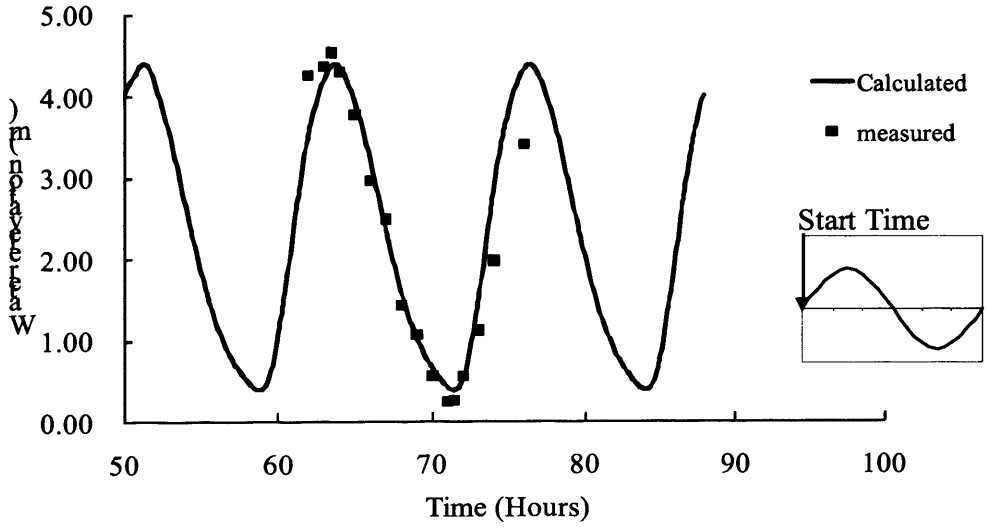

Figure 8-12 Calibration of predicted water elevations at Loughor Bridge for neap tide

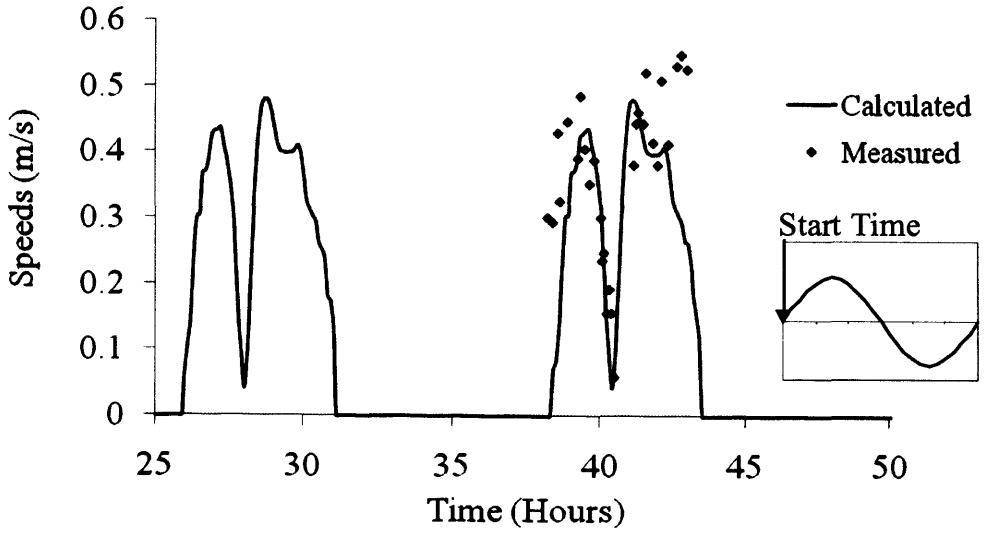

Figure 8-13 Calibration of predicted current speeds at site A1 for spring tide

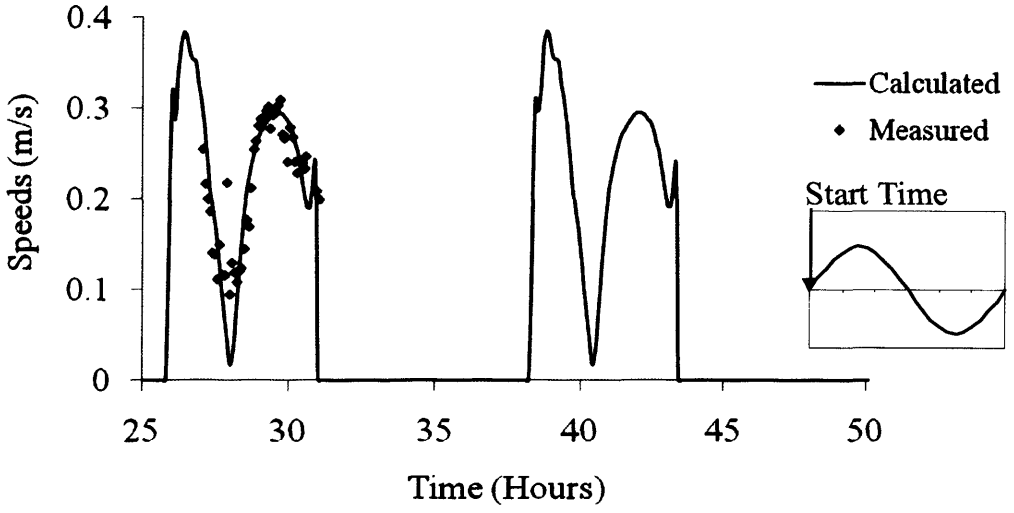

Figure 8-14 Calibration of predicted current speeds at site A2 for medium tide

After calibration of the hydrodynamic model, the model was validated at site 1b for water elevations against observed data, and at site B for the current speeds against the Admiralty Chart data. The water elevation data were collected from the field survey on 2nd of June, 2008, with the tidal range at Burry Inlet being from 1.4m at low tide to 8.2m at high tide (relative to Chart Datum). The data were measured at one hour interval during the time of inundation. Figure 8-15 shows a

comparison between the model predicted water elevations and the field measured water elevations, where good agreement can be observed between both sets of results and with the difference being less than 5%. However, due to the restrictions of the field survey, the measured data did not cover the whole tidal cycle. Thus another validation of the model, the time for the tidal current was undertaken to examine the performance of the calibrated model.

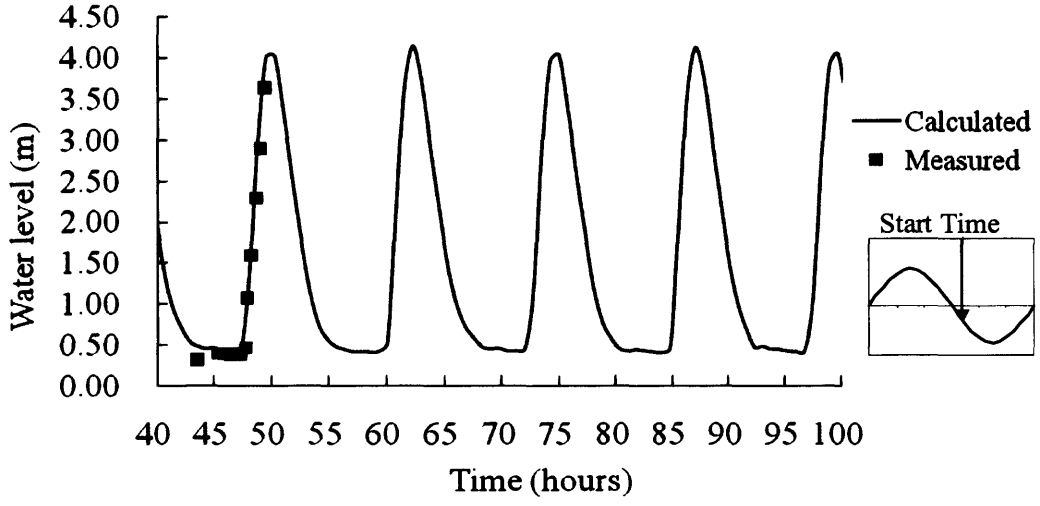

Figure 8-15 Validation of predicted water elevations at site 1b

Tidal currents data are more difficult to obtain than water levels in field surveys, and current speeds are prone to obstructions introduced in measurements. Moreover, the main channels were usually not easy to access. Therefore, the model predicted current speeds and directions were compared with the Admiralty Chart data at site B (Figure 8-16). Both the current directions and the current speeds were in good agreement with the measured data. The flow fields along the entire estuary for different tidal conditions are shown in Figures 17 and 18. Figure 8-17(a-d) show the predicted current speeds during a spring tidal cycle, and Figure 8-18(a-d) shows the predicted current speeds during a neap tidal cycle.

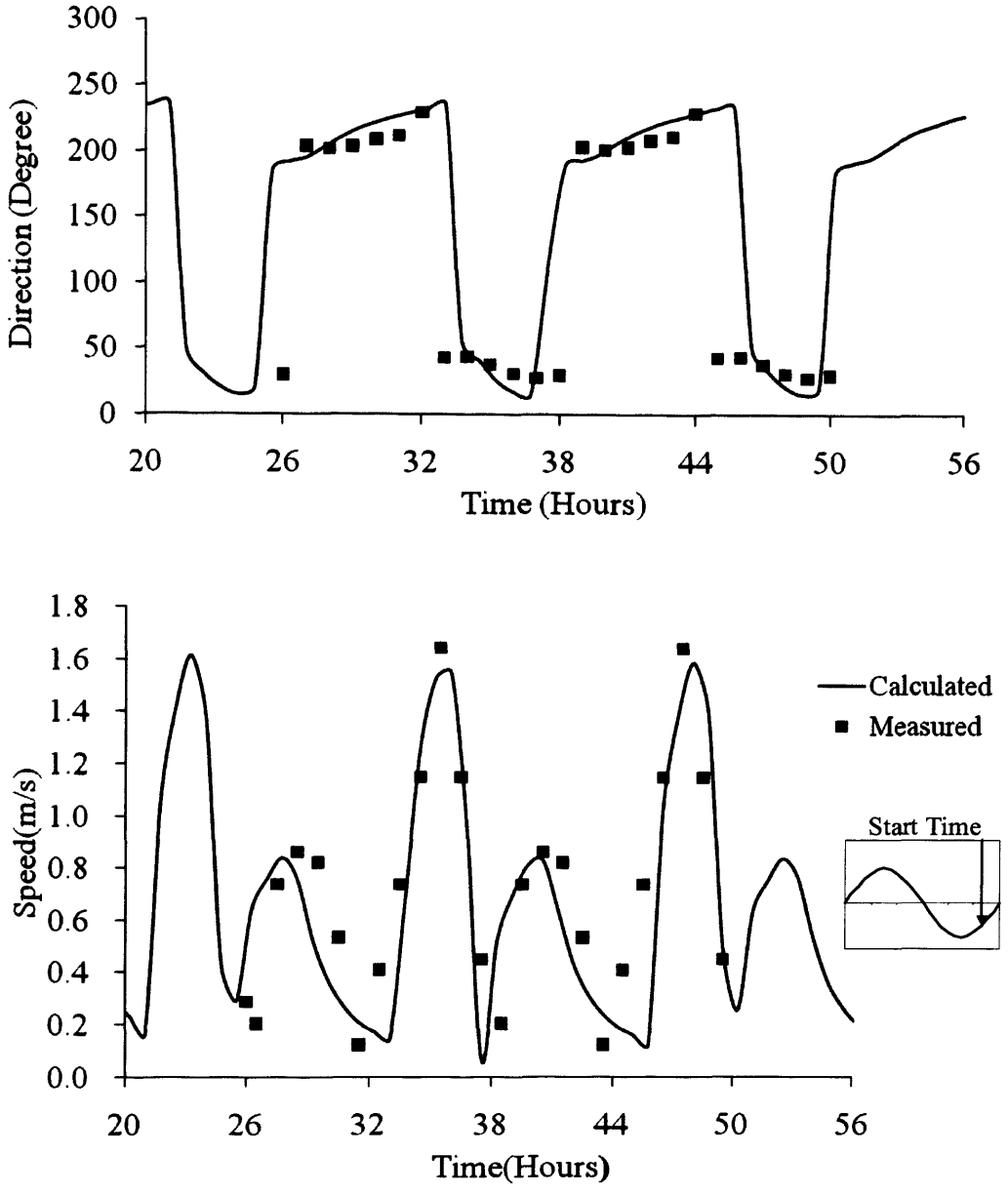

Figure 8-16 Comparison of measured and predicted current directions at site B during spring tide

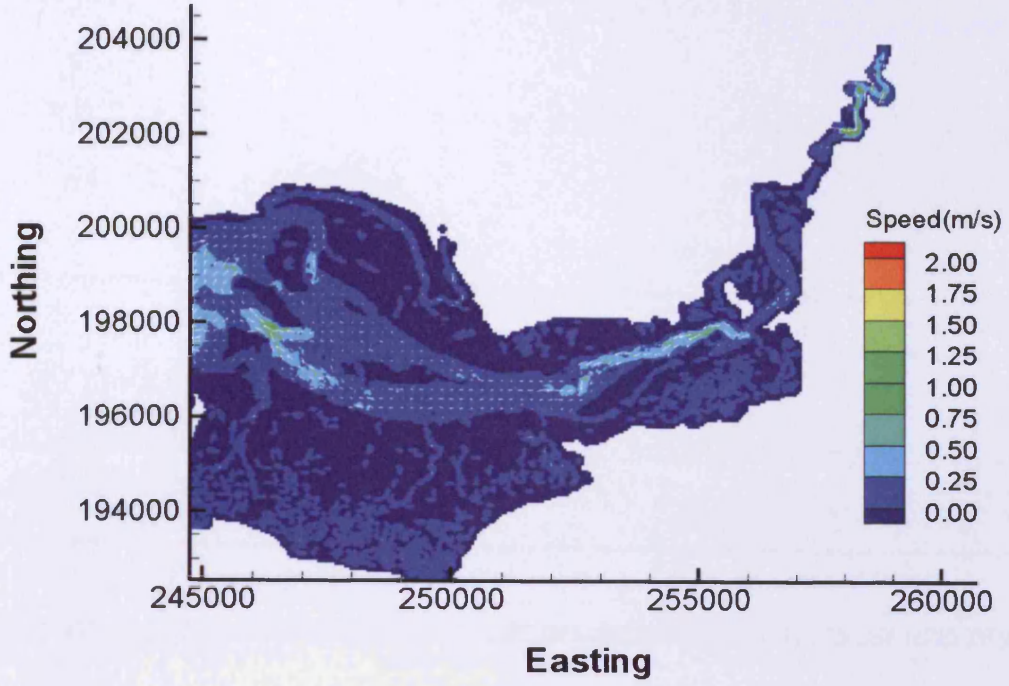

Figure 8-17a Predicted current speeds at low water for spring tide

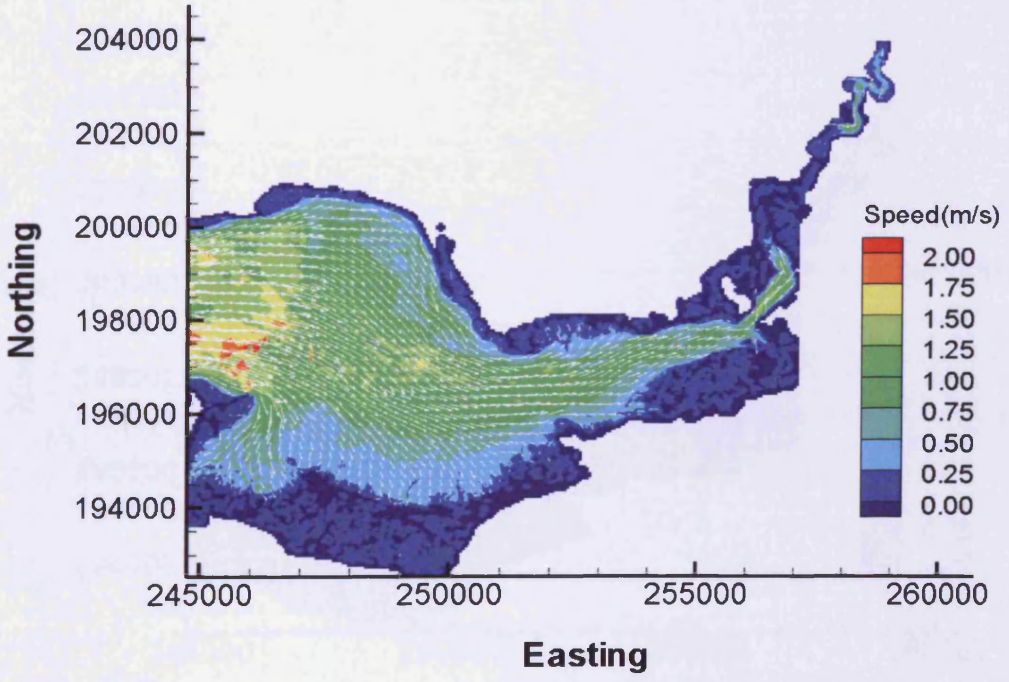

Figure 8-17b Predicted current speeds at mean flood for spring tide

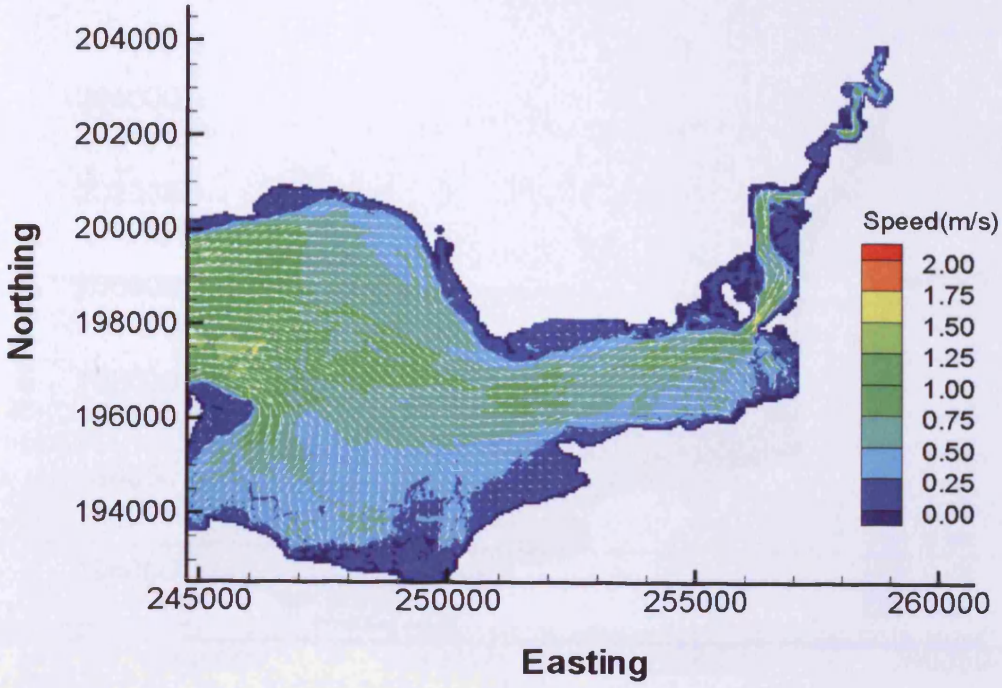

Figure 8-17c Predicted current speeds at high water for spring tide

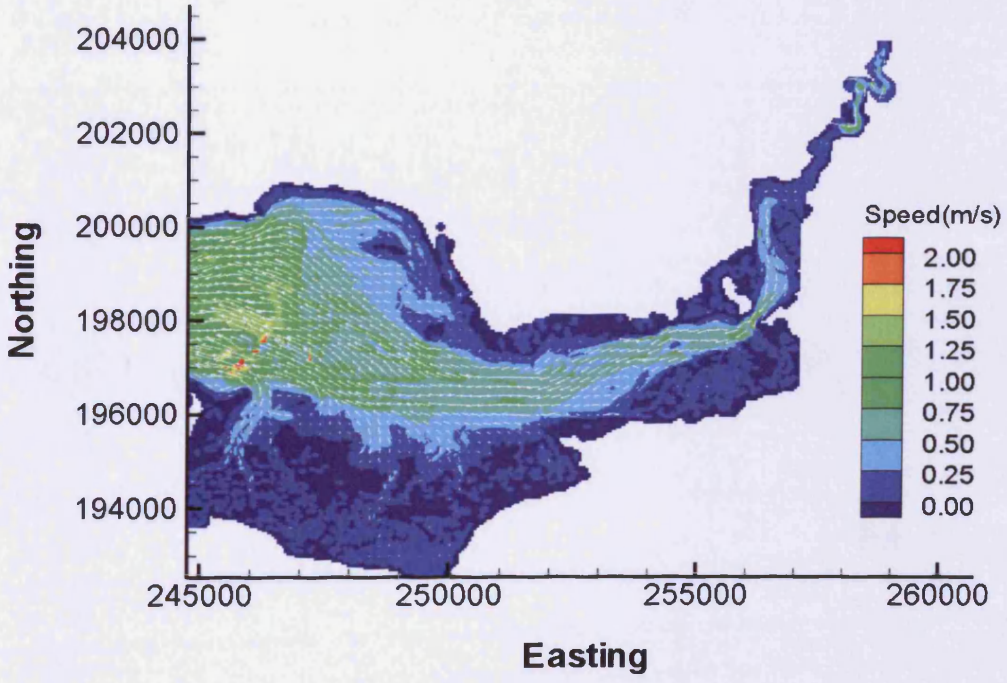

Figure 8-17d Predicted current speeds at mean ebb for spring tide

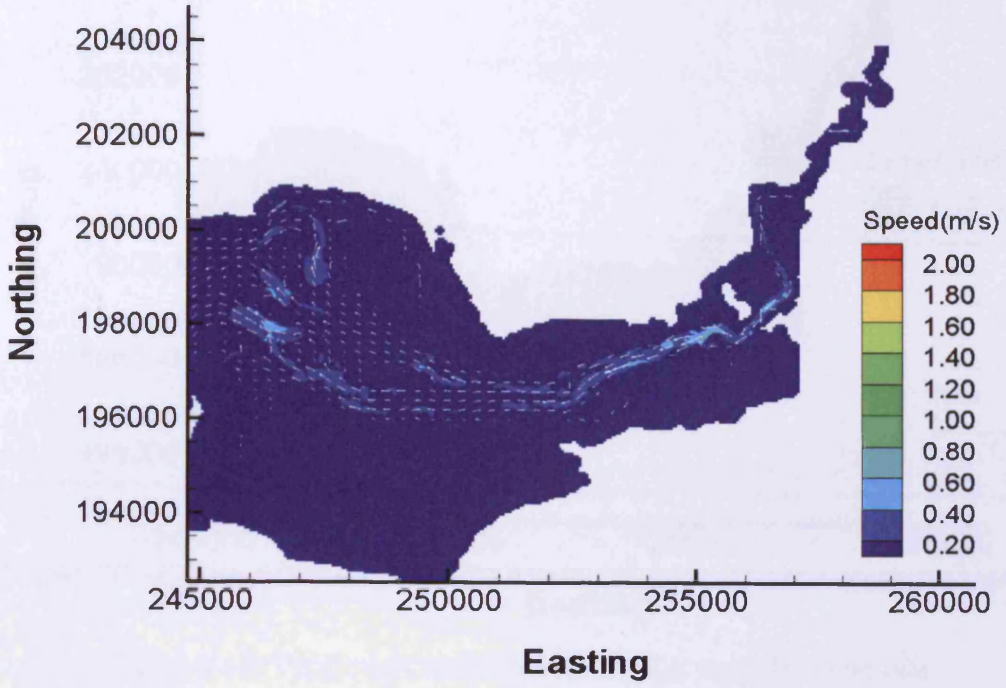

Figure 8-18a Predicted current speeds at low water for neap tide

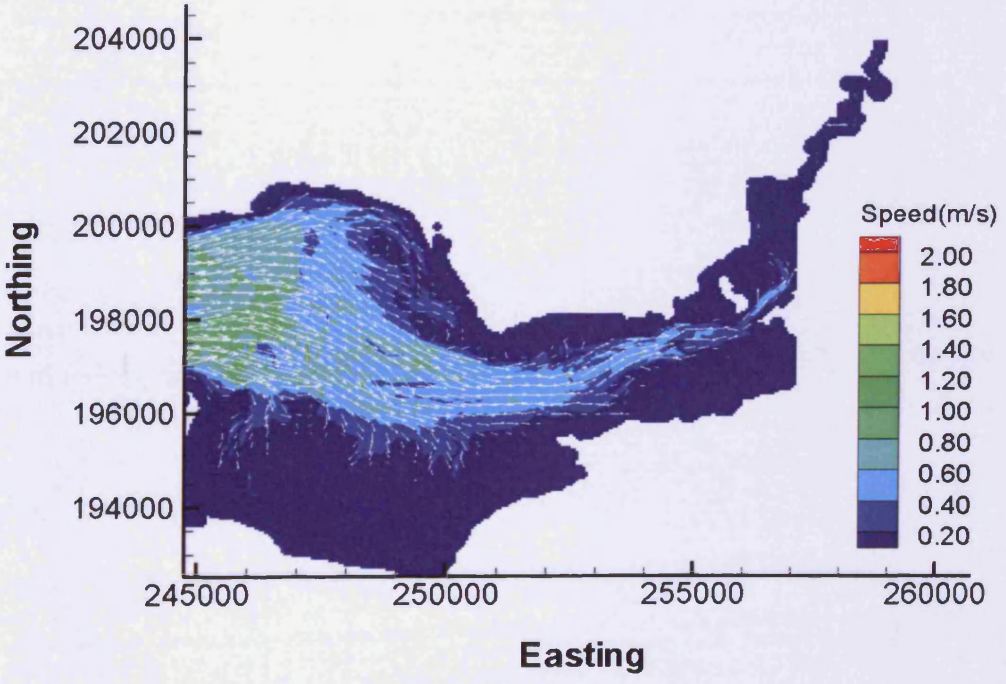

Figure 8-18b Predicted current speeds at mean flood for neap tide

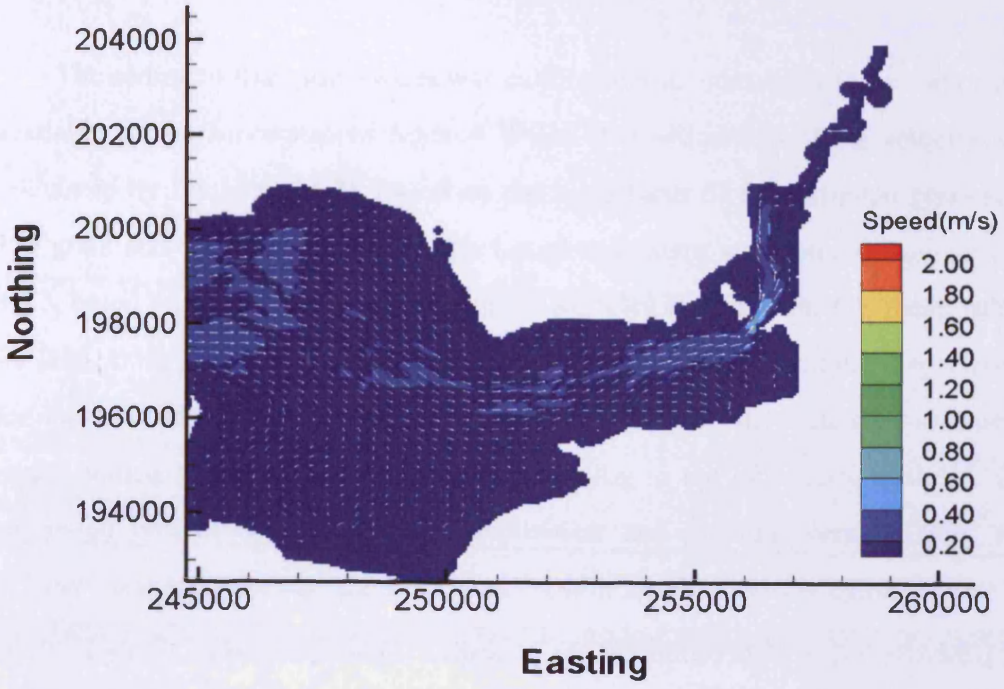

Figure 8-18c Predicted current speeds at high water for neap tide

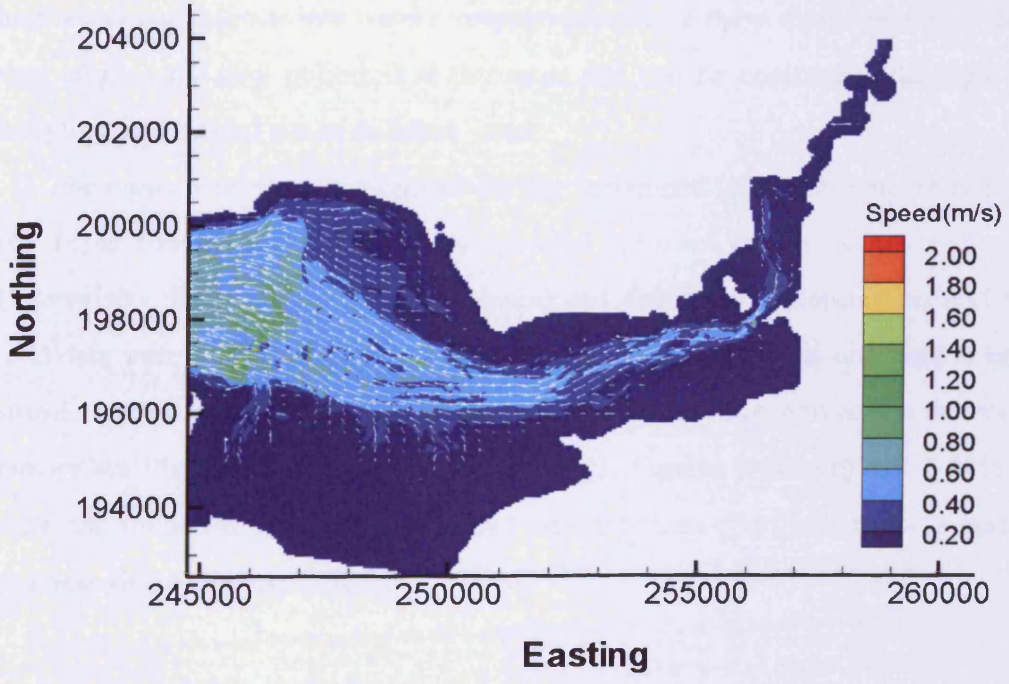

Figure 8-18d Predicted current speeds at mean ebb for neap tide

8.4.2 Sediment transport model

The sediment transport model was calibrated and validated against data made available by the Environment Agency Wales. The sediment settling velocity was calculated by Equation (2-3), based on the ingredients of the sediment grain size. The grain size of the sediments in the Loughor Estuary was derived from section 8.2.3, based on the analysis of the sediment samples at four sites. The mean values for D16, D50, D84 and D90 were 0.068, 0.121, 0.184 and 0.205mm, respectively, for the non-cohesive sediments. The average size for the cohesive sediments ranges varied from 0.005 to 0.063mm, according to the laboratory analysis. The calibrated critical shear stress for deposition and erosion were $0.1N/m^2$ and $0.5N/m^2$, respectively, and the empirical erosion coefficient was calibrated as 7.5 $\times 10^{-5}$ kg/m^2/s. The suspended sediment concentration data were provided by Environment Agency Wales, based on the analyses of the sediment samples collected at about hourly intervals from high tide to low tide, on 14th December 2007 (7.9m at high water and 2.1m at low water) and 13th March 2008 (7.9m at high water and 2.0m at low water), respectively. Since these tidal conditions were very similar, the data collected at the same site can be combined, although the sampling was carried out in different years.

The model was firstly calibrated for the suspended sediment concentration at site 1a, and then validated for the suspended sediment concentration at site 1b. Comparisons between the predicted suspended sediment concentrations and the field data were plotted in Figure 8-19(a-b). Good agreement was observed at both sites 1a and 1b. The distributions of suspended sediment transport across the entire estuary are illustrated in Figures 8-20 and 8-21. Figures 8-20(a-d) and 8-21(a-d) show the predicted suspended sediment concentration distributions for a spring and neap tide cycle respectively.

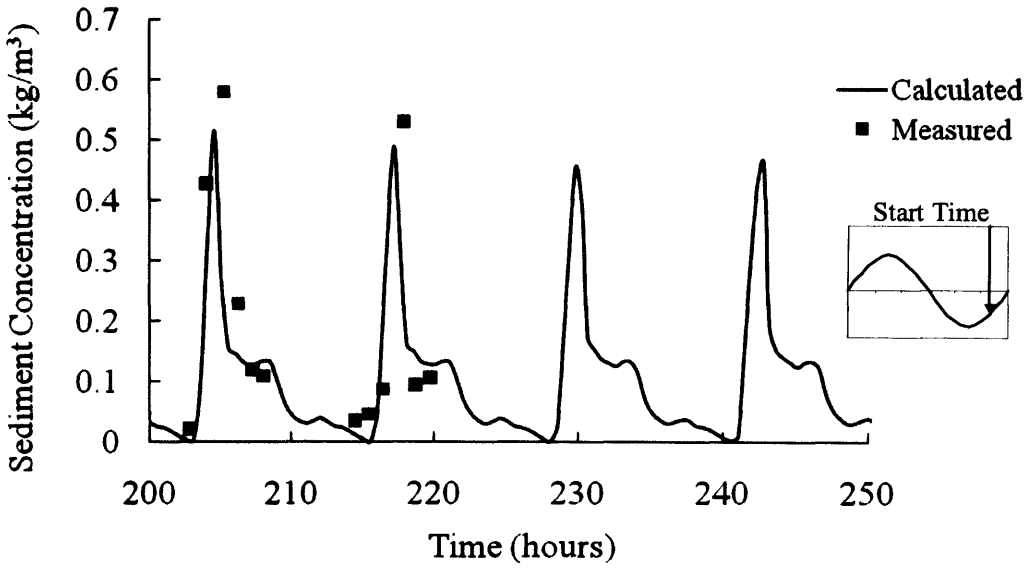

Figure 8-19a Calibration of predicted suspended sediment concentration at site 1a

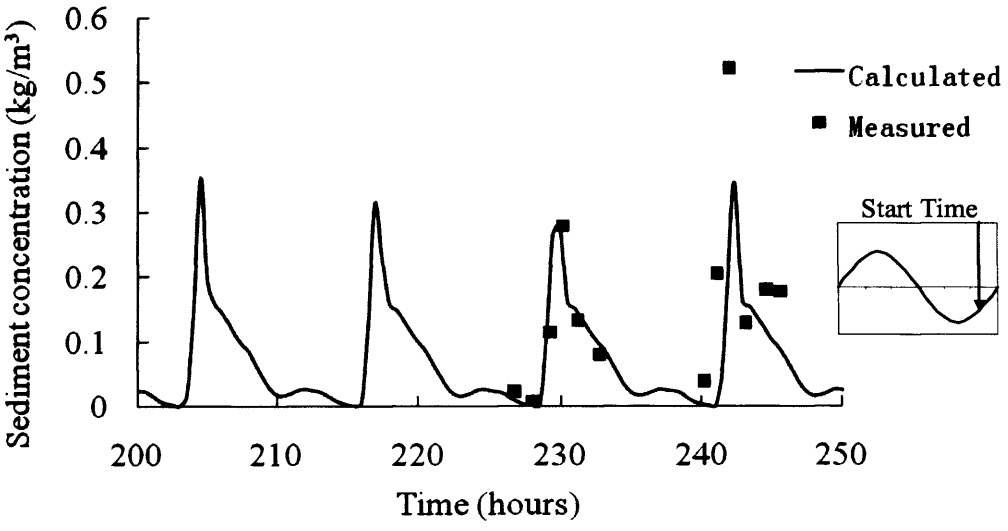

Figure 8-19b Validation of predicted sediment concentration at site 1b

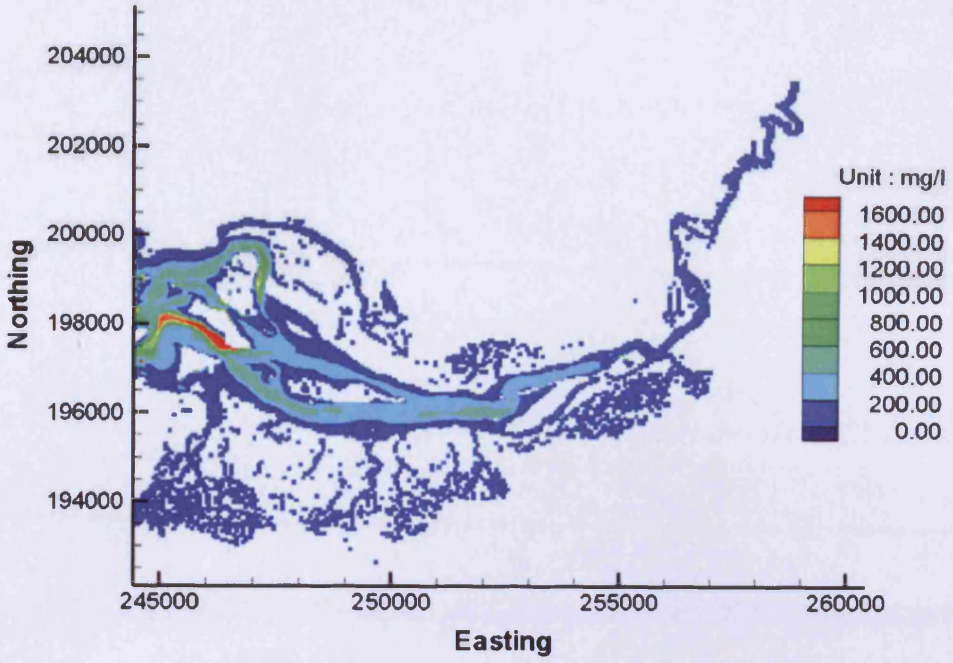

Figure 8-20a Suspended sediment concentration at low water spring tide

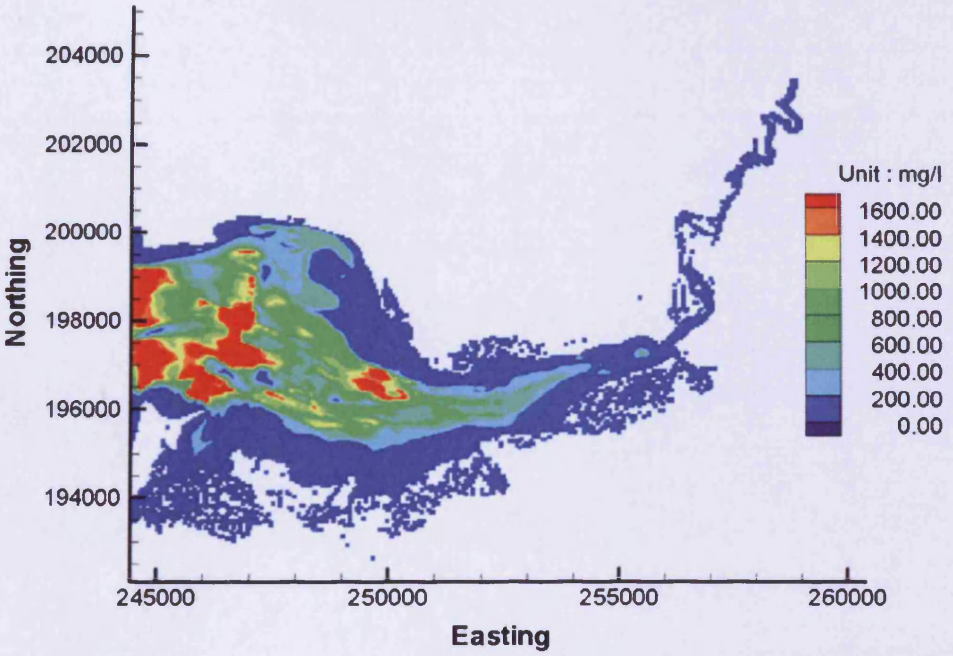

Figure 8-20b Suspended sediment concentration at mean flood spring tide

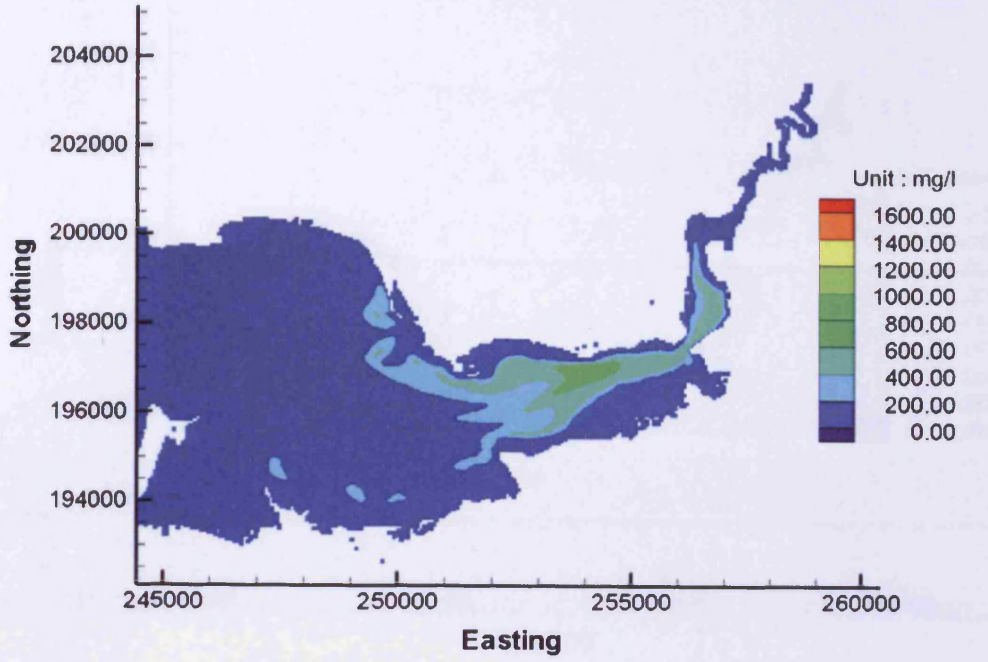

Figure 8-20c Suspended sediment concentration at high water spring tide

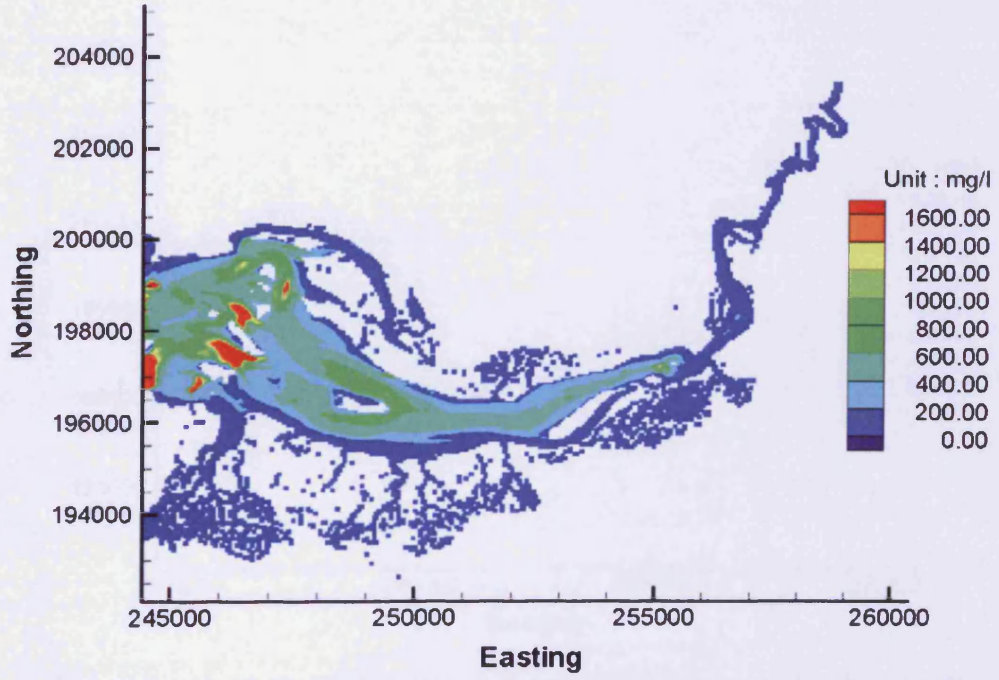

Figure 8- 20d Suspended sediment concentration at mean ebb spring tide

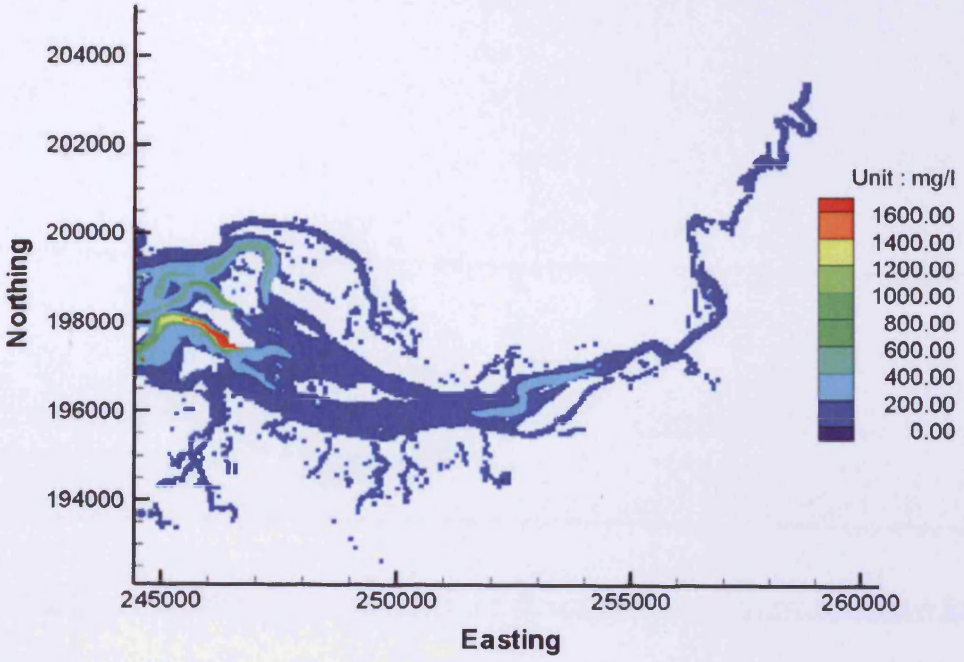

Figure 8-21a Suspended sediment concentration at low water neap tide

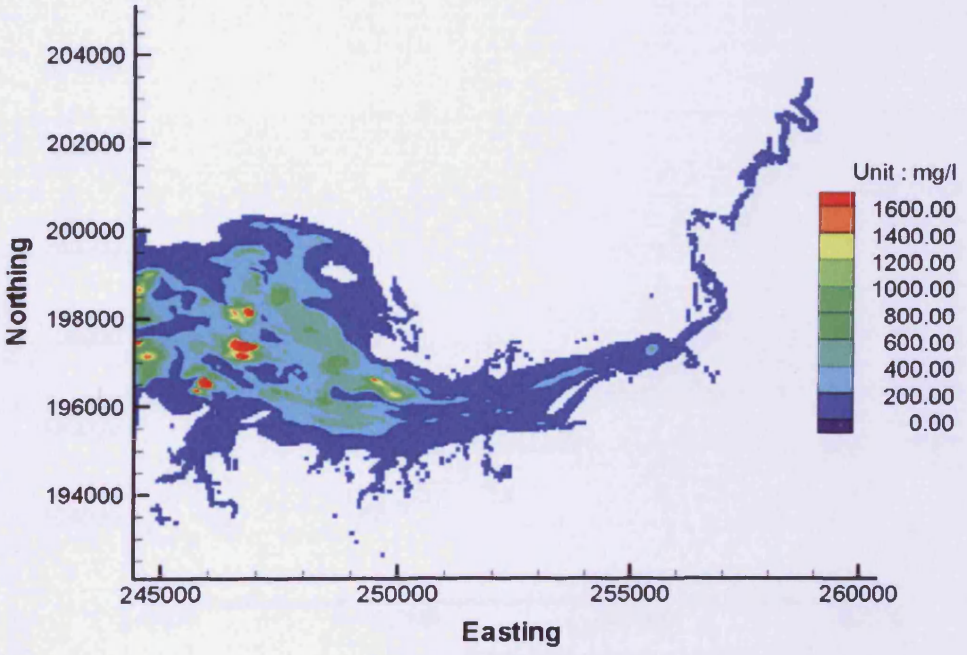

Figure 8-21b Suspended sediment concentration at mean flood neap tide

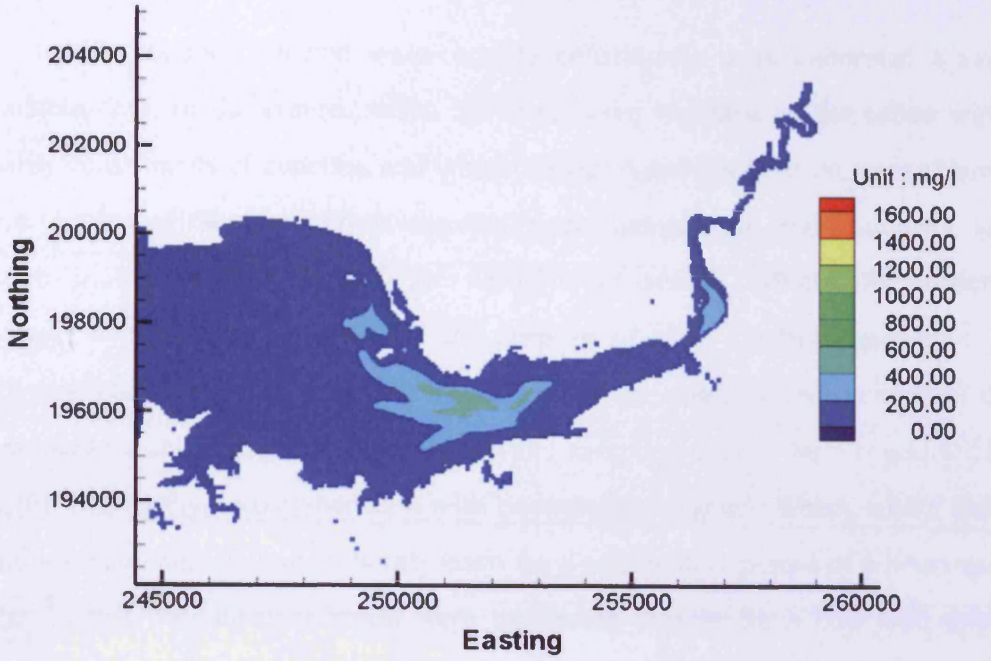

Figure 8-21c Suspended sediment concentration at high water neap tide

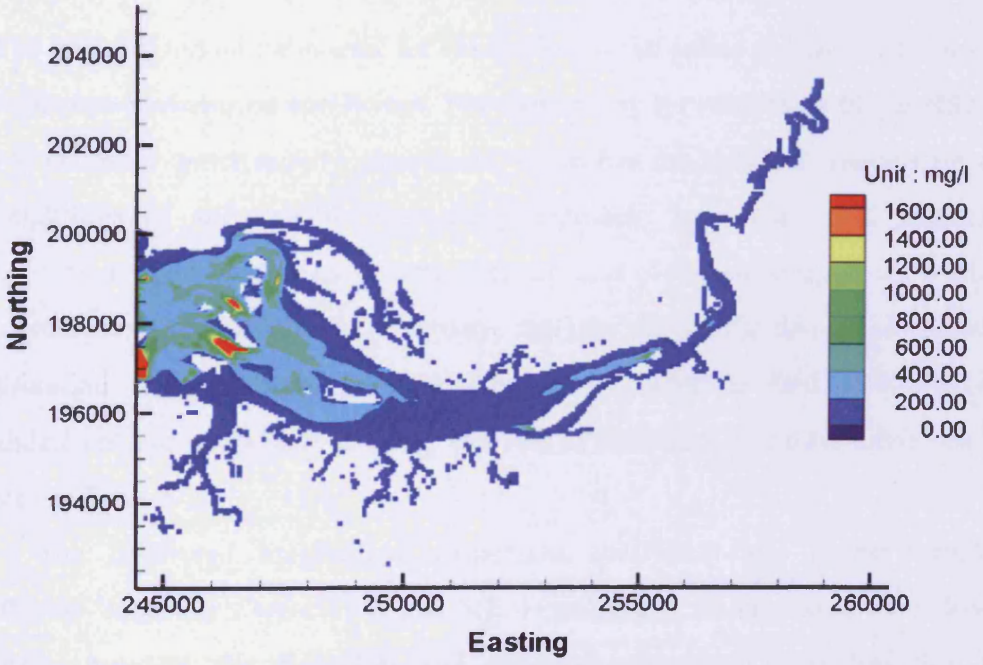

Figure 8-21d Suspended sediment concentration at mean ebb neap tide

8.4.3 Water quality model

In this section, selected water quality constituents were calibrated against available data. In the current study, nutrients were regarded as the prime water quality constituents of concern, and whose transport and distribution were affected by a number of factors, such as currents, water temperature, light intensity, and various biological decay rates. Water samples are usually collected for nutrients analyses at a monthly interval for the purpose of water quality supervision or statistics, but such a low sampling frequency can not meet the requirement of the numerical model calibration. A series of water sampling studies were conducted by Cardiff University, in collaboration with Environment Agency Wales, where water samples were collected on an hourly basis for a consecutive period of 6 hours each time. In this way nutrient levels were monitored closely for a half tidal cycle. These data were used for model calibration.

8.4.3.1 Salinity

The most important parameter for calibration of the solute transport equations is the dispersion-diffusion coefficient. The easiest way for calibrating this coefficient is to choose a water quality constituent which has the simplest source term and straightforward and reliable measuring approach. In a controlled laboratory experiment, dye is widely used to trace the process of the solute transport, while in a nature large area of the river estuary, the best choice for dispersion-diffusion calibration is the salinity gradient. The salinity level is first calibrated and validated at site 1a and site 1b using five sets of field data. The tidal conditions are listed in Table 8-2.

The calibrated longitudinal dispersion coefficient and lateral turbulent diffusion coefficient were 13.0 and 1.2, respectively, as suggested by Falconer (1991). Actually, the dispersion and diffusion effects are much less than the advection effect in the calculated domain, because the water motion is dominated

by tide in the Loughor Estuary, so the dispersion and diffusion coefficients can vary in large range.

Table 8-2 Tidal conditions for the salinity measurements

Sampling date	Tidal conditions
06/11/2007	From LW(2.3m) to HW(7.7m), medium tide
14/12/2007	From HW(7.9m) to LW(2.1m), medium tide
13/03/2008	From HW(7.9m) to LW(2.0m), medium tide
02/06/2008	From LW(1.4m) to HW(8.2m), spring tide
30/06/2008	From LW(2.1m) to HW(7.5m), medium tide

Although field salinity data were measured on five different days, the tidal conditions did not vary much, so five sets of measured data were combined to compare with model simulations for the spring tide. Figure 8-22(a-b) shows comparisons between the model predictions and field measurements. It can be seen that the predicted salinity levels were slightly higher than those of the measured data, but the overall level of agreement is quite close for both site 1a and site 1b. Figure 8-23a and 8-23b show the salinity distributions across the entire estuary at high water and low water for the spring tide.

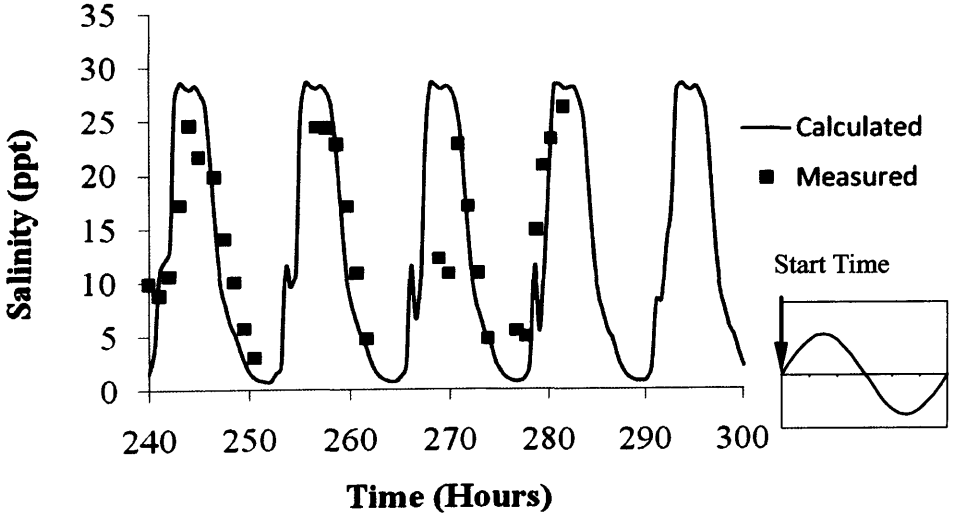

Figure 8-22a Calibration of predicted salinity levels at site 1a

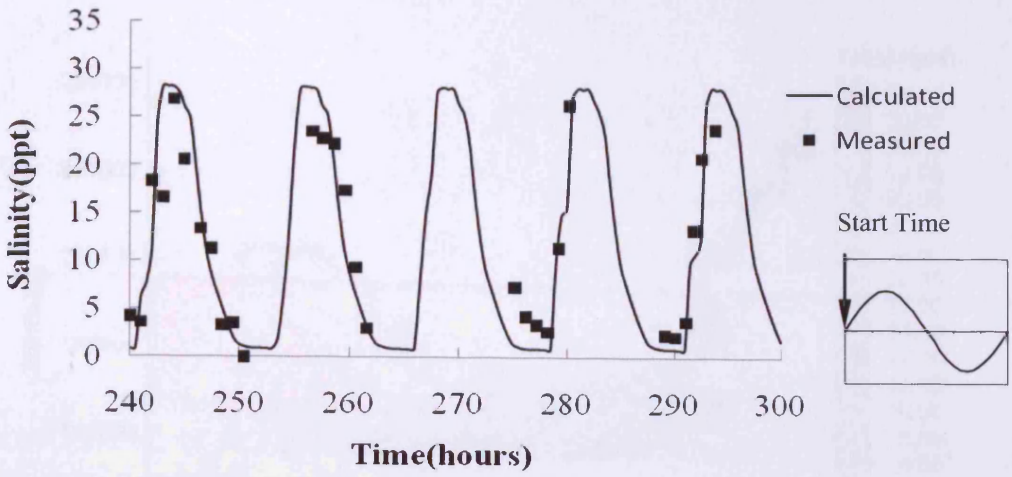

Figure 8-22b Validation of predicted salinity levels t site 1b

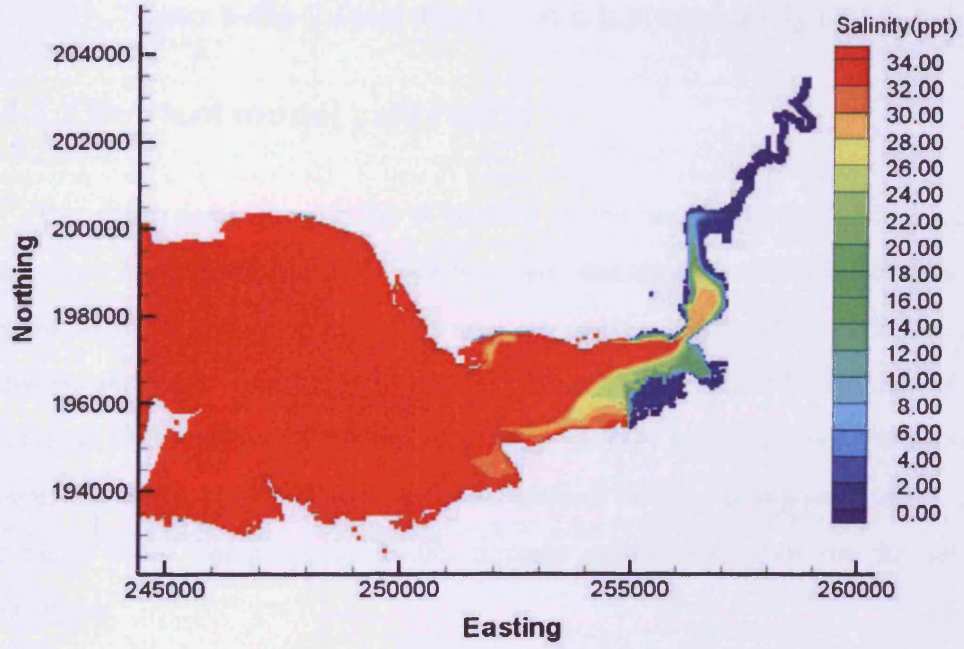

Figure 8-23a Salinity distribution at high water spring tide

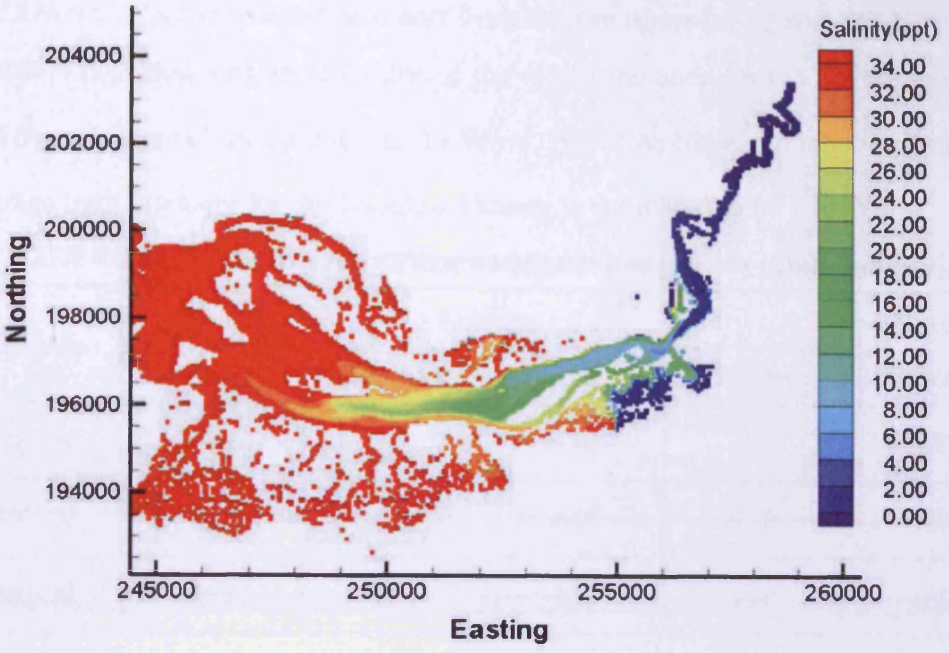

Figure 8-23b Salinity distribution at low water spring tide

8.4.3.2 Nutrient model calibration

The main parameters to be calibrated in the numerical model for nutrient predictions are the biochemical reaction rate and decay rate coefficients, which depend on various environmental parameters, such as temperature, light intensity, turbidity, and flow conditions. In practice, these chemical and biological reaction rates need to be estimated for the prevailing weather and water conditions at the time of the study. However, owing to the number of influencing parameters, there are many more uncertainties in the nutrient simulations than for the salinity simulations.

Table 8-3 lists typical clear sky values of light intensity for different latitudes and months, which are calculated from the seasonal mean values under clear sky conditions. These figures represent the upper limits of solar radiation energy at sea level (Weast and Astle, 1980). This table provides a reference value for the annual

mean light intensity for the latitude of 50° N, i.e. 460 Langley, which equals to 222.8 W/m^2. Another published report from the Environment Agency (Stapleton et al. 2007) provided a measured value of the total irradiance for the Severn Estuary and Bristol Channel, being 260 ± 14 W/m^2. Based on these reference values, the average light intensity for the Loughor Estuary is estimated to be 230 W/m^2.

Table 8-3 light intensity for different latitudes and months (unit: Langley)

Latitude	Season				Annual Mean
	Spring	Summer	Fall	Winter	
30° N	680	750	530	440	600
40° N	650	740	440	320	540
50° N	590	710	330	190	460

The light attenuation coefficient is usually calculated using Equation (5-7) in QUAL2E (see Chapter 5), while it can also be determined directly when field data are available. Devlin et al. (2008) measured the sub-surface light attenuation for the transitional, coastal and offshore waters around the UK between August 2004 and December 2005, and a mean value of 1.2 m^{-1} was estimated for the light attenuation at the Burry Inlet and Loughor Estuary (which is classified as a moderately exposed, macro-tidal water type by the WFD). The Environment Agency provides a reference value of 2.36m^{-1} as the average of median values measured at Loughor Road Bridge and Burry Port (Edwards, 2007). The calibrated value for light attenuation coefficient was 1.8 in this model.

Other biochemical rate coefficients for the nitrogen and phosphorus cycles were determined according to the reference values given in Table 5-2. After calibration, some of the more important coefficients were found to have appropriate values as given in Table 8-4.

Table 8-4 Calibrated values for nitrogen biochemical rate coefficients

Notation	Description	Value	Unit
α_1	Nitrogen fraction of algal biomass	0.07	mgN/mgA
β_1	Organic Notrogen mineralization rate at 20 °C	0.4	day^{-1}
β_2	Nitrification rate at 20 °C	1.0	day^{-1}
K_{mpc}	Half saturation constant for algae limitation of nitrogen recycle	1.0	mg A/L
K_{NIT}	Half saturation constant for oxygen limitation of nitrification	2.0	mg O_2/L
β_3	Denitrification rate at 20 °C	0.09	day^{-1}
K_{NO3}	Michaelis constant for denitrification	0.1	mg O_2/L
α_2	Phosphorus fraction of algal biomass	0.01	mg P/mg A
β_4	Organic phosphorus mineralization rate at 20 °C	0.15	day^{-1}

The model predicted concentrations of ammonium nitrogen and total oxidized nitrogen were compared with the EA measured data (collected on 14/12/2007 and 13/03/2008) for sites 1a and 1b. Figure 8-24(a-b) shows the model predictions and the measured data on 13/03/2008. Although the measurements are about two times higher than the predictions at some instants, the general trend of the variations are well captured. Considering the uncertainties and challenges in the nutrients simulations, the agreement between both sets of results can be deemed as satisfactory. Figure 8-25 shows a comparison of the total oxidized concentration between the model predictions and the measured data. Again, reasonable agreement is observed between both sets of results. The extremely large measured concentration in Figure 8-25b seems to be an outlier.

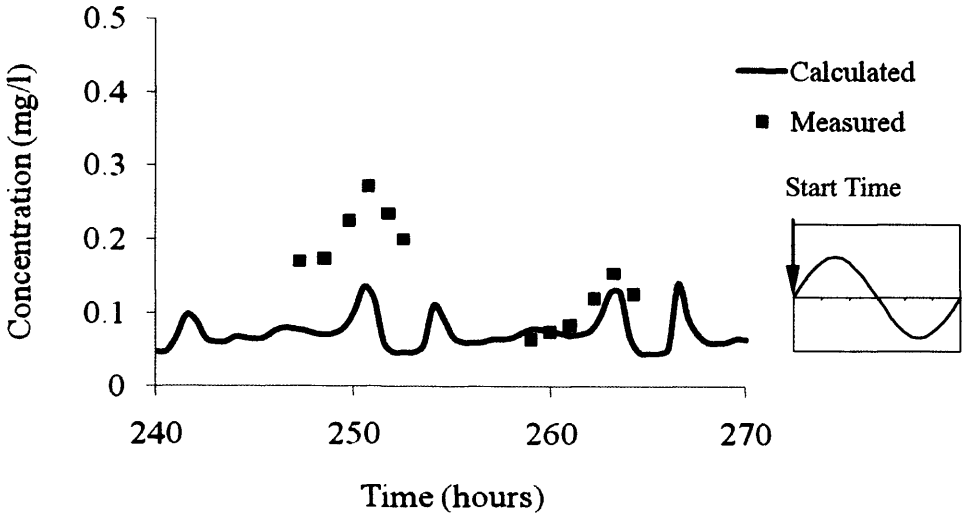

Figure 8-24a Calibration of predicted ammonium nitrogen concentrations at site 1a

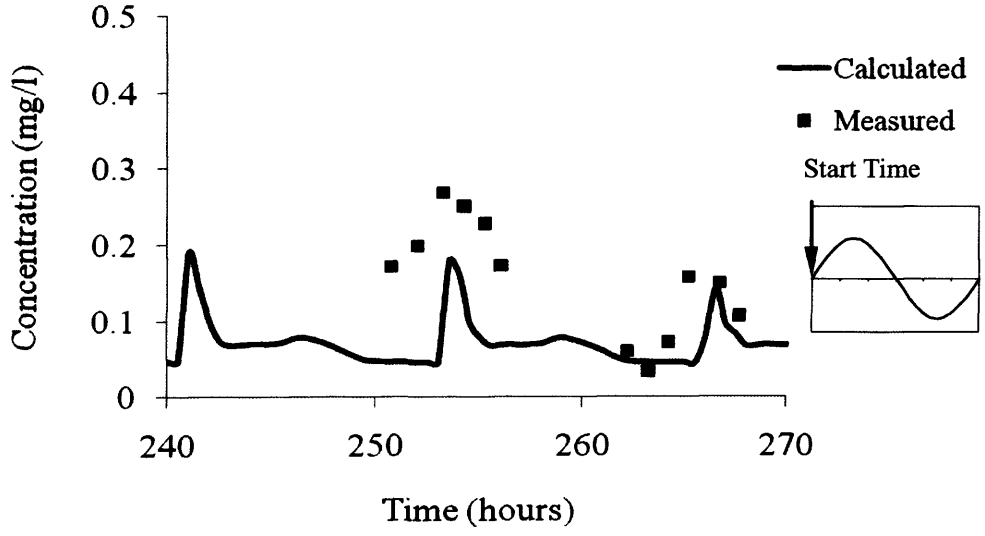

Figure 8-24b Calibration of predicted ammonium nitrogen concentrations at site 1b

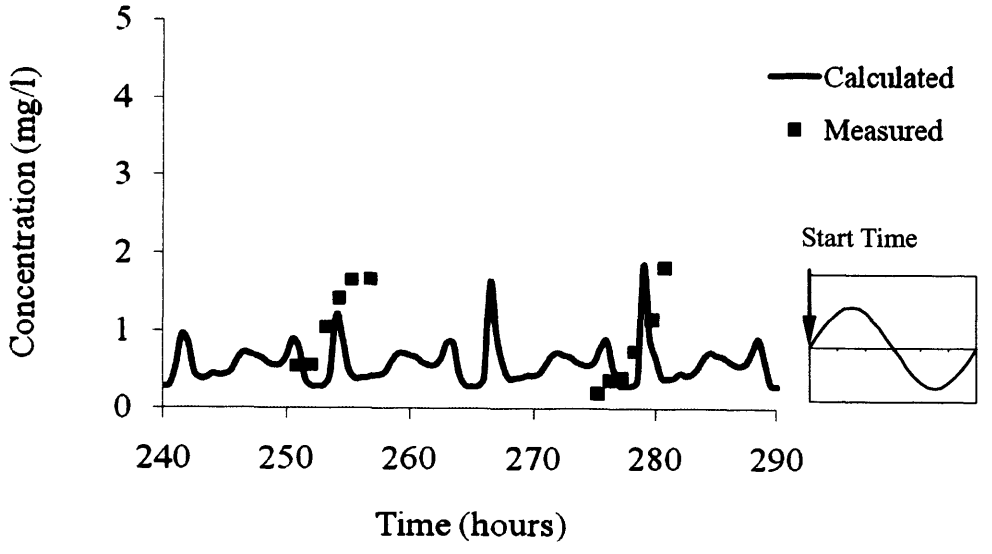

Figure 8-25a Calibration of predicted total oxidized nitrogen concentrations at site 1a

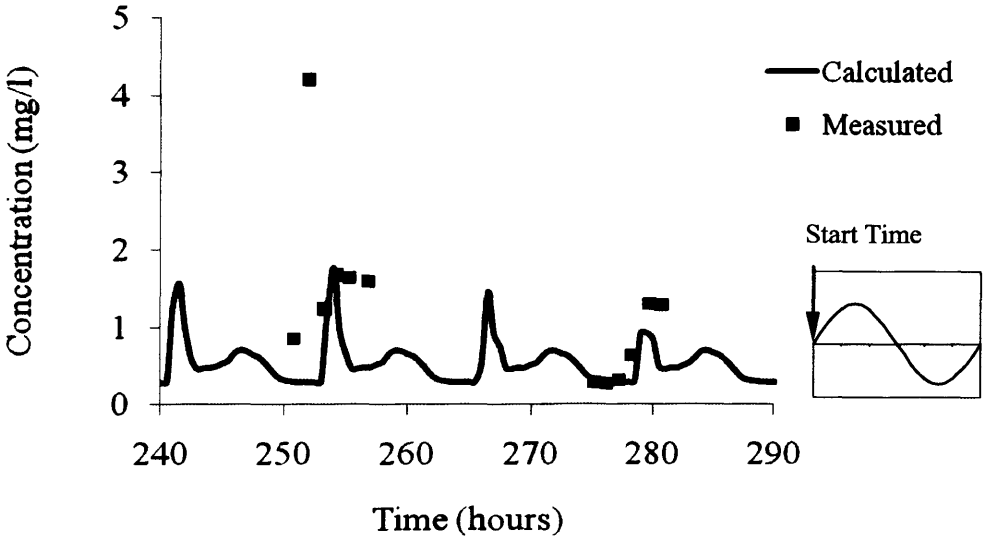

Figure 8-25b Calibration of predicted total oxidized nitrogen concentrations at site 1b

The model predicted concentrations of dissolved inorganic phosphorus concentration are compared with the measured data at site 1b, for which the field samples were collected on 13/03/2008, 02/06/2008 and 30/06/2008, followed by a laboratory analyses of the phosphorus adsorption behaviour, undertaken in the

Characterization Laboratory for Environmental Engineering Research, at Cardiff University. Figure 8-26 shows satisfactory agreement between the model predicted and the measured data.

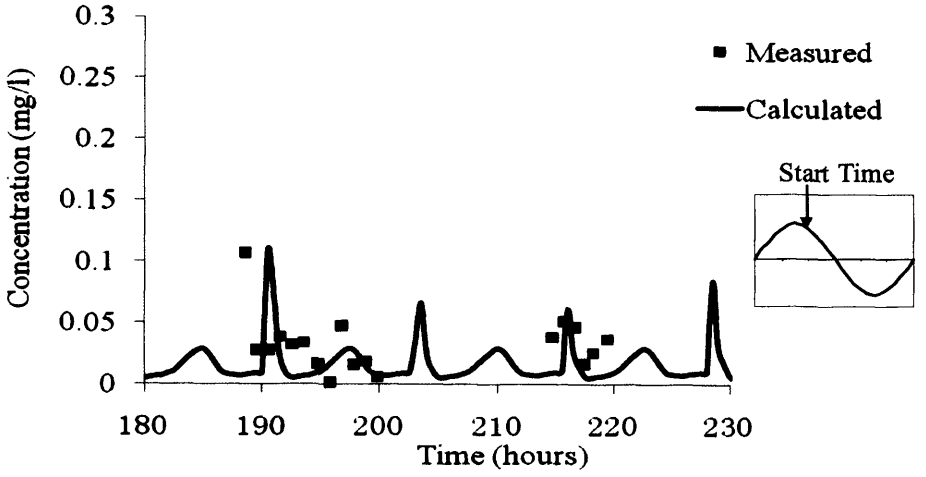

Figure 8-26 Calibration of predicted dissolved inorganic phosphorus concentrations at site 1b

8.4.3.3 Nutrients model validation

The nutrient calibration results were validated by comparing the model results and the field data along the estuary, based on a field survey in January 2004. Water samples were collected and analyzed by the Environment Agency for five locations (Table 8-5 and Figure 8-27) in the Burry Inlet and Loughor Estuary.

Table 8-5 Water sampling sites on January 2004

Site No.	Easting	Northing
72757	256300	200925
30407	256100	198100
72860	255750	197950
72643	254200	197400
72754	247900	197300
72753	244600	199500

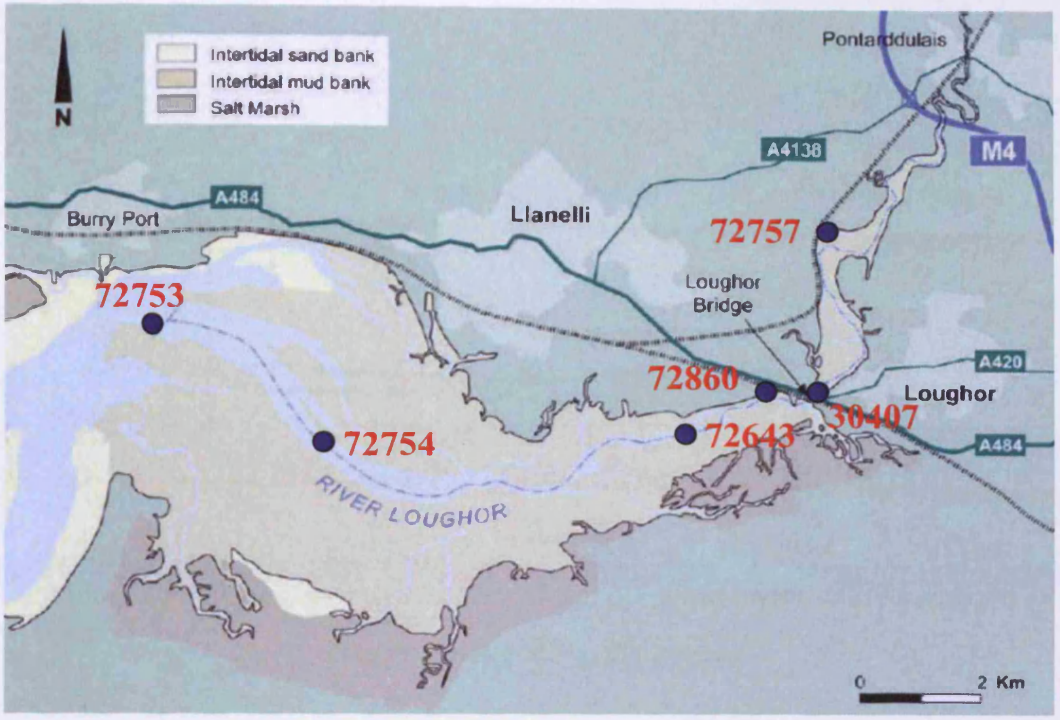

Figure 8-27 Location of water sample collection sites on January 2004

Figure 8-28(a-c) illustrates comparisons between the measured data and model predicted results of average, maximum and minimum concentrations of ammonium nitrogen, total oxidized nitrogen and dissolved inorganic phosphorus (orthophosphate) during one tidal cycle.

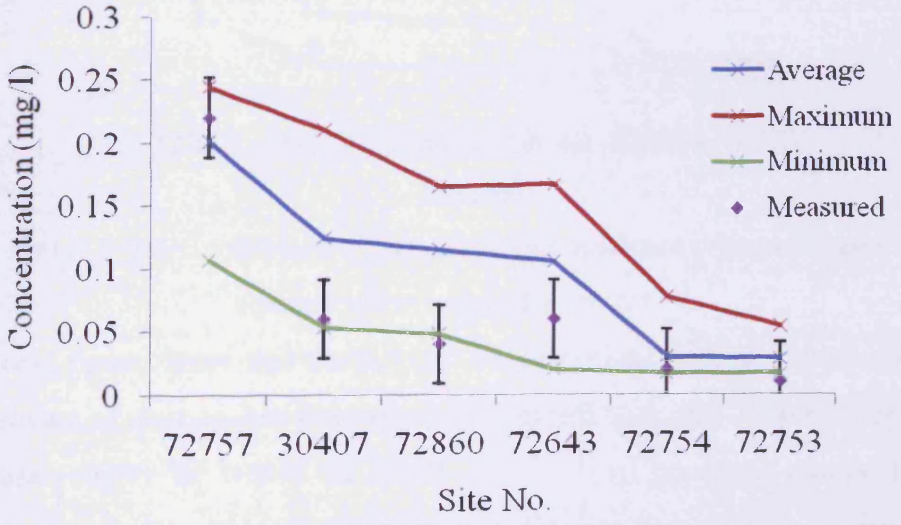

Figure 8-28a Comparison of measured and predicted ammonium nitrogen concentrations along the estuary

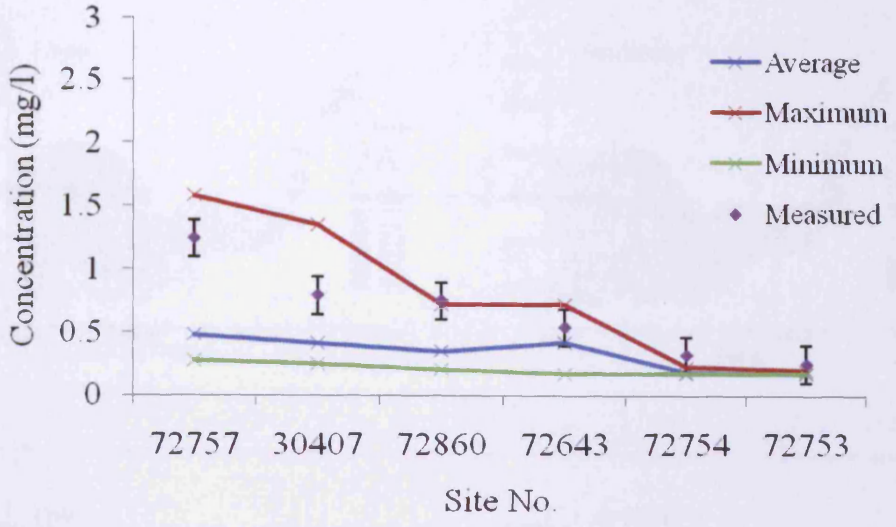

Figure 8-28b Comparison of measured and predicted total oxidized nitrogen concentrations along the estuary

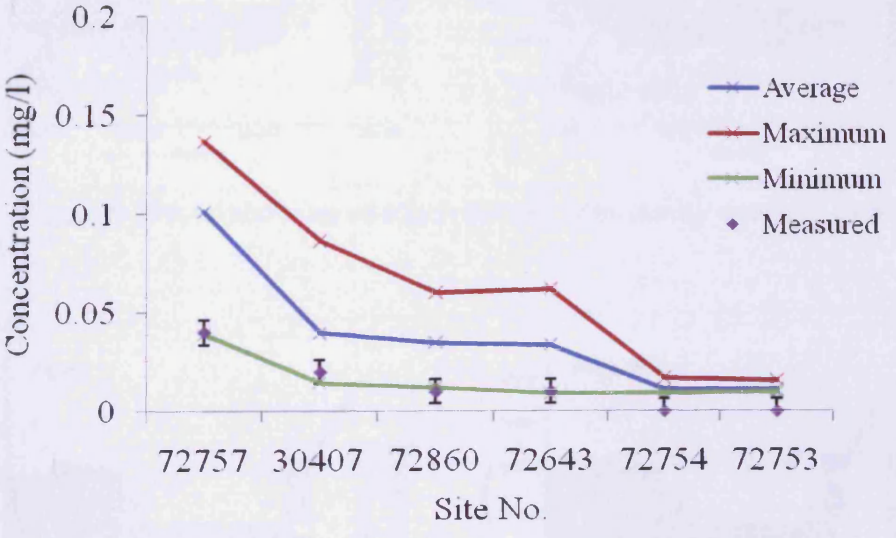

Figure 8-28c Comparison of measured and predicted orthophosphate concentrations along the estuary

These figures show that the nutrient concentrations generally decrease from the upstream of the Loughor Estuary to the seaward boundary at Burry Inlet. The field data roughly lie within the limits of the model predicted ranges. Figure 8-29(a-c) shows the nutrients distributions across the computational domain for the flood tide, high tide, low tide and ebb tide phases respectively, for the three nutrient constituents.

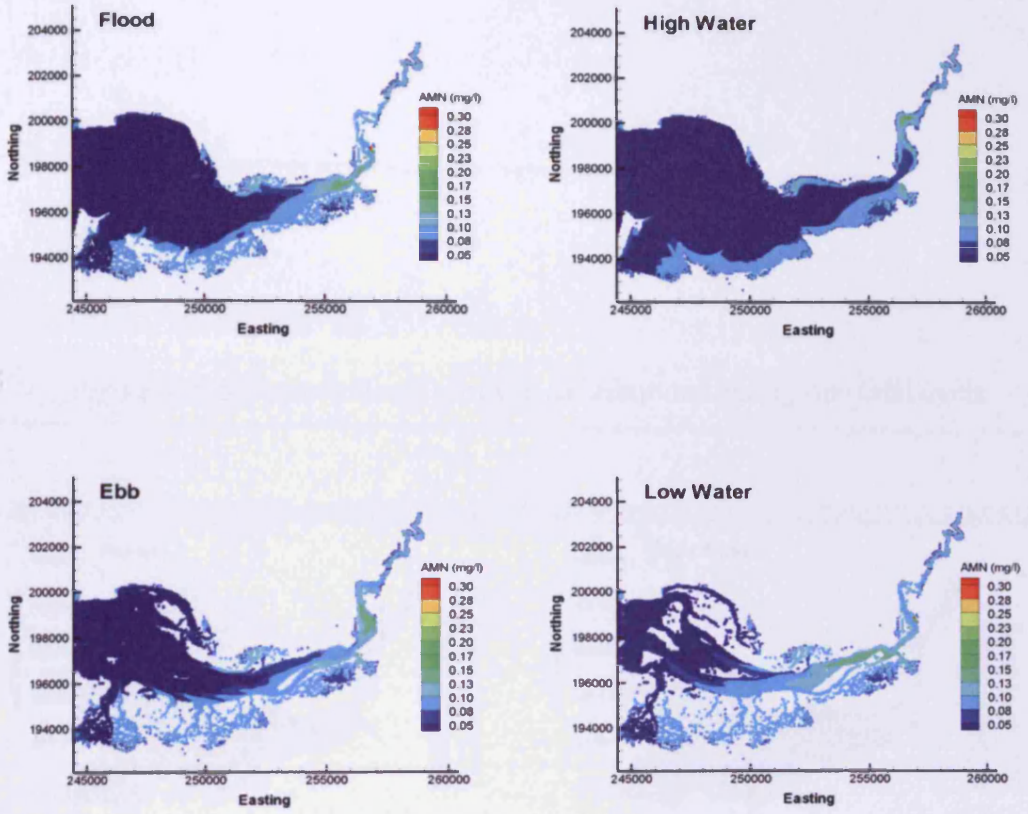

Figure 8-29a Ammonium nitrogen distributions during one tidal cycle

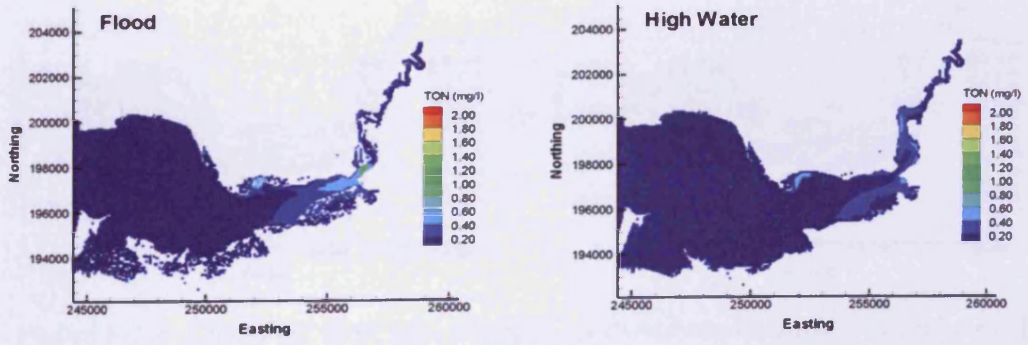

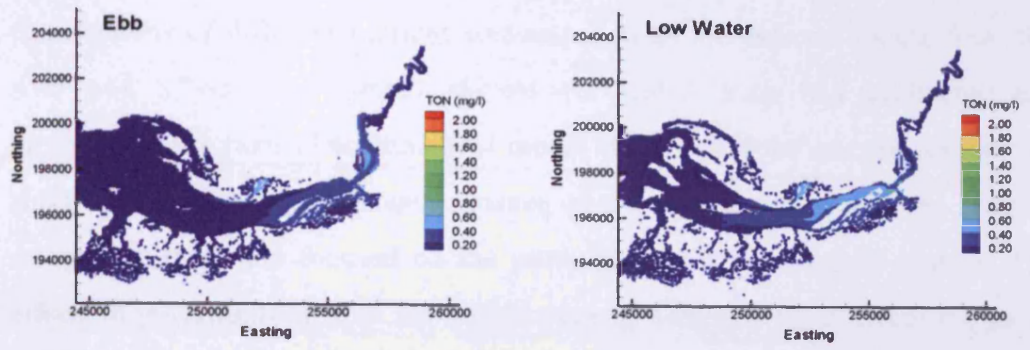

Figure 8-29b Total oxidized nitrogen distributions during one tidal cycle

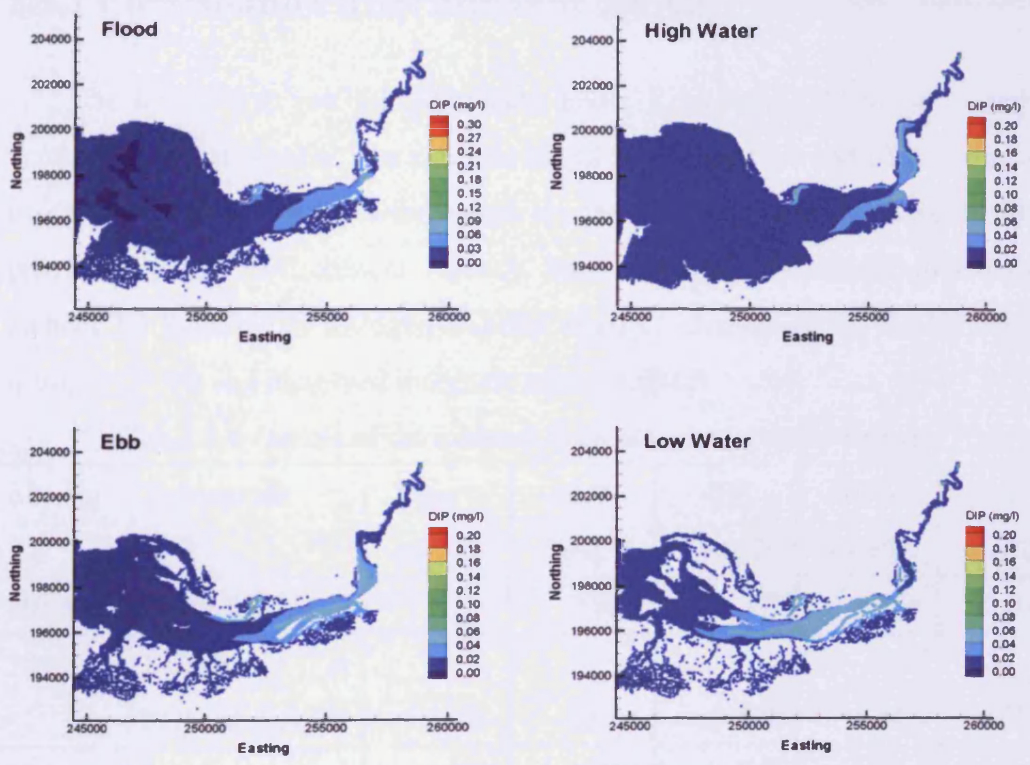

Figure 8-29c Dissolved inorganic phosphorus distributions during one tidal cycle

8.5 Model application

After calibration and validation, the numerical model was applied to simulate the hydrodynamic and water quality processes in the River Loughor and its estuary

for different hypothetical scenarios. The model was used to investigate the contributions of different nutrient sources, such as the external inputs from the river and STWs, the internal sources (or sinks) from bed sediments and biochemical reactions. The numerical model showed that the internal sources (or sinks) did not have a significant influence on this site compared with the external sources, so the study focused on the investigation of the external sources. The effects of point sources from the STWs were investigated for different discharge methods of the STWs. The effects of diffuse source were investigated for both dry and wet weather conditions.

8.5.1 Contribution from different sources

The model was run for 300 hours under a medium tide to get a stable concentration distribution. The external inputs from the rivers and STWs were set to constant values, which were based on the averaged monthly data in 2004 provided by the Environment Agency. Table 8-6 lists the details of external sources for ammonium nitrogen (AMN), organic nitrogen (ON), total oxidized nitrogen (TON) and dissolved inorganic nitrogen (DIP)

Table 8-6 Details of the external sources to the Loughor Estuary

Site No.	Description	Flow (m^3/s)	AMN (mg/l)	ON (mg/l)	TON (mg/l)	DIP (mg/l)
30392	Burry Pill	0.164	0.034	2.009	3.535	0.106
30406	Loughor at Pontardulais	3.976	0.094	0.577	1.123	0.072
30408	Llan	1.429	0.068	0.775	1.136	0.052
30409	Lliw	1.388	0.052	0.947	1.453	0.035
30410	Gwili	0.705	0.126	1.151	2.473	0.110
30461	Dulais	0.283	0.013	0.326	0.640	0.007
30470	Gowerton STW	0.261	0.376	4.580	9.428	1.249
30471	Llannant STW	0.126	5.127	3.805	3.844	1.430

30874	Dafen	0.156	0.177	1.067	2.729	0.055
72796	Llanelli STW	0.355	0.124	3.113	7.699	2.104
72799	Afon Morlais	1.518	0.076	1.500	2.472	0.057
72946	Salthouse Pill	0.184	0.044	0.774	0.694	0.051
72947	Dulas at pwll	0.157	0.033	0.999	2.992	0.046
72948	Llanrhidian Stream	0.059	0.097	1.101	1.689	0.102
75512	Lleidi	0.435	0.024	0.732	1.620	0.055
100333	Garnswllt STW	0.186	1.060	6.124	4.736	0.806
100345	Llangennech STW	0.053	2.599	3.165	8.112	2.277

Four investigation sites were selected, namely, 72757, 30407, 72643 and 72754 from upstream to downstream. The concentrations of AMN, TON and DIP were compared for four scenarios, described as follows:

(1) Only the sources from the biochemical reactions within the domain were included. The initial conditions and the sea boundary conditions for the nutrient levels were set to 0.017 mg/l, 0.17mg/l and 0.01mg/l for the AMN, TON and DIP concentrations, respectively, which were the same as the values used in the model calibration and verification.

(2) Only the sources from outfalls (the rivers and STWs) were considered. The initial conditions and the sea boundary conditions for nutrient levels were set to zero.

(3) Only the sources from the bed sediment re-suspension were accounted for. The initial conditions and the sea boundary conditions for the nutrient levels were set to zero. The initial concentrations of AMN and DIP in the bed sediments were set to 35μg/l and 15μg/l, respectively, which were the same as the values used for the model calibration and verification.

(4) All the sources mentioned in the above three scenarios were included in the computations. The initial conditions for the AMN, TON and DIP

concentrations in the water column were set to 0.017 mg/l, 0.17mg/l and 0.01mg/l, respectively. The initial concentrations of the AMN and DIP in the bed sediments were set to 35µg/l and 15µg/l respectively. The sea boundary conditions for the nutrient levels were set to the same values as the initial conditions.

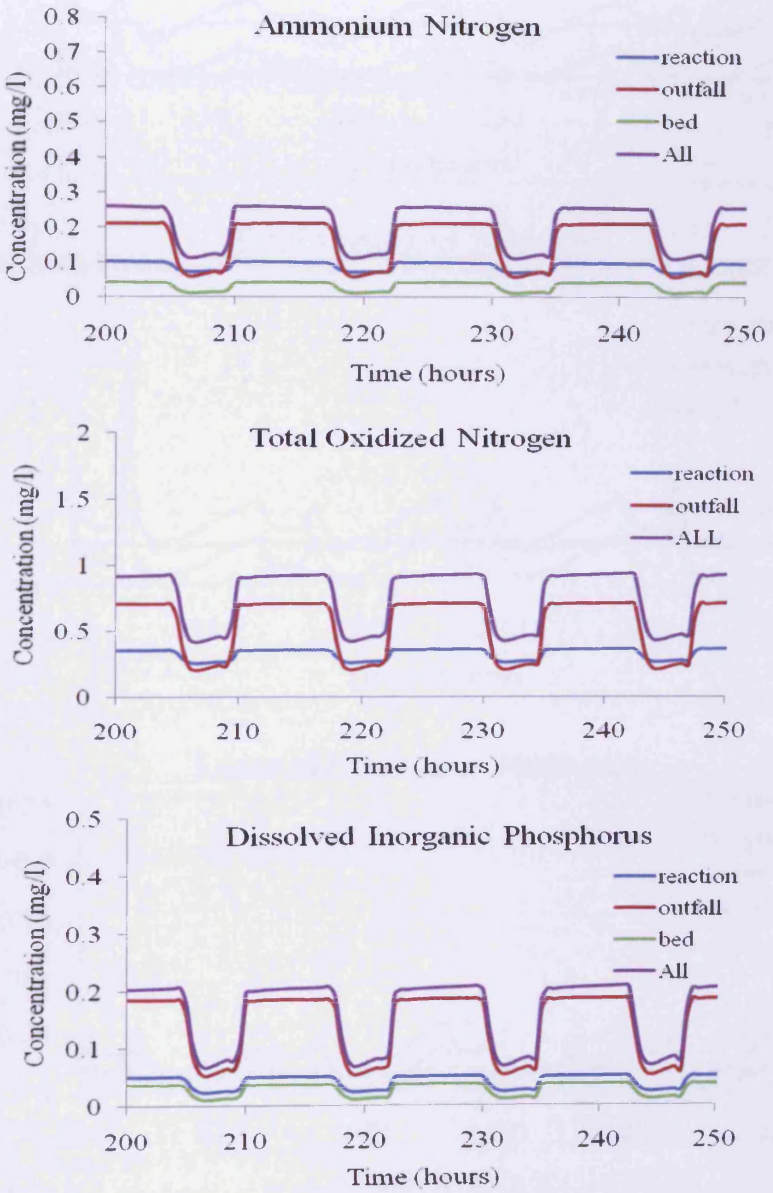

Figure 8-30a Comparisons of nutrient concentrations from different sources at site 72757

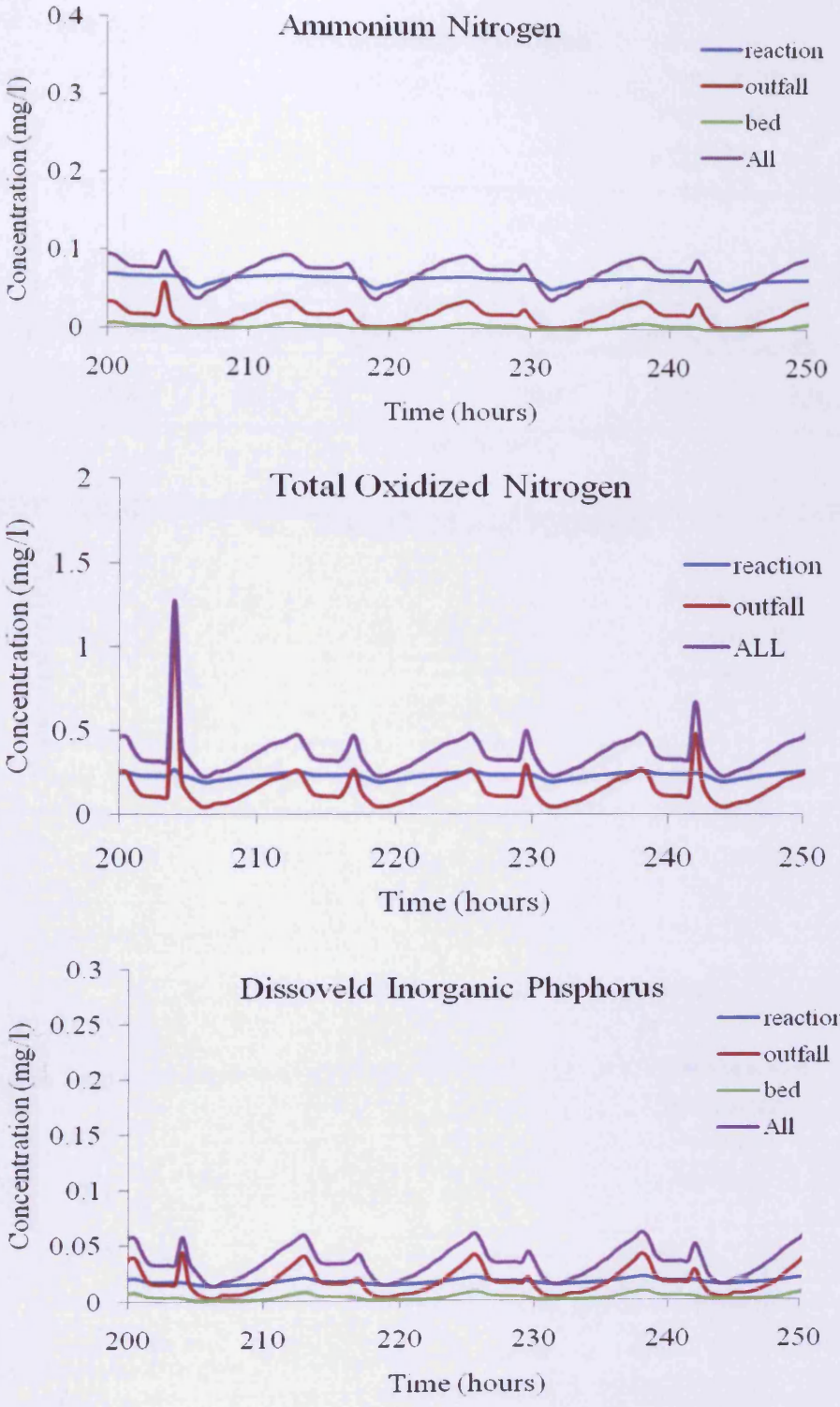

Figure 8-30b Comparisons of nutrient concentrations from different sources at site 30407

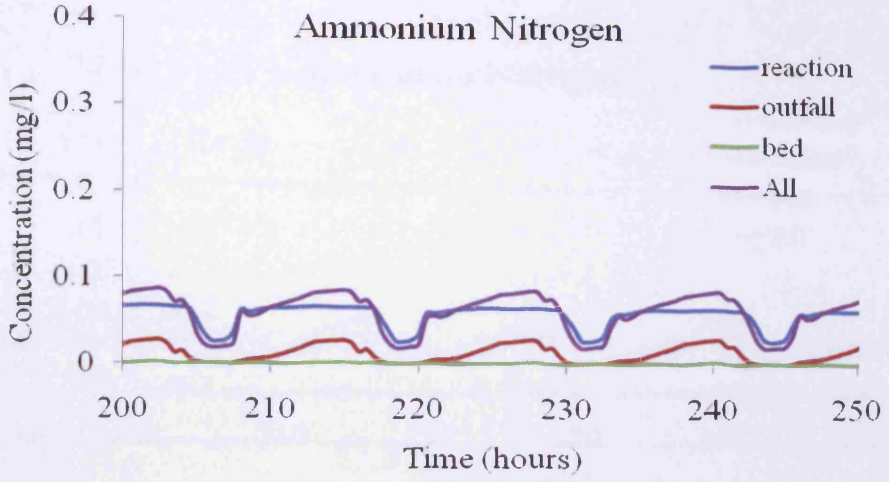

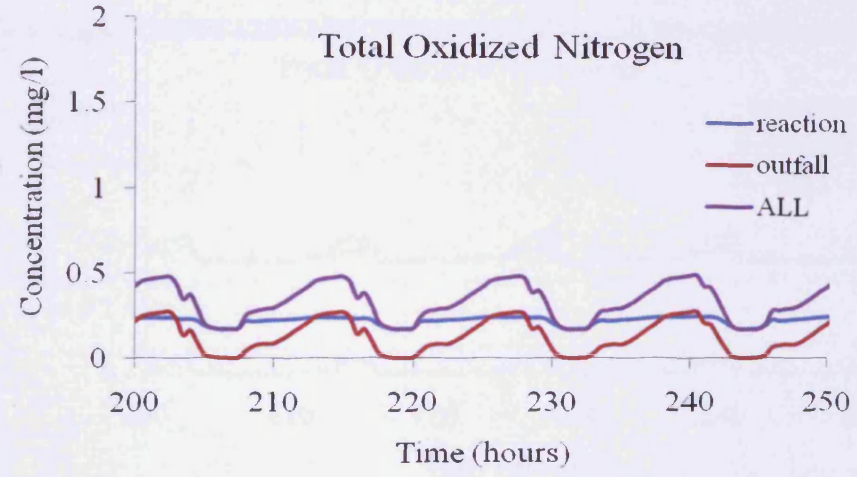

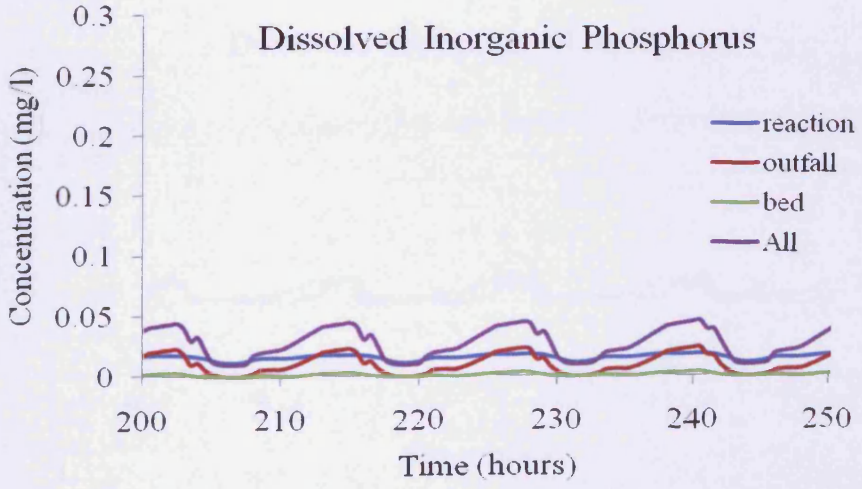

Figure 8-30c Comparisons of nutrient concentrations from different sources at site 72643

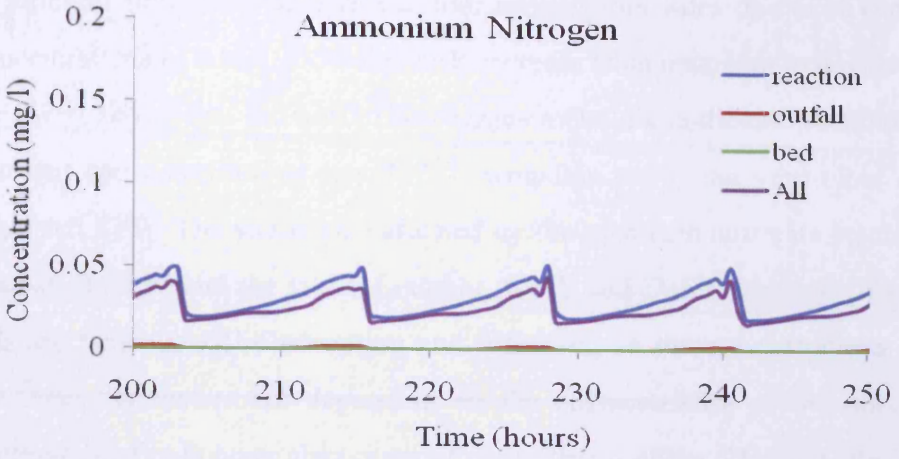

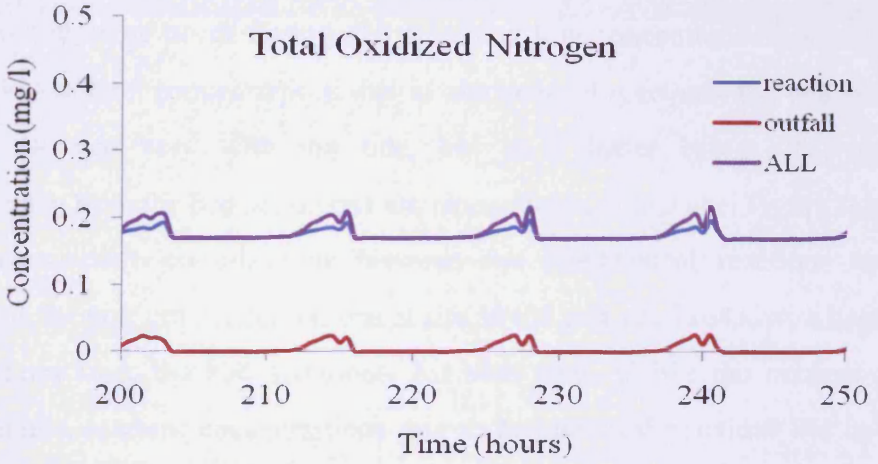

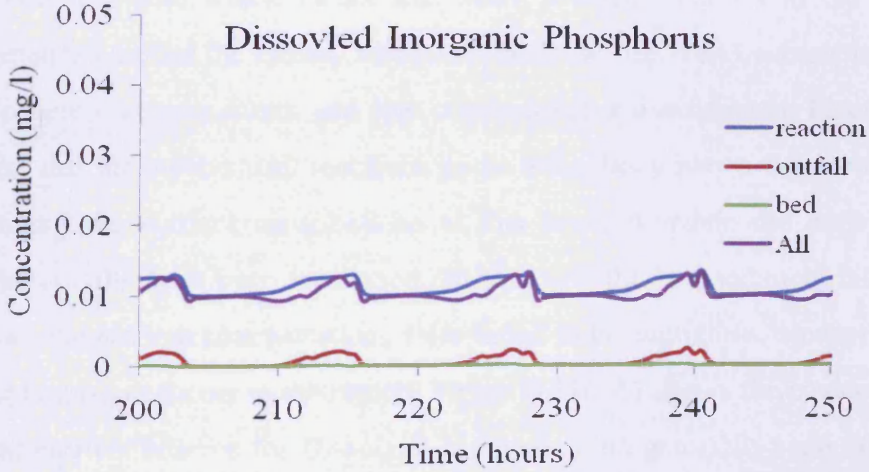

Figure 8-30d Comparisons of nutrient concentrations from different sources at site 72754

Figure 8-30(a-d) illustrates differences in the AMN, TON and DIP concentrations under different simulation scenarios at four investigation sites. It can be seen that the concentrations of AMN, TON and DIP decrease from upstream to downstream. Figure 8-30a shows that the outfall discharges make a significant contribution to the nutrient concentrations at site 72757, with this site being very close to the Llangennech STW. The site is also affected by the upstream nutrients inputs from the Garnswllt STW and the rivers Loughor, Gwili and Dafen. Nutrients from the outfalls are transported by advection and diffusion, so the concentrations in the nearby receiving waters are dependent on the characteristics of the tide. High concentrations of pollutants always occur downstream of the STW. At site 72757, high concentrations occur during ebb tide, and low concentrations occur during flood tide. Nutrient concentrations due to biochemical reactions and bed sediment interactions also vary with the tide, but to a lesser extent. The nutrient contributions from the bed sediments are recognisable at this site. Figure 8-30(b-c) shows comparable contributions between the biochemical reactions and the outfalls on the nutrient concentrations at site 30407 and site 72643, with negligible contributions from the bed sediments for both sites. Unlike the nutrient inputs from outfalls, nutrient concentrations due to biochemical reactions did not vary much with the tide, which meant that small gradients existed in the nutrient concentrations around the estuary, except for AMN at site 72643, where there were high concentrations upstream and low concentrations downstream. Figure 8-30d indicates that the biochemical reactions in the water body play a dominant role in determining the nutrient contributions at this location, while the contributions from the outfalls have been weakened. At this site, the bed sediment interaction effects on the nutrient concentrations were found to be negligible, because of little sediment transport fluxes in the region. Figure 8-31(a-b) shows the percentages of different nutrient sources for Dissolved Inorganic Nitrogen (DIN) and Dissolved Inorganic Phosphorus (DIP) at the four monitoring sites.

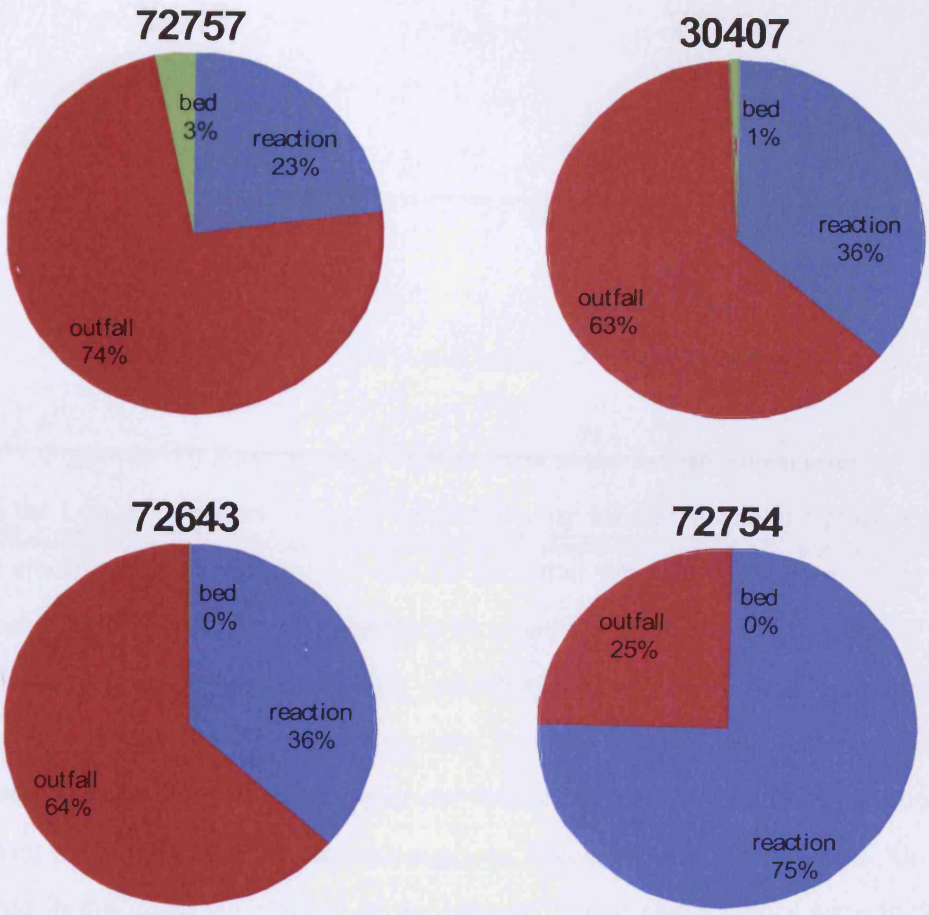

Figure 8-31a Percentage of DIN sources at the investigation sites

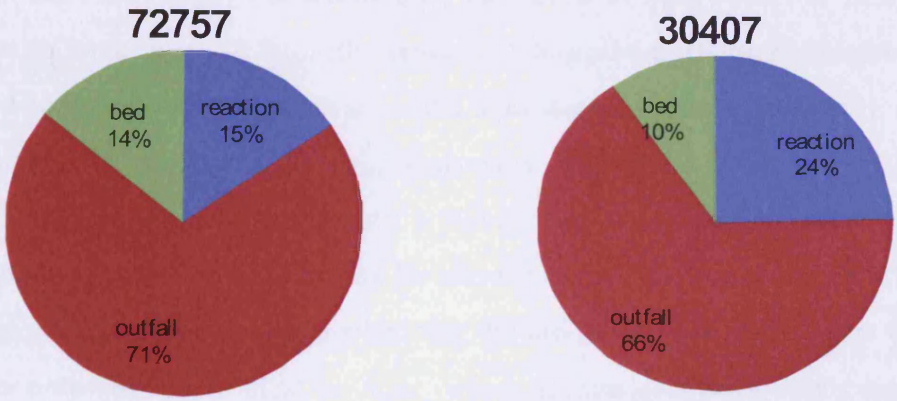

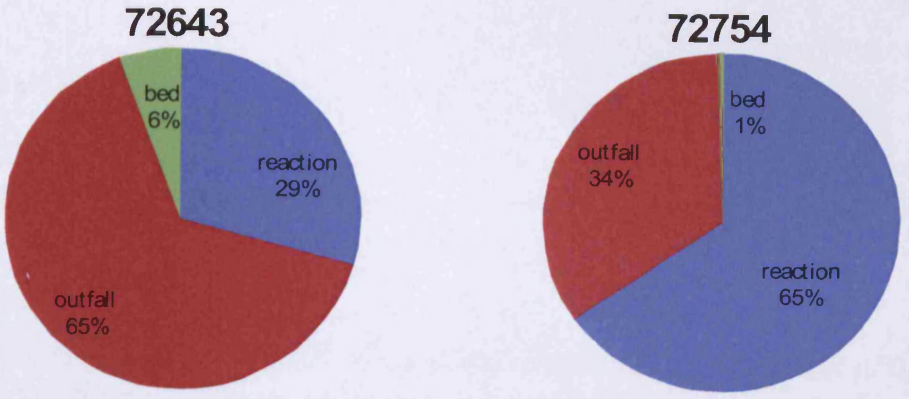

Figure 8-31b Percentage of DIP sources at the investigation sites

In the Loughor Estuary, most of the outfalls are located in the upstream region of the estuary. Correspondingly, it can be seen that the nutrient contributions are dominated by the outfall discharges from the rivers and STWs at the upstream site 72757, and the significance of this contribution decreases from upstream to downstream. In the middle of the estuary, i.e. site 72754, the contributions of biochemical reactions prevail. The nutrient contributions due to bed sediments also decrease from upstream to downstream, as higher sediment transport fluxes occurred in the upstream reaches of the estuary, where the currents were higher. The bed sediment effects on the DIP concentrations were higher than their effects on the DIN concentrations, which can be attributed to a relatively high level of DIP in the bed sediments in this estuary. The levels of AMN and DIP in the bed sediments were found to be in the range of 5-85μg/l and 0-20μg/l, respectively, according to the laboratory analyses of the field samples collected at site 1b during the field survey conducted by Cardiff University in 2007 and 2008.

It was also observed from Figure 8-30d that the AMN and DIP concentrations were higher by only considering the biochemical reactions than those when all the sources were included, which implied that the biochemical reactions were limited by the concentration of algal biomass, which in turn consumes AMN and DIP. When the concentration of algal biomass increased from the outfall sources, more AMN and DIP would be consumed through biochemical reactions, and a new balance would be established for the concentrations of DIN (AMN+TON) and

DIP.

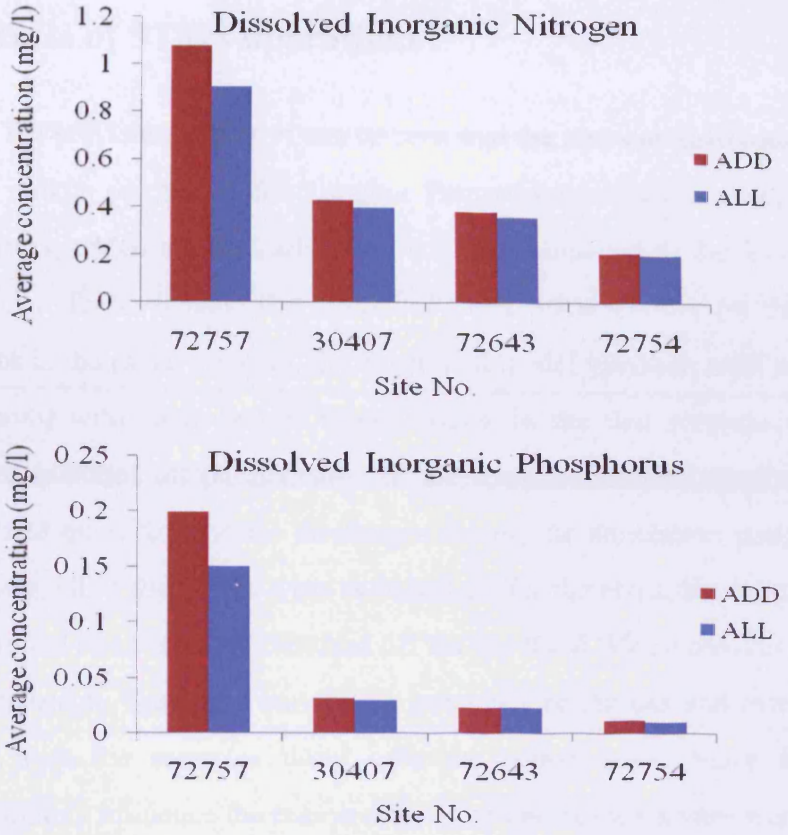

Figure 8-32 Comparison of nutrient concentrations from separated sources and combined sources

Figure 8-32 compares the average concentrations between the summation of the contributions from separate sources (i.e. outfalls, biochemical reactions and bed sediments) and the concentrations can be compared by directly considering the combined sources. It is obvious that the summations are higher than the concentrations of the combined sources, especially at the upstream site 72757. In order to identify each contribution from different sources, the biochemical reactions are excluded when evaluating the contributions of nutrient sources, other than the biochemical reaction itself, which contradicts the reality that the biochemical reactions always exist regardless of the source of the nutrients. This non-linear effect is most significant at site 72757, which is close to the outfalls. Therefore, the large amount of nutrients discharged from the outfalls is consumed

by algal biomass through the biochemical reaction process.

8.5.2 Effects of STWs operations

From the previous section, it can be seen that the nutrient distributions in the upper and middle reaches of the Loughor Estuary are mainly dependent on the outfall sources, which are basically point sources connected to the STWs on the estuary banks. To investigate the effects of these point sources on the nutrient distributions in the estuary waters, the developed model has been used to simulate three scenarios with controlled STW operations. In the first scenario, all of the STWs were switched off permanently. In the second scenario, all of the STWs were switched on with constant discharges during the simulation period. In the third scenario, all of the STWs were switched on for the ebb tide to discharge the pollutants to the open sea, and switched off for the flood tide to prevent pollutants reaching the beach. The initial conditions, boundary conditions and external input conditions were the same as those used in section 8.5.1. Since the STWs discharges mainly influence the region close to outfall sites, six sites were selected upstream and downstream of Llannant STW, Gowerton STW and Llanelli STW, respectively, to investigate the effects of different STWs operations (see Figure 8-33).

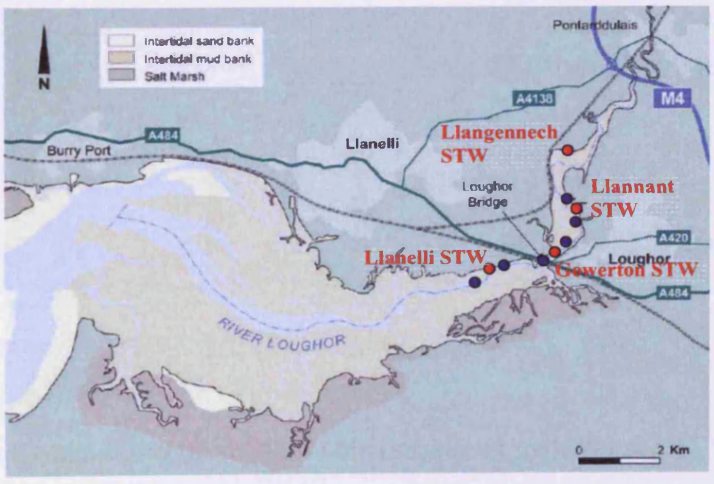

Figure 8-33 Locations of the STWs (red) and the study sites (blue)

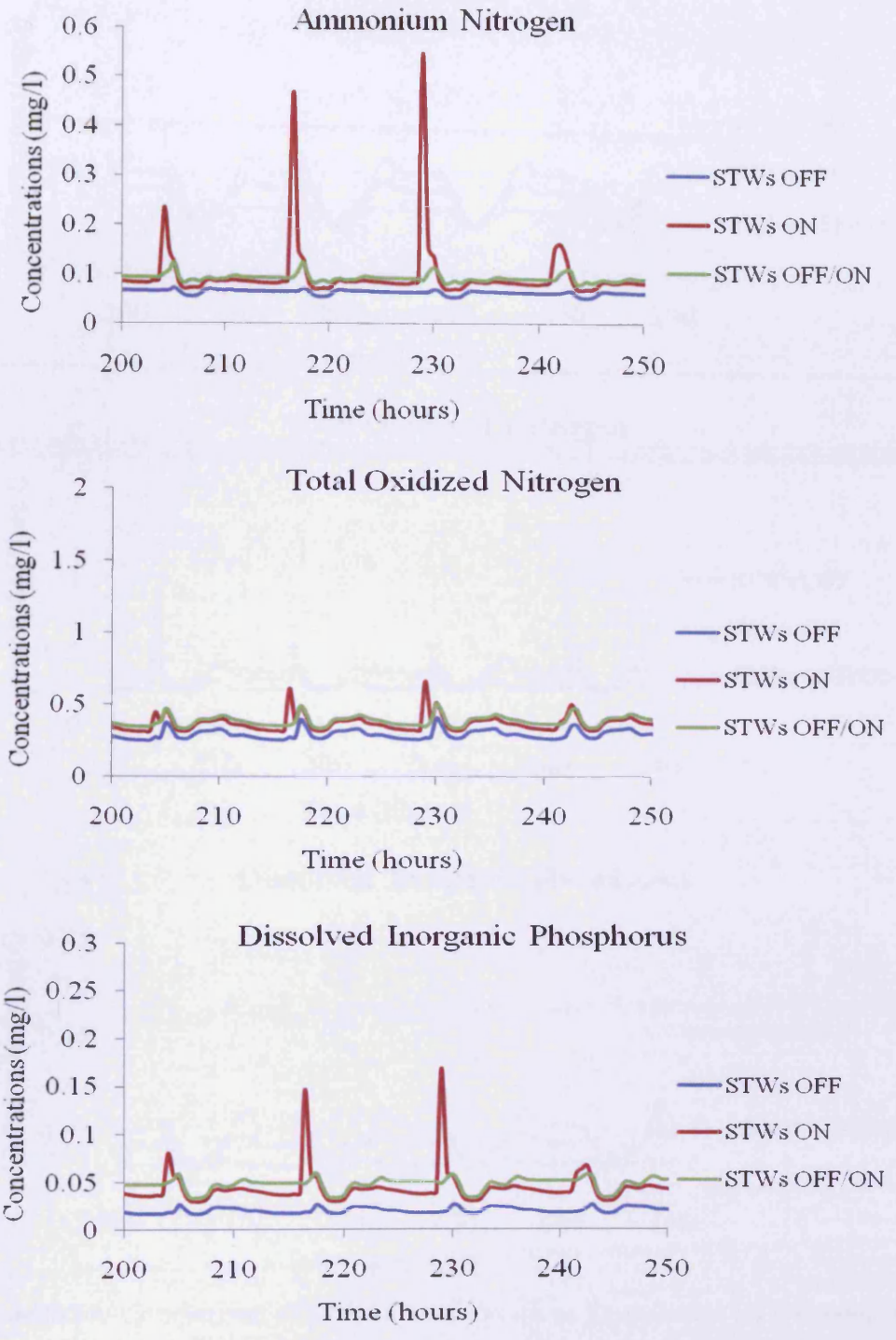

Figure 8-34a Comparison of nutrient concentrations for different STWs scenarios at a site upstream of Llannant STWs

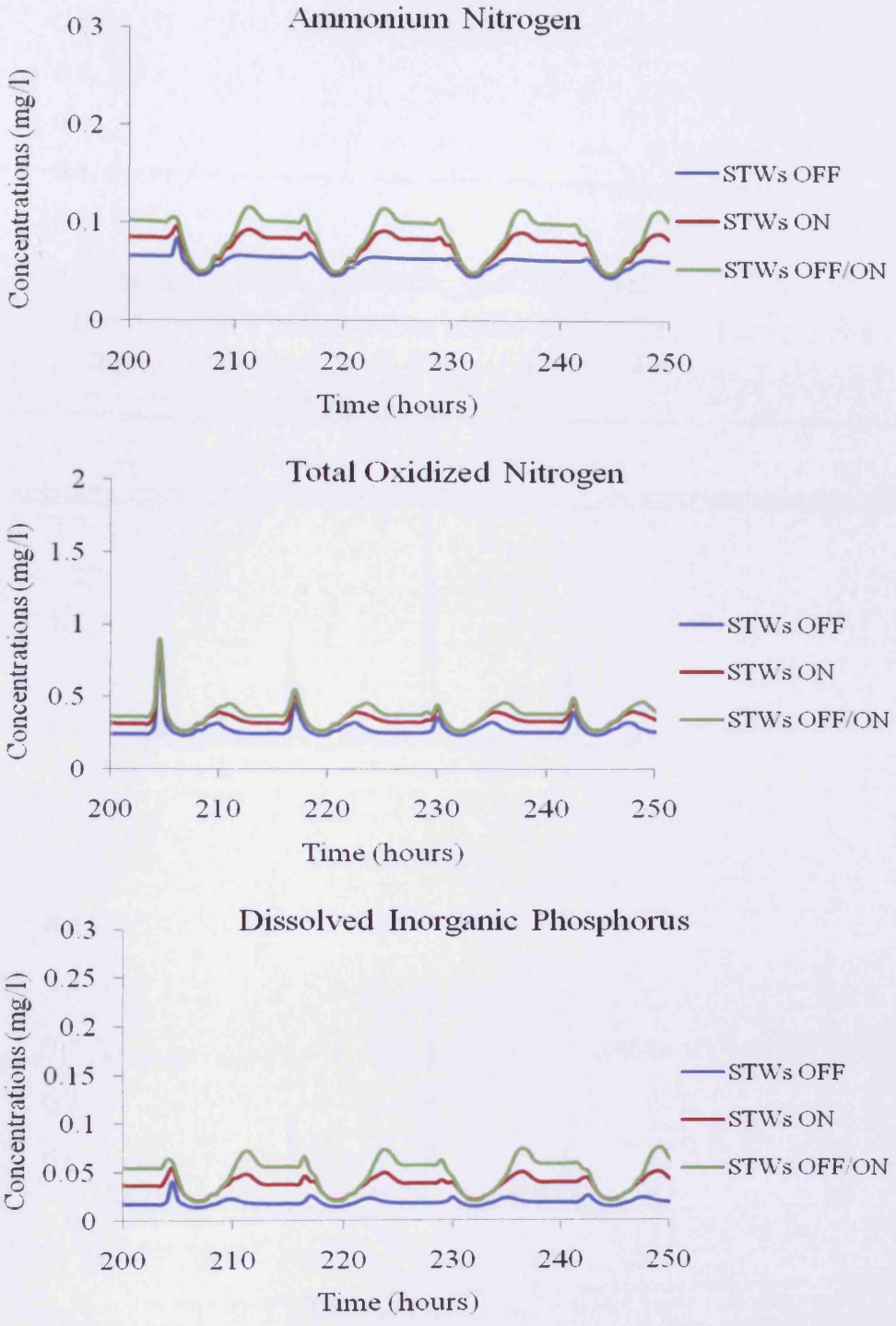

Figure 8-34b Comparison of nutrient concentrations for different STWs scenarios at a site downstream of Llannant STWs

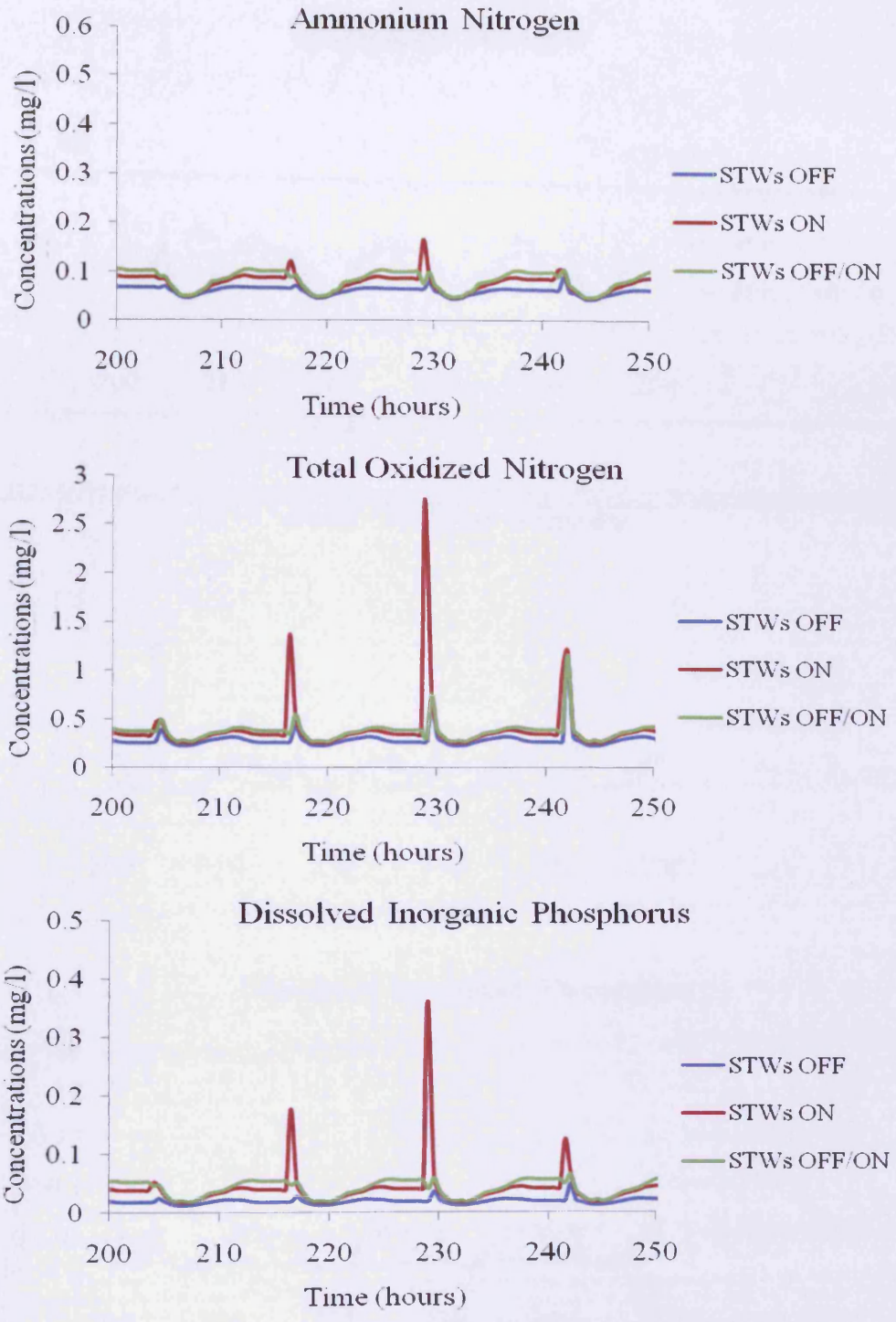

Figure 8-34c Comparison of nutrient concentrations for different STWs scenarios at a site upstream of Gowerton STWs

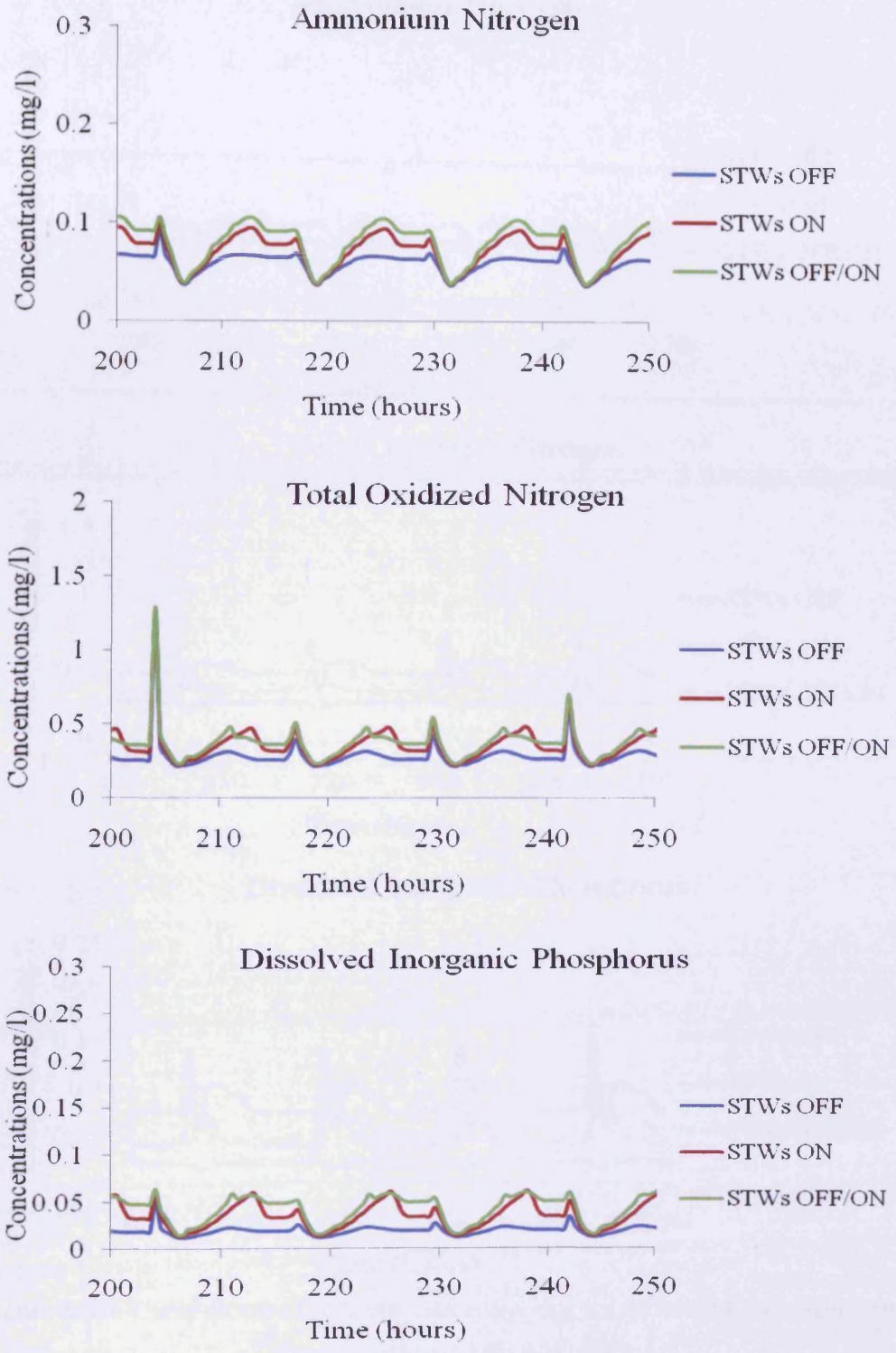

Figure 8-34d Comparison of nutrient concentrations for different STWs scenarios at a site downstream of Gowerton STWs

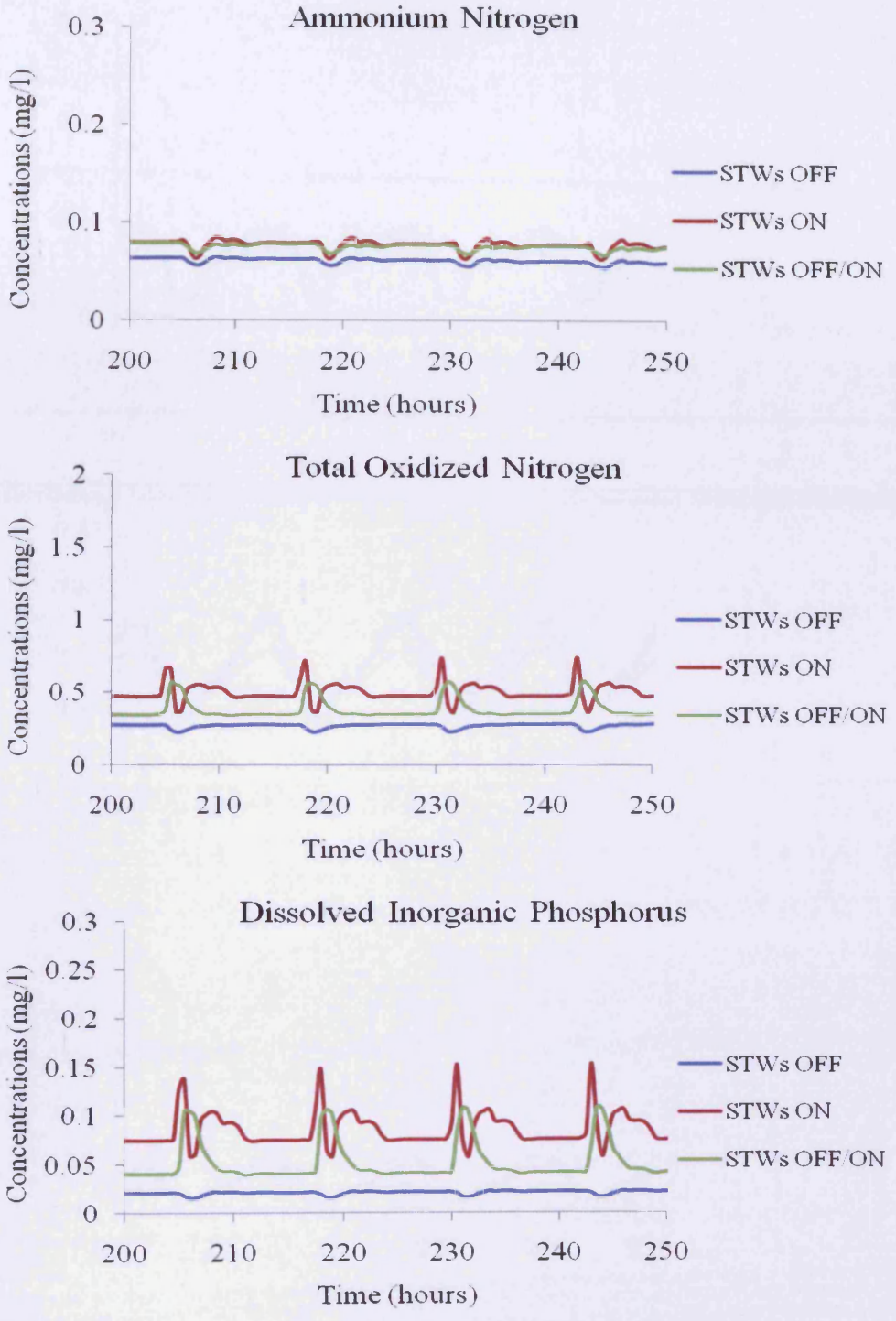

Figure 8-34e Comparison of nutrient concentrations for different STWs scenarios at a site upstream of Llanelli STWs

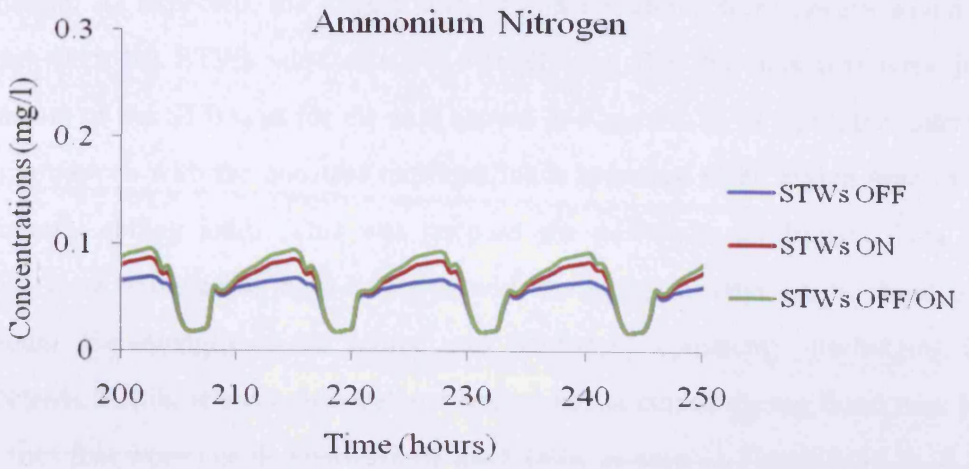

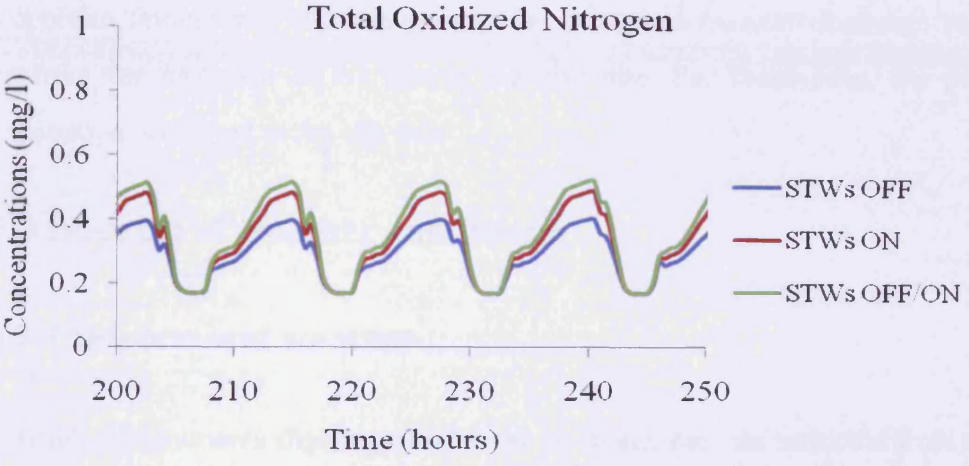

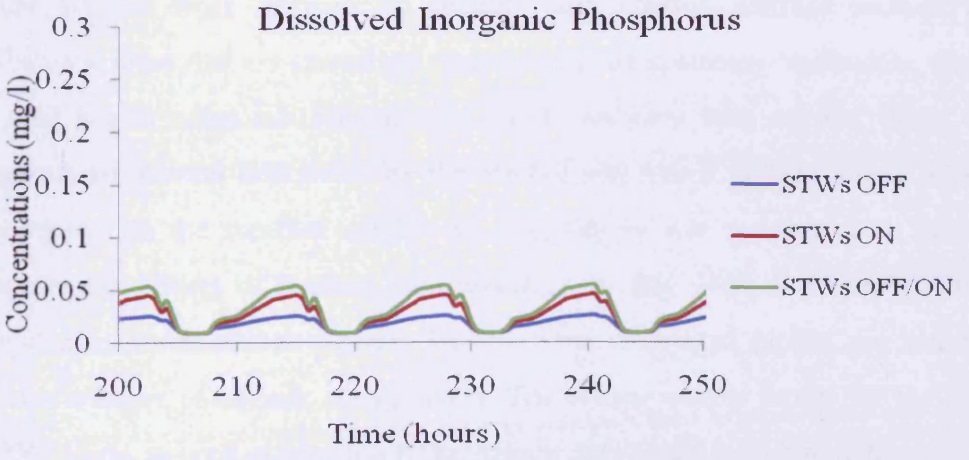

Figure 8-34f Comparison of nutrient concentrations for different STWs scenarios at a site downstream of Llanelli STWs

From Figure 8-34(a-f), it can be seen that the nutrients loads from the STWs have more of an effect on the sites downstream of the works than the sites

upstream. As expected, the lowest nutrient concentrations were always found to occur when the STWs were shut off at each site. For the sites that were just upstream of the STWs, as for the case shown in Figure 8-34 (a, c, e), the nutrient concentrations with the constant nutrients loads appeared to be higher than those with only ebbing loads. This was because the pollutants discharged from the STWs were advected to these locations with the ambient water on the flood tide, although the strength of the source was halved by constantly discharging the pollutants. For these sites, the peak concentrations occurred during flood tide. For the sites that were just downstream of the STWs, as seen in Figure 8-34 (b, d, f), the opposite finding was observed, since the increased nutrient discharge rates were from the upstream STWs during the ebb tide. For these sites, the peak concentrations occurred at the ebb tide.

8.5.3 Impacts of weather conditions

8.5.3.1 Dry and wet weather

Unlike the nutrients discharged from the point sources, the nutrients from the diffuse sources were difficult to quantify and control. Diffuse sources are attributed to areas that are spread out across the entire upstream catchments, where the land use is often not homogeneous and can vary with season. Since the pollutants are carried into rivers by the rainfall and runoff, diffuse source inputs also depend on the weather conditions, e.g., dry or wet weather. This section compares the effects of nutrient concentrations in July 2004 and October 2004 (provided by Environment Agency Wales), which represent typical dry weather and wet weather conditions, respectively. The diffuse source inputs for the DIN and DIP loads, as well as the run-off discharges, are plotted in Figure 8-35.

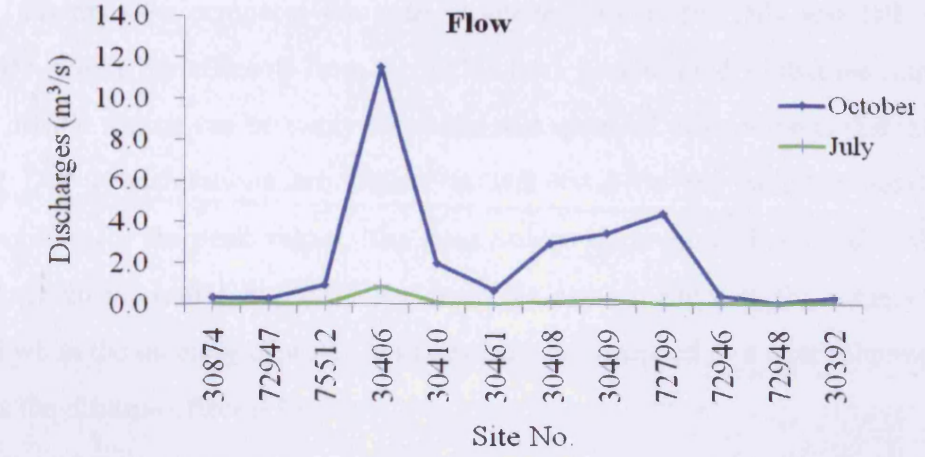

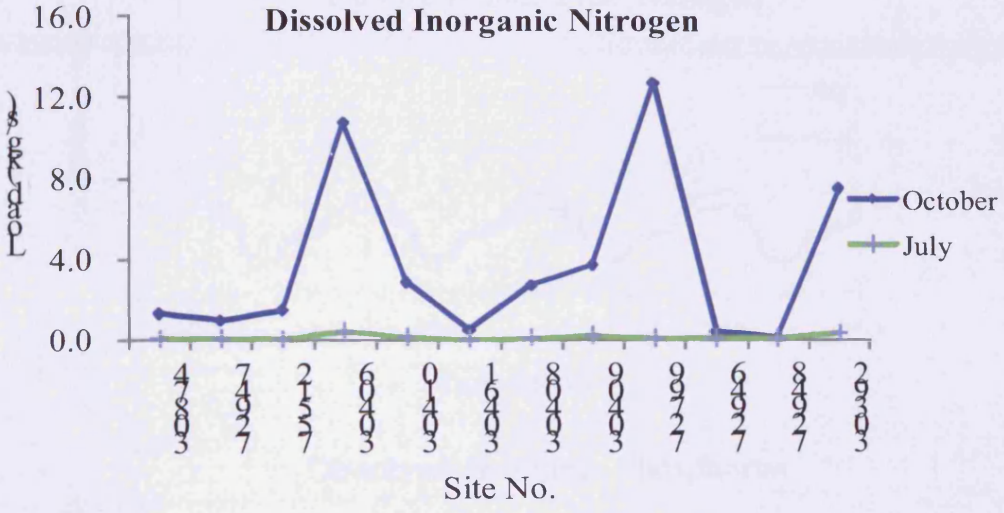

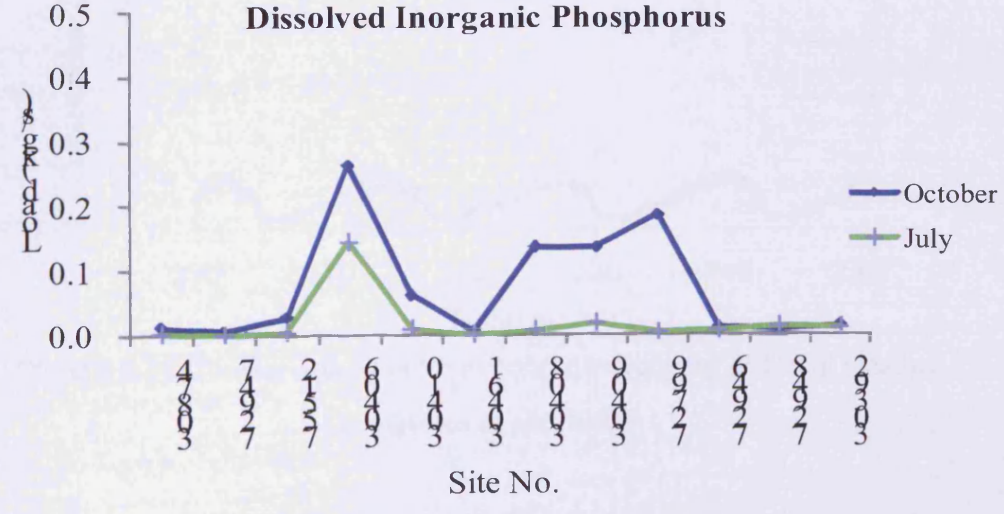

Figure 8-35 Nutrients loads and flow discharges for different weather conditions

Figure 8-36 compares the nutrient concentrations for DIN and DIP at site 72643, where the effluents from the STWs have been diluted so that the impact of the diffuse source can be easily identified and assessed. It is obvious that the DIN and DIP concentrations are higher in wet vis-à-vis dry weather conditions, especially for the peak values. The peak values occur immediately after the ebb tide, when the nutrients are flushed from the estuary edges to the estuary centre and when the quantity of water in the estuary has dropped to a near minimum and thus the dilution effect is low.

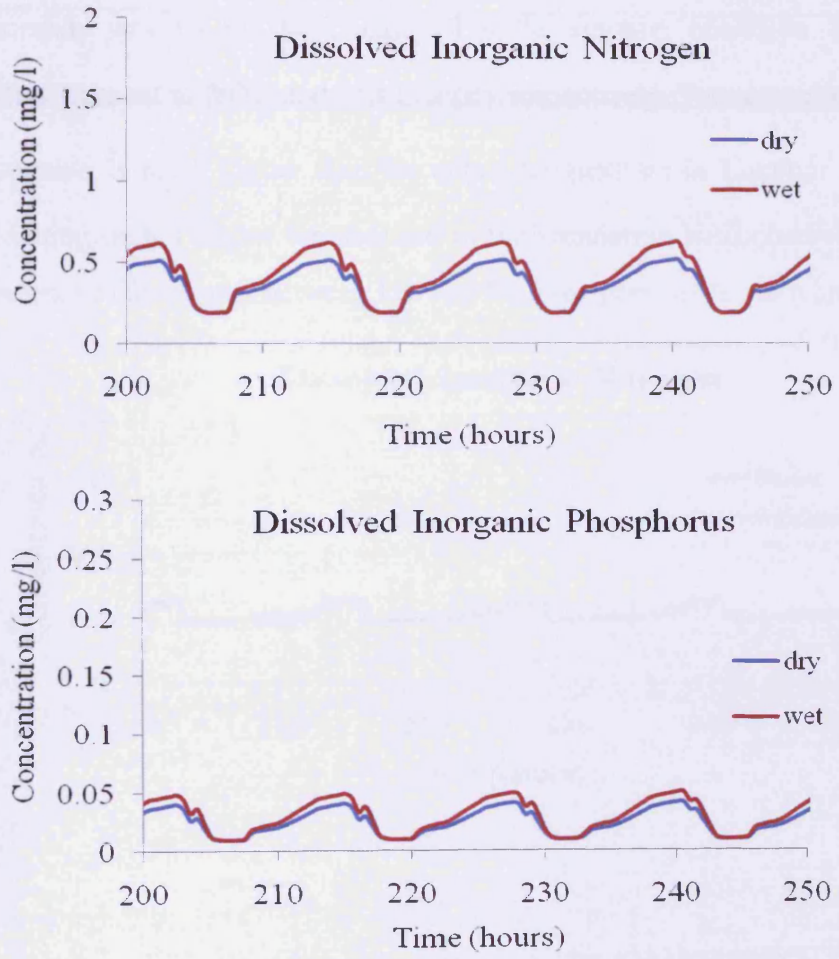

Figure 8-36 Comparison of nutrient concentrations for different weather conditions at site 72643

8.5.3.2 Winter and summer

Aside from the variation in the dry and wet weather conditions, the nutrient concentrations also depend on various biochemical reaction rates which are influenced by the environmental factors, such as water temperature and light intensity. These factors are distinct from season to season. The model simulated the nutrient concentrations in a typical winter and summer condition. For the winter condition, the water temperature was specified to be 5℃ and the average light intensity was set to 190 Langley. For the summer condition, these two parameters were set to 20℃ and 710 Langley respectively. The temperature of 20 ℃ in summer is much higher than the actual temperature in Loughor area. The aim of setting such a higher temperature in the simulation is to observe whether the difference of the results between low and high temperature is obviours.

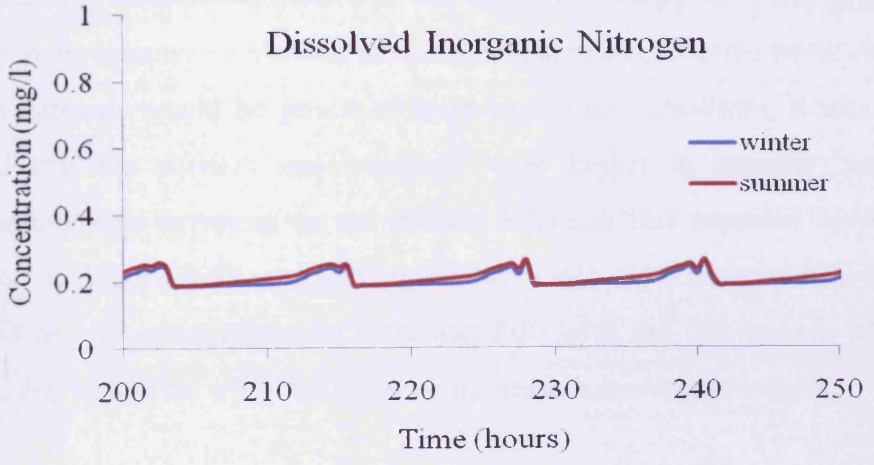

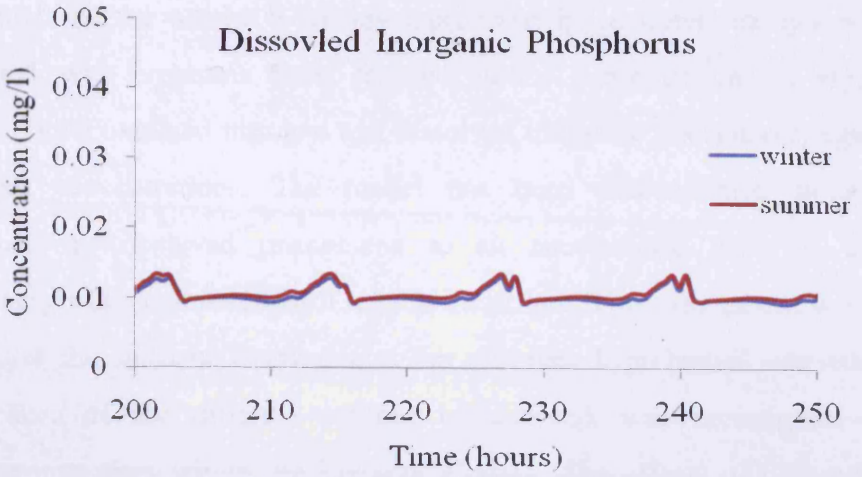

Figure 8-37 Comparison of nutrient concentrations for winter and summer conditions at site 72754

Figure 8-37 compares the DIN and DIP concentrations for typical winter and summer conditions at site 72754, where the nutrient concentrations are mainly determined by biochemical reactions and thus their impacts on the nutrients level could be readily observed and assessed. The high water temperature and large light intensity in the summer accelerated the biochemical reactions in the water column, so more nutrients would be produced from organisms. Therefore, it was to be expected that the nutrient concentrations were higher in summer than the corresponding concentrations in the winter. Although this expected result was confirmed in Figure 8-37, the differences were not significant, which can be explained by the consumption of DIN and DIP with the fast growth of algal biomass, that somewhat offset the aforementioned biochemical processes.

8.6 Summary

In this chapter, the numerical model has been applied to simulate the hydrodynamic and water quality processes in the River Loughor and its estuary. The hydrodynamic model was firstly calibrated and verified against a series of available data, followed by calibration and verification of the sediment transport and salinity distributions against appropriate field data. Finally, the parameters

associated with the nutrient biochemical processes in the water quality model were calibrated, with emphasis being focused on the concentrations of ammonium nitrogen, total oxidized nitrogen and dissolved inorganic phosphorus, against the measured concentrations. The model has been demonstrated to generally reproduce the observed phenomena to an encouraging level of accuracy, particularly when compared with reliable field data. Then, the model was applied to predict the nutrient distributions for different hypothetical scenarios. The significance of the different sources of nutrients was investigated at four representative sites within the Loughor Estuary. The effects of different STWs discharge schemes on the nutrient concentrations in regions upstream and downstream of the outfall sites were evaluated. The impacts of the diffuse source inputs on the nutrient distributions under dry and wet weather conditions were also examined. The sensitivity of the temperature and light intensity was also investigated by choosing typical winter and summer values. An analysis of these results provided informative findings on the behavior and response of nutrients in the estuary to different physical, hydrodynamic and kinetic boundary conditions and biochemical and sediment interactions.

Chapter 9

Conclusions and recommendations for further research

9.1 Conclusions

This study reports on the development and application of a refined hydro-environmental model for predicting the hydrodynamic, solute and sediment transport water quality indicator processes in river, estuarine and coastal waters. The main conclusions and findings from these studies are summarized as follows:

- A second-order shock-capturing numerical scheme, based on a relatively simple five-point TVD-MacCormack scheme, has been refined and applied to solve the depth-integrated solute transport equation, which includes advection, diffusion and kinetic reactions. This separate solute transport model can be linked with different hydrodynamic models, which provide background velocity fields and water depth distributions through a linked computer file. This modeling strategy greatly enhances the flexibility and efficiency of the calibration of water quality models. The model is ideally suited to being linked to an earlier TVD-MacCormack hydrodynamic model, developed within the research centre. This model was originally developed for flood inundation modelling and particularly for dam break and embankment breach flows, for which the TVD-MacCormack scheme is ideally suited.
- The nutrient adsorption/desorption processes have been coupled with a sediment transport model, in order to simulate the nutrient exchange between the bed sediments and the water column. This interaction between the sediments and water column was shown to be a particularly important source of nutrient nourishment or depletion, either to or from the water column

respectively. The sediment deposition and re-suspension processes were also included in calculating the nutrient concentrations in the water column. The coupled model was first verified against derived analytical solutions, which showed that the concentrations of nutrients adsorbed by the sediments were affected by the partition coefficients and the equilibrium concentration of the suspended sediments.

- Linear adsorption and Langmuir adsorption isotherms were used to describe the ammonium nitrogen adsorption process in controlled laboratory experiments. Comparisons between the experimental data and theoretical solutions showed that both linear and Langmuir adsorption isotherms were acceptable for ammonium adsorption at low equilibrium concentrations, while Langmuir adsorption isotherms were more accurate for simulating the adsorption process at high equilibrium concentrations.
- Field sediment samples were analysed for the salinity effects on the adsorption of ammonium nitrogen and orthophosphate. For an increase in salinity, a second-order attenuation was observed for nutrient adsorption, and a relationship between the salinity levels and the degree of nutrient adsorption has been formulated. These formulated relationships were also extended to include the effects of different nutrient equilibrium concentrations, with the nutrient adsorption being described as a function of the equilibrium concentration and salinity.
- Differences were observed in the amount of ammonium attached to the sediments in the ammonium adsorption/desorption experiments, for both distilled and saline water, which indicated that the ammonium adsorption/desorption process was not totally reversible. Therefore the linear adsorption isotherm was adjusted by adding a positive term to represent the amount of ammonium remaining on the sediments after an adsorption/desorption experiment cycle. Similar findings were also found by other researchers, including: Rosenfeld (1979); Hou et. al, (2003).

- Two types of hydrodynamic models, namely the ADI model and the TVD-MacCormack model, were compared in terms of their performances in solving the two dimensional shallow water equations. Different results were obtained for 1-D and 2-D dam-break simulations, while similar results were obtained for the simulations of the Persian/Arabian Gulf simulations, which indicated that the discrepancies between the ADI and TVD-MacCormack models were only apparent when simulating flows with strong water level gradients and regime transitions. In contrast, the two methods produced very similar results when simulating smooth flows. A Simplified Harmonic Method (SHM) for tidal predictions, based on the Admiralty Tide Tables (ATT), was used for the Persian/Arabian Gulf, where the water motion was mainly caused by the astronomic tide. Comparisons between the SHM predicted tidal elevations and the hydrodynamically predicted results at selected points showed good agreement, which verified the correctness of both predictions using the SHM and the hydrodynamic numerical models.
- A versatile water quality model has been established and refined, based on the framework of QUAL2E, and new formulae and coefficients have been introduced based on WASP6. These formulae and coefficients consider various factors for practical scenarios, and especially the exchange between dissolved pollutants and those attached to the sediments. The numerical model has been validated against analytical solutions with good agreement being obtained between the predicted and theoretical results. The parameters associated with the complex chemical, biological and physical processes have been calibrated against field data acquired within the Loughor Estuary, and on the whole good agreement has been obtained between measured and predicted nutrient data for this macro-tidal estuary, confirming that the model refinements are giving good predictions of nutrients in complex estuarine waters, with extensive flooding and drying and high tidal ranges.
- The integrated hydro-environmental model has been applied to simulate the hydrodynamics and the transport of nutrients in the River Loughor and its

estuary. Investigations of nutrient sources showed that the external inputs contributed most of the nutrient fluxes in the upper and middle reaches of the Loughor Estuary, and the biochemical processes were the more important factor in the lower reaches, as compared to the external nutrient inputs. Sediment transport was shown to have a noticeable influence on the nutrient levels in the upper reaches of the basin, but the sediment interactions were far less significant in the lower reaches of the Loughor Estuary.

9.2 Recommendations for further study

Based on the outcomes of this research study, the following key recommendations are proposed for further research:

- The current water quality model considers chlorophyll-a as the representative of phytoplankton, with all of the biological processes calculated based on the parameters related to chlorophyll-a. The diversity of the phytoplankton group should be considered in more detail and more complexity in future studies, with the biological parameters being directly related to the phytoplankton processes.
- The model application to the Loughor Estuary highlighted that the nutrient exchanges between the water and sediments had no obvious effects on the overall nutrient distributions, which was due to the low sediment transport rate and the low adsorption capacity for this site. Further studies should focus on another site, with a higher sediment flux and a higher adsorption capacity, in order to investigate the sediment-nutrient interaction processes.
- This study focused on the hydro-environmental evolution over a relatively short time scale. The deformation of the bed elevation due to sediment deposition and re-suspension was not considered. In a long term study, bed morphological processes would need to be taken into account, particularly when considering the impact on water quality.
- The measured nutrient data used for calibrating the water quality model were

very limited, owing to the restrictions of the field survey. Consecutive water sampling of the nutrient levels during one or two tidal periods would be ideal to achieve a better calibration and verification dataset for the numerical model. It is therefore proposed that more comprehensive field studies be undertaken in the future.

- This study included a preliminary investigation of the diffuse source inputs from upstream catchments. These diffuse sources were specified according to statistical data, while the variations of diffuse sources depended on seasonal variations of land use. Further studies could be undertaken to dynamically link the hydraulic model with a hydrological model, so that the land use variations could be reflected more accurately when modelling water quality indicator processes in the estuary.

References:

1. Abdulgawad, F. (2010) *Field and Laboratory Investigations of the Adsorption of Nitrogen Compounds on Estuarine Based Sediments.* PhD Thesis. Cardiff University.
2. Ambrose, R.B. (1987) Modeling Volatile Organics in the Delaware Estuary. *Journal of Environmental Engineering*, ASCE, 113(4): 703-721.
3. Ambrose, R.B. (1988). *WASP4, A Hydrodynamic and Water Quality Model--Model Theory, User's Manual, and Programmer's Guide.* U.S. Environmental Protection Agency, Athens, GA. EPA/600/3-87-039.
4. Andrieux-Loyer, F. and Aminot, A. (2001) Phosphorus forms related to sediment grain size and geochemical characteristics in French coastal areas. *Estuarine Coastal and Shelf Science,* 52: 617-629.
5. Anggara-Kasih, G. A. and Kitada, T. (2004) Numerical simulation of water quality response to nutrient loading and sediment resuspension in Mikawa Bay, central Japan: quantitative evaluation of the effects of nutrient-reduction measures on algal blooms. *Hysrological Processes* 18: 3037-3059.
6. APHA, (1992). *Standard Methods For The Examination of Water and Waste Water.* American Public Health Association, 18th ed, Academic Press, 214-218, Washington D.C.
7. Armenio, V. (1997) An improved MAC method (SIMAC) for unsteady high-Reynolds free surface flows. *International Journal for Numerical Methods in Fluids,* 24: 185-214.
8. Azam, M. H. and Elshorbagy, W. and Lchikawa, T. et al. 2006. 3D model application to study residual flow in the Arabian Gulf. *Journal of Waterway, Port, Coastal, and Ocean Engineering* 132(5): 388-400.
9. Bao, X.W., Yan, J. and Sun, W.X. (2000) A three-dimensional tidal model in boundary-fitted curvilinear grids. *Estuarine Coastal and Shelf Science,* 50:

775-788.

10. Barnwell, T. O. and Brown, L. C. (1987) *The Enhanced Stream Water Quality Models QUAL2E and QUAL2EUNCAS: Documentation and User Manual.* EPA/600/3-87/007. U.S. Environmental Protection Agency, Washington, DC.
11. Berner, R. A. 1980. *Early diagenesis: A theoretical approach.* Princeton, N. J. Princeton University Press.
12. Blumberg, A.F., Herring, J.J., (1987) Circulation modeling using curvilinear coordinates. In *Three-Dimensional Models of Marine and Estuarine Dynamics,* ed. J. Nihoul, Jamart, B. Elsevier, Amsterdam, Netherlands: 55-88.
13. Blumberg, A.F., Mellor, G.L. (1983) Diagnostic and prognostic numerical circulation studies of the South Atlantic Bight. *Journal of Geophysics Research,* 88: 4579–4592.
14. Blumberg, A.F. and Mellor, G.L. (1987) A Description of a Three-Dimensional Coastal Ocean Circulation Model. IN HEAPS, N. S. (Ed.) *Three-Dimensional Coastal Ocean Models.* American Geophysical Union: Washington, D.C.: 208 pp.
15. Boatman, C.D.and Murray, J.W. (1982) Modelling exchangeable NH_4^+ adsorption in marine sediments: process and controls of adsorption. *Limnology and Oceanography*, 27: 99-110
16. Bockelmann-Evans, BN; Davies, R; Falconer, RA. (2008) Measuring bed shear stress along vegetated river beds using FST-hemispheres. *Journal of Environmental Management.* 88(4): 627-637.
17. Bockelmann-Evans, B. and Schnauder, I. and Fenrich, E. et al. 2007. Development of a catchment-wide nutrient model. *Water Management* 160: 35-42.
18. Bonnefille, R., (1963). Essais de synthese des lois de debut d'entrainment des sediment sous l'action d'un courant en regime uniform. Bull. Du CREC, No. 5, Chatou.
19. Bowie, G. L., Mills, W. B., Porcella, D. B., Campbell, C. L., Pagenkopf, J. R., Rupp, G. L., Johnson, K. M., Chan, P. W. H., Gherini, S. A. & Chamberlin, C.

E. (1985) *Rates, Constants, and Kinetics Formulations in Surface Water Quality Modeling (Second Edition)*. Report EPA/600/3-85/040, U.S. EPA, Athens, GA, USA.

20. Brown, L.C. and Barnwell, T.O. (1987) *The Enhanced Stream Water Quality Models QUAL2E and QUAL2E-UNCAS: Documentation and User Manual.* Report EPA 300/3- 87/007, U.S. EPA, Athens, GA, USA
21. Butler, H.L. (1980) Evolution of a numerical model for simulating long-period wave behavior in ocean-estuarine systems. In *Proceedings of the Symposium on Mathematical-Hydrodynamical Investigations of Physical Processes in the Sea,* Univeristy of Hamburg. 55-59.
22. Camp. (1963). First expanded BOD-DO model. *Basic river water quality models*, IHP-V Project 8.1, D. G. Jolankai, ed., 1997, 27–29.
23. Carlson R.E. and J. Simpson (1996) A Coordinator's Guide to Volunteer Lake Monitoring Methods. *North American Lake* Management Society. 96 pp.
24. Cerco, C. F., and Cole, T. (1993). Three-dimensional eutrophication model of Chesapeake Bay. *Journal of Environmental Engineering*, 119(6): 1006–1025.
25. Chao, X. B., Jia, Y. F., Cooper, C. M., Shields, D. and Wang, S. S. Y. (2006) Development and application of a phosphorus model for a shallow oxbow lake. *Journal of Environmental Engineering*, 132(11):1498-1507.
26. Chapra, S. C. (1997) *Surface Water-Quality Modelling*, McGraw Hill, New York, 844 pp.
27. Chapra, S. C., and Canale, R. (1991). Long-term phenomenological model of phosphorus and oxygen for stratified lakes. *Water Research*, 25, 707–715.
28. Chen, B.F. (1994) Nonlinear Hydrodynamic Pressures by Earthquakes on Dam Faces with Arbitrary Reservoir Shapes. *Journal of Hydraulic Research,* 32: 401-413.
29. Chen, C.S., Liu, H.D. and Beardsley, R.C. (2003) An unstructured grid, finite-volume, three-dimensional, primitive equations ocean model: Application to coastal ocean and estuaries. *Journal of Atmospheric and Oceanic Technology,* 20: 159-186.

30. Chu, W. and Barker, B. L. and Akbar, A. M. (1988). Modeling tidal transport in the Arabian Gulf. *Journal of Waterway, Port, Coastal, and Ocean Engineering* 114(4): 455-471.
31. CHURCHILL, M.A.; ELMORE, H.L. and BUCKINGHAM, R.A. (1962). Prediction of stream reaeration rates. *Journal of the Sanitary Engineering Division*, ASCE 88(1): 1–46.
32. Countryside Council for Wales. 2005. *Carmarthen Bay and Estuaries.European Marine Site.* Countryside Council for Wales.
33. Craig, J. and Rudd, H. and Michael, P. et al. (2007) Review of seven UK tidal energy case studies. *Tidal Power in the UK-Research Report 5.* AEA Energy & Environment. 94-105.
34. Collins, M. B. and Ke, X. and Gao, S. 1998. Tidally-induced flow structure over intertidal flats. *Estuarine, Coastal and Shelf Science,* 46: 233-250.
35. Connolly, J.P. and R. Winfield. (1984) *A User's Guide for WASTOX, a Framework for Modeling the Fate of Toxic Chemicals in Aquatic Environments. Part 1: Exposure Concentration.* U.S. Environmental Protection Agency, Gulf Breeze, FL. EPA-600/3-84-077.
36. De Groot, G.W. (1983) Modelling the multiple nutrient limitation of algal growth. *Ecological modelling.* 18: 99-119
37. de Jonge VN, Elliott M. (2001). *Eutrophication. In Encyclopedia of Marine Sciences.* Steele J, Thorpe S, Turekian K (eds). Academic Press: London.
38. D'Elia, C. F., Sanders, J. G., Boynton, W. R. (1986). Nutrient enrichment studies in a coastal plain estuary: phytoplankton growth in large-scale, continuous culture. *Canadian Journal of Fisheries and Aquatic Science.* 43: 397-406
39. Del Bubba, M., Arias, C.A. and Brix, H. (2003) Phosphorus adsorption maximum of sands for use as media in subsurface flow constructed reed beds as measured by the Langmuir isotherm. *Water Research,* 37: 3390-3400.
40. DELVIGNE, G.A.L. (1980). *Natural reaeration of surface water.* WL | Delft Hydraulics, Report on literature study R1149. Delft, WL | Delft Hydraulics,

(In Dutch.)

41. Di Toro, D.M., D.J. O'Connor, and R.V. Thomann. (1971). A Dynamic Model of the Phytoplankton Population in the Sacramento San Joaquin Delta. *Advances in Chemical Series*. 106, Am. Chem. Soc., Washington, DC., pp. 131-180.
42. Di Toro, D.M. and W.F. Matystik. (1980) *Mathematical Models of Water Quality in Large Lakes, Part 1: Lake Huron and Saginaw Bay.* EPA-600/3-80-056. pp.28-30.
43. Di Toro, D.M. and J.P. Connolly. (1980) *Mathematical Models of Water Quality in Large Lakes, Part 2: Lake Erie.* EPA-600/3-80-065. pp. 90-101.
44. Di Toro, D.M., J.J. Fitzpatrick, and R.V. Thomann. (1981) rev. 1983. *Water Quality Analysis Simulation Program (WASP) and Model Verification Program (MVP) - Documentation.* Hydroscience, Inc., Westwood, NY, for U.S. EPA, Duluth, MN, Contract No. 68-01-3872.
45. Dobbins W E. (1964) BOD and oxygen relationships in streams. *Journal of the Sanitary Engineering Division*, ASCE, 90(SA3): 53-78.
46. DTI 2004. Atlas of UK marine renewable energy resources.*A Strategic Environmental Assessment Report.* Report to the Department of Trade and Industry. pp. 154
47. Edwards, P. (2007) *An assessment of eutrophication risks and impacts in the Burry Inlet and Loughor Estuary.* Environment Agency, Report Ref: EATW/07/02.
48. Einstein, H.A., (1942). Formula for the transportation of bed load. *Transaction of the American Society of Civil Engineers*, 107: 561-597.
49. Elshorbagy, W. and Azam, M. H. and Taguchi, K. (2006). Hydrodynamic characterization and modeling of the Arabian Gulf. *Journal of Waterway, Port, Coastal, and Ocean Engineering* 132(1): 47-56.
50. Engelund, F.A. & Hansen, E., (1972) *A monograph on sediment transport.* Teknisk Vorlag, Copenhagen.
51. Falconer, R.A., (1977). *Mathematical Modelling of Jet-Forced Circulation in*

Reservoirs and Harbours. Ph.D. Thesis, University of London, London, England, 237p.

52. Falconer, RA. (1991) Review of modelling flow and pollutant transport processes in hydraulic basins. *Proceedings of first international conference on water pollution*, Southampton, pp 3-23.
53. Falconer, R.A and Chen, Y. 1996. *Modeling sediment transport and water quality processes on tidal floodplains*. In: Anderson MG, Walling DE, Bates PD, editors. Floodplain processes, Chichester: Wiley.
54. Falconer, R.A., Lin, B., Wu, Y., and Harries, E. (2001) *DIVAST Model: Reference Manual*. Hydro-environmental Research Centre, Cardiff University, 35pp.
55. Fevre, N. M. L. and Lewis, G. D. (2003) The role of resuspension in enterococci distribution in water at an urban beach. *Water Science and Technology*. 47(3): 205-210.
56. Fischer, H.B., List, E.J., Koh, R.C.Y., Imberger, J., Brooks, N.H., (1979). *Mixing in inland and coastal waters*. San Diego, Academic Press, Inc., 483 pp.
57. Fisher, T R. Jr. Harding, L. W. Jr, Stanley, D. W., Ward, L. G. (1988). Phytoplankton, nutrients, and turbidity in the Chesapeake, Delaware, and Hudson estuaries. *Estuarine, Coastal and. Shelf Science*. 27: 61-93
58. Fitzsimons, M. F., Millward G. E., D. M. Revitt, Dawit, M. D. (2006) Desorption kinetics of ammonium and methylamines from estuarine sediments: Consequences for the cycling of nitrogen. *Marine Chemistry* 101: 12–26.
59. Fletcher, C.A.J., (1991). *Computational Techniques for Fluid Dynamics. Volume II: Specific Techniques for Different Flow Categories*. Second Edition, Springer Verlag, Berlin.
60. Fraccarollo L, Toro EF. (1995) Experimental and numerical assessment of the shallow water model for two-dimensional dam-break type problems. *Journal of Hydraulic Research*, 33: 843-864.

61. Gao, L., Li, D.J. and Ding, P.X. (2008) Variation of nutrients in response to the highly dynamic suspended particulate matter in the Changjiang (Yangtze River) plume. *Continental Shelf Research,* 28: 2393-2403.

62. Gardner,W.S., Seitzinger, S.P., Malczyk, J.M. (1991) The effects of sea salts on the forms of nitrogen released from estuarine and freshwater sediments: does ion pairing effect ammonium flux? *Estuaries*, 14: 558-568.

63. Godunov S.K. (1959) A difference scheme for numerical solution of discontinuous solution of hydrodynamic equations, Math. Sbornik, 47: 271-306

64. Harten A. (1983) High resolution schemes for hyperbolic conservation laws. *Journal of computational physics*, 49: 357-393

65. Harten A, Engquist B, Osher S, and Chakravarthy SR. (1987) Uniformly high order accurate essentially non-osscillatory schemes III. *Journal of computational physics*, 71: 231-303

66. Hendry, G.S. (1977). *Relationships Between Bacterial Levels and Other Characteristics of Recreational Lakes in the District of Muskoka.* Interim Microbiology Report, Laboratory Services Branch, Ontario Ministry of the Environment.

67. Henrici, Arthur T., (1938). Seasonal Fluctuation of Lake Bacteria in Relation to Plankton Production. *Journal of Bacteriology*, 35:129-139.

68. Hills, J.H. and Pirzada, I.M. (1984) An Examination of the Accuracy of an Approximate Solution to Isothermal Packed-Bed Adsorption with a Linear Isotherm. *Chemical Engineering Science,* 39: 919-922.

69. Hipsey, M.R., Romero, J.R., Antenucci, J.P. and Hamilton, D. (2006) *Computational Aquatic Ecosystem Dynamics Model: CAEDYM v2.* Centre for Water Research, University of Western Australia.

70. Hirt C.W and Nichols B.D. (1981) Volume of fluid (VOF) method for dynamics of free boundaries. *Journal of computational physics*, 39: 201-225

71. Holly F.M and Usseglio-Polatera J.M. (1984) Dispersion in two-dimensional flow. *Journal of hydraulic engineering*, 110: 905-926

72. Horsburgh, K.J., 1999. *Observations and modelling of the Western Irish Sea Gyre.* PhD Thesis, University of Wales, Bangor, Bangor, United Kingdom, 171 pp.

73. Hou, L.J. and Liu, M. and Jiang, H.Y. et al. (2003) Ammonium adsorption by tidal flat surface sediments from the Yangtze Estuary. *Environmental Geology* 45: 72-78.

74. Hou, L.J., Liu, M., Yang, Y., Ou, D.N., Lin, X., Chen, H. and Xu, S.Y. (2009) Phosphorus speciation and availability in intertidal sediments of the Yangtze Estuary, China. *Applied Geochemistry,* 24: 120-128.

75. HydroQual Inc., (2002) *A Primer for ECOMSED Version 1.3 User Manual.* http://www.hydroqual.com/ehst_ecomsed.html

76. Ishikawa, M., and Nishmura, H. (1989). Mathematical model of phosphate release rate from sediment considering the effect of dissolved oxygen in overlying water. *Water Research*, 23: 351–359.

77. James, R. T. and Martin, J. and Wool, T. et al. 1997. A sediment resuspension and water quality model of lake Okeechobee. *Journal of the American Water Resources Association* 33(3): 661-680.

78. Jogensen, S.E., (1999). State-of-the-art of ecological modeling with emphasis on development of structural dynamic models. *Ecological Modelling.* 120: 75–96.

79. JRB, Inc. (1984) *Development of Heavy Metal Waste Load Allocations for the Deep River, North Carolina.* JRB Associates, McLean, VA, for U.S. EPA Office of Water Enforcement and Permits, Washington, DC.

80. Kampf, J. and Sadrinasab, M. (2005). The circulation of the Persian Gulf: a numerical study. *Ocean Science Discussion* (2): 129-164.

81. Kankara, R. S., Subramanian, B. R. and Sampath, V. (2007) Validation of a deterministic hydrodynamic model in the ICZM framework for Gulf of Kachchh, India. *Journal of Coastal Research,* 23: 1324-1331.

82. Karickhoff, S.W., Brown, D.S. and Scott, T.A. (1979) Sorption of Hydrophobic Pollutants on Natural Sediments. *Water Research,* 13: 241-248.

83. Kashefipour, S. M., Lin, B., Harris, E. and Falconer, R. A. (2002) Hydro-environmental modelling for bathing water compliance of an estuarine basin. *Water Research,* 36: 1854-1868.

84. Kalff, J., 2002. *Limnology*. Prentice-Hall, New Jersey, pp. 592

85. Krom, M. D. and Berner, R. A. (1980) Adsorption of phosphate in anoxic marine sediments. *Limnology and Oceanography* 25(5): 797-806.

86. Krone, R.B. (1962). *Flume Studies of the Transport of Sediment in Estuarial Shoaling Processes*, Technical Report, Hydraulic Engineering Laboratory, University of California, Berkeley California.

87. Langmuir, I. (1916) The constitution and fundamental properties of solids and liquids Part I Solids. *Journal of the American Chemical Society,* 38: 2221-2295.

88. Lardner, R. W. and Belen, M. S. and Cekirge, H. M. (1982). Finite difference model for tidal flows in the Arabian Gulf. *Computers and Mathematics with Applications* 8(6): 425-444.

89. Leo, A., Hansch, C. and Elkins, D. (1971) Partition Coefficients and Their Uses. *Chemical Reviews,* 71: 525-616.

90. Levasseur, A., Shi, L., Wells, N. C., Purdie, D. A. and Kelly-Gerreyn, B. A. (2007) A three-dimensional hydrodynamic model of estuarine circulation with an application to Southampton Water, UK. *Estuarine Coastal and Shelf Science,* 73: 753-767.

91. Liang, D., Falconer, R. A. and Lin, B. (2006) Improved numerical modelling of estuarine flows. *Proceedings of the Institution of Civil Engineers-Maritime Engineering,* 159: 25-35.

92. Liang, D. Lin, B and Falconer, RA. (2007) Simulation of rapidly varying flow using an efficient TVD-MacCormack scheme. *International journal for numerical methods in fluids*, 53: 811-826.

93. Liang D, Wang X, Falconer RA and Bockelmann-Evans BN (2010) Solving the depth-integrated solute transport equation with a TVD-MacCormack scheme, *Environmental modelling & Software*, 25:1619-1629.

94. Liggett, J. A. 1994. *Fluid Mechanics*. McGraw-Hill, Inc., pp. 264-272.

95. Lin B and Falconer RA. (1997) Tidal flow and transport modeling using ULTIMATE QUICKEST scheme. Journal of hydraulic engineering, 123 (4): 303-314

96. Lin, B., Wicks, J. M., Falconer, R. A. and Adams, K. (2006) Integrating 1D and 2D hydrodynamic models for flood simulation. *Proceedings of the Institution of Civil Engineers-Water Management,* 159: 19-25.

97. Liu, X., Landry, B. J. and Garcia, M. H. (2008) Two-dimensional scour simulations based on coupled model of shallow water equations and sediment transport on unstructured meshes. *Coastal Engineering,* 55: 800-810.

98. Louaked M, Hanich L. (1998) TVD scheme for the shallow water equations. *Journal of Hydraulic Research,* 36 (3): 363-378.

99. Lowe, W.E. (1976). Canada Centre for Inland Waters 867 Lakeshore Road, Burlington, Canada L7R 4A6. Personal communication.

100. Mackin, J. E. and Robert C, A. (1984) Ammonium adsorption in marine sediments. *Limnology and Oceanography* 29(2): 250-257.

101. Martin, J.L., McCutcheon, S.C. and Schottman R.W. (1999) *Hydrodynamics And Transport For Water Quality Modeling.* CRC Press, Inc., 194pp.

102. Menon, A.S., W.A. Gloschenko, and N.M. Burns. (1972). Bacteria-Phytoplankton Relationships in Lake Erie. *Proc. 15th Conf. Great Lakes Res.* 94-101. Inter. Assoc. Great Lakes Res.

103. Mingham CG, Causon DM. (1998) High-resolution finite volume method for shallow water flows. *Journal of Hydraulic Engineering,* 124(6): 605-614.

104. Mingham CG and Causon DM. (2008) A simple high-resolution advection scheme. *International Journal for Numerical Methods in Fluids,* 56: 469-484.

105. Morin, J. and Morse, J. W. (1999) Ammonium release from resuspended sediment in the Lagona adre estuary. *Marine Chemistry* 65: 97-110.

106. Namin, M., Lin, B. & Falconer, R. A. (2004) Modelling estuarine and coastal flows using an unstructured triangular finite volume algorithm.

Advances in Water Resources, 27: 1179-1197.

107. Nedwell DB, Jickells TD, Trimmer M, Sanders RW. (1999). Nutrients in estuaries. In *Advances in Ecological Research*, vol. 29, Nedwell DB, Raffaelli DG (eds). Academic Press.

108. Nixon SW. (1995). Coastal marine eutrophication: a definition, social causes, and future concerns. *Ophelia* 41: 199–219.

109. O'CONNOR, D.J. and DOBBINS, W.E. (1958). Mechanism of reaeration in natural streams. *Transactions of the American Society of Civil Engineers*, 123:. 641–66.

110. O'Connor, D.J., J.A. Mueller, and K.J. Farley. (1983) Distribution of Kepone in the James River Estuary. *Journal of the Environmental Engineering*, ASCE. 109(EE2):396-413.

111. OWENS, M.; EDWARDS, R.W. and GIBBS, J.W. 1964. Some reaeration studies in streams. *International Journal of Air and Water Pollution*, 8:. 469–86.

112. Paerl, H. W. and Whitall, D. R. (1999) Anthropogenically-derived atmospheric nitrogen deposition, marine eutrophication and harmful algal bloom expansion: Is there a link? *Ambio,* 28: 307-311.

113. Partheniades, E. (1962). *A Study of Erosion and Deposition of Cohesive Soils in Salt Water*, Ph.D. Thesis, University of California, Berkeley.

114. Rao C N R (1994) *Chemical approaches to the synthesis of inorganic materials.* New Delhi: Wiley Eastern Ltd.

115. Rao, S.S. (1976). *Observations on Bacteriological Conditions in the Upper Great Lakes*. 1968-1974. Scientific Series. No. 64. Inland Waters Directorate CCIW Branch, Burlington, Ontario.

116. Raudkivi, A. J. 1998. *Loose Boundary Hydraulics*. Rotterdam, Netherlands: A.A. Balkema Publishers.

117. Reddy, K. R. and Fisher, M. and Ivanoff, D. (1996) Resuspension and diffusive flux of nitrogen and phosphorus in a hypereutrophic lake. *Journal of Environmental Quality* 25(2): 363-371.

118. Riley, G.A., H. Stommel and D.F. Bumpus. (1949). Quantitative Ecology of the Plankton of the Western North Atlantic. Bull. Bingham Oceanog. Coll. 12(3): 1-169.

119. Roache, P. J. (1972). *Computational Fluid Dynamics*. Albuquerque, New Mexico: Hermosa Publishers.

120. Rodrigues, C. C., de Moraes, D., da Nobrega, S. W. and Barboza, M.G. (2007) Ammonia adsorption in a fixed bed of activated carbon. *Bioresource Technology*. 98: 886-891.

121. Roe PL. (1981) Approximate Riemann solvers, parameter vectors, and difference schemes. Journal of computational physics, 43: 357-372

122. Rosenfeld., J. K. (1979) Ammonium adsorption in near shore anoxic sediments. *Limnology and Oceanography*. 24: 356-364.

123. Ruley, J. E., and Rusch, K. A. (2004). Development of a simplified phosphorus management model for a shallow, subtropical, urban hypereutrophic lake. *Ecological Engineering*, 22: 77–98.

124. Sabbagh-Yazdi, S. R. and Zounemat-Kermani, M. and Kermani, A. (2007). Solution of depth-average tidal currents in Persian Gulf on unstructured overlapping finite volumes. *International Journal for Numerical Methods in Fluids* (in press).

125. Scavia D. and Park R.A. (1976) Documentation of Selected Constructs and Parameter Values in the Aquatic Model of CLEANER. *Ecological modelling*. 2: 38-58

126. Schnauder, I., Bockelmann-Evans, B. and Lin, B. (2007) Modelling faecal bacteria pathways in receiving waters. *Proceedings of the Institution of Civil Engineers-Maritime Engineering,* 160: 143-153.

127. Schnoor, J. L. (1996) *Environmental modelling, fate and transport of pollutants in water, air and soil*. New York, Wiley.

128. Scott CR, Hemingway KL, Elliott M, de Jonge VN, Penthick JS, Malcolm S, Wilkinson M. (1999). *Impact of Nutrients in Estuaries. Phase 2: Summary Report*. Environment Agency of England and Wales.

129. Sheilds, A., (1936). *Anwendung der Ahnlichkeitsmechanik und Turbulenzforschung auf Geschiebebewegung.* Mitteilungen der Preuss. Versuchsanst. f. Wasserbau u. Schiffbau, Heft 26, Berlin.

130. Smith, E.L. (1936) Photosynthesis in Relation to Light and Carbon Dioxide, *Proceedings of the National Academy of Science*, 22: 504-510.

131. Stapleton, C.M., Wyer, M.D., Kay, D., Bradford, M., Humphrey, N., Wilkinson, J., Lin, B., Yang, Y., Falconer, R.A., Watkins, J., Francis, C.A., Crowther, J., Paul,N.D., Jones, K. and McDonald, A.T., 2007. *Fate and Transport of Particles in Estuaries, Volume III.* Environment Agency Science Report SC000002/SR1-4.

132. Steele, J.H. 1962. Environmental Control of Photosynthesis in the Sea. *Limnology and Oceanography.* 7:137-150.

133. Straskraba, M., (1994). Ecotechnological models for reservoir water quality management. *Ecological Modelling.* 74: 1–38.

134. Streeter, H.W. and Phelps, E.B, (1925) *A Study of the pollution and natural purification of the Ohio river*, U.S. Public Health Service, Washington D.C.

135. Swarbrick, J. (1984) *Burry Inlet/Three Rivers: A Survey of Shellfish Stocks.* MAFF Commission, Technical Report No.261.

136. Swartzman G.L. and Bentley R. (1979) A review and comparison of phytoplankton simulation models. Journal of the International Society for *Ecological Modelling.* 1(2): 30-81

137. Tetra Tech, Inc., (2002): *Theoretical and computational aspects of sediment and contaminant transport in EFDC.* A report to the U. S. Environmental Protection Agency, Fairfax, VA.

138. Thomann, R. V. (1970) *System Analysis and Water Quality Management*, McGraw Hill, New York.

139. Thomann, R.V. (1975) *Mathematical Modeling of Phytoplankton in Lake Ontario, 1. Model Development and Verification.* U.S. Environmental Protection Agency, Corvallis, OR. EPA-600/3-75-005.

140. Thomann, R.V., R.P. Winfield, D.M. Di Toro, and D.J. O'Connor. (1976) *Mathematical Modeling of Phytoplankton in Lake Ontario, 2. Simulations Using LAKE 1 Model.* U.S. Environmental Protection Agency, Grosse Ile, MI, EPA-600/3-76-065.

141. Thomann, R.V., R.P. Winfield, and J.J. Segna. (1979) *Verification Analysis of Lake Ontario and Rochester Embayment Three Dimensional Eutrophication Models.* U.S. Environmental Protection Agency, Grosse Ile, MI, EPA-600/3-79-094.

142. Thomann, R.V. and J.J. Fitzpatrick. (1982) *Calibration and Verification of a Mathematical Model of the Eutrophication of the Potomac Estuary.* Prepared for Department of Environmental Services, Government of the District of Columbia, Washington, D.C.

143. Thomann, R.V. and Mueller, J.A. (1987) *Principles of Surface Water Quality Modeling and Control.* New York: Harper Collins Publishers Inc.

144. Thomas H. A. (1948) Pollution load capacity of streams. *Water and Sewage Works*, 95: 409.

145. Tseng MH, Chu CR. (2000) Two-dimensional shallow water flows simulation using TVD-MacCormack scheme. *Journal of Hydraulic Research*, 31: 123-131.

146. UKHO 2007. *Admiralty Tide Tables*. The United Kingdom Hydrographic Office.

147. USACE, Hydrologic Engineering Center (2004) *HEC-RAS Hydraulic Reference Manual.* http://www.hec.usace.army.mil

148. USEPA, (2002) *Environmental Fluid Dynamics Code, Hydro Version.* http://www.epa.gov/athens/wwqtsc/html/efdc.html

149. Van Leer, B., (1979). Towards the ultimate conservative difference scheme. V. A second order sequel to Godunov's scheme. *Journal of computational physics* 32: 101-136.

150. VAN PAGEE, J.A. (1978). *Natural reaeration of surface water by the wind.* Report on literature study R1318-II. Delft, the Netherlands, WL | Delft

Hydraulics. (In Dutch.)

151. Van Rijn, L.C., (1984a), Sediment Transport, Part I: Bed Load Transport, *Journal of Hydraulic Engineering*, ASCE, 110(10): 1431-1457.

152. Van Rijn, L.C., (1984b), Sediment Transport, Part II: Suspended Load Transport, *Journal of Hydraulic Engineering*, ASCE, 110(11): 1613-1641.

153. Van Rijn, L.C., (1993), *Principles of Sediment Transport in Rivers, Estuaries and Coastal Seas*, Aqua Publications, Netherlands.

154. Vidal M, Duarte CM, Sa′ nchez MC. (1999). Coastal eutrophication research in Europe: progress and imbalances. *Marine Pollution Bulletin* 38: 851–854.

155. Vitousek, P. M., Aber, J. D., Howarth, R. W., Likens, G. E., Matson, P. A., Schindler, D. W., Schlesinger, W. H. and Tilman, G. D. (1997) Human alteration of the global nitrogen cycle: Sources and consequences. *Ecological Applications,* 7: 737-750.

156. Vollenweider, R.A., and Kerekes, J. (1982). *Eutrophication of waters. Monitoring, assessment and control.* OECD Cooperative programme on monitoring of inland waters (Eutrophication control), Environment Directorate, OECD, Paris. 154 pp.

157. Vreugdenhil, C. B. (1994) *Numerical Methods for Shallow-Water Flow.* Dordrecht: Kluwer Academic Publishers.

158. Wang, H. and Appan, A. and Gulliver, J. S. (2003a). Modeling of phosphorus dynamics in aquatic sediments: I—model development. *Water Research.* 37: 3928-3938.

159. Wang, H. and Appan, A. and Gulliver, J. S. (2003b). Modeling of phosphorus dynamics in aquatic sediments: II—examination of model performance. *Water Research.* 37: 3939-3953.

160. Wang, J.D., Blumberg, A.F., Butler, H.L., Hamilton, P. (1990) Transport prediction in partially stratified tidal water. *Journal of Hydraulic Engineering,* 116(3): 380-396.

161. Wang JS, Ni HG, He YS. (2000) Finite-difference TVD scheme for

computation of dam-break problems. *Journal of Hydraulic Engineering,* 126(4): 253-262.

162. Wang, S. G., Jin, X. C., Pang, Y., Zhao, H. C., Zhou, X. N. and Wu, F. C. (2005) Phosphorus fractions and phosphate sorption characteristics in relation to the sediment compositions of shallow lakes in the middle and lower reaches of Yangtze River region, China. *Journal of Colloid and Interface Science,* 289: 339-346.

163. Weast, R.C., and M.J. Astle, ed. (1980). *CRC Handbook of Chemistry and Physics*. CRC Press, Boca Raton, FL.

164. Weston, N. B., Giblin, A. E., Banta, G. T., Hopkinson, C. S. and Tucker, J. (2010) The Effects of Varying Salinity on Ammonium Exchange in Estuarine Sediments of the Parker River, Massachusetts. *Estuaries and Coasts,* 33: 985-1003.

165. Winterwerp, J.C. and Van Kesteren, W.G.M. (2004) *Introduction to the Physics of Cohesive Sediment in the Marine Environment.* ELSEVIER B.V., 576pp.

166. Wlosinski, J. H. and Minshall, G. W. (1983) Predictability of Stream Ecosystem Models of Various Levels of Resolution. *Fontaine, T. D. Iii and S. M. Bartell (Ed). Dynamics of Lotic Ecosystems.* Ann Arbor Science Publishers: Ann Arbor, Mich., USA. Illus. Issbn 0-250-40612-8, pp 69-86.

167. Wool, T. A., Ambrose, R. B., Martin J. L. and Comer, E. A. (2001) *Water Quality Simulation Program (WASP) Version 6 Draft: User's Manual.* US Environmental Protection Agency.

168. Wu, Y. Falconer R.A. and Lin B. (2005). Modelling trace metal concentration distributions in estuarine waters. *Estuarine, Coastal and Shelf Science*. 64: 699-709.

169. Xia, J. Q., Lin, B. L., Falconer, R. A. and Wang, G. Q. (2010) Modelling dam-break flows over mobile beds using a 2D coupled approach. *Advances in Water Resources,* 33: 171-183.

170. Yalin, M.S., (1972) *Mechanics of Sediment Transport.* Pergamm Press,

N.Y., 290 pp.

171. Yuan, D. (2007). *Development of An Integrated Hydro-environmental Model and its Application to a Macro-tidal Estuary*. PhD Thesis. Cardiff University.